UNIVERSITY OF SOUTHAMPTON
FACULTY OF ENGINEERING AND THE ENVIRONMENT
INSTITUTE OF SOUND AND VIBRATION RESEARCH

FLUID COUPLING AND WAVES IN THE COCHLEA

BY

GUANGJIAN NI

THESIS FOR THE DEGREE OF DOCTOR OF PHILOSOPHY

NOVEMBER 2012

UNIVERSITY OF SOUTHAMPTON

ABSTRACT

FACULTY OF ENGINEERING AND THE ENVIRONMENT

INSTITUTE OF SOUND AND VIBRATION RESEARCH

Doctor of Philosophy

Fluid Coupling and Waves in the Cochlea

by Guangjian Ni

The cochlea plays an important role in human hearing. Its basic function is to map sounds of different frequencies onto corresponding characteristic positions on the basilar membrane, BM. When sounds enter the fluid-filled cochlea, deflections of the BM occur due to pressure differences between the cochlear fluid chambers. These deflections propagate along the cochlea to a frequency-dependent characteristic position and then decay away rapidly. The mechanics of the cochlea are modelled using both analytic and numerical models. In this thesis, the passive response of the cochlea is analysed, corresponding to its behaviour at high sound levels, to study the fluid coupling and waves in the cochlea.

The fluid coupling is studied in 1D and 3D, uniform and non-uniform, uncoiled and coiled geometries, all with a passive basilar membrane. A ‘uniaxial model’, which is dependent on only a single dimension, is developed to represent the three-dimensional cochlea. The finite element method is also used to provide an independent check of the results from the analytic model.

Analytic methods are used to predict waves due to different mechanisms in the passive cochlea, such as 1D and 3D fluid coupling and longitudinal BM dynamics. The wave finite element, WFE, method is then used to decompose the results of a full finite element model of the coupled cochlea into wave components. Results show that apart from the conventional slow wave, other additional types of wave in the passive cochlea do not appear to play a dominant role in normal passive cochlear function.

Table of Contents

List of Figures

List of Tables

Declaration of Authorship

I, Guangjian Ni,

declare that the thesis entitled

Fluid Coupling and Waves in the Cochlea

and the work presented in the thesis are both my own, and have been generated by me as the result of my own original research.

I confirm that:

- ➢ this work was done wholly or mainly while in candidature for a research degree at this University;
- ➢ where any part of this thesis has previously been submitted for a degree or any other qualification at this University or any other institution, this has been clearly stated;
- ➢ where I have consulted the published work of others, this is always clearly attributed;
- ➢ where I have quoted from the work of others, the source is always given. With the exception of such quotations, this thesis is entirely my own work;
- ➢ I have acknowledged all main sources of help;
- ➢ where the thesis is based on work done by myself jointly with others, I have made clear exactly what was done by others and what I have contributed myself;
- ➢ parts of this work have been published as:

  - ✓ Ni, G., Elliott, S. J. and Mace, B. R. (**2010**) A fluid-structural model of the cochlea using wave finite element method. In Brennan, M.J., Kovacic, Ivana, Lopes, V., Murphy, K., Petersson, B., Rizzi, S. and Yang, T., editors, *Recent Advances Structural Dynamics: Proceedings of the X International Conference*, Southampton.
  - ✓ Elliott, S. J., Lineton, B. and Ni, G. (**2011**) *Fluid coupling between the elements in a discrete model of cochlear mechanics,* ISVR Technical Memorandum 990, University of Southampton, 98pp.

- ✓ Elliott, S. J., Lineton, B. and Ni, G. (**2011**) Fluid coupling in a discrete model of cochlear mechanics, *The Journal of the Acoustical Society of America*, 130 (3), 1441-1451.
- ✓ Ni, G., Elliott, S. J., Lineton, B. and Saba, R. (**2011**) Finite element modelling of fluid coupling in the coiled cochlea. In Shera, C.A. and Olson, E.S., editors, *What Fire is in Mine Ears: Progress in Auditory Biomechanics*, pp 350-355. (DOI: 10.1063/1.3658164)
- ✓ Elliott, S. J., Ni, G., Mace, B. R. and Lineton, B. (**2011**) How many waves propagate in the cochlea? In Shera, C.A. and Olson, E.S., editors, *What Fire is in Mine Ears: Progress in Auditory Biomechanics*, pp 563-568. (DOI: 10.1063/1.3658164)
- ✓ Elliott, S. J., Lineton, B. and Ni, G. (**2011**). Fluid coupling in a discrete cochlear model. In Shera, C.A. and Olson, E.S., editors, *What Fire is in Mine Ears: Progress in Auditory Biomechanics*, pp 328-332. (DOI: 10.1063/1.3658164)
- ✓ Ni, G., Elliott, S. J. and Langley, A. (**2012**) Waves in Loudspeaker Cones, *ISMA 2012*, Leuven, Belgium.
- ✓ Elliott, S. J., Ni, G. and Lineton, B. (**2012**) Decomposition of the cochlear response using wave finite elements, *19th International Congress on Sound and Vibration*, Vilnius, Lithuania.
- ✓ Ni, G., Elliott, S. J. and Mace, B. R. (**2012**). *Wave Propagation and Decomposition in the Cochlea with Orthotropic Basilar Membrane*, Innovations in Wave Modelling (InnoWave 2012), Nottingham, UK (Poster).
- ✓ Elliott, S. J., Ni, G., Mace, B. R. and Lineton, B. (**2012**) A Wave Finite Element Analysis of the Passive Cochlea, *The Journal of the Acoustical Society of America* (submitted).
- ✓ Elliott, S. J., Ni, G., Mace, B. R. and Lineton, B. (**2012**) *Wave Propagation in the Cochlea*, ISVR Technical Memorandum 996, University of Southampton, 98pp.

Signed: ………………………………………………………………………..

Date:……………………………………………………………………….

Acknowledgements

I would like to thank Professor Stephen Elliott, Professor Brian Mace and Doctor Ben Lineton for their valuable guidance, patient help and comprehensive support. Their comments are always helping and encouraging me to move forward. It was my great pleasure and fortune to work with them. Particular appreciation to Professor Elliott for his kind hearted support. His passion and rigorous attitude for research set a good example for me and will benefit me for a lifetime.

I would like to thank my parents not only for giving me life but also for teaching me how to be a good man. A big thank you to my wife for her continuous support and understanding.

I also want to thank those I have met at the ISVR. They have provided a lifelong wealth of friendship.

I would like to take this thesis as a present to my new-born daughter and wish she is happy and health always.

Symbols and Abbreviations

General Symbols

$\| \ \|$	Absolute value of a quantity
$(\ )^{T}$	Transpose
$\angle$	Phase of a quantity [cycles]
$\sum$	Summation operator
∂	Partial differential operator
Re( )/ Im( )	Real/imaginary part of a complex variable
$\mathbf{I}$	Unit matrix
ω	Angular frequency [radian/s]
f	Frequency [Hz]
ρ	Density [kg/m^3]
c	Sound speed [m/s]
k	Wavenumber [m^{-1}]
λ	Wavelength [m]; eigenvalue
ζ_0	Damping ratio
η	Loss factor
E	Young’s modulus [Pa]
D	Flexural rigidity [N m^2]
G	Shear modulus [Pa]
υ	Poisson’s ratio
$\mathbf{H}$	Acoustic stiffness matrix
$\mathbf{Q}$	Acoustic inertia matrix
$\mathbf{M}$	Mass matrix
$\mathbf{K}$	Stiffness matrix
$\mathbf{S}$	Structural-acoustic coupling matrix
$\mathbf{R}$	Acoustic-structural coupling matrix
$\mathbf{T}$	Transfer matrix
ϕ	Velocity potential [m^2/s]; cumulative phase
$\boldsymbol{\Psi}$	Left eigenvector
$\boldsymbol{\varphi}$	Right eigenvector
$\mathbf{a}$	Amplitude vector

Abbreviations

FFT	Fast Fourier Transform
IFFT	Inverse Fast Fourier Transform
BM	Basilar Membrane
CP	Cochlear Partition
IHC	Inner Hair Cell
OHC	Outer Hair Cell
LC	Longitudinal Coupling
LR	Locally-reacting
OC	Organ of Corti
SM	Scala Medium
SV	Scala Vestibuli
ST	Scala Tympani
TM	Tectorial Membrane
CF	Characteristic Frequency
WKB	Wentzel-Kramers-Brillouin approximation
FE	Finite Element
WFE	Wave Finite Element
SPL	Sound Pressure Level
DOF	Degree of Freedom

General Comments

- Matrices are presented in upper case, bold typeface; vectors are presented in lower case, bold typeface; scalars are presented in italic typeface.
- Time harmonic vibration is assumed throughout the thesis and the notation of a given variable's dependency on x, ω or t is occasionally suppressed for convenience.
- "$\dot{u}$" and "$\ddot{u}$" indicate the first and second derivatives of a variable, u, with respect to time.

Chapter 1. Introduction

This thesis is concerned with modelling the mechanics of the mammalian cochlea, which forms part of the inner ear. Both analytic and numerical methods are used for modelling. In particular, the wave finite element (WFE) method, which has previously been used to analyse uniform, or periodic, engineering structures, is used here for the first time to link the wave approach, found in analytic methods, with the finite element approach, found in numerical methods.

This introductory chapter begins with a brief review of the structure and function of the cochlea. A general overview of methods of modelling the mechanics of the cochlea is then provided. The structure of the remainder of the thesis and its main contributions are then discussed at the end of the chapter.

1.1 The Cochlea

The human ear consists of three main components, the outer, middle and inner ears. The main functions of the outer ear are to enhance the amplitude of the sound wave at the eardrum and to assist with locating sound. The middle ear includes three small bones whose geometry provides a lever arrangement that optimises energy transfer from the outer ear, which is filled with air, to the cochlea, which is filled with fluid. In other words, the middle ear provides an impedance matching mechanism between the outer ear and the cochlea. The inner ear consists of two parts which are housed in the temporal bones, the cochlea and the vestibular organs. The vestibular organ is related with the sense of balance but we will focus on the cochlea in this research.

1.1.1 Cochlear Structure

The length of the cochlea itself is about 35 mm in humans. From a structural point of view, the cochlea is housed in a rather inaccessible part of the skull, totally embedded in bone. Furthermore, the cochlea is also notable for its complicated geometry and small physical size. In spite of these, Retzius, Huschke, Reissner, Kölliker, Deiters, Hensen, and Corti studied its anatomical mystery in the mid-nineteenth century (Dallos, *et al.*, 1996). They described that the cochlea is composed of a bony labyrinth, within which is found the cellular structures comprising a membranous labyrinth, as shown in Figure 1.1.

Figure 1.1 shows a bony tube spiralling around the modiolus, which forms the central axis of the cochlea, from the base to apex. The interior of the bony labyrinth is partitioned into three tubes or spaces (scalae). The upper, more apical space (scala vestibule, SV) is separated from the middle (scala media, SM) by Reissner’s membrane, which is only two cell layers thick and has a similar density to that of the fluid in the cochlea. The main function of Reissner’s membrane is to separate endolymph from perilymph and is generally assumed to be “acoustically transparent” having no influence to the cochlear mechanical functions (Dallos, *et al.*, 1996). From the vantage point of cochlear mechanics, the SV and SM can thus be thought as a single fluid chamber. The SM is separated from the lower space (scala tympani, ST) by parts of osseous spiral lamina and the basilar membrane (BM). The BM is one of the most important elements in the passive cochlear mechanics. If the BM was flattened and unfolded, it would be wedge-shaped with its width gradually increasing from the base to the apex. The change in width results in a highly significant reduction of the BM stiffness from the base to apex. The ST and SV are connected at the apical tip of the cochlea by a narrow opening called the helicotrema.

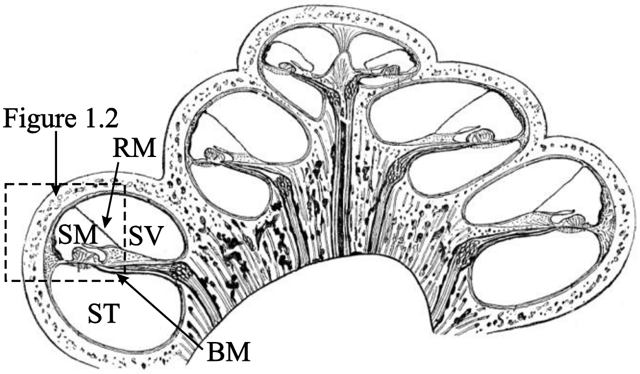

Figure 1.1 A mid-modiolar section through the human cochlea, the membranous labyrinth can be seen housed in bone. The fluid-filled tubes scala tympani (ST), scala vestibuli (SV) and scala media (SM) are separated from each other by the basilar membrane (BM) and the Reissner’s membrane (RM).

An important component of the human cochlea is the organ of Corti (OC), the sensory organ of hearing, which is distributed along the partition separating the fluid chambers and located on the SM side of the BM. Figure 1.2 shows a detailed structure of the OC, which includes a complement of support cells and two types of sensory cells (hair cells) from a unit segment, which is repeated about 3,500 times along the length of the OC. Another cochlear structure of great importance is the tectorial membrane (TM). The space between the tectorial membrane and reticular lamina is apparently open to the endolymph. Consequently, the apical faces of hair cells and the entire reticular lamina are bathed in this fluid. The complex consisting of the TM, the OC and the BM may be taken as the accessory structures to the hair cells. Their role is to deliver a processed mechanical signal to the appropriate group of sensory receptor cells whose primary mechanical input is related to the relative motion between the TM and reticular lamina (Dallos, *et al.*, 1996). The stria vascularis maintains a potential difference of about 80 ~ 100 mv between the SM and ST (Dallos, 1992), which powers the active behaviour of the outer hair cells.

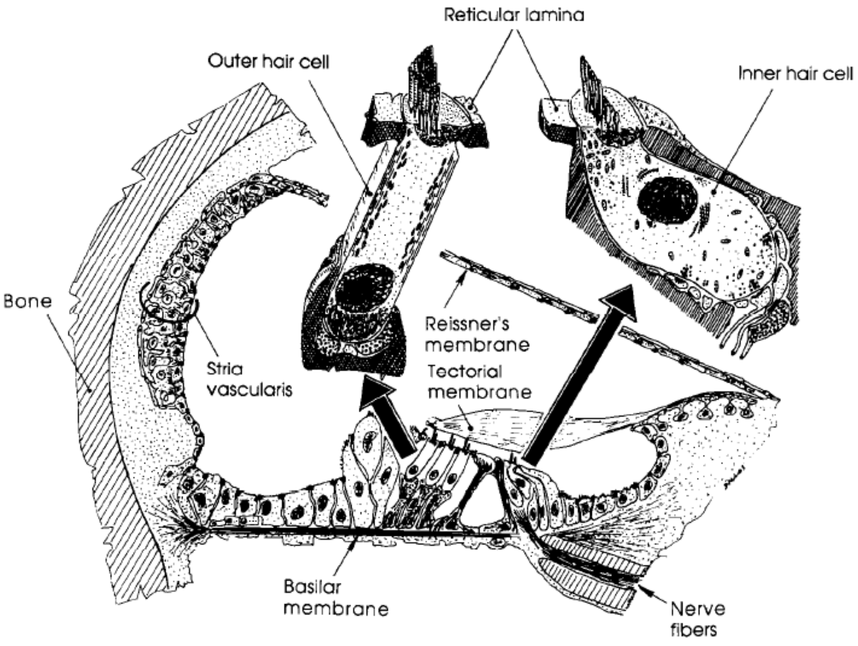

Figure 1.2 Cross section of the cochlear partition and the scala media, with one of three outer hair cells, OHCs (left) and an inner hair cell, IHC (right) shown enlarged. Boundaries of the partition are the Reissner’s membrane, basilar membrane, and the peripheral wall, lined by the stria vascularis. The organ of Corti is on the scala media side of the basilar membrane; it contains an array of supporting cells and the OHCs and IHCs. The tectorial membrane is above the organ of Corti. Nerve fibres enter the organ from the central bony core of the cochlea. Inside the partition is endolymph; outside it and within the organ of Corti spaces is perilymph. The reticular lamina, formed by support cell processes, is a flat plate covering the organ of Corti (Fig. 2, Dallos, 1992) (*with permission from the Journal of Neuroscience*).

1.1.2 Cochlear Functions

The principal role of the cochlea is to transform the hair cell motions induced by the incoming sound wave into electrical signals. These electrical signals then travel as action potentials along the auditory pathway to structures in the brainstem for further processing. The whole transformation can be seen as a procedure of a real time spectral decomposition of the acoustic signal in producing a spatial frequency map in the cochlea.

Carterette (Carterette, 1978) summarised the history, from the ancient Greeks to modern day, of auditory anatomies and functions. It showed that at the early stages, the studies were mainly focusing on anatomy and identifying the major features of the auditory system like the eardrum, cochlea and bones of the middle ear. von Békésy (von Békésy, 1960) carried out pioneering work to reveal the waves in the cochlea extracted from human cadavers in the 1940s. He found that a travelling wave generated by a pure tone excitation will propagate along the BM with the wave amplitude that gradually increased. After a peak at a specific location, where resonance occurs, the vibration decays quickly along the BM. The frequency of the input tone determines the location at which the peak occurs and this peak is more basal at high frequencies and more apical at low frequencies. This behaviour is one of the most critical evaluation criteria for cochlear models.

1.1.3 The Active and Nonlinear Cochlear Mechanics

In the classic travelling wave model, the cochlea is taken as a hydromechanical element, determined by the physical structure of the cochlea, which provides the basis for frequency analysis. This passive, travelling wave model was first proposed by von Békésy (von Békésy, 1960), who measured the travelling wave in cadaver ears, using an optical method that required very high input levels to make the responses large enough to be observed. For this kind of behaviour, the response is not dependent on stimulus level, except for amplitude scaling, and is described as “passive”.

With the development of more refined measurement technologies, more and more evidences showed that the cochlea is active and nonlinear. The idea of active processes in the cochlea was first raised by Gold (Gold, 1948) and evidenced by Kemp (Kemp, 1978) in the form of objective tinnitus and oto-acoustic emissions. These active processes provide a frequency-sharpening mechanism. Lyon (Lyon, 1990) and Mead (Lyon and Mead, 1988) emphasized that the active processes function primarily as an automatic gain control, allowing the amplification of sounds that would otherwise be too weak to hear. The response of the BM in the living ears was found to be different both qualitatively and quantitatively from that seen in the dead ears. Figure 1.3 (a) shows the BM amplitude normalized to the input stimulus level and represents the gain functions between the BM displacement and stimulus. The gain is significantly dependent on stimulus level. When measured at a high level stimulus, the BM displacement is similar to that found in the dead cochlea, which indicates that the passive cochlear model can reflect response at high level stimulus reasonably well. As stimulus level decreases, however, the gain functions become increasingly sharper and this gain increase only occurs in the vicinity of the characteristic frequency (CF). For frequencies less than an octave below CF, the gain is independent of level, which reflects a band-limited nonlinearity around the CF (Rhode, 1971).

From Figure 1.3 (b), the nonlinearity, as well as the sharp tuning behaviour, of the living cochlea is seen to be different from that of the dead cochlea. In the living cochlea, the gain is higher at the lower stimulus level, but for the dead cochlea this gain difference disappears and the tuning becomes independent of the stimulus level providing evidence of a nonlinear active process. Other evidence of the active behaviour for the living cochlea is given by the detection of sound in the ear canal, due to spontaneous oscillations originating from the cochlea, retransmitted by the middle ear, in the absence of any excitation. (Wilson, 1980).

Although the passive cochlea loses the active and nonlinear behaviours of the living ears, it is still capable of performing the basic cochlear function of mapping frequency onto place reasonably well, especially for high level stimulus, higher than about 80 dB SPL for example. It is also convenient as a first step in modelling, since the function is relatively well understood and agreed upon, and it allows the more complicated active behaviour, some elements of which are still controversial, to be ignored. In this research, only the passive cochlear is modelled to reveal the fluid coupling and wave propagation, which will help to understand the cochlear mechanics for future active cochlear models.

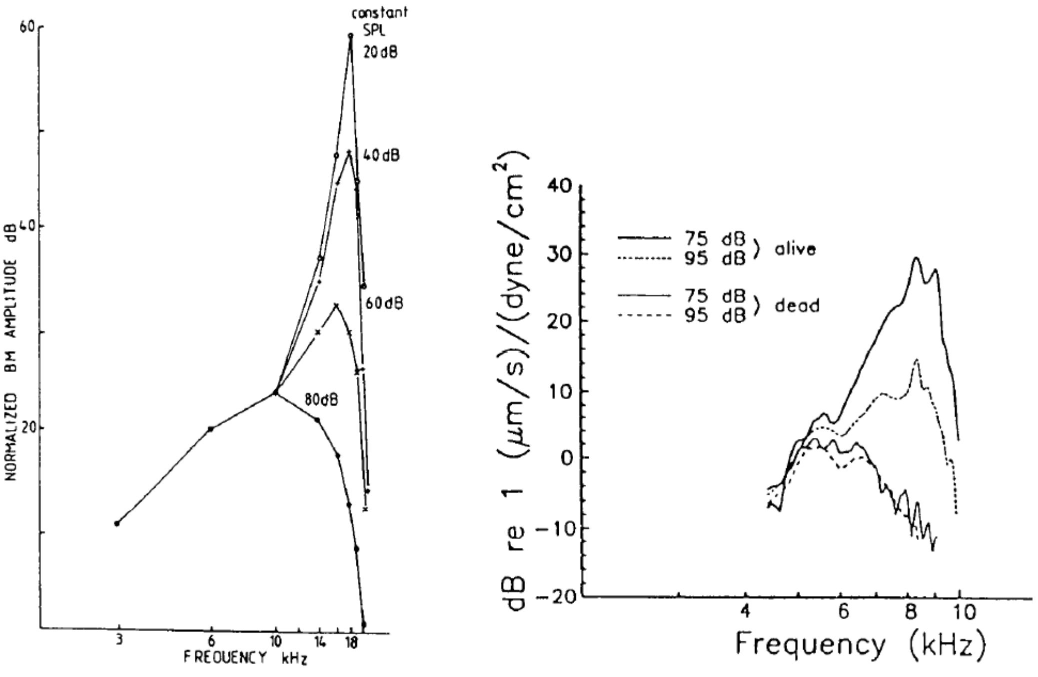

(a) (b)

Figure 1.3 (a) The normalized BM amplitude at different sound pressure levels, SPL. All curves converge below 10 kHz, indicating linear response and equal gain, independent of the SPL. Measurements were performed using the Mössbauer technique in the basal turn of the guinea pig cochlea. Maximal response frequency is at about 17 kHz (Johnstone, *et al.*, 1986) (*with permission from Hearing Research*). (b) Gain functions of the BM displacement measured in the basal turn of the chinchilla cochlea with laser Doppler velocimetry. Maximal response frequency is at about 8.5 kHz. Measurements are shown at two sound pressure level, 75 and 95 dB, and in conditions of living and dead cochlea (Ruggero and Rich, 1991) (*with permission from the Journal of Neuroscience*).

1.2 Analytic Models

The original studies of the cochlea were primarily anatomical. By the mid-1800s, with the developments of microscopes and chemical tissue fixatives, people were able to describe a finer structure of the cochlea. Reissner (1851), Corti (1851) and Deiters (1860) applied those new technologies and discovered the cochlear structures now named after them (Dallos, *et al.*, 1996).

Compared to reality, cochlear models may be incredibly simplified, but these crude models can still reflect how the real organ works. The motivations of modelling the cochlea are to represent, within one framework, the results from a large variety of experiments and to explain the functions of the hearing system. In principle, models should also be tested by providing predictions of experiments that have yet to be done. Cochlear models have been formulated and constructed in various forms. These models are concerned with mechanical structures built up with structural elements like plate, beam coupled with fluid (Elliott, *et al.*, 2011, Parthasarathi, *et al.*, 2000, Wittbrodt, *et al.*, 2004) or electrical networks (Crawford and Fettiplace, 1981, Fuchs, *et al.*, 1988, Kros, *et al.*, 1992) consisting of inductors, resistances, capacitors, diodes and amplifiers. After construction, these structures can be put into mathematical form and then be solved by computer.

1.2.1 Travelling Waves in the Cochlea

The travelling wave theory of the cochlea (Zwislocki, 1948, Zwislocki, 1974) predicts the delay of the travelling wave to accumulate with increasing distance from the stapes. von Békésy (von Békésy, 1970) studied the cochlea as a passive mechanical filter that utilizes a system of elastic components immersed in a fluid for analysis of incoming sounds. He observed that a pure tone input generates a travelling wave propagating along the BM. The wave amplitude increases gradually to a peak at a characteristic location along the BM, after which it decays rapidly. The characteristic location depends on the driving frequency, for example, the peak is close to the stapes at high frequencies, and further towards the apex at lower frequencies. This ‘‘place principle’’ is a crucial mechanism of frequency analysis in the cochlea.

In the 1970s, the cochlea was recognized as a wave propagation medium in which the physical parameters vary slowly. Steele (Steele, 1974) firstly adopted the Wentzel–Kramers–Brillouin (WKB), or Liouville-Green (LG) method to solve cochlear mechanical problems and found closed-form solutions for a 1D cochlear model. Zweig *et al*. (Zweig, *et al.*, 1976) found the closed-form WKB solutions for a 1D long-wave model in 1976. Steel, Taber and Miller also extended the WKB method to solve 2D (Steele and Miller, 1980) and 3D (Steele and Taber, 1979, Taber and Steele, 1981) cochlear problems. de Boer and Viergever (de Boer and Viergever, 1982, de Boer and Viergever, 1984) further developed the WKB approach for cochlear mechanics. The WKB solutions for the 2D and 3D cochlear model showed good agreement with more detailed numerical solutions, except for the high-frequency region and the reason for these errors appeared to be the non-uniqueness of the complex WKB wavenumber in 2D and 3D models (de Boer and Viergever, 1982).

To explain the travelling wave model, a simpler example of wave propagation in a stretched string is considered first. When a uniform semi-infinite string is driven by a sinusoidal source at the left hand side, as shown in Figure 1.4, the transverse displacement, $w(x,t)$, can be given by (Graff, 1991)

$$w(x,t) = Ae^{i(kx-\omega t)}, \tag{1.1}$$

where A is the wave initial amplitude which depends on the driving source, ω is driving frequency and k is complex wavenumber. If the wavenumber k is written in terms of real and imaginary parts, as

$$k = \kappa + i\alpha, \tag{1.2}$$

equation (1.1) can then be written as

$$w(x,t) = Ae^{\alpha x}e^{i(\kappa x-\omega t)}, \tag{1.3}$$

where $e^{\alpha x}$ reflects the effects of energy gains or losses and therefore determines whether, and how quickly, the wave amplitude raises or decays as it travels (Shera, 2007) and $e^{i\kappa x}$ determines the phase change with respect to position x. For a passive system, the imaginary part α of a forward-going wave should always be expected to be either zero or negative.

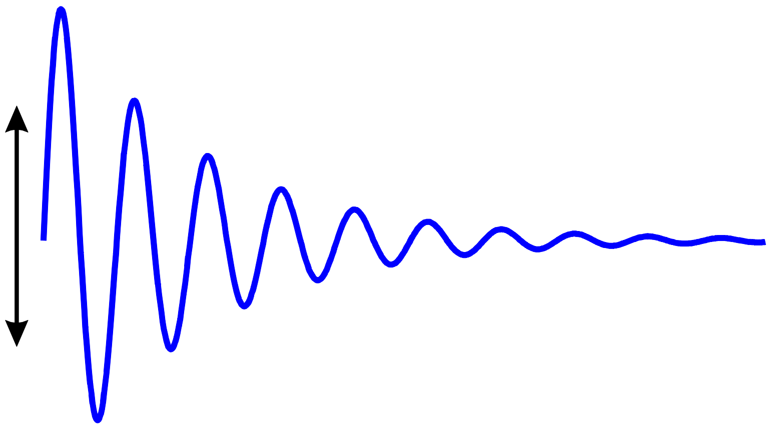

Figure 1.4 Instantaneous wave motion along a uniform semi-infinite loose string under sinusoidal excitation showing both decay and phase change.

When the properties of the medium vary with position, as in the cochlea for example, the waves manifest a more complicated relationship to the wavenumber *k*. For example, the displacement of the BM produced by a pure tone has the approximate form, WKB approximation, (de Boer and Viergever, 1982) as

$$w(x,t) = Ak(x,\omega)^{3/2} e^{i[\omega t - \phi(x)]}, \tag{1.4}$$

where $\phi(x) = \int_0^x k(x',\omega)dx'$ denotes the integral of the accumulating phase shift and gains or losses as the wave propagates along the cochlea, x' is dummy integration variable, and factor *A* is the wave amplitude at the base. The additional $k(x,\omega)^{3/2}$ term is necessary for conservation of energy when the wavenumber changes with *x*. The WKB method is discussed in more detail in Appendix A.

1.2.2 Wavenumber for a Simple Box Model

An initial estimate of the way in which the real and imaginary parts of the wavenumber vary along the length of the passive cochlea can be obtained from an analysis of a simple box model shown in Figure 1.5. This analysis will be gone over in detail in Chapter 6, but for now we can just note that the wave equation is obtained by combining the conservation of mass and momentum equations for the fluid coupling to give

$$\frac{\partial^2 p(x)}{\partial x^2} = -\frac{2i\omega\rho}{h}\, v(x), \tag{1.5}$$

where *v*(*x*) is the distribution of the transverse BM velocity being complex quantities at a single driving frequency, *ω*. The parameter *h* corresponds to the physical height of the two fluid chambers if the BM velocity is assumed to be uniform across its width.

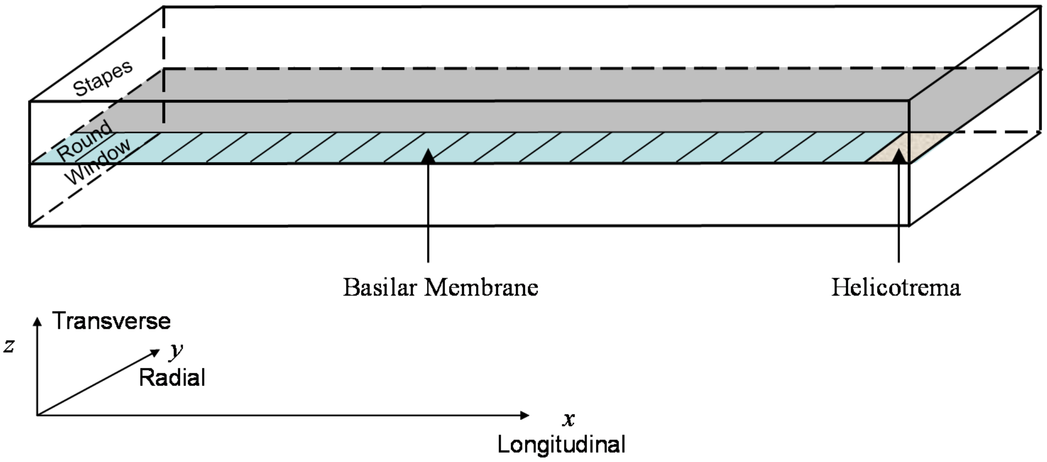

Figure 1.5 A simple box model of the cochlea consists of two fluid chambers separated by the BM.

The BM is assumed to react only locally so that

$$v(x) = -\frac{p(x)}{Z_{\mathrm{BM}}(x)}, \tag{1.6}$$

where the minus sign indicates that a positive pressure difference generates a negative BM velocity in the sign convention used here and $Z_{\mathrm{BM}}(x)$ is the local BM impedance, which is assumed to be that of a single degree of freedom system, whose parameters are listed in Table 2.1.

These quantities can be combined to give the wave equation as

$$\frac{\partial^2 p(x)}{\partial x^2} - \frac{2i\omega\rho}{h\, Z_{\mathrm{BM}}(x)}\, p(x) = 0. \tag{1.7}$$

Assuming that $p(x)$ is locally proportional to $e^{-ik(x)x}$, the wavenumber can be obtained as

$$k(x) = \pm\sqrt{\frac{-2i\omega\rho}{h\, Z_{\mathrm{BM}}(x)}}. \tag{1.8}$$

The real and imaginary parts of the wavenumber are plotted for four different frequencies in Figure 1.6, from which it is clear that each frequency corresponds to a different characteristic place along the cochlea.

As can be seen in Figure 1.6, the travelling wave propagates along the cochlear length with a slowly decreasing wavelength at a given driving frequency until it reaches a characteristic place without decay, since the imaginary part of its wavenumber is zero. , The characteristic place depends on driving frequency and moves towards the apex when the driving frequencies decrease. The wave becomes an evanescent wave decaying away quickly beyond that point since the real part of wavenumber tends to zero and the imaginary parts are non-zero. The negative imaginary parts of wavenumber indicate those waves propagate in a positive direction from the base towards the apex.

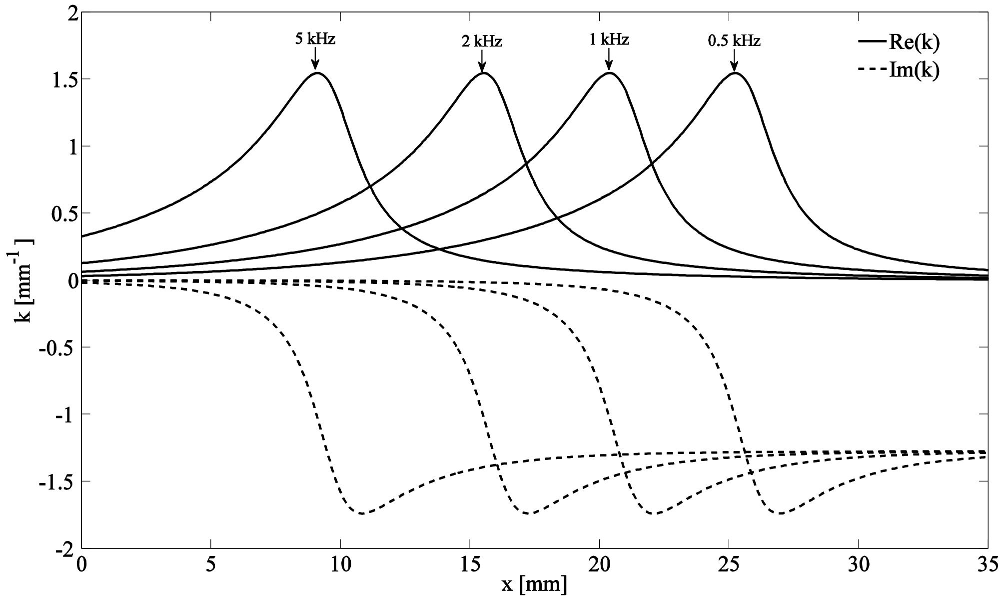

Figure 1.6 The distribution of the real (solid lines) and imaginary (dashed lines) parts of the wavenumber calculated from a simple box model of the cochlea with 1D fluid coupling at driving frequencies of 5 kHz, 2 kHz, 1 kHz and 0.5 kHz.

1.2.3 Inverse Method

Shera (Shera, 2007) has proposed an inverse method for using the experimentally obtained BM velocity transfer function at a location along the vivo cochlea in the frequency domain to calculate the propagation and gain functions. He then goes on to reconstruct the BM velocity distribution, $V_{\mathrm{BM}}(x, f_{\mathrm{o}})$ in the spatial domain to test the theory. This method gives a strong evidence for travelling wave amplification in the mammalian cochlea based on measurements, which are the real and imaginary parts of the complex wavenumber.

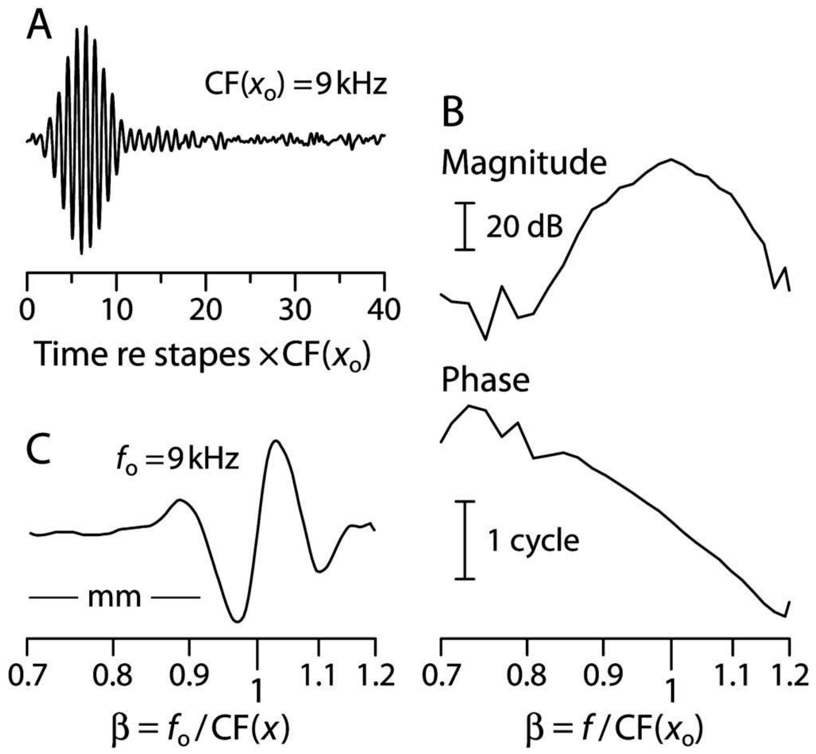

Figure 1.7 Estimate of the BM frequency response from measurements of the BM click response, $v_{\mathrm{BM}}(x_0,t)$, at the cochlear location x_o tuned to approximately 9 kHz in chinchilla (A). The response estimate has been normalized by its peak value. Time, shown along the abscissa in units of the CF period, is measured relative to the approximate onset of stapes vibration by subtracting out estimates of acoustic and synaptic transmission delays amounting to a total of 1.225 ms. The magnitude and phase of the Fourier transform of $v_{\mathrm{BM}}(x_0,t)$ provide an estimate of the BM mechanical transfer function, $v_{\mathrm{BM}}(x_0, f)$, at the cochlear location x_o (B). Frequency, normalized by CF(x_o) =9 kHz, increases along the logarithmic abscissa. Application of local scaling provides an estimate of the travelling wave by reinterpreting the abscissa $f/\mathrm{CF}(x)$ as a spatial axis at fixed frequency (C). The figure shows a snapshot of the 9 kHz wave whose envelope and phase are shown in (B) The 1 mm scale bar is based on estimates of the chinchilla cochlear map (Shera, 2007) (*with permission from AIP*).

To find travelling waves from the transfer functions obtained from experiments, Shera (Shera, 2007) applied the local scaling symmetry (Zweig, *et al.*, 1976) manifest by BM transfer functions (Gummer, *et al.*, 1987, Rhode, 1971) and neural tuning curves (Kiang and Moxon, 1974, Liberman, 1978). A dimensionless factor $\beta(x, f) = f/\mathrm{CF}(x)$, where $\mathrm{CF}(x)$ is the characteristic frequency at location x (i.e. the cochlear position-frequency map), is defined to let $v_{\mathrm{BM}}(x, f)$ depend on the two variables x and f rather than depend on position or frequency independently. When the BM velocity is scaled, the function $v_{\mathrm{BM}}\left[\beta(x, f)\right]$ describes both the transfer function and the travelling wave. In other words, if frequency domain measurement of the transfer function $v_{\mathrm{BM}}(x_0, f)$ is plotted against $f/\mathrm{CF}(x_0)$, it provides spatial domain measurement of the travelling wave $v_{\mathrm{BM}}(x, f_0)$ plotted against $f_0/\mathrm{CF}(x)$, as shown in Figure 1.7.

To define the relation between the complex wavenumber, *k*, and the BM velocity, v_{BM}, Shera (Shera, 2007) adopted a two dimensional box model of the cochlea. By averaging the pressure difference over the physical height of the scalae and applying boundary conditions at the scalae walls and BM, the averaged pressure difference, $\overline{p}(x, f)$, satisfies the one dimensional wave equation (Shera, *et al.*, 2005)

$$\frac{\partial^2 \overline{p}}{\partial x^2} + k^2 \overline{p} = 0. \tag{1.9}$$

The BM velocity $v_{\mathrm{BM}}(x, f)$ is related to the second spatial derivative of the pressure difference through the equation

$$\frac{\partial^2 \overline{p}}{\partial x^2} = BZ_{\mathrm{FC}} v_{\mathrm{BM}}, \tag{1.10}$$

where *B* is the BM width and Z_{FC} is the fluid coupling impedance (Shera, *et al.*, 2005). If $v_{\mathrm{BM}}(x, f)$ is obtained by measurement, the pressure difference $\overline{p}$ in equation (1.10) can be solved by double integration as

$$\overline{p}(x, f) = BZ_{\mathrm{FC}} \int_x^L \int_{x'}^L v_{\mathrm{BM}}(x'', f)\, dx'' dx', \tag{1.11}$$

where x' and x'' are dummy integration variables and *L* is the length of the cochlea. The constants of integration are chosen to satisfy the assumed boundary conditions. Combining equations (1.9) to (1.11), the wavenumber can be given by

$$k(x, f) = \pm i \sqrt{\frac{v_{\mathrm{BM}}(x, f)}{\int_x^L \int_{x'}^L v_{\mathrm{BM}}(x'', f)\, dx'' dx'}}. \tag{1.12}$$

This wavenumber inversion formula suggests how to estimate the complex wavenumber, as shown in Figure 1.8, from the measured BM velocity. The method can also be used to reconstruct the BM velocity distribution by combining the WKB approach. Figure 1.9 shows a good agreement between the original measured BM magnitude and phase distributions and those reconstructed from the derived wavenumber using the WKB approximation (Shera, 2007). This gives both strong theoretical and practical evidences to support the travelling wave theory in the cochlear mechanism.

Since these measurements were taken on an active cochlea, the imaginary part of the wavenumber is not entirely negative, indicating that the active processes are amplifying the wave at positions just before it reaches its peak. Apart from this aspect the distributions of the real and imaginary wavenumbers are similar to those predicted from the simple analytic passive model in Figure 1.6.

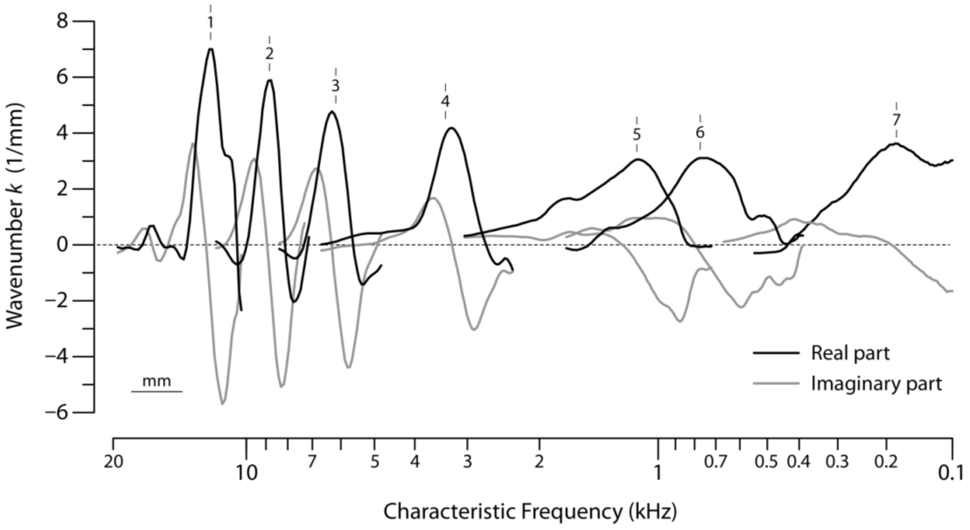

Figure 1.8 The distribution of the real (black lines) and imaginary (grey lines) parts of the wavenumber inferred from measurements of the BM frequency response at seven positions along the length of the cochlea using an inversion procedure (Shera, 2007) (*with permission from AIP*).

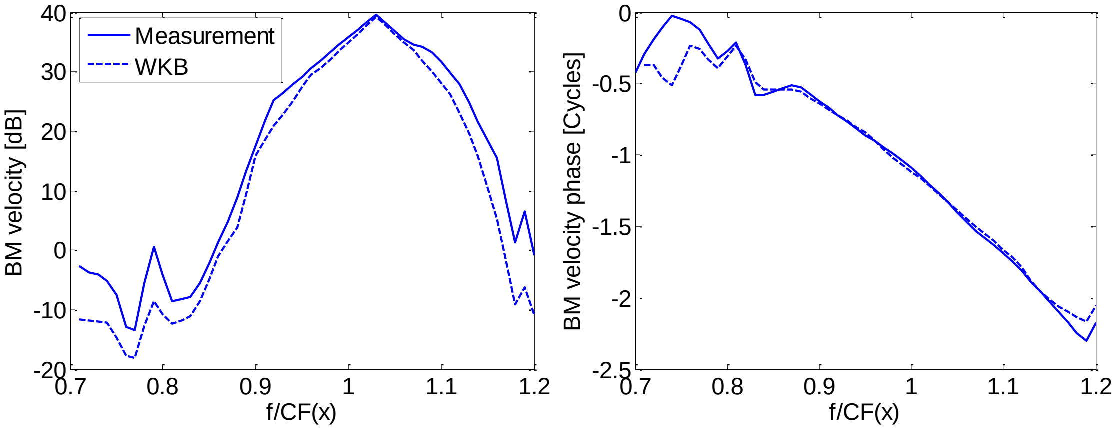

Figure 1.9 The BM velocity distribution reconstructed from the derived wavenumber using the WKB approximation. The reconstructed response (dashed lines), obtained using the WKB approximation, shows a good agreement with that from measurement (solid lines) (reproduced based on Fig.5, Shera 2007) (*with permission from AIP*).

1.3 Numerical Models

1.3.1 Discrete Cochlear Model

It is computationally convenient to divide a continuous system into a number of discrete elements, which may be taken as an accurate representation of the continuous system if there are at least six elements within the shortest wavelength present, which is a condition commonly used in finite element analysis (Fahy and Gardonio, 2007). The coupled behaviour of the cochlear dynamics, which are assumed to be linear, can then be represented by matrix representations of two separate phenomena. First, the way that the pressure distribution is determined by the fluid coupling within the cochlear chambers when driven by the BM velocity, and second, the way in which the BM dynamics respond to the imposed pressure distribution. This kind of discrete model was used, for example, by Neely and Kim (Neely and Kim, 1986), to simulate an early model of the active cochlea, and has been used by many authors since then. These discrete models have generally been applied to uniform and symmetric box models of the cochlea, using the finite difference method to represent only the far-field, long wavelength, components of the fluid coupling.

A widely used geometry for the three-dimensional cochlea is the rectangular box model, as discussed by de Boer (de Boer, 1996), for example, and illustrated in Figure 1.5. The cochlea is assumed to be uncoiled, consisting of uniform cross section and symmetric fluid chambers, ST and SV (including SM) for the lower and upper chamber, separated by the BM. The RM is assumed to be flexible enough to play no significant part in the dynamics of the fluid motion in the upper chamber. The cochlea is driven by the motion of the stapes at the oval window. At very low frequencies the cochlear fluids can flow along the upper chamber, through the gap at the helicotrema, and back through the lower chamber to drive the motion of the flexible round window. At audio frequencies a “slow” travelling wave is generated by the interaction between the fluid’s inertia and BM stiffness, which propagates to a frequency-dependent characteristic place, beyond which it rapidly decays.

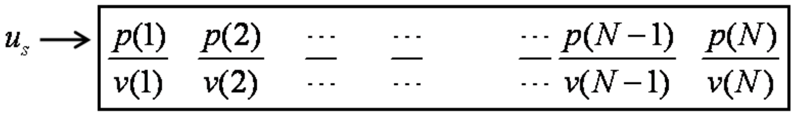

Figure 1.10 The discrete approximation for a straightened cochlear box model.

The radial variation of BM velocity over the width of the cochlear partition (CP), *W*, is assumed to be proportional to a single mode shape, $\psi(y)$, which is independent of the distribution of the pressure acting upon it. The analysis can be generalised to the case in which the radial BM velocity is the sum of a number of such modes (Neely, 1985), but in practice the fluid coupling is relatively insensitive to the exact form of the radial BM velocity distribution and so it is reasonable to assume a single shape for this. Its upward *modal* amplitude at longitudinal position *x* is defined to be

$$v(x) = \frac{1}{W}\int_0^W \psi(y)v(x,y)dy, \tag{1.13}$$

where *v*(*x*, *y*) is the distribution of complex BM velocity which is a function of longitudinal and radial position, at a single frequency, the dependence on which is suppressed for notational convenience. Similarly, the modal pressure difference across the BM, can be defined as (Elliott, *et al.*, 2011)

$$p(x) = \frac{1}{W}\int_0^W \psi(y)p(x,y,0)dy, \tag{1.14}$$

where *p*(*x*, *y*, *z*) is the 3D distribution of the complex pressure difference across the BM.

The boundary conditions for this modal pressure difference are determined by its anti-symmetric forms. For the modal pressure difference, the pressure in the upper chamber must be equal but opposite to the pressure in the lower chamber and so the volume excitation at the round window must be equal but opposite to that at the oval window. Transverse BM motion is also allowed in this case since the resulting excitation of the upper chamber is equal but opposite to that of the lower chamber. It is thus only the pressure difference that interacts with the BM dynamics and generates the “slow” wave motion noted above. The chambers are connected at the helicotrema, which is, for now, assumed to equalise the pressures in the two chambers, so that the modal pressure difference must then be zero at the helicotrema.

If the single longitudinal variables, for the modal pressure difference and the modal BM velocity, are spatially sampled as finely as required, dividing the cochlea into N segments, we can define, at a single frequency, the vectors of complex modal pressure differences and modal BM velocities, **p** and **v**, to be

$$\mathbf{p} = \left[p(1), p(2), \cdots p(N) \right]^{\mathrm{T}}, \tag{1.15}$$

and

$$\mathbf{v} = \left[v(1), v(2), \cdots v(N) \right]^{\mathrm{T}}, \tag{1.16}$$

whose elements are shown in Figure 1.10.

The BM, however, is assumed only to extend from element 2 to element $N - 1$. Element 1 is used to account for the effect of the stapes velocity, shown as u_s in Figure 1.10. The final element, N, is used to account for the behaviour of the helicotrema. With the stapes velocity set to zero, the vector of pressures due to the vector of BM velocities can be written as

$$\mathbf{p} = \mathbf{Z}_{\mathrm{FC}} \mathbf{v}, \tag{1.17}$$

where $\mathbf{Z}_{\mathrm{FC}}$ is a matrix of the impedances due to the fluid coupling. Much of this thesis is concerned with analysing the form of the elements in its fluid coupling matrix. Similarly, the vector of BM velocities can be written as

$$\mathbf{v} = \mathbf{v}_\mathrm{s} - \mathbf{Y}_\mathrm{BM}\mathbf{p}, \tag{1.18}$$

where $\mathbf{v}_\mathrm{s}$ is vector whose first element is the stapes velocity and $\mathbf{Y}_\mathrm{BM}$ is a matrix of the BM admittances. The first and last diagonal elements are zero, since the BM only extends from element 2 to element $N - 1$. If the BM reacts only locally, then $\mathbf{Y}_\mathrm{BM}$ is a diagonal matrix. Substituting equation (1.17) into (1.18) gives the vector of BM velocities as

$$\mathbf{v} = \left[\mathbf{I} + \mathbf{Y}_\mathrm{BM}\mathbf{Z}_\mathrm{FC}\right]^{-1}\mathbf{v}_\mathrm{s}. \tag{1.19}$$

The total pressure vector due to both stapes motion and motion of the BM can be written, using linear superposition, as

$$\mathbf{p} = \mathbf{p}_\mathrm{s} + \mathbf{Z}_\mathrm{FC}\mathbf{v}, \tag{1.20}$$

where $\mathbf{p}_\mathrm{s}$ is the vector of pressures due to the stapes velocity. Combining equations (1.17) and (1.18) gives

$$\mathbf{p} = \left[\mathbf{I} + \mathbf{Z}_\mathrm{FC}\mathbf{Y}_\mathrm{BM}\right]^{-1}\mathbf{p}_\mathrm{s}. \tag{1.21}$$

An advantage of this discrete formulation is that complicated geometries need to be analysed only once to determine the elements of $\mathbf{Z}_\mathrm{FC}$, using finite element method for example, and equation (1.19) then provides a very simple method of calculating the coupled responses, for a variety of models, coiled cochlea for example, of BM dynamics.

1.3.2 Finite Element Cochlear Model

Although the finite element (FE) cochlear model is a discrete representation of the real continuous cochlea, the flexibility of the finite elements allows the possibility of considering more detailed and complicated cochlear structure than in the discrete model above. In many areas, the finite element analysis (FEA) is a key and indispensable technology in the modelling and simulation procedures. However, a good understanding of physical, mathematical and computational modelling plays an important role in utilizing those advantages of the finite element method.

Kolston and Ashmore (Kolston and Ashmore, 1996) applied a 3D Finite Element Network to build a 3D cochlear model with individual cellular and membrane components of the organ of Corti being embedded within the fluid in their real biological positions and then solved the problem using the conjugate gradient method. They suggested that both the TM radial stiffness and especially the Deiters' cell (DC) axial stiffness play a crucial role in the OHC-BM feedback loop.

Givelberg and Bunn (Givelberg and Bunn, 2003) constructed a comprehensive 3D cochlear model consisting of the BM, spiral bony shelf, the tubular walls of SV and ST, semi-elliptical walls sealing the cochlear canal, the oval window and the round window membranes, to study the motion of the BM under a pure tone input at a given frequency. They observed a travelling wave propagating from the stapes, in the longitudinal direction, to the helicotrema. The amplitude of the wave is gradually increasing to a peak at a characteristic location along the BM, which depends on the input frequency. The speed of the wave is sharply reduced as it propagates further along the BM after the peak. The higher the value of input frequency, the closer the peak is to the base. Those observations are similar to experiments qualitatively, but this kind of comprehensive numerical model is computationally expensive.

In the research reported here, the 3D finite element box model of the cochlea, as shown in Figure 1.5, is used mostly as the basis of the finite element modelling and analysis. Compared with other FE models, built by other authors, this box model may be crude and incredibly simple, but it does reflect the basis of the cochlear functions and provide a way of modelling the passive cochlea at low computation cost. It also allows that the use of the wave finite element can be introduced in a relatively simple manner.

1.4 Motivation and Outline of the Thesis

It is important to understand the mechanisms of human hearing not only because of the scientific challenges it presents, but also because such a knowledge is helpful in diagnosing and potentially treating the multiple forms of hearing problems that people suffer from. Modelling the biological cochlea assists in this understanding by allowing assumptions about how its functions to be verified or by comparing responses predicted by mathematical models with experimental observations. The motivation of this research is to get a better understanding of the cochlear functions. The core of the work is the modelling of the dynamics of the cochlea by studying the fluid coupling and waves in a passive cochlea, analytically and numerically, which constitute the two main parts of the thesis.

Another important aspect for improving our knowledge on cochlear functions is to understand wave propagation in the cochlea. The classic cochlear model is based on the hypothesis that there is only a single wave, “slow wave”, which is of primary importance. In general, however, there are many other mechanisms, apart from 1D fluid coupling, that give rise to longitudinal coupling in the cochlea, even if the cochlea is passive and each of these forms of longitudinal coupling could give rise to wave motion. Analytic methods are used to predict the wavenumber of the additional waves due to 3D fluid coupling and longitudinal BM dynamics. In general the fully coupled response of the cochlea to middle ear excitation can be calculated using a numerical model, such as obtained with the finite element method, although the insight gained from the wave approach is then lost. The wave finite element, WFE, method is used here to decompose the results of a full finite element model of the coupled cochlea into wave components. The WFE method predicts the properties of as many types of waves as there are degrees of freedom across each cross-section of the finite element model. Almost all of the forward-going components of these waves have large negative imaginary components, indicating that they decay away very quickly along the cochlear length. The mode shapes associated with the waves predicted from the WFE analysis then have been used to decompose the results of the full finite element model into wave components. Although additional types of wave are thus predicted to exist, in addition to the conventional “slow wave”, in the passive cochlea, they do not appear to play a dominant role in normal cochlear function.

The overall structure and framework of the thesis are illustrated in Figure 1.11 and details can be found in following chapters.

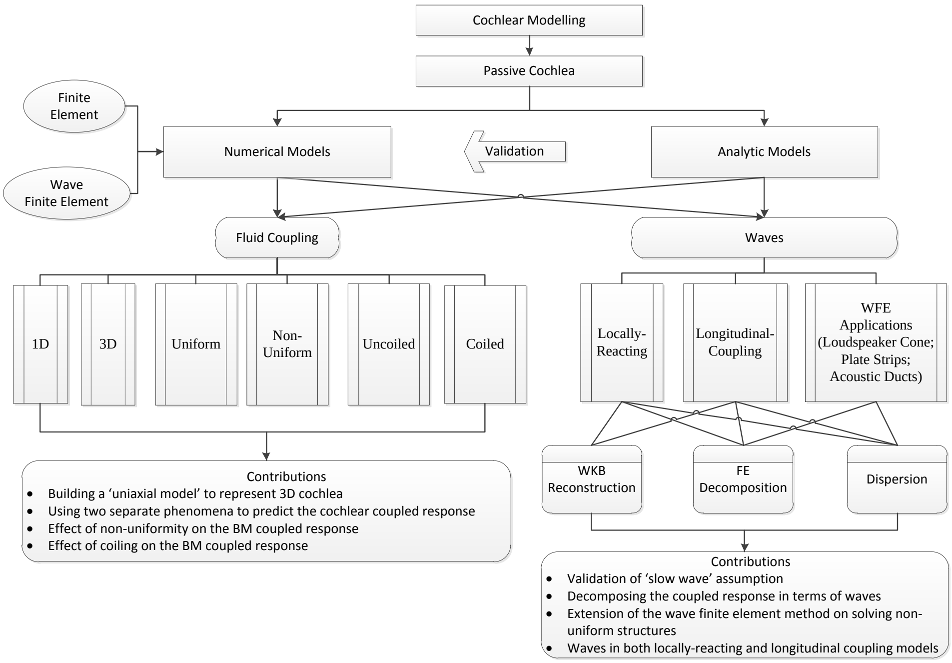

Contributions
- Building a 'uniaxial model' to represent 3D cochlea
- Using two separate phenomena to predict the cochlear coupled response
- Effect of non-uniformity on the BM coupled response
- Effect of coiling on the BM coupled response

Contributions
- Validation of 'slow wave' assumption
- Decomposing the coupled response in terms of waves
- Extension of the wave finite element method on solving non-uniform structures
- Waves in both locally-reacting and longitudinal coupling models

Figure 1.11 The diagram of thesis structure.

1.5 Contributions of the Thesis

The primary contributions of my work are as follows:

- Applications of the wave finite element to study various non-uniform systems, such as loudspeaker cone and orthotropic plate strips, which provide a new way to illustrate dynamic behaviours of non-uniform structures in terms of waves.
- Co-development and validation of a 'uniaxial model' of the cochlea which can incorporate 3D fluid coupling and non-uniformity.
- Comparison of coupled responses from coiled and uncoiled cochlea models which shows the coiling does affect the cochlear dynamics based on the parameters used here.
- Study of waves in the passive cochlea using the wave finite element method, providing the opportunity to analyse different types of wave that can propagate in the cochlea and, more importantly, decompose the response of the fully-coupled finite element model into the components due to each of these waves, in order to study interaction between each wave.
- An interpretation of how the longitudinal BM coupling affects the coupled cochlear response.

Some of these outcomes have been published through journal papers and conference presentations:

Ni, G., Elliott, S. J. and Mace, B. R. (**2010**) A fluid-structural model of the cochlea using wave finite element method. In Brennan, M.J., Kovacic, Ivana, Lopes, V., Murphy, K., Petersson, B., Rizzi, S. and Yang, T., editors, *Recent Advances Structural Dynamics: Proceedings of the X International Conference*, Southampton.

Elliott, S. J., Lineton, B. and Ni, G. (**2011**) *Fluid coupling between the elements in a discrete model of cochlear mechanics*, ISVR Technical Memorandum 990, University of Southampton, 98pp.

Elliott, S. J., Lineton, B. and Ni, G. (**2011**) Fluid coupling in a discrete model of cochlear mechanics, *The Journal of the Acoustical Society of America*, 130 (3), 1441-1451.

Ni, G., Elliott, S. J., Lineton, B. and Saba, R. (**2011**) Finite element modelling of fluid coupling in the coiled cochlea. In Shera, C.A. and Olson, E.S., editors, *What Fire is in Mine Ears: Progress in Auditory Biomechanics*, pp 350-355. (DOI: 10.1063/1.3658164)

Elliott, S. J., Ni, G., Mace, B. R. and Lineton, B. (**2011**) How many waves propagate in the cochlea? In Shera, C.A. and Olson, E.S., editors, *What Fire is in Mine Ears: Progress in Auditory Biomechanics*, pp 563-568. (DOI: 10.1063/1.3658164)

Elliott, S. J., Lineton, B. and Ni, G. (**2011**). Fluid coupling in a discrete cochlear model. In Shera, C.A. and Olson, E.S., editors, *What Fire is in Mine Ears: Progress in Auditory Biomechanics*, pp 328-332. (DOI: 10.1063/1.3658164)

Ni, G., Elliott, S. J. and Langley, A. (**2012**) Waves in Loudspeaker Cones, *ISMA 2012*, Leuven, Belgium.

Elliott, S. J., Ni, G. and Lineton, B. (**2012**) Decomposition of the cochlear response using wave finite elements, *19th International Congress on Sound and Vibration*, Vilnius, Lithuania.

Ni, G., Elliott, S. J. and Mace, B. R. (**2012**). *Wave Propagation and Decomposition in the Cochlea with Orthotropic Basilar Membrane*, Innovations in Wave Modelling (InnoWave 2012), Nottingham, UK (Poster).

Elliott, S. J., Ni, G., Mace, B. R. and Lineton, B. (**2012**) *Wave Propagation in the Cochlea*, ISVR Technical Memorandum 996, University of Southampton, 98pp.

Elliott, S. J., Ni, G., Mace, B. R. and Lineton, B. (**2012**) A Wave Finite Element Analysis of the Passive Cochlea, *The Journal of the Acoustical Society of America* (submitted).

Chapter 2. Fluid Coupling in the Uncoiled Cochlea

2.1 Introduction

The aim of this chapter is to review the approaches that have been taken to calculate the fluid coupling in the cochlea, and to derive the form of the fluid coupling matrix in the discrete model of the cochlea introduced in Chapter 1. Most authors assume that the coiling of the cochlea does not play a significant part in determining the fluid coupling (Cai*, et al.*, 2005, Steele and Zais, 1985), and so in this chapter the uncoiled cochlea will be considered, leaving the effects of coiling to be considered separately in the next chapter.

It has also been common to assume a uniform box model for the cochlea, which is where the analysis begins in this chapter, initially using the wavenumber approach pioneered by Steele and Taber in 1979 (Steele and Taber, 1979). The pressure due to a moving element of the BM is seen to be due to two components, called the far-field and the near-field components here. The far-field component is obtained from the 1D model of fluid coupling outlined in the introduction and is associated with wavelengths that are large compared with the size of the fluid chamber, giving plane wave acoustic propagation. The near-field component is associated with wavelengths that are not large compared with the size of the fluid chamber, and can be identified being due to evanescent higher order acoustic modes within the chamber.

A three-dimensional cochlea can be simply represented by a single dimension using a radially-averaged BM velocity and a radially-averaged pressure difference acting upon the cochlea. In this chapter a general approach is taken to the derivation of the discrete cochlear model, using modal BM velocity and modal pressure difference, which allows the definition of generic matrices to describe the fluid coupling and BM dynamics of the cochlea.

2.2 Wavenumber Description

Following Steele and Taber (Steele and Taber, 1979), we consider an analysis in the wavenumber domain for a box model of the cochlea, which is assumed to be symmetric, i.e., the two fluid chambers, ST and SV, are of equal cross-sectional area. The pressure distributions in the two chambers are thus equal and opposite and it is convenient to work with the single distribution $p(x, y, z)$, defined as the pressure difference, which is twice the pressure in the SV or ST. The fluid is assumed to be incompressible and inviscid and so the conservation of fluid mass then leads to the equation

$$\frac{\partial^2 p(x,y,z)}{\partial x^2}+\frac{\partial^2 p(x,y,z)}{\partial y^2}+\frac{\partial^2 p(x,y,z)}{\partial z^2}=0. \tag{2.1}$$

The fluid chamber has a width of W and height H. The boundary conditions on the sides and the top of the cochlear chamber above the BM are assumed to be rigid, so that we must have

$$\left.\frac{\partial p(x,y,z)}{\partial y}\right|_{y=0,W}=0, \tag{2.2}$$

and

$$\left.\frac{\partial p(x,y,z)}{\partial z}\right|_{z=H}=0. \tag{2.3}$$

The fluid velocity at $z = 0$ must equal that of the BM, $v(x, y)$, so that

$$\left.\frac{\partial p(x,y,z)}{\partial z}\right|_{z=0}=-2i\omega\rho v(x,y), \tag{2.4}$$

where the factor of 2 is due to the pressure doubling when $p(x, y, z)$ is defined as the pressure difference. The BM velocity is now assumed to have a given distribution across its width, B, and in the longitudinal direction it has a sinusoidal variation with wavenumber k, so that

$$v(x,y)=v(x)\psi(y)=V(k)\psi(y)e^{-ikx}, \tag{2.5}$$

where $v(x)$ is the modal BM velocity distribution along the cochlea and $\psi(y)$ is the BM velocity distribution in the radial direction, y. The velocity distribution $\psi(y)$ is normalised such that

$$\int_0^W \psi^2(y)dy = W, \tag{2.6}$$

so that $v(x)$ can be calculated from $v(x, y)$ as

$$v(x) = \frac{1}{W}\int_0^W v(x,y)\psi(y)dy. \tag{2.7}$$

The pressure field is assumed to be described by a summation of modes of the form

$$p(x,y,z) = \sum_{n=0}^{\infty} B_n \phi_n(y,z)e^{-ikx}, \tag{2.8}$$

where each mode shape, $\phi_n(y,z)$, must satisfy the boundary conditions above. A suitable choice of pressure mode shape (Neely, 1985, Steele and Taber, 1979) is

$$\varphi_n(y,z) = \cos\left(\frac{n\pi y}{W}\right)\cosh\left[m_n(z-H)\right]. \tag{2.9}$$

In order for each term in the model expansion to satisfy the equation for mass conservation, equation (2.1), then the real parameter m_n must satisfy the equation

$$m_n^2 = k^2 + \frac{n^2\pi^2}{W^2}. \tag{2.10}$$

The coefficients B_n are determined by the boundary condition at the BM, so that using equation (2.4) with (2.5) and (2.8) gives

$$\sum_{n=0}^{\infty} B_n \left.\frac{\partial\phi_n(y,z)}{\partial z}\right|_{z=0} = -2i\omega\rho V(k)\psi(y). \tag{2.11}$$

If $\phi_n(y,z)$ is given by (2.9), then equation (2.11) can be written as

$$\sum_{n=0}^{\infty} B_n m_n \sinh(m_n H)\cos\left(\frac{n\pi y}{W}\right) = 2i\omega\rho\psi(y)V(k). \tag{2.12}$$

Multiplying each side of (2.12) by $\cos(n\pi y/W)$ and integrating from 0 to W over y, the orthogonality of the $\cos(n\pi y/W)$ function yields

$$B_n = \frac{2i\omega\rho A_n}{m_n \sinh\left(m_n H\right)} V\left(k\right), \tag{2.13}$$

where the coupling coefficient for $n = 0$ is defined as

$$A_0 = \frac{1}{W}\int_0^W \psi\left(y\right) dy, \tag{2.14}$$

and for $n \geq 1$ is

$$A_n = \frac{2}{W}\int_0^W \cos\left(\frac{n\pi y}{W}\right)\psi\left(y\right) dy. \tag{2.15}$$

We now explicitly define the “modal” pressure difference to be

$$p(x) = \frac{1}{W}\int_0^W p\left(x,y,0\right)\psi\left(y\right) dy. \tag{2.16}$$

The longitudinal pressure distribution is defined to have this modal form so that the ratio of pressure to BM velocity is equal to the BM impedance, and the product of modal pressure and BM velocity is equal to acoustic power. The modal pressure can be written using (2.8) and (2.9) as

$$p\left(x\right) = \frac{1}{W}\sum_{n=0}^{\infty} B_n \cosh\left(m_n H\right)\int_0^W \cos\left(\frac{n\pi y}{W}\right)\psi\left(y\right) dy\, e^{-ikx}, \tag{2.17}$$

so that using equations (2.13), (2.14) and (2.15) and writing the modal pressure by analogy with the modal velocity in equation (2.5) as

$$p\left(x\right) = P\left(k\right) e^{-ikx}, \tag{2.18}$$

then

$$P\left(k\right) = 2i\omega\rho\left[\frac{A_0^2}{k}\coth\left(kH\right) + \sum_{n=1}^{\infty}\frac{A_n^2}{2m_n}\coth\left(m_n H\right)\right] V\left(k\right). \tag{2.19}$$

The form of the BM vibration across the cochlea, $\psi(y)$ in equation (2.6), is assumed to take a half sinusoidal form across its width, *B*, and although we initially consider the case where the BM is positioned arbitrarily across the cochlear partition, most of the simulations are performed assuming that the BM is positioned at the side, as both shown in Figure 2.1.

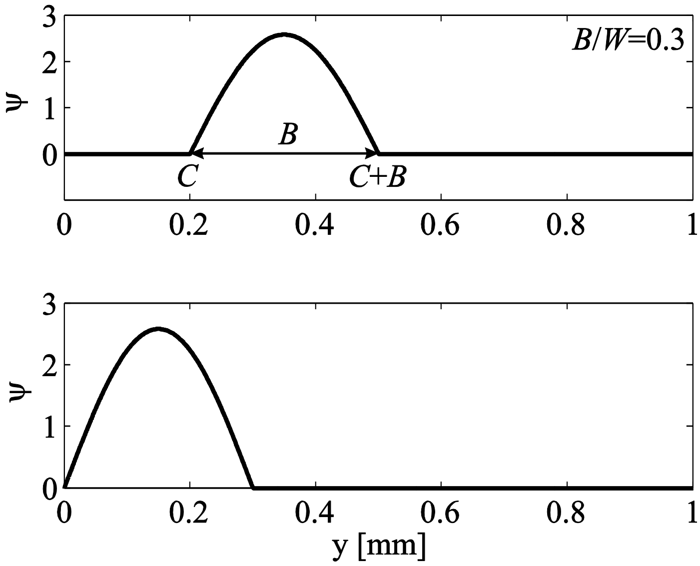

Figure 2.1 General form of the BM velocity distribution across the cochlear partition (above) and specific case used in this thesis (below).

Thus for the general case, in our coordinate system,

$$\psi(y) = \begin{cases} \sqrt{\frac{2W}{B}} \sin\left[\frac{\pi(y-C)}{B}\right], & \text{for } C \le y \le C+B, \\ 0, & \text{otherwise,} \end{cases} \tag{2.20}$$

where the factor of $\sqrt{\frac{2W}{B}}$ ensures that $\psi(y)$ is normalised in the way defined in equation (2.6).

Following the approach of Steele and Taber (Steele and Taber, 1979), the modal pressure difference in the wavenumber domain can be written as

$$P(k) = Z_{\mathrm{FC}}(k)V(k), \tag{2.21}$$

where $V(k)$ is the wavenumber spectrum of the modal BM velocity distribution along the cochlea and $Z_{\mathrm{FC}}(k)$ is the wavenumber representation of the fluid coupling impedance. It is convenient, de Boer (de Boer, 1984), to express $Z_{\mathrm{FC}}(k)$ in the form

$$Z_{\mathrm{FC}}(k)=2i\omega\rho Q\left(k\right), \tag{2.22}$$

where $Q\left(k\right)$, which is called the "equivalent height" (de La Rochefoucauld and Olson, 2007), has the dimensions of length and can be expressed, according to equation (2.19), as

$$Q(k)=\frac{A_0^2}{k}\coth\left(kH\right)+\sum_{n=1}^{\infty}\frac{A_n^2}{2a_n}\coth\left(m_nH\right). \tag{2.23}$$

Although a rectangular cross-section for the fluid chambers is assumed here, de Boer (de Boer, 1991) has shown that similar results are obtained if the cross section is assumed to be semi-circular. The equivalent height $Q\left(k\right)$ can be split into two components, one due to the far-field fluid coupling, $Q_{\mathrm{F}}(k)$, and one due to the near-field fluid coupling, $Q_{\mathrm{N}}(k)$, so that

$$Q\left(k\right)=Q_{\mathrm{F}}\left(k\right)+Q_{\mathrm{N}}\left(k\right). \tag{2.24}$$

Figure 2.2 shows the variation of $Q(k)/H$ with kH, where H is the physical height of one fluid chamber, for the parameters listed in Table 2.1. The BM is assumed to be located on one side of the cochlear partition, i.e. C=0, and its width, B, is assumed to be 0.3 times that of the cochlear partition, W, for the uniform cochlear model. In Figure 2.2, there are two components of $Q(k)$ corresponding to the far-field and near-field components. For long wavelengths, small k, the near-field coupling, $Q_{\mathrm{N}}(k)$, becomes a constant. For short wavelengths, large k, $Q_{\mathrm{N}}(k)$ is equal to $1/k$, whatever the BM width.

For small values of k, however, the near-field term becomes a constant which can be interpreted as an effective fluid thickness, T, due to the fluid coupling, which adds to the physical mass of the BM (Neely, 1985). The value of T as a function of the BM width can be derived by taking two terms in the series expansion of the first part of equation (2.23) and the limiting case of the remaining parts to give (Elliott, *et al.*, 2011)

$$T=\frac{8BH}{3\pi^2W}+\sum_{n=1}^{\infty}\frac{4B}{n\pi^3}\coth\left(n\pi H/W\right)\left[\frac{1+\cos\left(n\pi B/W\right)}{1-n^2B^2/W^2}\right]^2. \tag{2.25}$$

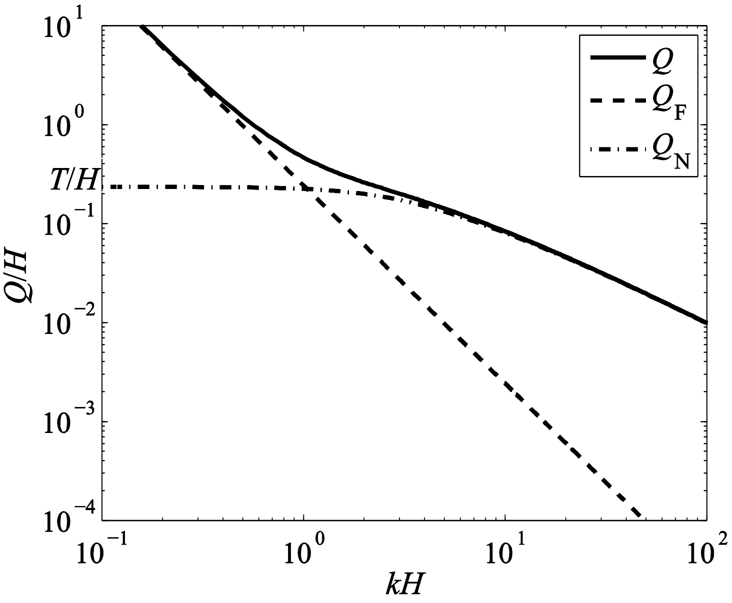

Figure 2.2 The wavenumber description of the total fluid coupling in the box model of the cochlea (solid line) and its decomposition into far-field components (dashed line) and near-field components (dot-dashed line).

It should be noted that the near-field term here is different from the "short wave" component discussed by de Boer (de Boer, 1996), for example, where the limit for large k is taken to yield a fluid coupling impedance proportional to $1/k$. The definition of $Q_N(k)$ used here includes all the elements of $Q(k)$ except the term $Q_F(k)$. This definition is, however, similar to that used by Mammano and Nobili (Mammano and Nobili, 1993) for the long-range and short-range parts of their fluid coupling Green's function. This is because the long wave components are associated with the pressure response some distance from the source of excitation on the BM, and so is descripted as the far-field components, whereas the short wave components are, as well can be seen, associated with the pressure response close to the source of excitation and so is called the near-field components. Note, however, that formally speaking both terms describe the behaviour in the hydrodynamic near-field of the source, if the fluid is sufficiently incompressible that the wavelength is large compared with the length of the cochlea, so that it is the geometric near and far-fields referred here.

Table 2.1 Values of physical parameters used for the passive cochlear simulations.

Variable	Parameter	Value
L	Length of cochlea	35 mm
W	Width of fluid chamber	1 mm
B	Width of basilar membrane	0.3 mm
H	Physical height of single fluid chamber	1 mm
h	Effective chamber height for 1D model	4.1 mm
ρ	Density of fluid	1,000 kg m^{-3}
N	Number of elements in discrete model	512
$\Delta = L/N$	Length of element	68 μm
m_0	BM mass, 1D model	0.3 kg m^{-2}
m_{3D}	BM mass, 3D model	0.05 kg m^{-2}
f_B	BM natural frequency at base	20,000 Hz
ω_0	BM natural frequency distribution	$2\pi f_B e^{-x/l}$
l	Natural frequency length scale	7 mm
$s_0(x)$	BM stiffness	$m_0\omega_0^2(x)$
ζ_0	BM damping ratio	0.1
r_0	BM damping	$2m_0\zeta_0\omega_0$
d	Characteristic distance	0.8 mm

The far-field fluid component is defined so that it obeys the equation derived from a one dimensional analysis of the incompressible fluid coupling and given by (Elliott, *et al.*, 2011)

$$\frac{\partial^2 p_F(x)}{\partial x^2} = -\frac{2i\omega\rho}{h} v(x), \tag{2.26}$$

where h is the effective chamber height, assumed here to be independent of x, so that in the wavenumber domain

$$P_F(k) = \frac{2i\omega\rho}{k^2 h} V(k), \quad Z_F(k) = \frac{2i\omega\rho}{k^2 h} \quad \text{and} \quad Q_F(k) = \frac{1}{k^2 h}. \text{(2.27)(2.28)(2.29)}$$

We can thus decompose $Q(k)$ in equation (2.22) as in equation (2.24) and define the near-field component to be

$$Q_N(k) = Q(k) - Q_F(k). \tag{2.30}$$

The effective height can be expressed in terms of the physical height of the fluid chamber, H, its width, W, and the width of the BM, B, as (Elliott, *et al.*, 2011)

$$h = \frac{\pi^2 WH}{8B}, \tag{2.31}$$

so that for the ratio of B to W used here, 0.3, the effective chamber height is about 4.1 times the physical chamber height.

The assumed BM motion in equation (2.20) corresponds to that of a beam with simply-supported boundary conditions at both ends. Steele and Taber (Steele and Taber, 1979) also consider clamped boundary conditions, for which they assumed that the transverse BM mode shape is proportional to $\sin^2(\pi y/B)$, in which case the equivalent value of h, in our notation, is $3WH/2B$. The effective height, h, is thus again proportional to WH/B but with the constant of proportionality being 1.5, instead of about 1.23 in equation (2.31). This illustrates how the results are relatively insensitive to the exact mode shape of the transverse BM velocity, which is, in fact more closely modelled as having a simply-supported boundary condition at one end and a clamped boundary condition at the other (Homer, *et al.*, 2004). Whereas the exact expression for the BM mode shape with a simply-supported boundary condition at one end and a clamped boundary condition at the other is more complicated and cannot give an explicit expression for the modal BM velocity and modal pressure. So for this analytic analysis, simply-supported boundary conditions are assumed for both ends and the more accurate boundary conditions given by Homer *et al*. (Homer, *et al.*, 2004) are used for the FE cochlear model. A comparison has also been made to show the effect of different BM boundary conditions on the overall response of the BM, as shown in Appendix D, using a FE cochlear model.

To illustrate the change in the pressure distribution with wavenumber, Figure 2.3 shows the equal-pressure contours in a cross-section of the box model for various values of kH.

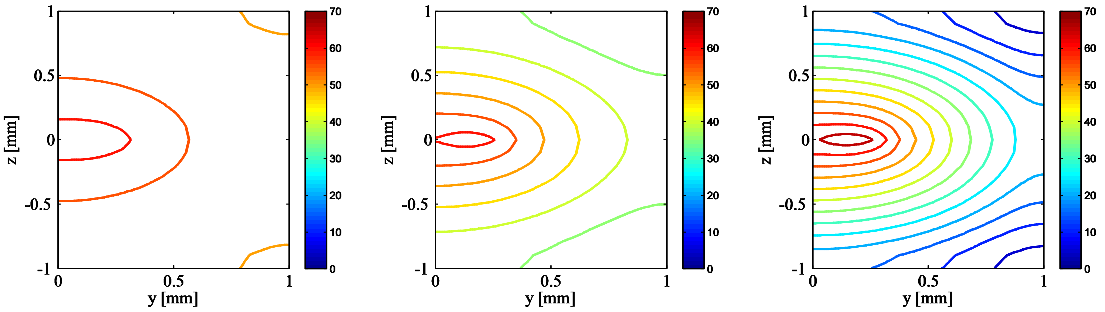

Figure 2.3 Contours of equal pressure, at 5 dB intervals, in a cross-section of the box model of the cochlea when the BM, which is on the left hand third of the cochlear partition in this case, has a longitudinally sinusoidal variation with normalised wavenumbers of kH = 1.5 (left), kH = 3 (centre) and kH = 6 (right), corresponding to wavelengths $\lambda\approx 4H$, $\lambda\approx 2H$ and $\lambda\approx H$, where H is the physical height of a single chamber.

For low values of kH the wavelength of the longitudinal BM vibration is much greater than the height of the fluid chamber, and so $Q_N(k)$ is very small compared with $Q_F(k)$, which is proportional to $1/k^2$, and the pressure is almost uniform across the cross-sectional area. As the wavelength becomes comparable with the height, $Q_N(k)$ becomes comparable with $Q_F(k)$ and significant variation can be seen in the pressure across the cross-section. When the wavelength is small compared with the height, $Q_N(k)$ becomes equal to $1/k$, which is large compared with $Q_F(k)$ and the pressure is much greater close to the BM than it is in the rest of the fluid chamber.

The far-field component is often referred to as the 1D fluid coupling, since it can be readily derived from a one-dimensional box model of the cochlea with the assumption that the wavelength is long compared with the height of the fluid chamber (de Boer, 1996). The full fluid coupling model, including near-field components, is then referred to as 3D fluid coupling. It must be emphasised, however, that when the cochlear mechanics is formulated in terms of the longitudinal variation of a single velocity and a single pressure variable, this formulation can clearly still incorporate the 3D fluid coupling. It may thus be misleading to call this a 1D formulation, even though it does only have one dimension, and so it is described as “uniaxial” to represent this single axis model of the cochlear mechanics.

2.3 Calculation of the Far-field Component

The far-field component of the fluid coupling in the discrete model can be readily calculated using the finite difference approach used by Neely (Neely, 1981) and Neely and Kim (Neely and Kim, 1986), so that the spatial derivative in equation (2.26) is written as

$$\frac{p_{\mathrm{F}}(n-1)-2p_{\mathrm{F}}(n)+p_{\mathrm{F}}(n+1)}{\Delta^2}=-\frac{2i\omega\rho}{h}v(n). \qquad (2.32)$$

The length of one element is Δ and if the first and last elements, representing the boundary conditions at the base and apex, are assumed to have the same length as the BM elements, then $\Delta = L/N$, where L is the assumed length of the cochlea.

The boundary conditions at the base and apex of the cochlea are assumed to be determined by the velocity of the stapes, corrected for the difference between the Stapes and the chamber area, u_{s} , and a zero pressure difference condition at the helicotrema, so that

$$\frac{\partial p_{\mathrm{F}}(x)}{\partial x}\Big|_{x=0}=-2i\omega\rho u_{\mathrm{s}} \quad \text{and} \quad p_{\mathrm{F}}(x)\big|_{x=L}=0. \qquad (2.33)(2.34)$$

In the discrete representation, the finite difference method can be used at the base to express these boundary conditions as

$$\frac{p_{\mathrm{F}}(2)-p_{\mathrm{F}}(1)}{\Delta}=-2i\omega\rho u_s \quad \text{and} \quad p_{\mathrm{F}}(N)=0. \qquad (2.35)(2.36)$$

The complete discrete model of the far-field fluid coupling can thus be written in matrix form as

$$\frac{1}{\Delta^2}\begin{bmatrix} -\Delta & \Delta & & & & \\ h & -2h & h & & & \\ 0 & h & -2h & h & & \\ & & \ddots & & & \\ & & & h & -2h & h \\ & & & 0 & 0 & \Delta^2 \end{bmatrix}\begin{bmatrix} p_{\mathrm{F}}(1) \\ p_{\mathrm{F}}(2) \\ \\ \vdots \\ p_{\mathrm{F}}(N-1) \\ p_{\mathrm{F}}(N) \end{bmatrix}=-2i\omega\rho\begin{bmatrix} 0 \\ v(2) \\ \\ \vdots \\ v(N-1) \\ 0 \end{bmatrix}-2i\omega\rho\begin{bmatrix} u_{\mathrm{s}} \\ 0 \\ \\ \vdots \\ 0 \\ 0 \end{bmatrix}, \qquad (2.37)$$

or, more compactly, as

$$\mathbf{F}\,\mathbf{p}_{\mathrm{F}} = -2i\omega\rho\left(\mathbf{v}+\mathbf{v}_{\mathrm{s}}\right), \tag{2.38}$$

so that

$$\mathbf{p}_{\mathrm{F}} = \mathbf{p}_{\mathrm{Fs}} + \mathbf{Z}_{\mathrm{F}}\mathbf{v}, \tag{2.39}$$

where $\mathbf{Z}_{\mathrm{F}}$ is equal to $-2i\omega\rho\mathbf{F}^{-1}$ and denotes the far-field fluid coupling matrix, and $\mathbf{p}_{\mathrm{Fs}}$ is equal to $-2i\omega\rho\mathbf{F}^{-1}\mathbf{v}_{\mathrm{s}}$ and denotes the pressure vector due to the stapes motion.

Taking only the far-field components of the fluid coupling into account and using the expression for $\mathbf{Z}_{\mathrm{F}}$ above, the vector of pressures, as shown in equation (1.21), in the coupled cochlea can be written as

$$\mathbf{p}_{\mathrm{F}} = \left[\mathbf{I} - 2i\omega\rho\mathbf{F}^{-1}\mathbf{Y}_{\mathrm{BM}}\right]^{-1}\mathbf{p}_{\mathrm{Fs}}. \tag{2.40}$$

Using the expression for $\mathbf{p}_{\mathrm{Fs}}$ above and the properties of the matrix inverse, this can be written as

$$\mathbf{p}_{\mathrm{F}} = \left[\mathbf{F} - 2i\omega\rho\mathbf{Y}_{\mathrm{BM}}\right]^{-1}\mathbf{v}_{\mathrm{s}}, \tag{2.41}$$

which is the form of equation originally suggested by Neely (Neely, 1981) and used by Neely and Kim (Neely and Kim, 1986). The matrix to be inverted in equation (2.41) is tri-diagonal, for which the inverse can be efficiently computed, using Gaussian elimination, for example.

Figure 2.4 illustrates the spatial distribution of this far-field pressure difference, proportional to the columns of the matrix $\mathbf{F}^{-1}$, for excitation at a number of different locations along the cochlea with the assumption that u_{s} is set to zero. The imaginary component has been plotted for the assumed velocity excitation here and below, but it would be real for an acceleration source. These distributions are very similar to those obtained from an analytic solution to the differential equation for the far-field fluid coupling, equation (2.26), with the appropriate boundary conditions, which can be obtained by assuming that $v(x)$ is equal to v_0 between $x_0 - \Delta$ and x_0, and is zero elsewhere, and setting $\partial p_{\mathrm{F}} / \partial x$ equal to the slope of the linear fall off in pressure for x greater than x_0, and is given by

$$p_{\mathrm{F}}(x)\big|_{0 < x < x_0 - \Delta} = 2i\omega\rho \frac{(L - x_0)}{h} \Delta v_0 , \tag{2.42}$$

$$p_{\mathrm{F}}(x)\big|_{x_0 < x < L} = 2i\omega\rho \frac{(L - x)}{h} \Delta v_0 , \tag{2.43}$$

where, for continuity, it has been assumed below that Δ is very small compared with L.

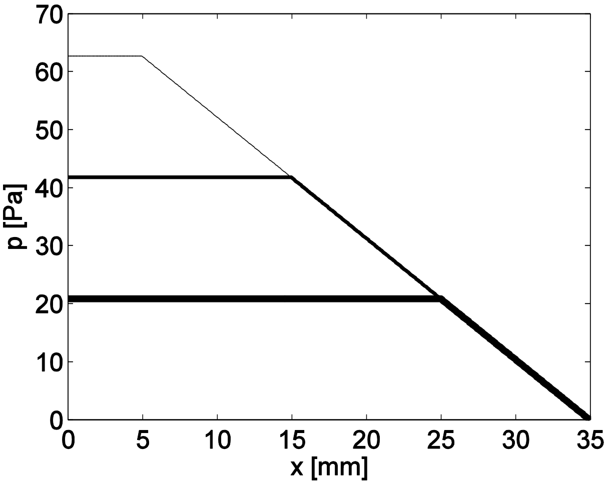

Figure 2.4 Distributions of the pressure difference along the cochlea due to the far-field component of the fluid coupling when only a single element of the discrete BM at x = 5 mm (faint line), 15 mm (medium line) or 25 mm (bold line) is driven sinusoidally with a velocity of 10 mm·s^{-1} at a frequency of 1 kHz.

2.4 Calculation of the Near-field Component

We now define the full fluid coupling matrix for the discrete model to be

$$\mathbf{Z}_{\mathrm{FC}} = \mathbf{Z}_{\mathrm{F}} + \mathbf{Z}_{\mathrm{N}} , \tag{2.44}$$

where $\mathbf{Z}_{\mathrm{N}}$ contains the terms due to the near-field fluid coupling. When transformed into the spatial domain, the inverse Fourier transform of $Z_{\mathrm{N}}(k)$ in equation (2.24) contains singularities, due to the implicit assumption of a velocity distribution equal to a spatial delta function. In the discrete model, however, the motion of the n-th single BM element represents a finite velocity distribution given by

$$v_n(x) = \begin{cases} v_0 & (n-1)\Delta \le x \le n\Delta \\ 0 & x \ge n\Delta \text{ or } x \le (n-1)\Delta \end{cases}, \tag{2.45}$$

where v_0 is independent of *x*.

The wavenumber spectrum of this velocity distribution is

$$V_n(k) = v_0 \frac{\sin k\Delta/2}{k\Delta/2} e^{-ik(n-\frac{1}{2})\Delta}. \tag{2.46}$$

The component of the pressure distribution generated by this velocity distribution due to the near-field fluid coupling is then

$$P_n(k) = Z_\mathrm{N}(k)V_n(k). \tag{2.47}$$

Equation (2.47) can be numerically evaluated using the above variation for $V_n(k)$ and the fact that $Z_\mathrm{N}(k)$ is equal to $Z_\mathrm{FC}(k)$ minus $Z_\mathrm{F}(k)$. The inverse Fourier transform of equation (2.47) can then be used to calculate the near-field component of the pressure in the spatial domain, as shown in Figure 2.5 for excitation by a single element. Averaging this continuous pressure distribution over each element of the discrete model then provides the discrete pressure distribution due to the near-field wave coupling, as also shown in Figure 2.5.

Since the near-field component of the fluid coupling impedance is equal to a constant for kH less than about unity, as shown in Figure 2.2, then for such small values of k, $Z_\mathrm{N}(k)$ can be written as $2i\omega\rho T$, where T is an effective fluid thickness. The near-field pressure contribution, equation (2.47), for $k = 0$, $P_n(0)$, is thus equal to $2i\omega\rho T v_0$, where the limiting case of equation (2.46) has also been taken. Using the properties of the wavenumber transform, then $P_n(0)$ is also equal to the integral of the near-field component of the pressure in the spatial domain, or, equivalently, to the sum of the elements of the discrete pressure distribution shown in Figure 2.5. This observation can be used to provide an independent check on the magnitude of the near-field components. It also suggests that an approximation to the near-field component, which is valid if the wavelength of the slow cochlear wave is long compared with *H* or so range of the near-field pressure shown in Figure 2.5, is a single pressure acting at the point of excitation having a magnitude $2i\omega\rho T v_0$. The variable T can thus be interpreted as the effective thickness of the fluid loading on the BM due to the near-field components of the pressure (Neely, 1985).

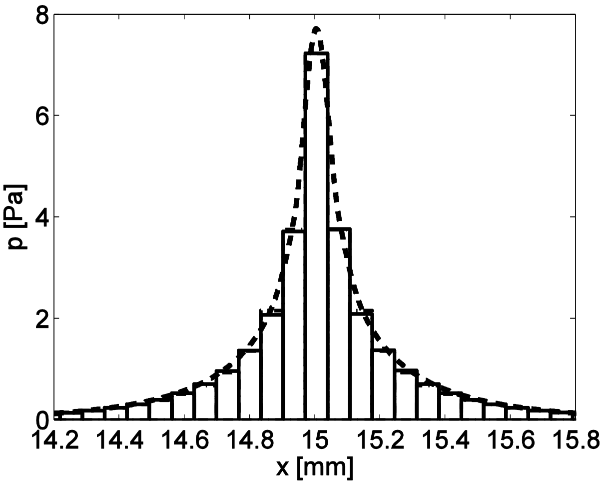

Figure 2.5 Distributions of the modal pressure along the cochlea due to the near-field fluid coupling (dashed line) and the average pressure over discrete elements of the BM used to calculate the columns of $\mathbf{Z}_\mathrm{N}$ (solid line), when excited by a single element at x = 15 mm with a velocity of 10 mm·s^{-1} at a frequency of 1 kHz. Also shown is the approximation to the averaged pressure given by equation (2.49) (dot-dashed lines).

The distribution of the near-field component of the fluid pressure can also be derived using an analysis of the acoustic field due to an elemental source in a duct, following Doak (Doak, 1973). The modal pressure distribution is shown to be due to the contributions from a number of evanescent higher order modes in the duct, whose amplitudes decay exponentially, which can be written as

$$p_\mathrm{N}(x) = \sum_{m=1}^{\infty} a_m e^{-r/l_m}, \tag{2.48}$$

where m denotes the order of the mode, a_m is its amplitude, r is equal to $|x - x_0|$ and l_m its characteristic decay length. The characteristic length decreases as the mode order gets higher and so it is the lower order modes that dominate when some distance from the source.

In fact, a reasonable approximation to the averaged near-field pressure in the discrete model, due to a single BM element, is obtained using only two terms of such a series, so that

$$p_{\mathrm{NA}}(n') = 2i\omega\rho\left(Q_1 e^{-n'\Delta/l_1} + Q_2 e^{-n'\Delta/l_2}\right)v_0, \tag{2.49}$$

where n' is equal to the number of elements from the position where the averaged pressure is evaluated to the exciting element, and is equal to $|n - n_0|$ for excitation of the n_0-th element, Δ is the length of one element and l_1 and l_2 are characteristic decay lengths. The near-field pressure amplitudes are proportional to the equivalent height Q_1 and Q_2, to the n_0-th excitation velocity, v_0, in equation (2.45). This approximation to the average pressure over the discrete elements is also shown in Figure 2.5, with Q_1 and Q_2 equal to 16·μm and 41.56 μm, l_1 equal to $H/3.47$ and l_2 equal to $H/12.8$, and is seen to provide a good approximation to the result obtained from the inverse Fourier transform of equation (2.47).

A position-shifted sequence of these pressure distributions, normalised by the velocities of each element, can then be used to define the columns of the matrix $\mathbf{Z}_{\mathrm{N}}$, which determines the fluid coupling due to the near-field components in the discrete model. The total distributions due to both the far and near-field fluid coupling are then obtained by summing these two contributions, as illustrated in Figure 2.6. These distributions are similar to those shown by other authors, for example Parthasarathi *et al.* (Parthasarathi, *et al.*, 2000), except that the singularity induced by assuming that the velocity is concentrated at a single point has been removed by assuming a finite value of the velocity distribution over the length of an element.

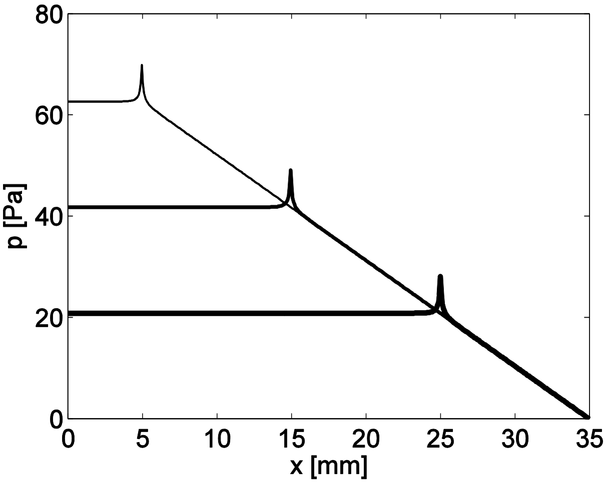

Figure 2.6 Distributions of the total pressure difference due to both the far and near-field components in the fluid coupling matrix along the length of the cochlea due to excitation of a single element on the BM at x = 5 mm, 15 mm and 25 mm with a velocity of 10 mm·s^{-1} at a frequency of 1 kHz.

2.5 The Coupled Response

Figure 2.7 shows a comparison of the predicted BM velocity in a uniform cochlea model having the properties with either 1D or 3D fluid coupling. In these models the BM mass per unit area has been assumed constant along the length of the cochlea. Its stiffness and damping have been adjusted to achieve an exponential distribution of natural frequency and a constant damping ratio. The value of the BM mass varies, however, between the models using the 1D and 3D fluid coupling, since in the former case this must include the added mass due to the near-field fluid loading, whereas in the latter case this is automatically included. The physical height of the fluid chamber is used in the 3D model, so that the effective chamber height is the same in both cases. These changes, which are similar to those assumed by de Boer (de Boer, 1996) in his “matched” model, for example, are made in order for the results using the 1D and 3D fluid coupling to be as consistent as possible, so that the effects of the fluid coupling can be seen most clearly.

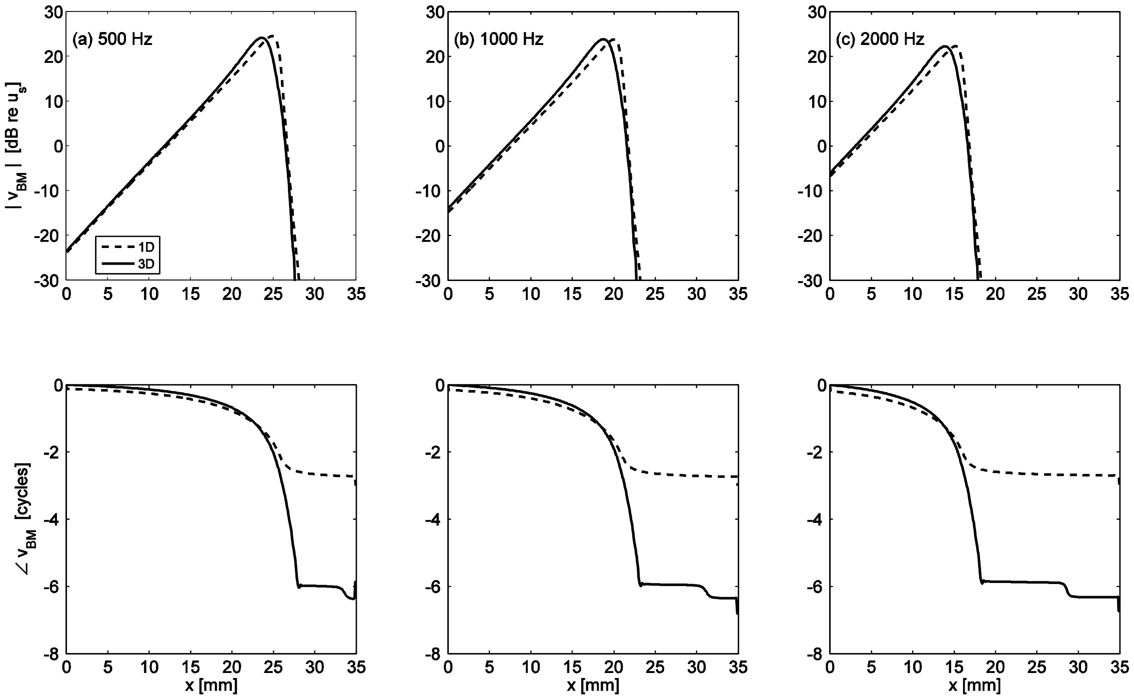

Figure 2.7 BM velocity, normalised to that of the stapes for the coupled model with either full 3D fluid coupling and a BM mass of 0.05 kg·m^{-2} or 1D fluid coupling and a BM mass of 0.3 kg·m^{-2}, with excitation frequencies of (a) 500 Hz, (b) 1 kHz and (c) 2 kHz and a damping ratio of 0.1.

Although a reasonable matching of the magnitudes can be obtained between 1D and 3D models, the roll-off of the model with the 3D fluid coupling is somewhat greater than that of the model with the 1D fluid coupling and the peak response of the 3D model is more basal than the corresponding 1D model as also observed by de Boer (de Boer, 1981). The accumulation of phase lag of the 1D model, however, is significantly less than that of the 3D model apical to the characteristic place as also observed by de Boer (de Boer, 1996) and Kolston (Kolston, 2000). This reflects the changes in the wavelength of the BM motion as it approaches the characteristic place, becoming comparable with the chamber height and invalidating the assumptions of the 1D model. There is then a reduction in longitudinal fluid flow and an increase in the local mass loading, slowing the wave and increasing the phase accumulation (Kolston, 2000).

2.6 Fluid Coupling in a Non-uniform Asymmetric Cochlea

2.6.1 Far-field Pressure

In this section a one-dimensional analysis is used to derive the far-field component of the pressure in each of the fluid chambers for a model of the cochlea with asymmetrical and non-uniform fluid chambers and hence the far-field contribution to the pressure difference. Since the near-field components of the pressure are not significantly affected by the shape of the cochlear chambers, they will continue to be approximately equal and opposite in the two chambers and can be calculated using the wavenumber approach for a uniform cochlea described above. An example is then given of the calculated pressure difference for two assumed variations of the chamber volumes. The effect of this modified fluid coupling on the coupled response of the passive cochlear model is then illustrated.

If areas of the upper fluid chamber, SM and SV, and the lower fluid chamber, ST, vary along the length of the cochlea as $A_1(x)$ and $A_2(x)$, the far-field component of the pressure will be still determined by the continuity and momentum equations. Assuming that the longitudinal fluid velocity in a single chamber, averaged across its cross-sectional area, is $\bar{u}(x)$, and that the radial BM velocity averaged across the width of the chamber is $\bar{v}(x),$ then the continuity equation for this chamber can be written as

$$\frac{\partial}{\partial x}\left[A(x)\bar{u}(x)\right]=W(x)\bar{v}(x), \tag{2.50}$$

where in general the CP width also varies along the cochlear as $W(x)$. This is equivalent to the equation used by Peterson and Bogert (Peterson and Bogert, 1950), except that the fluid is assumed here to be incompressible.

The momentum equation can also be written in terms of the complex pressure averaged across the cross-sectional area, $\bar{p}(x),$ as

$$\frac{\partial\bar{p}(x)}{\partial x}=-i\omega\rho\bar{u}(x). \tag{2.51}$$

Substituting $\bar{u}(x)$ in equation (2.51) into equation (2.50) gives an expression for $\bar{p}(x)$ in terms of $\bar{v}(x)$ as

$$\frac{\partial}{\partial x}\left[A(x)\frac{\partial \bar{p}(x)}{\partial x}\right] = -i\omega\rho W(x)\bar{v}(x), \tag{2.52}$$

which is an incompressible form of Webster's horn equation, described by Fletcher and Rossing (Fletcher and Rossing, 1998), for example.

Applying equation (2.52) to the upper chamber, it can be written in terms of the modal BM velocity, $v(x)$, and the modal pressure $p_1(x)$, by noting that the velocity distribution in the radial direction at position x is equal to $v(x)\,\psi(y)$, so that

$$\bar{v}(x) = \frac{v(x)}{W(x)}\int_0^{W(x)} \psi(y)\,dy, \tag{2.53}$$

and since, in the far-field limit, the pressure is uniform over the BM, then the definition of the modal pressure gives

$$p_1(x) = \frac{\bar{p}(x)}{W(x)}\int_0^{W(x)} \psi(y)\,dy. \tag{2.54}$$

If the BM velocity is a half sinusoid over a distance B on one side of the fluid chamber, as assumed for the uniform case, then in this case

$$\frac{1}{W(x)}\int_0^{W(x)} \psi(y)dy = \frac{2}{\pi}\sqrt{\frac{2B(x)}{W(x)}}. \tag{2.55}$$

The far-field fluid coupling equation in the upper chamber can thus be written in terms of the modal pressure, and modal velocity as

$$\frac{\partial}{\partial x}\left[A_1(x)\frac{\partial}{\partial x}\left(p_1(x)\sqrt{\frac{W(x)}{B(x)}}\right)\right] = -\frac{8i\omega\rho}{\pi^2}v(x)\sqrt{W(x)B(x)}. \tag{2.56}$$

In general, however, the in the lower fluid chamber is similarly related to the modal BM velocity by

$$\frac{\partial}{\partial x}\left[A_2(x)\frac{\partial}{\partial x}\left(p_2(x)\sqrt{\frac{W(x)}{B(x)}}\right)\right]=\frac{8i\omega\rho}{\pi^2}v(x)\sqrt{W(x)B(x)}. \tag{2.57}$$

The integral of $i\omega\rho v(x)$ with respect to x is thus equal to both of the expressions below

$$\frac{8i\omega\rho}{\pi^2}\int_0^x v(x')\sqrt{B(x')W(x')}dx'=A_2(x)\frac{\partial}{\partial x}\left(p_2(x)\sqrt{\frac{W(x)}{B(x)}}\right)=-A_1(x)\frac{\partial}{\partial x}\left(p_1(x)\sqrt{\frac{W(x)}{B(x)}}\right), \tag{2.58}$$

where x' is dummy integration variable, and the fact that both $\partial p_1(x)/\partial x$ and $\partial p_2(x)/\partial x$ are zero when x is equal to zero has been used to eliminate any constants of integration. The pressure gradients in the two chambers are thus related by

$$\frac{\partial}{\partial x}\left(p_2(x)\sqrt{\frac{W(x)}{B(x)}}\right)=-\frac{A_1(x)}{A_2(x)}\frac{\partial}{\partial x}\left(p_1(x)\sqrt{\frac{W(x)}{B(x)}}\right). \tag{2.59}$$

We can relate the far-field component of the modal pressure difference, $p_F(x)$, to the modal BM velocity, $v(x)$, via the effective area $A_d(x)$ in the expression

$$\frac{\partial}{\partial x}\left[A_d(x)\frac{\partial}{\partial x}\left(p_F(x)\sqrt{\frac{W(x)}{B(x)}}\right)\right]=-\frac{16i\omega\rho}{\pi^2}v(x)\sqrt{B(x)W(x)}, \tag{2.60}$$

where $p_F(x)$ is equal to $p_1(x) - p_2(x)$. The integral in equation (2.58) is thus also equal to

$$\frac{8i\omega\rho}{\pi^2}\int_0^x v(x')\sqrt{B(x')W(x')}dx'=-\frac{A_d(x)}{2}\left[\frac{\partial}{\partial x}\left(p_1(x)\sqrt{\frac{W(x)}{B(x)}}\right)-\frac{\partial}{\partial x}\left(p_2(x)\sqrt{\frac{W(x)}{B(x)}}\right)\right]. \tag{2.61}$$

Using equation (2.59) and equating (2.61) to the final form of equation (2.58) allows the effective area for the pressure difference to be written (Zwislocki, 1953) as

$$A_d(x)=\frac{2A_1(x)A_2(x)}{A_1(x)+A_2(x)}. \tag{2.62}$$

An analytic solution to the pressure difference can be obtained for excitation of a single BM element, having a velocity of v_0 from $x_0 - \Delta$ to x_0, by integrating equation (2.60) and using the boundary condition that $\partial p_\mathrm{F}(x)/\partial x$ is zero and assuming that $B(x)$ and $W(x)$ are independent of x at $x = 0$ to give

$$\frac{\partial}{\partial x}\left(p_\mathrm{F}(x)\sqrt{\frac{W(x)}{B(x)}}\right)\Bigg|_{0 < x < x_0 - \Delta} = 0, \tag{2.63}$$

$$\frac{\partial}{\partial x}\left(p_\mathrm{F}(x)\sqrt{\frac{W(x)}{B(x)}}\right)\Bigg|_{x_0 < x < L} = -\frac{16 i\omega\rho\Delta v_0\sqrt{B(x)W(x)}}{\pi^2 A_\mathrm{d}(x)} v(x). \tag{2.64}$$

The boundary condition that $p_\mathrm{F}(x)$ is zero at $x = L$ and the fact that Δ is small compared with L can then be used to integrate these expressions again to give the pressure distribution of the far-field pressure difference as

$$p_\mathrm{F}(x)\big|_{0<x<x_0-\Delta} = -16 i\omega\rho\Delta v_0\sqrt{\frac{B(x_0)W(x_0)B(x)}{W(x)}}\int_{x_0}^{L}\frac{1}{A_\mathrm{d}(x')}dx', \tag{2.65}$$

$$p_\mathrm{F}(x)\big|_{x_0<x<L} = -16 i\omega\rho\Delta v_0\sqrt{\frac{B(x_0)W(x_0)B(x)}{W(x)}}\int_{x}^{L}\frac{1}{A_\mathrm{d}(x')}dx'. \tag{2.66}$$

If the areas of the fluid chambers in the cochlear models are divided up into N discrete sections, as for the BM, equations (2.56), (2.57) and (2.62) can be used to calculate the effective area for the pressure difference at the n-th discrete element as $A_\mathrm{d}(n)$. The integrals in equations (2.65) and (2.66) can be approximated by summations to give the pressure at the n-th element as

$$p_\mathrm{F}(n)\big|_{0<n<n_0-1} = -16 i\omega\rho\Delta^2 v_0\sqrt{\frac{B(n_0)W(n_0)B(n)}{W(n)}}\sum_{n'=n_0}^{N}\frac{1}{A_\mathrm{d}(n')}, \tag{2.67}$$

$$p_\mathrm{F}(n)\big|_{n_0<n<N} = -16 i\omega\rho\Delta^2 v_0\sqrt{\frac{B(n_0)W(n_0)B(n)}{W(n)}}\sum_{n'=n}^{N}\frac{1}{A_\mathrm{d}(n')}, \tag{2.68}$$

where $n_0 = x_0/\Delta$.

Figure 2.8 shows an assumed variation of A_1 and A_2 along the length of the human cochlea, together with corresponding assumed variations in the width of the fluid chamber, *W*, and BM width, *B*. These are based on the area variations given by Zakis and Witte (Zakis and Witte, 2001), which are interpolated using a cubic spline function. They are reasonably consistent with the measurements of Thorne *et al.* (Thorne, *et al.*, 1999) and the earlier estimates shown in Fig. 79 of Fletcher (Fletcher, 1958) and Fig. 4.5 in Zwislocki (Zwislocki, *et al.*, 2003). The cross-sectional areas for the two fluid chambers used in equations (2.56) and (2.57), and the effective area for the pressure difference, equations (2.62) is also shown in Figure 2.8. Equations (2.67) and (2.68) can be used to calculate the far-field contribution to the pressure difference in the non-uniform cochlea due to asymmetry in two fluid chambers.

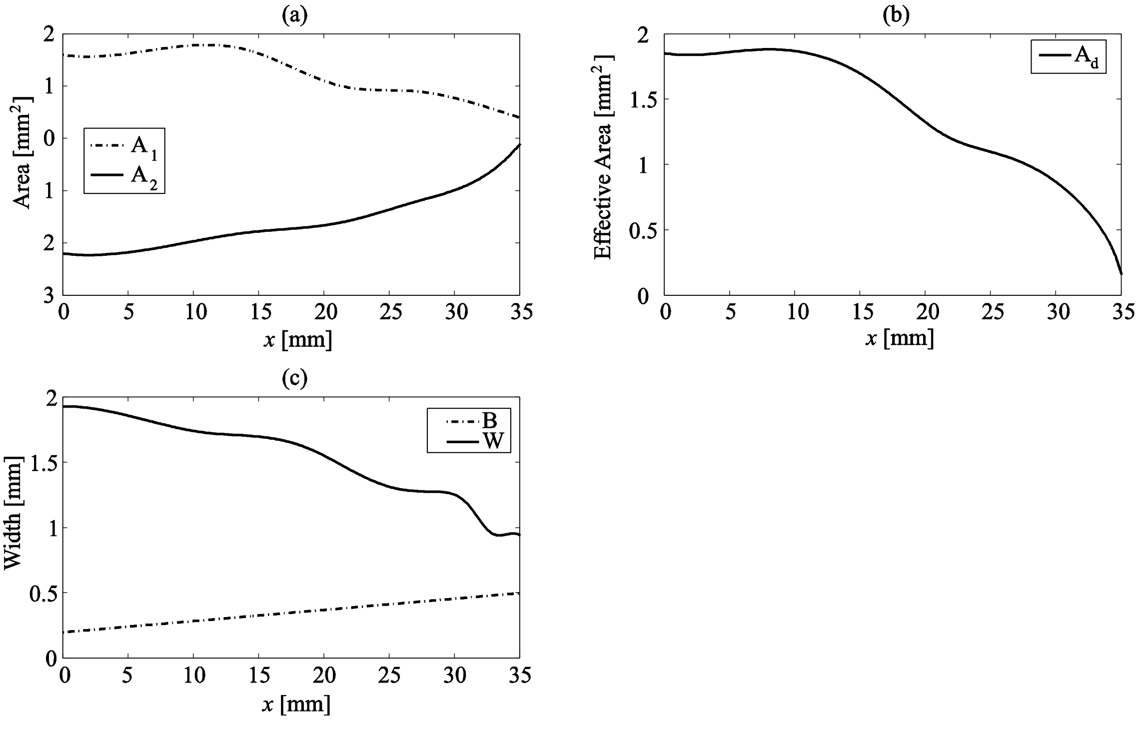

Figure 2.8 Assumed variation (a) in the cross-sectional area of the upper, A_1, and lower, A_2, fluid chambers as a function of longitudinal position in the asymmetric model, together with (b) the calculated effective area for the pressure difference and (c) the assumed variation in the width of the cochlear partition, *W*, and BM width, *B*.

2.6.2 Near-field Pressure and Coupled Response

Although the near-field component is assumed to be unaffected by the size of the fluid chambers (Elliott, *et al.*, 2011), it will depend on the proportion of the chamber width occupied by the BM. Figure 2.9 shows that there is not much variation over the range *B*/*W* = 0.11 to *B*/*W* = 0.99, as required for non-uniform cochlea. In fact, apart from the amplitude variation, the shape of these near-field components is relatively independent of *B*/*W*.

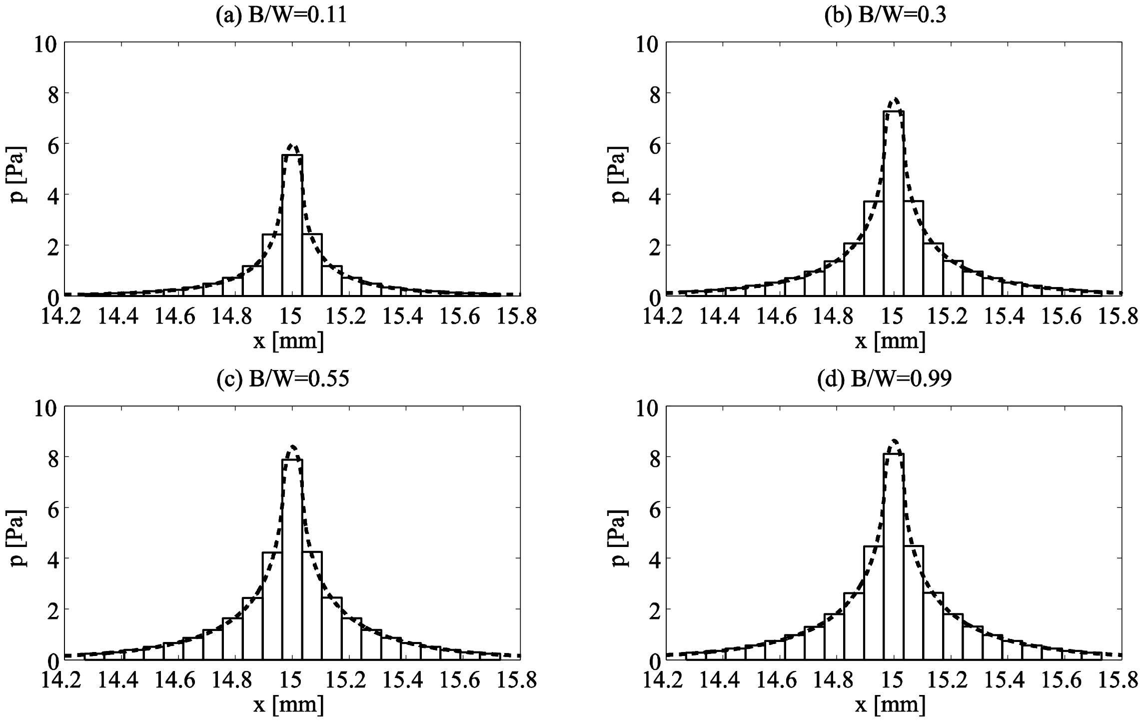

Figure 2.9 The variation of the modal pressure due to the short wavelength component of fluid coupling along the cochlea for *B*/*W* = 0.11, 0.3, 0.55 and 0.99 (dashed lines) together with the average pressure over the discrete elements (solid lines).

Figure 2.10 shows the value of effective thickness, *T*, normalized by *B*, plotted as a function of *B/W* for *W* equal to *H* and for the BM both at the edge of, and in the centre of, the cochlear partition, calculated using equation (2.25). When *B*/*W* is equal to unity, the BM extends over the whole width of the fluid chamber, so that the problem becomes almost two-dimensional. The ratio *T*/*B* then tends to about 0.27, as can be calculated by taking only the first term in equation (2.25) (Neely, 1985). When *B*/*W* becomes much less than unity, however, and the BM is in the centre of the cochlear partition, both sides of the BM element are essentially radiating as a line source into a three-dimensional space and the effective thickness becomes large compared with *B*, as seen in Figure

2.10. When B is much smaller than W, but the BM is on the edge of the cochlear partition, the effect of the side wall will be to double the pressure in front of the vibrating BM element and hence to approximately double the value of T/B, as also observed in Figure 2.10. If B is assumed to be 0.3 mm and W is assumed to be 1 mm, as in the box model above, where the BM is on the edge of the cochlear partition, then T/B is about 0.8, so that T is about 0.24 mm. The added mass due to fluid coupling, ρT, is then 0.24 kg·mm^{-1}, which is the difference between the assumed BM mass for the 1D and 3D models in Figure 2.7.

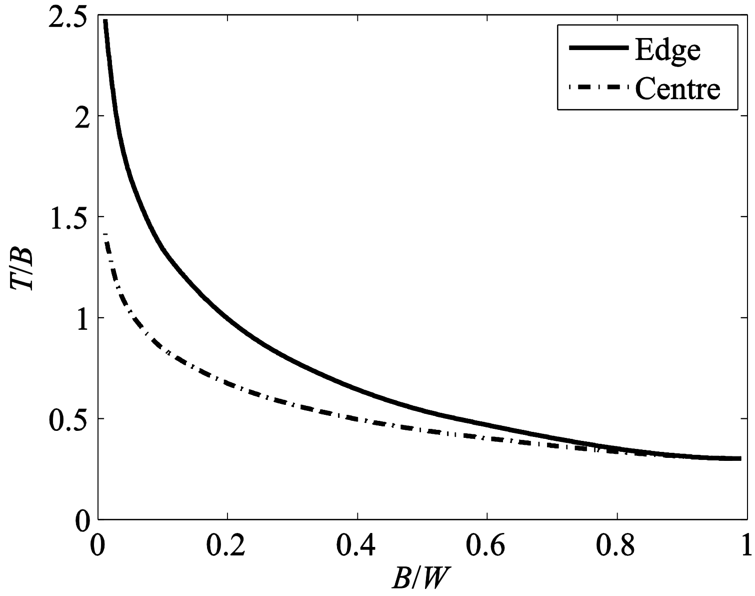

Figure 2.10 Variation of the effective thickness due to fluid loading, normalized by the BM width, T/B, as a function of the normalized BM width, B/W, for the BM both at the edge (solid line) and the centre (dashed line) of the cochlear partition.

The distribution of the modal pressure difference with both far and near-field components, due to BM excitation by a single element of the BM at 5 mm, 15 mm or 25 mm is shown in Figure 2.11. The curvature in the pressure difference distribution for x greater than x_0 is due to the reduction of the effective area with distance, as shown in Figure 2.8 (b), and also seen in Fig. A1 of Shera *et al.* (Shera, *et al.*, 2004), for example, which was calculated using a Green’s function approach.

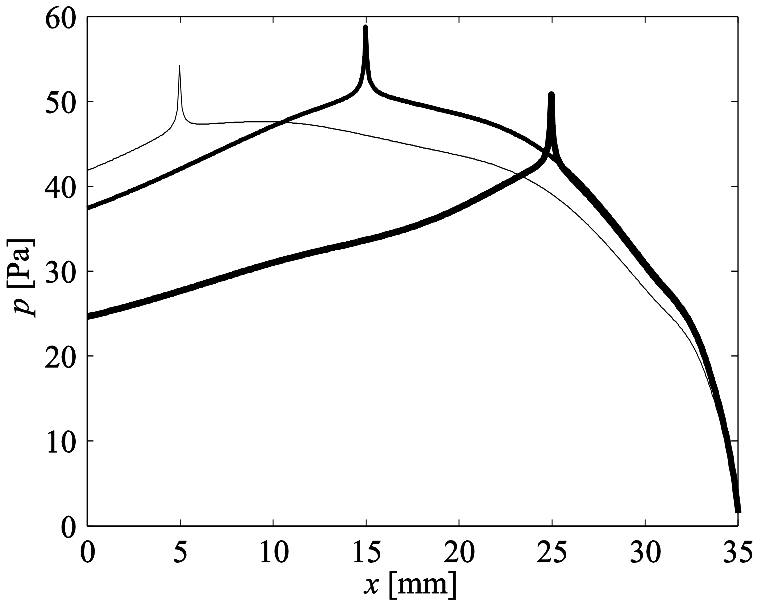

Figure 2.11 The calculated total variation in the modal pressure difference due to both far and near-field components for the model of an asymmetrical cochlea, due to the difference in chamber areas, CP width, *W*, and BM width, *B*, when only a single element of the discrete BM at x = 5 mm, 15 mm or 25 mm is driven sinusoidally with a velocity of 10 mm·s^{-1} at a frequency of 1 kHz.

Figure 2.12 shows the calculated distribution of the BM velocity calculated by combining the results shown in Figure 2.11 for the fluid coupling term with the passive BM dynamics along the length of the cochlea in the discrete model. These coupled responses do not look very different from those shown in Figure 2.7 for the uniform cochlea, particularly for frequencies of excitation. The roll-off of the non-uniform model is somewhat greater than that of the uniform model close to the characteristic place. For higher excitation frequencies, the accumulation of phase lag of the uniform model, however, is significantly less than that of the non-uniform model apical to the characteristic place. The pressures basal to the position where the BM is excited, as shown in Figure 2.11, are less than those shown in Figure 2.6, reflecting the fact that the effective height of the non-uniform model is greater than that of the uniform model, which causes the wavenumber, based on equation (6.7), has a smaller value for the non-uniform case. This indicates that the non-uniformity has a great effect on the changes in the wavelength of the BM motion as it approaches the characteristic place, since the effective area of the cochlear chambers becomes much less than that at the base. There is then a reduction in longitudinal fluid flow due to reflection and an increase in the local mass loading, slowing the wave and increasing the phase accumulation.

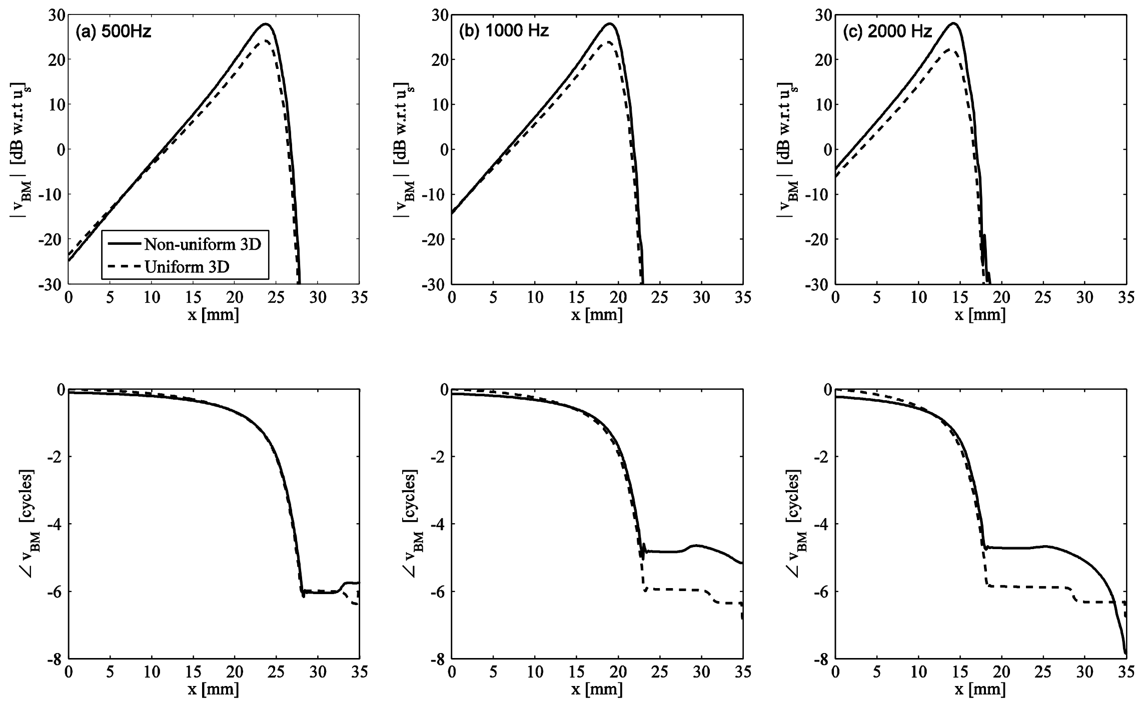

Figure 2.12 Coupled BM velocity distribution in the model of the non-uniform cochlea (solid lines) and the uniform cochlea (dashed lines) at excitation frequencies of 500 Hz, 1 kHz and 2 kHz with a damping ratio of 0.1.

2.7 Finite Element Modelling of Fluid Coupling in the Cochlea

The finite element method can be used to calculate the fluid coupling in more complicated geometries than the box model assumed in this chapter. It will be used in the next chapter to analyse fluid coupling in a coiled cochlea, but is introduced here in order to demonstrate some features of meshing and compressibility in a simple geometry.

2.7.1 Finite Element Model of a Uniform Cochlea

The finite element model assumes a rigid walled enclosure within which the BM has an imposed velocity contained in the vector $\mathbf{q}_{\mathrm{FE}}$, having dimensions of mass acceleration ($\mathrm{m} \cdot \mathrm{s}^{-2}$). The vector of pressures, $\mathbf{p}_{\mathrm{FE}}$, at all of the nodes is related to $\mathbf{q}_{\mathrm{FE}}$ by the equation

$$\mathbf{Q}\ddot{\mathbf{p}}_{\mathrm{FE}}+\mathbf{H}\mathbf{p}_{\mathrm{FE}}=\mathbf{q}_{\mathrm{FE}}, \tag{2.69}$$

where **Q** and **H** are acoustic inertia and stiffness matrices as discussed by Fahy and Gardonio (Fahy and Gardonio, 2007).

The imposed velocity at the BM has the half sinusoidal form and the discrete approximations to the modal velocity in equation (1.13) and modal pressure in equation (1.14) are calculated from the relevant elements of $\mathbf{q}_{\mathrm{FE}}$ and $\mathbf{p}_{\mathrm{FE}}$ respectively. The FE model is coded in MATLAB$^{\mathrm{TM}}$ and is divided into 512 longitudinal sections in order to ensure compatibility with the analytic results above. We initially investigated the effect of the number of elements in each cross-section on the predicted modal pressure distributions. The meshing in the cross-section has to be fine in order to capture the near-field pressure variation close to the vibrating BM, and four different mesh sizes are used to investigate the effect of this on the predicted results. Figure 2.13 shows the geometry of the FE meshes of cochlear model cross-section used in calculations.

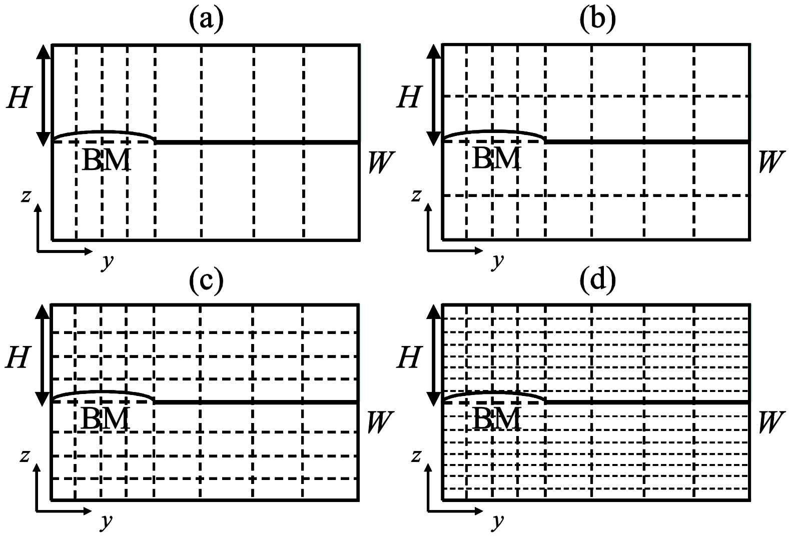

Figure 2.13 Grids used for finite element calculation of fluid coupling for a cross-section of the cochlea. Four meshes of (a) 8 ×1 elements, (b) 8 × 2 elements, (c) 8 × 4 elements and (d) 8 × 8 elements are used for each fluid chamber.

Figure 2.14 shows the distribution of the computed modal pressure difference along the cochlea, when a single longitudinal BM segment is driven at different locations, using four different mesh sizes for the fluid elements. It can be seen that with relatively few elements, the FE model reproduces the far-field behaviour of the pressure, which gives rise to the piecewise linear pressure distribution, reasonably well. A larger number of elements are required, however, to reproduce the details of the near-field pressure on the BM close to the point of excitation and hence the additional near-field component of the modal pressure. Figure 2.14 also shows the modal pressure difference distribution calculated using the analytic formulation shown above. It can be seen that the two methods have a good agreement along the whole length of the cochlea, although even with 8×8 elements the FE model still does not completely reproduce the analytic results in the near-field, since the local pressure distribution is then rather complicated around the BM.

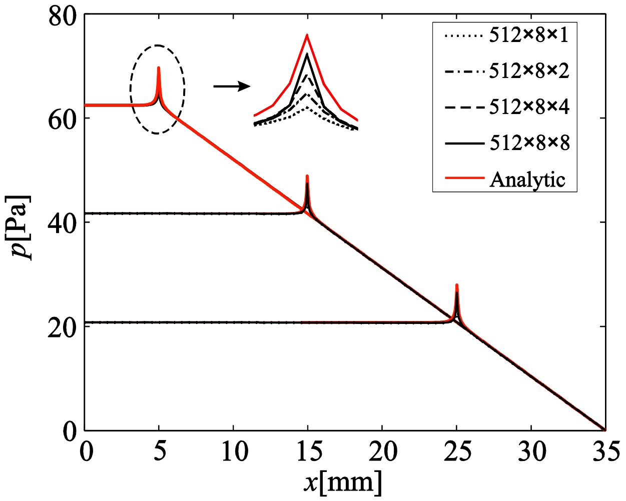

Figure 2.14 Modal pressure difference on the BM calculated using the FE model for excitation of a single longitudinal segment of the BM at x equal to 5 mm, 15 mm and 25 mm with a velocity of 10 mm·s^{-1} at a frequency of 1 kHz with 8 ×1 elements (dotted lines), 8 × 2 elements (dashed lines), 8 × 4 elements (dot-dashed lines), 8 × 8 elements (solid lines) and analytic solution (red lines).

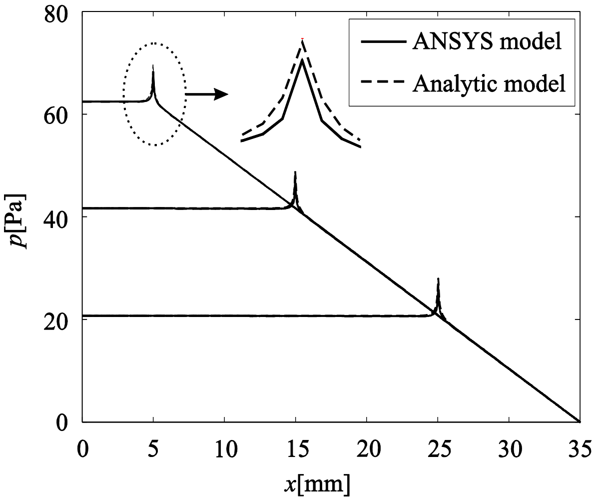

Figure 2.15 The distribution of the modal pressure difference along the uncoiled uniform cochlear model due to the fluid coupling when only a single element of the discrete BM at x=5 mm, is driven sinusoidally with a velocity of 10 mm·s^{-1} at a frequency of 1 kHz by using ANSYS (solid lines) and analytic model (dashed lines).

In order to use the commercial software ANSYS to analyse the effects of coiling on the cochlear dynamics, it is important to validate the ANSYS simulation. This has been achieved by comparing the ANSYS results of the uniform uncoiled model with those from the analytic model, as shown in Figure 2.15.

An advantage of the finite element method is that since the fluid is modelled using acoustic elements, the compressibility of the fluid, as well as its inertial properties, are taken into account. The widely used theoretical model assumes that the fluid is incompressible (Elliott, *et al.*, 2011). The effects of compressibility are expected to be greater at higher frequencies as the inertial forces become larger. Figure 2.16 shows the magnitude of the modal pressure difference calculated using the finite element model, with the BM driven at equal accelerations on a single element at x equal to 5 mm, for excitation at 1 kHz, 10 kHz, 15 kHz and 20 kHz. In the incompressible model the fluid pressure would be independent of frequency. It is clear, however, that the magnitude and shape of the fluid pressure change significantly with frequency in the finite element model. The magnitude increases at 10 kHz and the distribution of fluid pressure is no longer linear away from the excitation point.

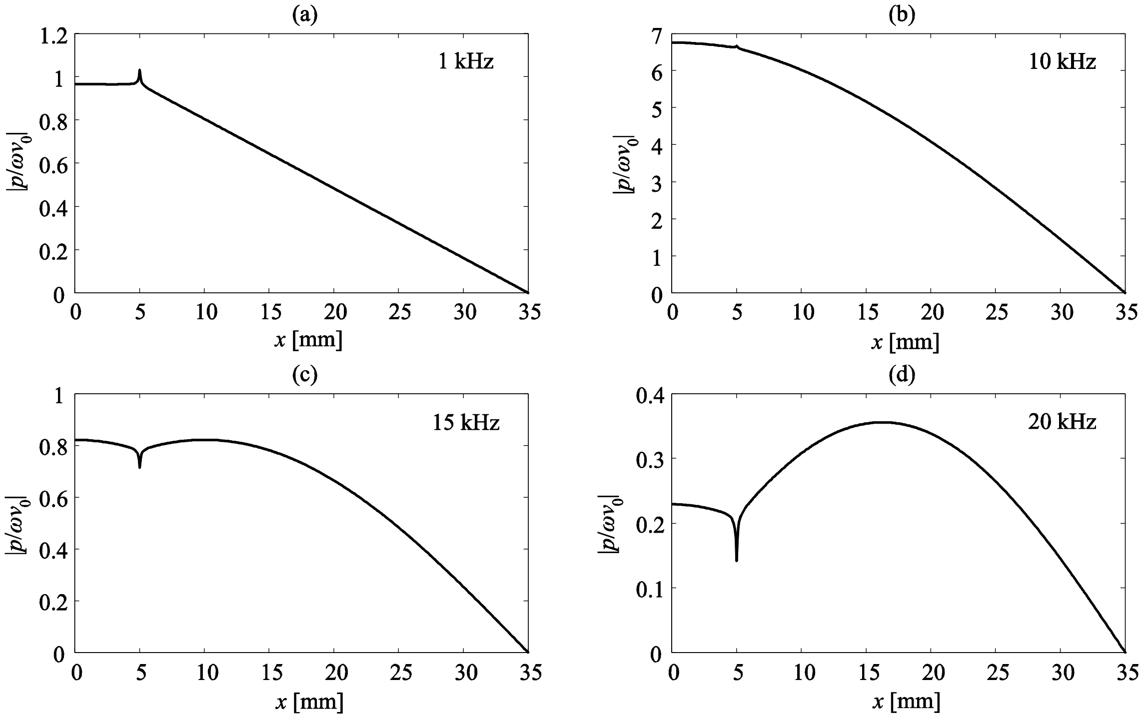

Figure 2.16 Magnitude of the modal pressure difference on the BM calculated using the finite element model for excitation of a single longitudinal element at x equal to 5 mm, normalised to the acceleration of the driving position at frequencies of (a) 1 kHz, (b) 10 kHz, (c) 15 kHz and (d) 20 kHz.

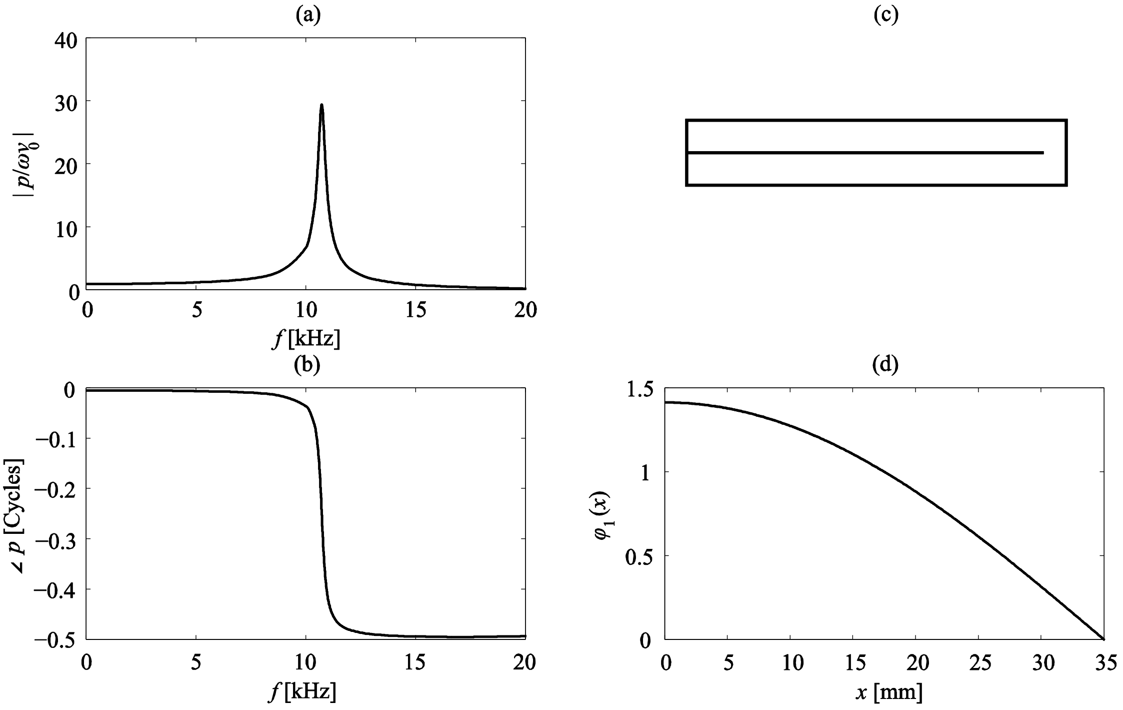

Figure 2.17 The magnitude (a) and phase (b) of the modal pressure difference at the base of the cochlea as a function of excitation frequency, calculated using the finite element method for excitation of a single longitudinal element at *x* equal to 5 mm. Also shown (c) is a sketch of the box model with the anti-symmetric pressure driven by the BM velocity and the resulting pressure distribution (d) when *L* is one quarter wavelength with the rigid boundary condition at the oval window and zero pressure difference at the helicotrema.

Figure 2.17 shows the predicted magnitude of the modal pressure at the base of the cochlea as a function of frequency. The peak at about 10.7 kHz can be associated with a resonance in the fluid column, which for the pressure difference has a rigid boundary condition where it is driven at the stapes and a pressure release boundary condition at the helicotrema. The cochlea length, 35 mm, thus corresponds to a quarter of a wavelength at this frequency, for an assumed wave speed of 1, 500 $\mathrm{m \cdot s^{-1}}$, which is the speed of a "fast wave" in the cochlea. This acoustic resonance increases the magnitude of the average pressure across any cross-section of the cochlea, but does not influence the near-field, short wavelength, components which are unaffected by the compressibility of the fluid (Lighthill, 1981). In order to limit the pressure magnitude at this peak, the finite element model has been modified to include a small imaginary component in the elements of the **H** matrix in equation (2.69) so that each element is multiplied by $1 + i\eta$, where η is the loss factor, which is 0.03 in this case (Elliott, *et al.*, 2011). The resonant peak at 10.7 kHz is accompanied by a phase change, so that the pressure distributions for excitation frequencies between 10.7 kHz and 20 kHz are almost entirely out of phase with those below 10.7 kHz.

Figure 2.18 compares the coupled BM velocity, calculated using the discrete approach outlined in Chapter 1, when the fluid coupling is assumed to be incompressible and compressible. For simplicity, the near-field components have not been considered in either case here and the BM mass for the passive BM model has been set to include the additional fluid loading. The columns of the fluid coupling impedance, $\mathbf{Z}_{\mathrm{FC}}$, used in the solution to the coupled dynamics, equation (1.19), are obtained either from samples of the analytic form of the pressure for the incompressible case given by equations (2.42) and (2.43) or from samples of the analytic form of the pressure for the compressible case given by equations (5.6) and (5.7) in Elliott *et al.* 2011 (Elliott, *et al.*, 2011).

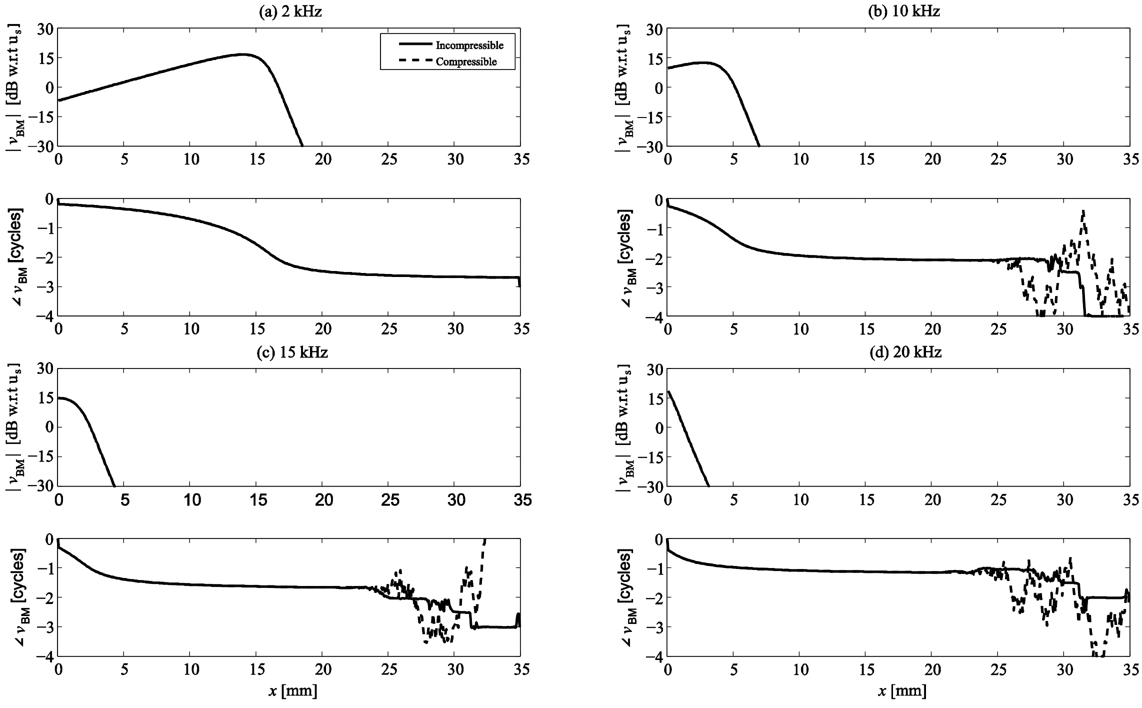

Figure 2.18 The coupled BM velocity calculated for high frequency excitation using the passive BM dynamics and long wavelength fluid coupling with the assumption that the fluid is either incompressible (solid lines) or compressible (dashed lines).

Despite the very significant change in the pressure distributions in the fluid coupling calculations due to fluid compressibility, as shown in Figure 2.16, this hardly appears to have any effect on the coupled cochlea response at all. This surprising result could be explained by returning to how the coupled model is formulated in Section 1.3.1. The fluid coupling effects are first calculated independently of any BM motion by defining the fluid coupling impedance matrix for the fluid chambers with rigid walls. It is this assumption that leads to the quarter wavelength resonance in the uncoupled fluid column. When the BM is allowed to move, in the coupled response, however, this resonance does not get a chance to become established since the BM is sufficiently mobile that it substantially equalises the pressures in the two fluid chambers well before the wave reaches the end of the cochlea. On the other hand, this also reflects that the fluid compressibility does not have a significant influence on the characteristic frequency location of the travelling wave in the cochlea (Lighthill, 1981).

2.7.2 Finite Element Model of a Non-uniform Asymmetric Cochlea

In order to compare the fluid coupling impedances derived analytically above with those derived using an alternative method, a non-uniform asymmetric uncoiled finite element model of the cochlea has been constructed. As well as providing an independent check of the behaviour of the fluid coupling in the uncoiled rectangular box model of the cochlea used above, the finite element model has the advantage that more complicated and realistic geometries, coiled cochlea for example, can also be analysed.

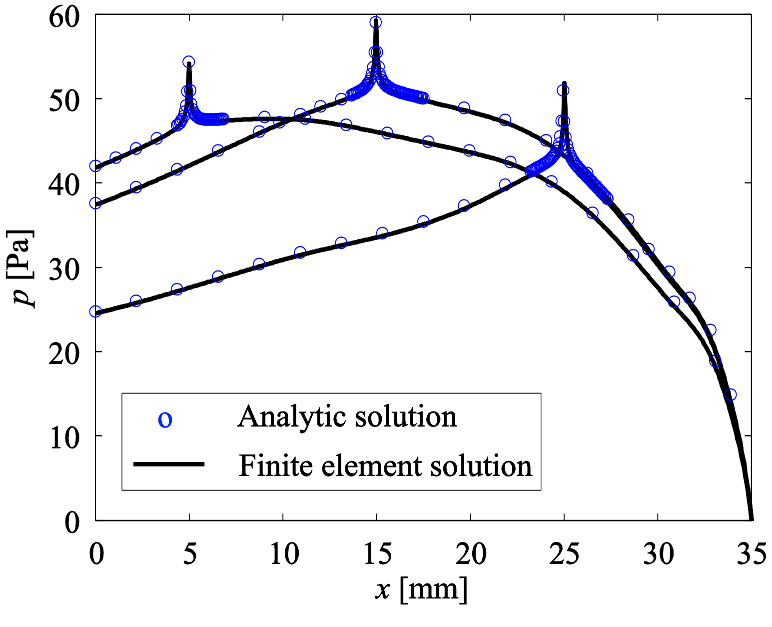

Figure 2.19 Comparison of modal pressure difference on the BM of a non-uniform asymmetric cochlear model calculated using the FE model (solid lines) and the analytic model (o) for excitation of a single longitudinal segment of the BM at *x* equal to 5 mm, 15 mm and 25 mm with a velocity of 10 mm·s^{-1} at a frequency of 1 kHz.

Similar to the uniform uncoiled cochlea, the non-uniform asymmetric cochlea can be represented by a straight box model with two fluid chambers, SV and ST, separated by the BM. The assumed variations of cross-sectional areas A_1 and A_2, associated with SV and ST respectively, the width of CP and the width of BM are same as those assumed in analytic model, as shown in Figure 2.8. Figure 2.19 shows good agreement between the FE model and the analytic model, and provides an alternative way to examine equations (2.65) and (2.66) for calculating modal pressure difference analytically in a non-uniform asymmetric cochlear model.

2.8 Conclusions

The interaction between the fluid coupling and BM dynamics in three-dimensional cochlear mechanics can be simplified by defining the pressure difference and the BM velocity as a function of a single longitudinal variable. This important simplification reduces the three-dimensional fluid coupling problem down to a uniaxial one, which consists of far and near-field components. The discrete model of the cochlea, which has a finite number of longitudinal sections, can effectively avoid singularities from appearing in the representation of the near-field fluid coupling due to the implicit assumption of a spatial delta function for the driving velocity in the continuous spatial domain, using the Green’s function approach for example, since the assumed BM velocity distributions remain finite and are described using linear algebra.

The near-field component of the fluid coupling is initially obtained from a conventional wavenumber analysis, and an approximation based on the theory of acoustic modes in a duct has also been derived, in which the near-field component is associated with the evanescent, higher order, modes in the fluid chambers, while the far-field pressure component is associated with the plane wave.

Realistic longitudinal variations of the cochlear geometry, including asymmetric fluid chambers, have also been incorporated into the fluid coupling and analysed both analytically and numerically. These coupled responses for the uncoiled non-uniform cochlea do not look significantly different from those for the uniform cochlea, except a significant difference of the accumulation of phase lag occurs in the non-uniform cochlea.

A finite element model of fluid coupling is also used to provide an independent check of the results of the analytic model. An advantage of using a finite element model of the fluid coupling is that various geometric complexities, which are difficult to account for analytically, and compressibility can be readily incorporated. The compressibility is seen to have a huge effect on fluid coupling close to a duct resonance, but a far smaller effect on the coupled cochlear response. It can be seen that the coupled responses from the incompressible analytic model match those from the finite element model, which includes compressibility, well.

Chapter 3. Fluid Coupling in the Coiled Cochlea

3.1 Introduction

It is believed that the coiled structure was an adaptation to the problem of fitting a long basilar membrane, to provide good low frequency hearing, into the relatively small heads of early mammals (Lieberstein, 1972). The origins of the coiled cochlea have recently been traced back 150 million years (Luo, *et al.*, 2011), for example, in morphogenesis of extant marsupials and placentals, the full coiling of the cochlear duct is inextricably linked with the formation of the cochlear ganglion and complex bony labyrinth structures, all during the late embryogenesis. Obviously, the coiled cochlea is a key evolutionary innovation of modern mammals. Despite providing a good blood and nerve supply, however, the effects of the coiling on the mechanics of the cochlea are still not fully understood. von Békésy (von Békésy, 1960) states that the coiling is not essential as far as mechanics are concerned because a few animals, for example the anteater, have a cochlea on the form of a slightly bent tube. The first mathematical attempt to analyse the possible mechanical effects of the spiral coiling was due to Huxley (Huxley, 1969), who derived an ordinary differential equation for the pressure in an unrolled 1D cochlear model similar to the box model which is widely used now and gave estimates indicating that coiling of the cochlear geometry could mechanically isolate adjacent sections along the cochlear partition and provide a sharp resonance effect. Hereafter, only a few researchers considered how spiral coiling may affect the BM dynamics, fluid coupling and low frequency perception. Fleischer (Fleischer, *et al.*, 2010) used a finite element model to study the effect of coiling on the stiffness distribution of the BM along the cochlea. They found that the coiling exerts its greatest influence on the apical third of the BM, although a much larger influence on the range of BM stiffness was the longitudinal variation of its thickness. This reinforced the earlier work of Viergever (Viergever, 1978), who also concluded that the mechanical behaviour of the cochlea is only slightly affected by its spiral form.

An analytic model of the fluid coupling in the coiled cochlea was developed by Steele and Zais (Steele and Zais, 1985), who concluded that the response was not significantly affected by the coiling. Kohllöffel (Kohllöffel, 1990) also suggested that the effect of the coiling on the pressure difference is small and that there is an equivalent straight cochlear in the limit of long wavelength. This author also noted that the frequency of the quarter wavelength resonance in the mean component of the pressure is raised by about half an octave due to coiling. Manoussaki and Chadwick (Manoussaki and Chadwick, 2000) considered fluid loading using an analytic model of the coiled "helical box" model of the cochlea using a wavenumber analysis and found that the fluid loading at the apex was only about 11% less in the coiled cochlea compared with the straight cochlea. In subsequent publications, however, Cai and Chadwick (Cai and Chadwick, 2003), Cai *et al.* (Cai, *et al.*, 2005), and Manoussaki *et al.* (Manoussaki, *et al.*, 2006) emphasised the redistribution of wave energy towards the outer wall of the cochlea generating a radial force on the organ of Corti that significantly increases its shear gain at the apex, which can lower the fluid impedance at the apex and thus helps detection of low frequency sounds.

In this chapter the effects of coiling in the cochlea are investigated using a three-dimensional finite element model, which is constructed based on the geometry data extracted from Figure 2 in Zakis and Witte (Zakis and Witte, 2001), to calculate the fluid coupling impedance. To examine the effects of spiral coiling, results will be compared with the three-dimensional finite element model of the uncoiled cochlea with same variation of area as the coiled cochlea. In the calculation of the fluid coupling impedance in the discrete model introduced in Chapter 1, the BM is divided up into a number of longitudinal sections and its radial velocity distribution is assumed to be known, for example a half sinusoidal mode shape, and independent of the fluid loading upon it. This allows complicated three-dimensional behaviour of the fluid coupling to be represented as a function of a single longitudinal variable for excitation at each point along the cochlea. These pressure distributions constitute the columns of the fluid coupling impedance matrix, which can be combined with a BM admittance matrix to give a simple model of the coupled cochlear dynamics.

The other potential application of this coiled three-dimensional cochlear model is to predict wave propagation in the coiled cochlea and examine the effects of the coiling on wave scattering.

3.2 Finite Element Model of the Coiled Cochlea

3.2.1 Geometry of the Coiled Cochlea

The real cochlea is a three-dimensional object with complicated spiral coiling and geometry. Most cochlear mechanics researchers reduce the real cochlea structure to a simple mathematical model with assumed physical and geometrical properties. An advantage of the finite element method is that these assumptions do not have to be made, although a description of the 3D geometry is necessary to mesh the model. It is extremely difficult to obtain the real geometry of a cochlea for modelling, since the cochlea itself is very small and enclosed in bony structure. Three-dimensional medical imaging is a recently developed technique that allows the production of accurate and interactive models of human anatomy, which can be used to visualise and model the cochlea. Current 3D modelling techniques depend on using the range finding method to collect 3D range data in order to determine an accurate range map of a subject to be modelled (refs). This range map can then be analysed using software, ANSYS for example, to recreate the object in virtual space. Zakis and Witte (Zakis and Witte, 2001) applied magnetic resonance imaging (MRI) technology to create splines to trace the outlines of the scalae and then used JAVA software to build a 3D cochlear model. In this research, the 3D coiled cochlear model is built based on the scanning pictures shown in Zakis and Witte (Zakis and Witte, 2001). The profiles of the scalae are then extracted and used in Solidworks for building the geometric cochlear model, as shown in Figure 3.1.

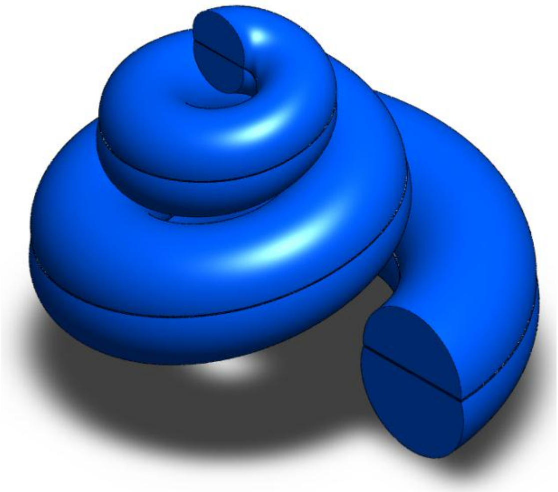

Figure 3.1 Geometric 3D cochlear model.

The geometric model is saved in Parasolid format with extension ‘x_t’ and then imported into ANSYS. The FE model of this coiled cochlea consists of 512 fluid elements in the axial direction which is compatible with the uncoiled cochlear model and 24 fluid elements along the cochlear outer wall circumferential direction as shown in Figure 3.2.

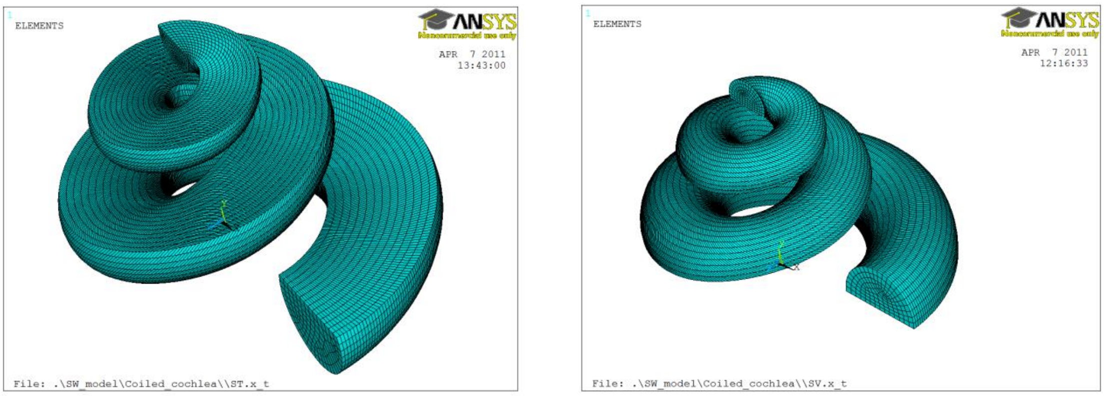

(a) (b)

Figure 3.2 Mesh of the coiled cochlear model decomposed to two fluid chambers, (a) scala tympani and (b) scala vestibuli.

3.2.2 Effects of the Coiling on the Fluid Coupling

To investigate the effects of the coiling on the fluid coupling, the radial variation of the BM velocity, $\psi(y)$, again is assumed to be independent of the pressure distribution acting upon it, so that a complex modal pressure difference can be defined at a single frequency that only has a longitudinal variation along the cochlea as (Elliott, *et al.*, 2011)

$$p(x) = \frac{1}{W}\int_0^W \psi(y)[p_1(x,y,0) - p_2(x,y,0)]dy, \tag{3.1}$$

where W is the width of the cochlear partition and $p_1(x, y, z)$ and $p_2(x, y, z)$ are the pressure distributions in the two fluid chambers, as shown in Figure 3.2.

This formulation allows complicated three-dimensional behaviour of the fluid coupling to be represented as a function of a single longitudinal variable for excitation at each point along the cochlea. These longitudinal distributions of the modal pressure can then be used to construct the columns of the fluid coupling impedance matrix, which can be combined with a BM admittance matrix to give a simple discrete model of the coupled cochlear dynamics. The FE coiled cochlear model is analysed using ANSYS and the computed modal pressure difference is compared with that from a non-uniform uncoiled analytic model of the cochlea, discussed above, which has the same variations of cross-sectional area and BM width, to show the effects of the coiling. The FE cochlea is assumed to be coiled and, for the time being, the width of the BM is equal to that of the CP. The distributions of the modal pressure difference with both far and near-field components, due to the BM is excited by a single element at x_0 equal to 5 mm, 15 mm or 25 mm are shown in Figure 3.3. It can be seen that in the uncoiled cochlea, denoted by the dashed line, the modal pressure difference is constant from the basal end and then gradually increases to a peak, due to the near-field component, and then shows a downward sloping behaviour when x is greater than x_0.

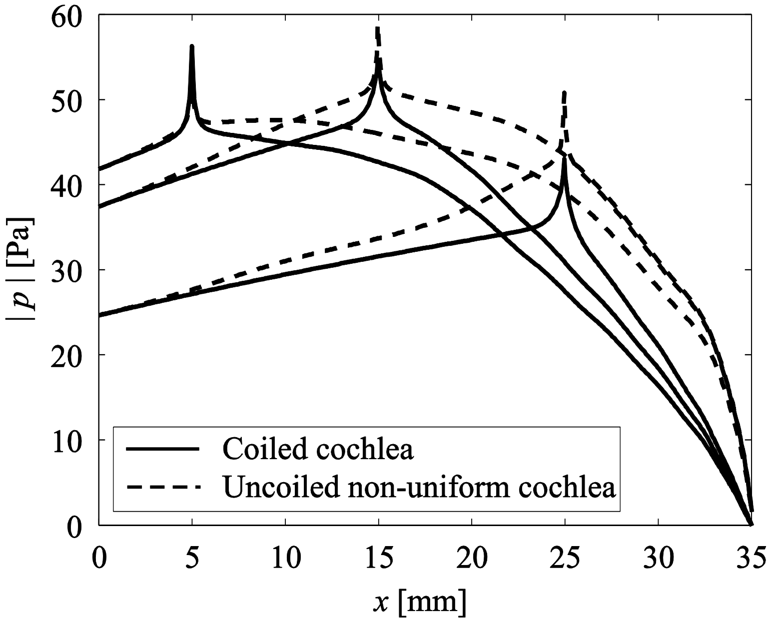

Figure 3.3 The distribution of modal pressure difference along the cochlea due to the fluid coupling when only a single element of the discrete BM at x equal to 5 mm, 15 mm and 25 mm, is driven sinusoidally with a velocity of 10 mm·s^{-1} at a frequency of 1 kHz by using an ANSYS coiled cochlear model (solid lines) and an analytic uncoiled cochlear model with same variations in scale area (dashed lines).

Similar distributions of the pressure difference are obtained from the coiled cochlear model except that some differences occur after each peak. It can be seen that the effects of the coiling on the far-field components are more obvious than that on the near-field components, since as stated previously, the near-field components of the pressure are not significantly affected by the shape of the cochlear chambers. Recalling equation

(1.17), $\mathbf{p} = \mathbf{Z}_{\mathrm{FC}}\mathbf{v}$, when the BM velocity is fixed, the pressure difference in the cochlear chambers only depends on fluid impedance. These magnitude reductions of the pressure difference occur after each peak imply the fluid impedance at those positions, which are close to the apex, is decreased due to the spiral coiling of the cochlea is greater at the apex. This implies that the spiral coiling could help perception of low frequency sounds which could be an evolutionary compensation of reducing the space for holding the cochlea done by the power of nature. Similar results were observed by Manoussaki *et al.* (Manoussaki and Chadwick, 2000) who suggested that the coiling helps to lower the fluid impedance particularly at the apex, where the BM curvature is greatest. In addition to this, Chadwick and his colleagues (Cai and Chadwick, 2003, Cai, *et al.*, 2005, Manoussaki, *et al.*, 2006, Manoussaki, *et al.*, 2006) also emphasised the redistribution of wave energy towards the outer wall of the cochlea generating a radial force on the organ of Corti that significantly increases its shear gain at the apex, which can lower the fluid impedance at the apex thus helps detection of low frequency sounds.

3.2.3 Effects of the Coiling on the Coupled Response

Although the effects of the coiling on the fluid coupling have been predicted in the current case, it is still necessary to explore its effects on the coupled responses, which are shown in Figure 3.4, using the discrete method.

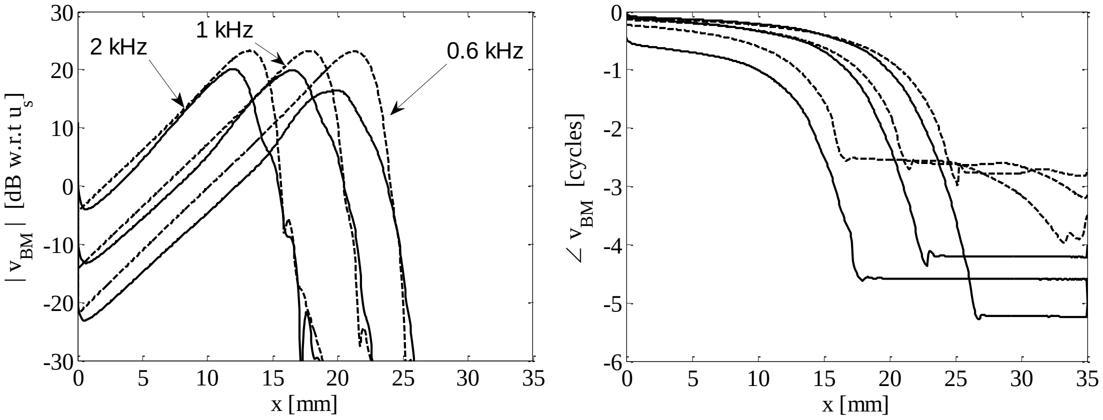

Figure 3.4 The BM response calculated using the coiled model (solid lines) and the uncoiled non-uniform model (dashed lines), at 0.6 kHz, 1 kHz and 2 kHz.

Although a reasonable matching of the magnitudes can be obtained between the coiled and uncoiled models, the peak response of the coiled model is less than that of the uncoiled model. The accumulation of phase lag of the coiled model, however, is greater than that of the uncoiled model apical to the characteristic. This reflects the curvature has some effects on the changes of wavelength of the BM motion as the motion approaches the characteristic place. Also, when driving frequency increases, the agreement of magnitude basal to peak between the two models increases. The curvature may have an effect on reducing axial fluid flow and an increase in the local mass loading, slowing the wave and increasing the phase accumulation.

3.3 Conclusions

An advantage of using a finite element model of the fluid coupling is that various geometric complexities, which are difficult to account for analytically, can be readily incorporated. In this chapter the flexibility of the finite element method is illustrated by using it to investigate the effects of the coiling on the fluid coupling and coupled response. Results for this set of parameters show that the coiling does change the modal pressure distribution, especially close to the apex indicating that the coiling reduces the fluid impedance in the apical region and thus somewhat reduces the coupled BM velocity near the apex. This conclusion is similar to that drawn by Steele and Zais (Steele and Zais, 1985) and Kohllöffel (Kohllöffel, 1990) who suggested that the effects of the coiling on the pressure difference are, although there is evidence for a greater effect at low frequencies, small and that there is an equivalent straight cochlea. For the region beyond the characteristic place, the BM velocity calculated using the coiled model is less than that from the uncoiled model, but the greater accumulation of phase from the coiled model suggests that the coiling has an influence on changes of wavelength of the BM motion.

Chapter 4. Fully Coupled Response Calculated Using the FE Method

4.1 Introduction

Up until now the discrete model has been used to calculate the coupled response of the cochlea, with separate models for the fluid coupling impedance and BM admittance. A fundamental assumption of the discrete model, however, is that the radial velocity distribution of the BM is known, and that this is unaffected by fluid coupling. In order to test this important assumption, the finite element method can be used to compute the response of the cochlea as a fully coupled fluid-structural system. For simplicity we continue to assume the box geometry for the cochlear model, divided into the same number of longitudinal elements as in the discrete model, but now the model is also meshed over each cross section, as in Figure 4.1. Using symmetry, the derivation of the equation of motion of the coupled system is only given for coupling between one fluid chamber and the BM.

The lower surface of the upper chamber, SV, is coupled with a flexible plate that represents the BM, as shown in Figure 4.1, so that the fluid field in the chamber is influenced by the motion of the BM and the vibration of the BM is perturbed by the fluid pressure loading. The vibrational behaviour of this coupled system can be derived using Hamilton’s principle. The integral of Hamilton’s principle equation for the acoustic system must include the work done by the BM on the fluid. Likewise, the integral for the structural system also must include the complementary work done by the fluid on the BM.

For the fluid-structural coupled system, each fluid element located with its lower surface coincident with the BM element, the elemental virtual work done over the *r*-th coupling face by the pressures $-p_r$ and virtual displacements δw_r of the matching BM element is given by (Craggs, 1971)

$$\delta W_e^f = -\int_{S_r} p_r \delta w_r dS_r = \rho_f \int_{-1}^{+1}\int_{-1}^{+1} \dot{\phi}\left(\xi_{r1,2,3},t\right)\delta w\left(\xi_{r1,2,3},t\right) a_{r1}a_{r2}\, d\xi_{r1}d\xi_{r2}, \qquad (4.1)$$

where $\xi_{r1,2,3}$ stands for local coordinates in the fluid element ξ_{r1}, ξ_{r2}, ξ_{r3} as shown in Figure 4.2, ξ_{r1} and ξ_{r2} are the a-dimensional coordinates of the *r*-th dissipative face of the fluid element with area $S_r = a_{r1} \times a_{r2}$ matched to the plate element, as shown in Figure 4.2, such that $a_{r1} = \xi$ and $a_{r2} = \eta$. The a-dimensional coordinate ξ_{r3} locates the position of the dissipative face and thus, $\xi_{r3} = -1$ for this example. The a-dimensional coordinates of the bottom face denoted by the nodal points 1, 2, 3 and 4 of the element in Figure 4.2(a) are given by $\xi_{r1} = \xi_1$, $\xi_{r2} = \xi_2$ and $\xi_{r3} = \xi_3 = -1$.

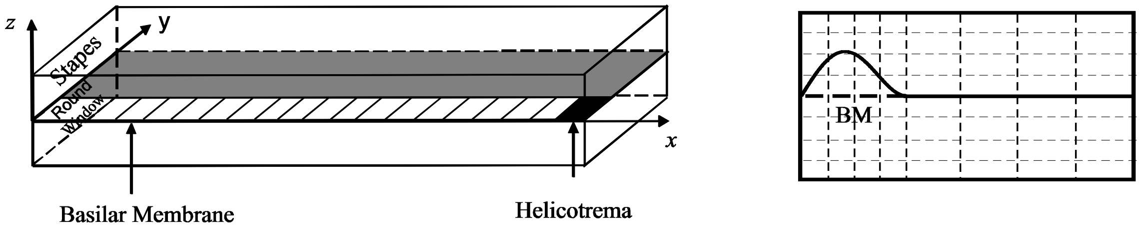

(a) (b)

Figure 4.1 (a) Geometry of the finite element model of the cochlea and (b) elemental grids used on each cross-section.

Although a general model is initially assumed for the BM structure, this will be used below for the particular case where the BM is locally reacting, and then when it is longitudinally coupled via an orthotropic model. The kinetic and potential energy terms for one fluid element, the virtual work done over the *r*-th coupling face by the pressures $-p_r$ and virtual displacements δw_r of the matching BM element and the virtual work done by acoustic excitations are given by (Fahy and Gardonio, 2007)

$$T_e^f = \frac{1}{2}\rho_f \boldsymbol{\phi}_e^{\mathrm{T}} \mathbf{H}_e \boldsymbol{\phi}_e, \tag{4.2}$$

$$U_e^f = \frac{1}{2}\rho_f \dot{\boldsymbol{\phi}}_e^{\mathrm{T}} \mathbf{Q}_e \dot{\boldsymbol{\phi}}_e, \tag{4.3}$$

$$\delta W_e^f = \rho_f \delta \dot{\boldsymbol{\phi}}_e^{\mathrm{T}} \mathbf{R}_e \mathbf{w}_e, \tag{4.4}$$

and

$$\delta W_e^q = -\rho_f \delta \dot{\boldsymbol{\phi}}_e^{\mathrm{T}} \mathbf{q}_e. \tag{4.5}$$

where $\mathbf{H}_e$ and $\mathbf{Q}_e$ are elemental acoustic inertia and stiffness matrices, $\mathbf{R}_e$ the elemental coupling matrix, $\mathbf{q}_e$ the elemental acoustic source vector, $\boldsymbol{\phi}_e$ the velocity potential of the fluid element and $\mathbf{w}_e$ the displacement vector of the BM element.

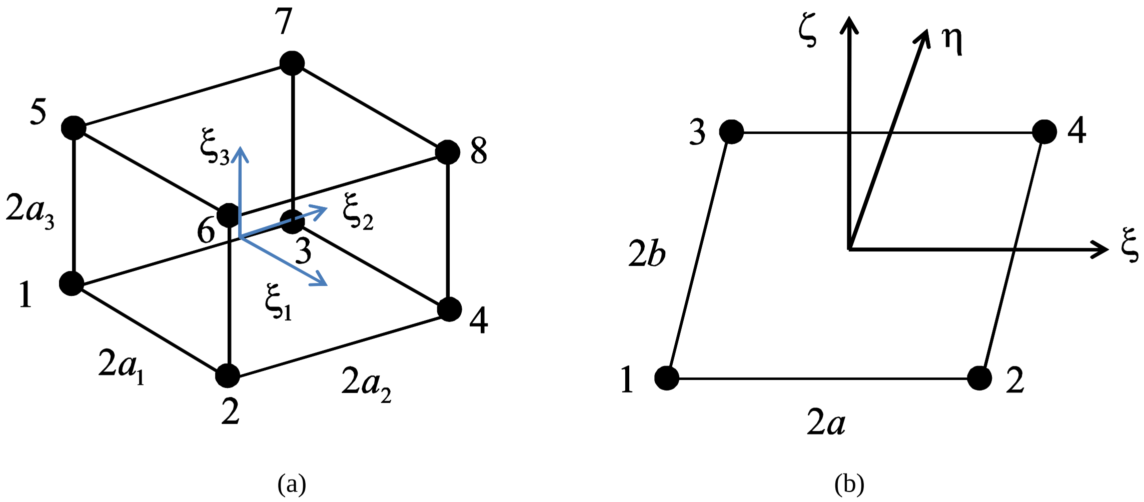

Figure 4.2 (a) Fluid element and (b) BM element and their coordinates and dimensions.

A four-node quadrilateral element is used to model the BM structure, which has three degrees of freedom (transverse displacement w, rotations $\theta_x = \partial w / \partial y$ and $\theta_y = -\partial w / \partial x$) at each node point, as shown in Figure 4.2 (b) (Petyt, 1990). The kinetic and potential energy terms for one BM element and the virtual work done by the pressure p_r and virtual displacements δw_r through the r-th face of the coupling element on the matching BM element are given by

$$T_e^s = \frac{1}{2} \dot{\mathbf{w}}_e^{\mathrm{T}} \mathbf{M}_e \dot{\mathbf{w}}_e, \tag{4.6}$$

$$U_e^s = \frac{1}{2} \mathbf{w}_e^{\mathrm{T}} \mathbf{K}_e \mathbf{w}_e, \tag{4.7}$$

and

$$\delta W_e^s = \rho_f \delta \mathbf{w}_e^{\mathrm{T}} \mathbf{S}_e \dot{\boldsymbol{\phi}}_e, \tag{4.8}$$

where $\mathbf{M}_e$ is elemental mass matrix, $\mathbf{K}_e$ elemental stiffness matrix and $\mathbf{S}_e$ elemental coupling matrix. Once the elemental stiffness, mass and coupling matrices are derived, the global matrices and vectors can be obtained through assembling these elemental matrices (Petyt, 1990). The BM is assumed to be isotropic for the locally-reacting case and orthotropic for the longitudinal coupling case, which leads to a different assembly between the two cases to make sure that there is no longitudinal coupling between adjacent BM elements for the locally-reacting one.

The kinetic and potential energy, the virtual work done by the volume acoustic sources and the work done by the BM on the fluid can be combined to give the total energies and virtual work for the fluid. These energy expressions can be substituted into Hamilton's principle to give (Craggs, 1971)

$$\begin{aligned}&\int_{t_1}^{t_2}[\delta(T-U)+\delta W^f+\delta W^q]\,dt\\&=\int_{t1}^{t2}\left[\delta\left(\frac{1}{2}\rho_f\boldsymbol{\phi}^T\mathbf{H}\boldsymbol{\phi}-\frac{1}{2}\rho_f\dot{\boldsymbol{\phi}}^T\mathbf{Q}\dot{\boldsymbol{\phi}}\right)+\rho_f\delta\dot{\boldsymbol{\phi}}^T\mathbf{R}\mathbf{w}-\rho_f\delta\dot{\boldsymbol{\phi}}^T\mathbf{q}\right]dt=\mathbf{0},\end{aligned} \tag{4.9}$$

where $\mathbf{H}$, $\mathbf{Q}$ and $\mathbf{R}$ are global acoustic stiffness, inertia and acoustic-structural coupling matrices respectively and $\mathbf{q}$ is the acoustic source vector. It should be noted that the coupling surface is located on the bottom surface of the fluid chamber for this condition. After integrating the second and third terms by parts and differentiating the expression to be integrated, which is valid for any arbitrary $\delta\boldsymbol{\phi}$, the equation of motion in terms of nodal pressure $\mathbf{p}=-\rho_f\left\{\partial\boldsymbol{\phi}/\partial t\right\}$ and plate displacement $\mathbf{w}$ is given by (Fahy and Gardonio, 2007)

$$\mathbf{H}\mathbf{p}+\mathbf{Q}\ddot{\mathbf{p}}+\rho_f\mathbf{R}\ddot{\mathbf{w}}=\mathbf{q}. \tag{4.10}$$

Similarly, the equation of motion of the BM coupled with the fluid chamber on the bottom surface as shown in Figure 4.1 is obtained based on Hamilton's principle as

$$\mathbf{M}\ddot{\mathbf{w}}+\mathbf{K}\mathbf{w}-\mathbf{S}\mathbf{p}=\mathbf{0}, \tag{4.11}$$

where $\mathbf{M}$ and $\mathbf{K}$ are the global mass and stiffness matrices and $\mathbf{S}$ the structural-acoustic coupling matrix. Because of reciprocity, the two coupling matrices $\mathbf{R}$ and $\mathbf{S}$ are related such that $\mathbf{R}=\mathbf{S}^{\mathrm{T}}$.

Combining the equations of motion of the fluid chamber and BM gives the equation of motion of the whole coupled system as

$$\begin{bmatrix} \mathbf{M} & 0 \\ \rho_f \mathbf{R} & \mathbf{Q} \end{bmatrix} \begin{bmatrix} \ddot{\mathbf{w}} \\ \ddot{\mathbf{p}} \end{bmatrix} + \begin{bmatrix} \mathbf{K} & -\mathbf{S} \\ \mathbf{0} & \mathbf{H} \end{bmatrix} \begin{bmatrix} \mathbf{w} \\ \mathbf{p} \end{bmatrix} = \begin{bmatrix} \mathbf{0} \\ \mathbf{q} \end{bmatrix}. \tag{4.12}$$

The dynamic stiffness matrix, as shown in equation (4.12), is not symmetric if both the pressure, **p**, and BM transverse displacement, **w**, are present, because of the incorporation of the coupling terms **S** and **R**. Mencik and Ichchou (Mencik and Ichchou, 2007) gave an example to rewrite the equation of motion of a fluid-structural coupled system in a symmetric form in terms of fluid velocity potential, $\boldsymbol{\phi}$, and the BM transverse displacement, **w**, as

$$\left\{ -\omega^2 \begin{bmatrix} \mathbf{M} & \mathbf{0} \\ \mathbf{0} & \mathbf{Q} \end{bmatrix} + i\omega \begin{bmatrix} \mathbf{0} & \rho_f \mathbf{S} \\ -\mathbf{R} & \mathbf{0} \end{bmatrix} + \begin{bmatrix} \mathbf{K} & \mathbf{0} \\ \mathbf{0} & \mathbf{H} \end{bmatrix} \right\} \begin{bmatrix} \mathbf{w} \\ \boldsymbol{\phi} \end{bmatrix} = \begin{bmatrix} \mathbf{0} \\ -\dfrac{1}{i\omega\rho_f}\mathbf{q} \end{bmatrix}. \tag{4.13}$$

Then, multiplying the second row of equation (4.13) by $-\rho_f$ results in the following symmetric system

$$\bar{\mathbf{D}} \begin{bmatrix} \mathbf{w} \\ \boldsymbol{\phi} \end{bmatrix} = \begin{bmatrix} \mathbf{0} \\ \dfrac{1}{i\omega}\mathbf{q} \end{bmatrix}, \tag{4.14}$$

where

$$\bar{\mathbf{D}} = -\omega^2 \begin{bmatrix} \mathbf{M} & \mathbf{0} \\ \mathbf{0} & -\rho_f \mathbf{Q} \end{bmatrix} + i\omega \begin{bmatrix} \mathbf{0} & \rho_f \mathbf{S} \\ \rho_f \mathbf{R} & \mathbf{0} \end{bmatrix} + \begin{bmatrix} \mathbf{K} & \mathbf{0} \\ \mathbf{0} & -\rho_f \mathbf{H} \end{bmatrix}, \tag{4.15}$$

is a symmetric dynamic stiffness matrix since $\mathbf{R}=\mathbf{S}^{\mathrm{T}}$ (Morand and Ohayon, 1995). It should be noted that both problems, equations (4.12) and (4.14), have the same eigenvalues. The advantages of the symmetric form are less computational cost (Everstine, 1981) and better matrix condition (Maess and Gaul, 2006). Everstine (Everstine, 1981) points out that non-symmetric matrix operations cost about twice as much to perform on a computer as symmetric operations. If the system, shown in equation (4.12), is modelled in SI-units (kg, m and s), the system is poorly conditioned, since nodal pressure values are about 10^{11} – 10^{12} times higher than the displacements in units of m for the present example. Vice versa, entries in block matrices **M** and $\rho_f\mathbf{R}$ are about 10^{10} – 10^{12} times higher as compared to the ones in **Q**. The same ratio occurs for the entries of **K** as compared to the ones in **H** and **S**, respectively. As a result, high condition measures result for global mass and stiffness matrices.

In this chapter, the distribution of the BM velocity magnitude and phase is first investigated using a locally-reacting model of the BM in Section 4.2, and is then calculated for the more complicated case including longitudinal coupling along the BM in Section 4.3.

4.2 Finite Element Model with Local BM Dynamics

The finite element model was illustrated in Figure 4.1 and consists of 512 longitudinal elements. The cross-section of each element is divided into an 8×4 grid of hexahedral fluid elements in each chamber, although the excitation is assumed to be symmetric so that the pressure in the lower chamber is opposite to that in the upper chamber and so need not be explicitly represented. The partition between the two fluid chambers is rigid apart from the BM, which is represented by four quadrilateral plate elements. Each BM slice vibrates independently across its width, with no mechanical coupling between the plates in the longitudinal direction. The mass per unit length of the BM, which is 0.2 $\text{kg}\cdot\text{m}^{-2}$, is kept constant along the cochlea. The mass assumed here is greater than that for the 3D analytic model, as a compensation for the relatively coarse mesh, used here for the sake of computational efficiency. The bending stiffness of each BM section varies as a function of longitudinal position x to match the place-frequency mapping characteristics in the human cochlea, since in the model the physical size and mass of the BM are assumed to be constant along the cochlear length. In this thesis, the boundary condition for the fluid chambers are defined to be rigid with a time harmonic source at the stapes (x=0), while at the helicotrema (x=L), the pressure gradient is assumed to be zero, i.e. an open end. The side and top walls are all assumed to be rigid. The boundary conditions for the BM are assumed to be simply-supported at $y = 0$ and clamped at $y \geq B$ (Allaire, *et al.*, 1974, Homer, *et al.*, 2004), by removing the corresponding degrees of freedom from the dynamic stiffness matrix. Such boundary conditions for the BM can give a good agreement with the measured radial BM displacement as shown in Fig. 2 by Homer *et al*. (Homer, *et al.*, 2004). The effects of the boundary conditions on the overall coupled responses are discussed in details in Appendix D.1.

The fundamental bending frequency of the BM can be expressed as (Rao, 2004)

$$f_\mathrm{B} = \frac{(\beta B)^2}{2\pi}\sqrt{\frac{EI}{A\rho B^4\left(1-v^2\right)}}, \tag{4.16}$$

where E is the BM Young's modulus, ρ density, I the second moment of area, v Poisson's ratio, A cross-sectional area, B the width of the BM and β is a coefficient with a dimension of m^{-1} depends on boundary condition. After some simple mathematical transformations, the Young's modulus variation of the BM can be given by

$$E(x) = \frac{4\pi^2 f_\mathrm{B}^2(x)A\rho\left(1-v^2\right)}{\beta^4 I}, \tag{4.17}$$

where $f_\mathrm{B}(x)$ is frequency distribution along the cochlear length, which is decaying exponentially from 20 kHz down to about 20 Hz (Dallos, 1992).

Damping is included in the BM by introducing a loss factor to define an imaginary component in each element of stiffness matrix, **K**, adjusted to give a damping ratio of 0.1, as used above. The complex stiffness matrix then becomes $\mathbf{K}(1+i\eta)$, where η is the loss factor. We assume that the imaginary term of the complex stiffness matrix is equivalent to the damping term, r(x), in the BM impedance, $Z_\mathrm{BM}(x) = i\omega m(x) + s(x)/i\omega + r(x)$. We can relate the loss factor and damping ratio as

$$i\eta(x)s(x) = i\omega\, r(x). \tag{4.18}$$

According to the definitions of $s(x)$ and $r(x)$ listed in Table 2.1, the loss factor can be given in terms of the damping ratio as

$$\eta(x) = \frac{2\omega\zeta_0 e^{x/l}}{\omega_\mathrm{B}}, \tag{4.19}$$

where ζ_0 is the BM damping ratio, which is equal to 0.1, used for the analytic models, ω driving frequency, l natural frequency length scale, which is 7 mm, and ω_B is natural frequency at the base.

The solution of the full finite element method is obtained in the usual way by solving equation (4.12), to give the vector of pressures and displacements at every node. The modal BM velocity can be obtained from a continuous BM displacement distribution, $w(x, y)$, as

$$v_{\mathrm{BM}}(x) = \frac{2i\omega}{B} \int_0^B w(x, y) \sin \frac{\pi y}{B} dy. \tag{4.20}$$

The finite element model provides the BM displacement in discrete form, as elements of the vector $\mathbf{w}$, which can be written in terms of the radial BM velocity distributions at each longitudinal slice along the cochlea as

$$\mathbf{w} = \left[\mathbf{w}^{\mathrm{T}}(1) \quad \mathbf{w}^{\mathrm{T}}(2) \quad \cdots \mathbf{w}^{\mathrm{T}}(N)\right]^{\mathrm{T}}, \tag{4.21}$$

where $\mathbf{w}(n)$ is the radial BM displacement due to the plate motion at the n-th longitudinal element, and N is the number of longitudinal elements, which is 512 in this case.

The modal BM velocity at the n-th position can then be estimated from the radial BM displacement distribution at this position using a discrete approximation to equation (4.20),

$$v_{\mathrm{BM}}(n) = 2i\omega\, \mathbf{s}_{\mathrm{BM}}^{\mathrm{T}} \mathbf{w}(n), \tag{4.22}$$

where $\mathbf{s}_{\mathrm{BM}}^{\mathrm{T}}$ is the vector of normalised values of the mode shape, $\sin(\pi y/B)$, at the nodal locations across the BM.

Figure 4.3 shows the predicted BM motion along the cochlear length using the full finite element model with locally-reacting BM dynamics. It can be seen that the motion represents the first bending mode all the way along the cochlea, which provides an independent check for the assumption made for the discrete model in Chapter 2. The asymmetric behaviour of the mode shape about the BM’s mid-point is due to the assumed boundary conditions that is simply-supported at y=0 and clamped at y=B, which is also noted by Homer *et al*. (Homer, *et al.*, 2004).

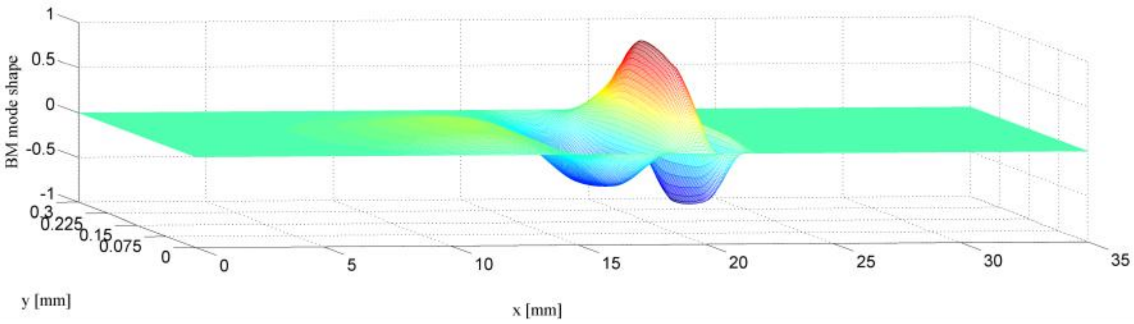

(a) BM mode shape along the cochlear length.

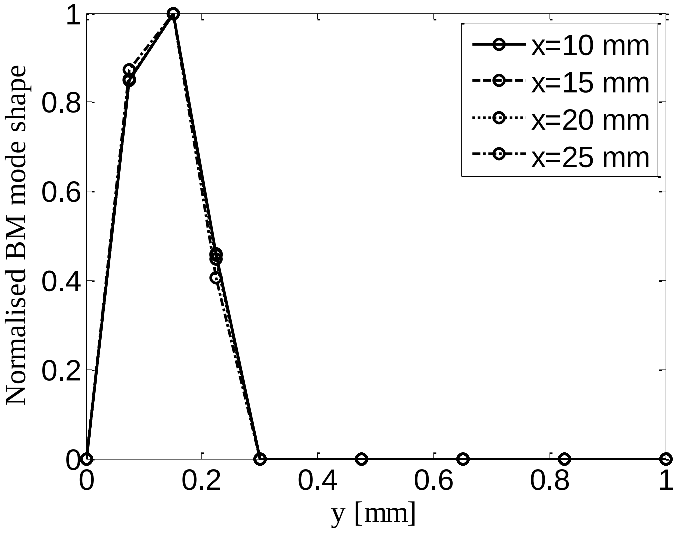

(b) BM mode shape at four positions along the cochlear length.

Figure 4.3 BM mode shape along the cochlear length predicted using the locally-reacting finite element model.

The cochlear model is driven at the stapes by a volume acoustic velocity source vector, **q**, over all the fluid elements of the upper chamber. The amplitude and phase of the modal BM velocity at 1 kHz is plotted in Figure 4.4, normalised with respect to the driving velocity at the stapes. The results are seen to be reasonably similar to those predicted from the 3D and 1D discrete cochlear model.

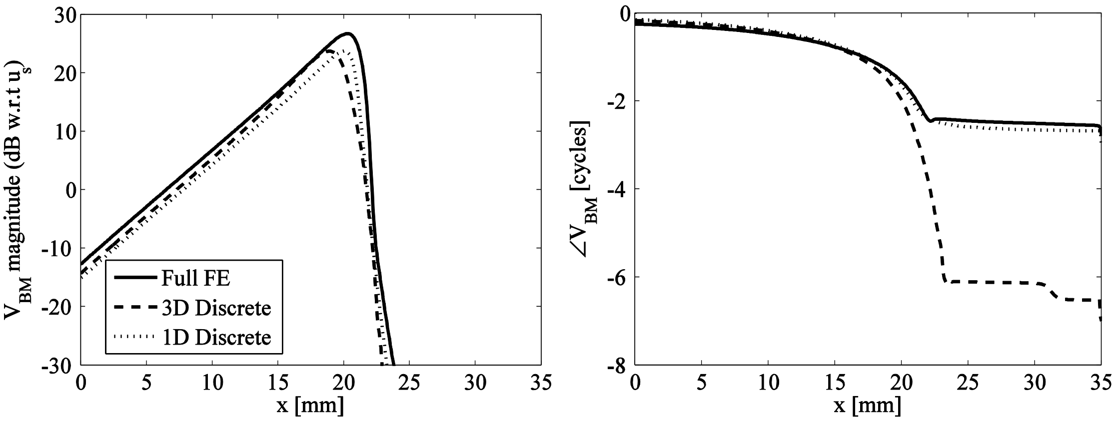

(a) (b)

Figure 4.4 The (a) magnitude and (b) phase of the modal BM velocity at 1 kHz, calculated from the full finite element model with locally reacting BM (solid lines) and the 3D discrete model assuming a half sine radial distribution of the BM velocity with a damping ratio of 0.1.

These results are found to change by less than 0.5 dB if the number of fluid elements on each cross section is increased from 8×4 to 8×16, but computation time increases by factor of 460.

4.3 Finite Element Model with Longitudinal BM Dynamics

In most cochlear models, the BM is conventionally assumed to be locally-reacting and to have no longitudinal mechanical coupling. It is thus the fluid chambers that are the only source of longitudinal coupling. The finite element method provides a way of testing this assumption, by modelling the BM as an orthotropic plate, so that the stiffness in the longitudinal direction can be varied independently of the stiffness in the radial direction. The governing equation of a bending orthotropic plate, as shown in Figure 4.5, can be expressed as (Szilard, 2004)

$$D_x \frac{\partial^4 w(x,y)}{\partial x^4} + 2T \frac{\partial^4 w(x,y)}{\partial x^2 \partial y^2} + D_y \frac{\partial^4 w(x,y)}{\partial y^4} = p(x,y), \tag{4.23}$$

where $D_x = \frac{E_x h^3}{12\left(1-\upsilon_{xy}\upsilon_{yx}\right)}$, $D_y = \frac{E_y h^3}{12\left(1-\upsilon_{xy}\upsilon_{yx}\right)}$ are the flexural rigidities of the orthotropic plate associated with the longitudinal, *x*, and the radial, *y*, direction, respectively, $T \approx \upsilon_{xy} D_y + 2D_s$ is the *effective torsional rigidity* of the orthotropic plate,

υ_{xy} and υ_{yx} are the Poisson's ratios corresponding to a contraction in direction x or y when an extension is applied in direction y or x respectively and D_s is equal to $G_{xy}h^3/12$ which represents torsional rigidity where G_{xy} is shear modulus. Based on Betti's reciprocal theorem (Werner, 2004), we can write

$$\upsilon_{yx}E_x = \upsilon_{xy}E_y \text{ or } \upsilon_{yx}D_x = \upsilon_{xy}D_y. \tag{4.24}$$

We assume that D_x, D_y and G_{xy} vary in proportion with D_y, which varies in proportional to $e^{-2x/l}$, where l is the natural frequency length scale, 7 mm, and x is the position in the cochlear longitudinal direction, in order to give the required distribution of the BM stiffness.

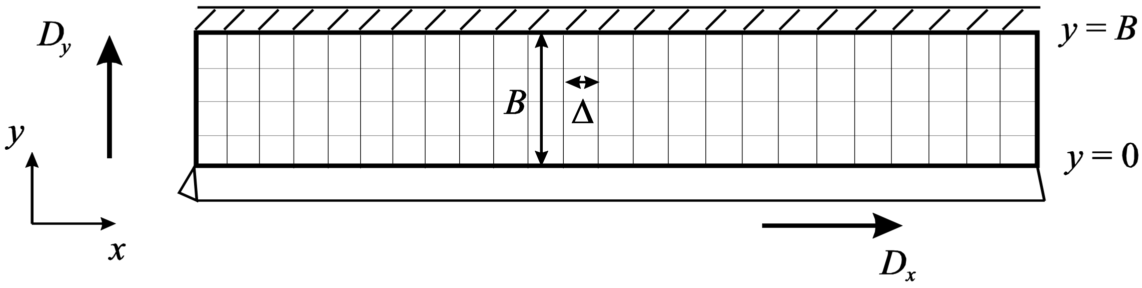

Figure 4.5 Sketch diagram of an orthotropic plate with boundary conditions simply supported at y = 0 and clamped at y = B.

In a similar way to the FE analysis described above, the orthotropic finite element model for each of the 512 segments of the cochlea has 8 × 4 hexahedral fluid elements to describe the fluid motion in each chamber and four plate elements to describe the BM radial structural response as a beam, but now with weak mechanical coupling due to orthotropy in the longitudinal direction. The cochlea is still assumed to be symmetric so that only one fluid chamber needed to be modelled. There are thus 9 × 5 nodes on each face of the fluid chamber segment, each having 1 degree of freedom, and 5 × 1 nodes on each edge of the BM segment, each having three degrees of freedom which are transverse displacement w, rotations θ_x and θ_y. (4.25)(4.26)(4.27)

A value for the ratio of longitudinal to radial BM stiffness D_x/D_y needs to be chosen for the FE simulation. It is assumed that υ_{yx} , υ_{xy} are given by equation (4.24) and G_{xy}=1.1×10^6 Pa at the base. Various estimates appear in the literatures (Liu and White, 2008, Meaud and Grosh, 2010) suggesting that the range is from 0.01 to 0.1.

The distributions of the BM velocity magnitude and phase using the orthotropic plate are plotted in Figure 4.6. Similar to those predicted from the locally-reacting model, the BM velocity gradually increases to a characteristic place which depends on driving frequency, and then sharply decreases. The incorporation of the longitudinal BM coupling moves the peak towards the apex compared with those from the isotropic case since the additional coupling stiffens the BM, but the effect of D_x/D_y changes can hardly been seen in this scale.

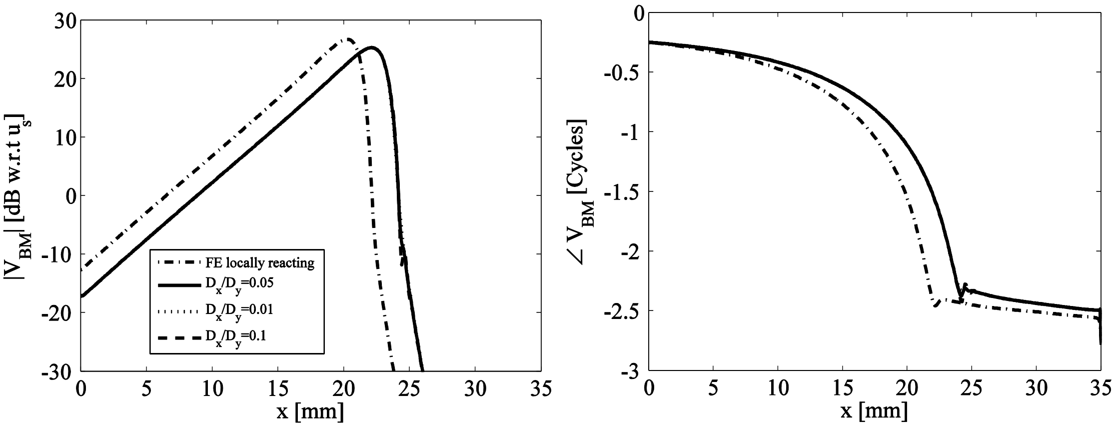

(a) (b)

Figure 4.6 The (a) magnitude and (b) phase of the modal BM velocity at 1 kHz, calculated from the full finite element model with locally reacting BM (dot-dashed lines) and the orthotropic BM with different *Dx*/*Dy* ratios, 0.05 (solid lines), 0.01 (dotted lines) and 0.1 (dashed lines) and a damping ratio of 0.1.

4.4 Conclusions

In this chapter, the uncoiled cochlea is modelled using finite elements as a fluid-structural coupled system, with three-dimensional fluid and two-dimensional BM elements. By driving the stapes at a given frequency, numerical prediction of the modal BM responses have been obtained. Two kinds of cochlear models, which include the local BM dynamics or longitudinal BM dynamics, are constructed and studied. Generally for both cases, the BM velocity increases gradually to a peak, whose location depends on driving frequency, and starts to decrease quickly afterwards. This observation is similar to those predicted by other models, like discrete cochlear model in Chapter 1, or the WKB reconstruction in Chapter 5.

The longitudinal BM coupling introduces additional interaction, which stiffens the BM, in the longitudinal direction and leads to a peak shift towards the apical end compared with the isotropic case at the same driving frequency. The original distribution of natural frequencies along the cochlea could, however, be recovered by adjusting the way that the Young's modulus is defined. By carefully defining the stiffness distribution of the orthotropic nature of more detailed cochlear models, other effects, such as longitudinal coupling of the TM motion for example, could also be taken account into consideration.

Chapter 5. Applications of the Wave Finite Element Method

5.1 Wave Finite Element Method

The wave finite element (WFE) method is a numerical approach to investigate wave motion in waveguides and slender structures at low computational cost (Duhamel, *et al.*, 2006, Houillon, *et al.*, 2005, Mace, *et al.*, 2005, Zhong and Williams, 1995). The WFE method starts by first modelling a short section of a waveguide or a structure using conventional finite elements, so that the equation of motion is defined in terms of a finite number of degrees of freedom (DOFs) in order to find the dynamic stiffness matrix; second, the transfer matrix of the section is formed using elements of the dynamic stiffness matrix; finally, the eigenvalues and eigenvectors of the transfer matrix, which represent the free wave propagation characteristics such as the wavenumbers and wave modes, are obtained from solving the eigenvalue problem of the transfer matrix after applying periodicity conditions (Duhamel, *et al.*, 2006, Mace, *et al.*, 2005).

The WFE method originated from the use of the finite element method to study periodic structures (Orris and Petyt, 1974, Orris and Petyt, 1975). Researchers utilized the finite elements to model periodic structures and predicted wave propagation in the structures. Abdel-Rahmen (Abdel-Rahmen, 1980) did extensive work to predict free wave propagation in 1D, 2D and 3D periodic structures using a FE model of a single periodic section. When a periodicity condition was applied to the equation of motion formed from the FE model, an eigenvalue problem was formulated. Free wave propagation characteristics were determined from solutions to the eigenvalue problem. Shorter (Shorter, 2004) utilized the waveguide finite elements for viscoelastic laminates and set out the discrete problem using Lagrange’s equations. He solved for the wavenumber at different frequencies and hence found dispersion relations. Nilsson (Nilsson, 2004) derived and validated six wave finite elements, straight and curved pre-stressed, orthotropic or anisotropic shell elements, straight and curved fluid elements, and straight and curved fluid-shell coupling elements, and he also calculated forced response and input power for infinite and periodic waveguides. Using a similar method, Gry (Gry, 1996) used the finite elements to model a rail cross-section, calculated wave propagation in rails and dispersion relations. He then extended the work (Gry and

Gontier, 1997) to take the periodic structure of the track into account by solving the problem in terms of a transfer matrix approach.

The wave finite element method, WFE, has been widely used on periodic or uniform structures, but few applications have been published for non-uniform structures. The WFE method was originally proposed for studying waves in periodic and uniform waveguides and a periodic condition must be applied to form the eigenvalue problem. However, it is possible to use the WFE to study certain structures with “slowly varying” properties such as the cochlea (Ni, *et al.*, 2010). So, for example the criterion commonly used for the WKB approximation holds (de Boer and Viergever, 1982)

$$\left| \frac{1}{k^2(x)} \frac{dk(x)}{dx} \right| < 1. \tag{5.1}$$

For our models this criterion is reasonably well satisfied at positions not too close to the base of the cochlea. Before considering the use of the WFE to analyse the response of the cochlea, in this chapter, we illustrate the WFE method and extend its use to study waves in slowly varying structures, using several other applications: plate strips, acoustic ducts and, particularly, loudspeaker cones.

5.1.1 Calculation of the Transfer Matrix form a Finite Element Model

The equation of motion of the *n*-th element of length Δ of a general uniform waveguide, as shown in Figure 5.1, can be written as

$$\mathbf{D}(n)\mathbf{q}(n) = \mathbf{f}(n), \tag{5.2}$$

where

$$\mathbf{D}(n) = \mathbf{K}(n) + i\omega\mathbf{C}(n) - \omega^2\mathbf{M}(n), \tag{5.3}$$

is the dynamic stiffness matrix, **q** is nodal displacement vector, **f** is nodal force vector, **K**, **C** and **M** are stiffness, damping and mass matrices, calculated from a finite element model for example, ω is angular frequency and $i = \sqrt{-1}$.

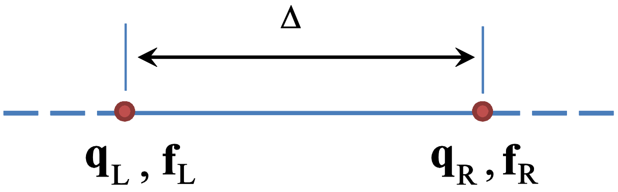

Figure 5.1 Sketch of a section of a uniform waveguide.

Note that time harmonic motion is implicit throughout and suppressed for brevity. After partitioning of the nodal displacement and force vectors into components on the left and right hand sides of the element, so $\mathbf{q}(n)=\left[\mathbf{q}_\mathrm{L}(n),\mathbf{q}_\mathrm{R}(n)\right]^\mathrm{T}$ and $\mathbf{f}(n)=\left[\mathbf{f}_\mathrm{L}(n),\mathbf{f}_\mathrm{R}(n)\right]^\mathrm{T}$, the equation can be expressed as

$$\begin{bmatrix} \mathbf{D}_\mathrm{LL}(n) & \mathbf{D}_\mathrm{LR}(n) \\ \mathbf{D}_\mathrm{RL}(n) & \mathbf{D}_\mathrm{RR}(n) \end{bmatrix} \begin{bmatrix} \mathbf{q}_\mathrm{L}(n) \\ \mathbf{q}_\mathrm{R}(n) \end{bmatrix} = \begin{bmatrix} \mathbf{f}_\mathrm{L}(n) \\ \mathbf{f}_\mathrm{R}(n) \end{bmatrix}, \tag{5.4}$$

where the subscripts L and R represent the response and forcing vector on the left and right hand side of the section. The transfer matrix can be defined as

$$\begin{bmatrix} \mathbf{q}_\mathrm{R}(n) \\ -\mathbf{f}_\mathrm{R}(n) \end{bmatrix} = \mathbf{T}(n) \begin{bmatrix} \mathbf{q}_\mathrm{L}(n) \\ \mathbf{f}_\mathrm{L}(n) \end{bmatrix}, \tag{5.5}$$

and expressed in terms of the dynamic matrix as (Mace, *et al.*, 2005)

$$\mathbf{T}(n) = \begin{bmatrix} -\mathbf{D}_\mathrm{LR}^{-1}(n)\mathbf{D}_\mathrm{LL}(n) & \mathbf{D}_\mathrm{LR}^{-1}(n) \\ -\mathbf{D}_\mathrm{RL}(n)+\mathbf{D}_\mathrm{RR}(n)\mathbf{D}_\mathrm{LR}^{-1}(n)\mathbf{D}_\mathrm{LL}(n) & -\mathbf{D}_\mathrm{RR}(n)\mathbf{D}_\mathrm{LR}^{-1}(n) \end{bmatrix}. \tag{5.6}$$

If

$$\begin{bmatrix} \mathbf{q}_\mathrm{R}(n) \\ -\mathbf{f}_\mathrm{R}(n) \end{bmatrix} = \lambda_j \begin{bmatrix} \mathbf{q}_\mathrm{L}(n) \\ \mathbf{f}_\mathrm{L}(n) \end{bmatrix}, \tag{5.7}$$

where λ_j is an eigenvalue of $\mathbf{T}$ and relates to wave propagation over the distance Δ, such that

$$\lambda_j = e^{-ik_j\Delta}, \tag{5.8}$$

where k_j represents the wavenumber for the *j*-th wave. The wavenumber can be purely real, purely imaginary or complex, associated with a propagating, a near-field (evanescent) or oscillating decaying wave respectively. Positive-going waves are those for which the magnitude of the eigenvalues is less than 1, such that the power is positive-going. The wavenumber k can be expressed as

$$k = \Re + i\Im, \tag{5.9}$$

where $\Re$ is the real part of the wavenumber, which represents the phase change associated with wave propagation and $\Im$ is the imaginary part of the wavenumber, which represents attenuation of the wave. If $\Im < 0$, it denotes the amplitude of the wave attenuates. If $\Im > 0$, it indicates the amplitude of the wave increases. The eigenvector represents a wave mode and contains information about both the displacements and the internal forces.

5.1.2 Eigenvalues and Eigenvectors

The right eigenvectors of the transfer matrix of the *n*-th section can be defined as

$$\mathbf{T}(n)\boldsymbol{\varphi}_i(n) = \lambda_i(n)\boldsymbol{\varphi}_i(n), \tag{5.10}$$

for the *i*-th eigenvalue λ_i and $\boldsymbol{\varphi}_i$ is a column vector of the right eigenvector. Similarly, the left eigenvector can be expressed as

$$\boldsymbol{\psi}_j(n)\mathbf{T}(n) = \lambda_j(n)\boldsymbol{\psi}_j(n), \tag{5.11}$$

and $\boldsymbol{\psi}_j$ is a row vector of the left eigenvector for the *j*-th eigenvalue and given by (Duhamel, *et al.*, 2006)

$$\boldsymbol{\psi}_j(n) = \left[\mathbf{q}^{\mathrm{T}}_{1/\lambda_j}(n)\left(\mathbf{D}_{\mathrm{RR}}(n) + \lambda_j(n)\mathbf{D}_{\mathrm{LR}}(n)\right) \quad \mathbf{q}^{\mathrm{T}}_{1/\lambda_j}(n)\right], \tag{5.12}$$

where subscript $1/\lambda_j$ denotes the displacement vector associated with the eigenvalue which is the reciprocal of λ_j and $\boldsymbol{\psi}_j$ can be written in the form of $\boldsymbol{\psi}_j(n) = \left[\mathbf{f}^{\mathrm{T}}_j(n) \quad \mathbf{q}^{\mathrm{T}}_j(n)\right]$. Combining equation (5.10) and (5.11) gives

$$\boldsymbol{\psi}_j(n)\mathbf{T}(n)\boldsymbol{\varphi}_i(n)=\lambda_i(n)\boldsymbol{\psi}_j(n)\boldsymbol{\varphi}_i(n)=\lambda_j(n)\boldsymbol{\psi}_j(n)\boldsymbol{\varphi}_i(n). \tag{5.13}$$

This relation leads to

$$\left(\lambda_i(n)-\lambda_j(n)\right)\boldsymbol{\psi}_j(n)\boldsymbol{\varphi}_i(n)=0. \tag{5.14}$$

It is easy to find that if $\lambda_i(n)\neq\lambda_j(n)$, $\boldsymbol{\psi}_j(n)\boldsymbol{\varphi}_i(n)=0$. Thus the orthogonal relationship between left and right eigenvectors can be expressed in terms of delta function as

$$\boldsymbol{\psi}_j(n)\boldsymbol{\varphi}_i(n)=d_i\delta_{ij}, \tag{5.15}$$

where δ_{ij} is Kronecker delta, such that $\delta_{ij}=\begin{cases}1 & (i=j)\\ 0 & (i\neq j)\end{cases}$, and d_i is arbitrary. This orthogonal relationship can then be utilized to calculate the wave assurance criterion value which shows the degree of consistency between one left eigenvector and another right eigenvector.

5.1.3 Wave Assurance Criterion Value

For general waveguides, there are many wave modes, so that many eigenvalues and associated eigenvectors are calculated at each different frequency (or at each different position in the cochlear model). It is important to recognize and distinguish the mathematical or physical similarity of these eigenvectors at two adjacent frequencies or positions. In other words, pre-processing must be utilized to check and then match the eigenvectors or eigenvalues in order to draw the correct wave dispersion curves (Allemang, 2003, Houillon, *et al.*, 2005). In this research, a wave assurance criterion (WAC) value is used to check the coherence of the initial propagation branches, which is similar to the MAC number used by Houillon (Houillon, et al., 2005). The wave assurance criterion value is defined as a normalised scalar relating the degree of consistency between one left eigenvector and another right eigenvector at two adjacent frequencies or positions as follows:

$$\mathrm{WAC}_{i,j}\left(n,n-1\right)=\left|\frac{\left[\boldsymbol{\psi}_j\left(n-1\right)\boldsymbol{\varphi}_i\left(n\right)\right]\left[\boldsymbol{\psi}_i\left(n\right)\boldsymbol{\varphi}_j\left(n-1\right)\right]}{\left[\boldsymbol{\psi}_j\left(n\right)\boldsymbol{\varphi}_j\left(n\right)\right]\left[\boldsymbol{\psi}_i\left(n-1\right)\boldsymbol{\varphi}_i\left(n-1\right)\right]}\right|, \tag{5.16}$$

where n and $n-1$ represent the frequency of n-th and ($n-1$)-th discrete frequency step, or for cochlear model n-th and ($n-1$)-th position along the length, $\boldsymbol{\psi}$ and $\boldsymbol{\varphi}$ are left eigenvector and right eigenvector associated with i-th or j-th wave at the n-th or ($n-1$)-th frequency or position. This WAC value is different from the MAC number defined by Houillon (Houillon, et al., 2005), since they only use right eigenvector to calculate the coherence, which is a general approach in modal analysis (Allemang, 2003). The advantage of this WAC value is that it is based on the orthogonal relationship, equation (5.15), between the left and right eigenvectors, which makes the WAC value more distinct. The WAC value can be calculated from two complex eigenvectors associated with two distinct eigenvalues. The WAC value takes on values from zero which represents no consistent correspondence, to unity that denotes that the eigenvectors are correlated. In particular all values of WAC are calculated at each junction in order to pair the eigenvectors in adjacent elements. If $k\Delta$ is much less than unity, the correct pairing typically gives WAC≈0.99 and incorrect WAC≈0.01. Figure 5.2 shows the WAC values between eigenvectors of the i-th and j-th wave modes calculated before and after applying the WAC using the locally-reacting cochlear model. It can be seen that the original correlations between each eigenvector are not strictly diagonal indicating the dispersion curves are not distinguishable, but after applying the WAC processing they are strictly diagonal, which means that each eigenvector associated with the corresponding wave is distinguished and thus the dispersion curves can now be clearly plotted out and used further for either WKB approximation or wave decomposition.

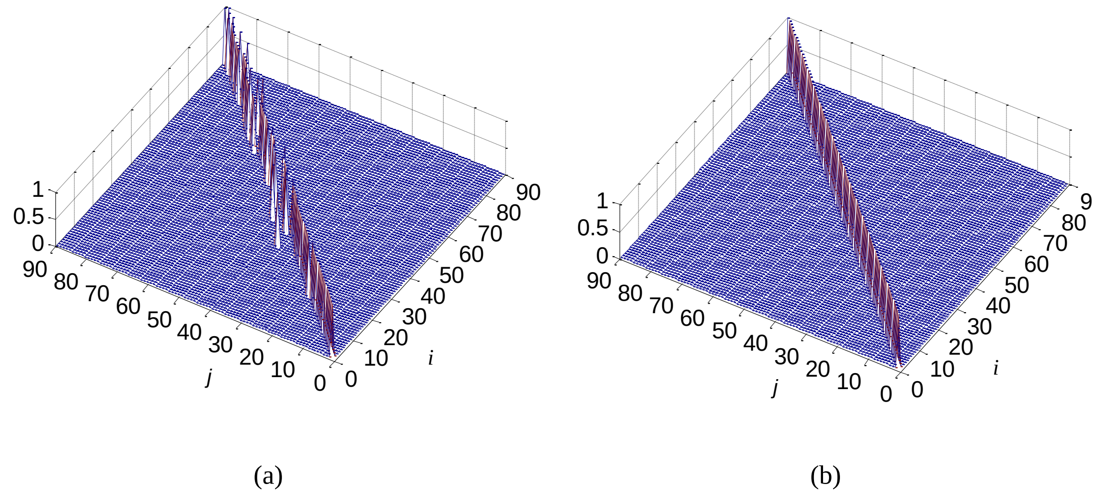

(a) (b)

Figure 5.2 The WAC value between eigenvectors of *i*-th and *j*-th wave mode calculated (a) before and (b) after applying WAC using the locally-reacting cochlear model.

5.1.4 Numerical Errors

Sometimes, the WFE method runs into difficulties due to the inversion of ill-conditioned matrices and the cumulative errors due to the transfer matrix assembly. Zhong (Zhong, *et al.*, 1991, Zhong and Williams, 1995) offered several approaches for solving the eigenvalue problems for linear periodic structures, which are a kind of state space eigenvalue problem, wherein the main parameters are the displacements at both sections of the considered system. The reasons for the WFE numerical errors can be classified as FE discretization errors and round-off of inertia terms, such that the frequency range analysed is limited. There is a trade-off between these two kinds of errors.

5.1.4.1 FE discretization error

When the phase change over the length of an element Δ becomes large, the FE discretization error becomes large. Since the FE modelling is an approximation to represent a system, there are always numerical errors. In the WFE method, the phase change over an element is recommended to be (Waki, *et al.*, 2009)

$$\left|k\Delta\right| \leq 1. \tag{5.17}$$

In general, the wavenumbers may be purely real, purely imaginary or complex. For complex wavenumbers, either the equation above or the condition

$$\left|\mathrm{Re}\left(k\Delta\right)\right| \le 1 \text{ and } \left|\mathrm{Im}\left(k\Delta\right)\right| \le 1, \qquad (5.18)(5.19)$$

is recommended (Waki, *et al.*, 2006). The criterion should be satisfied in both the directions of wave propagation and across the cross-section of a waveguide for small FE discretisation errors. The criterion on imaginary part of $k\Delta$ and hence on magnitude of $k\Delta$ is only required if accurate representation of evanescent terms is required, but that this is not the case here. It should be mentioned that the FE discretisation errors depend on the *shape function* of an element. Even if the values of $k\Delta$ are the same, errors in the WFE results using a *cubic polynomial shape function* are smaller than those using a *linear shape function* (Waki, *et al.*, 2009).

5.1.4.2 Round-off of inertia terms

The upper bound to the length Δ of the element can be decided from the FE discretization error, e.g. equation (5.17), considering the maximum wavenumber of interest in the frequency range analysed. On the other hand, the lower bound of Δ may be defined considering round-off of inertia terms.

In the WFE method, the round-off error can be significant specifically when $\mathbf{D} = \mathbf{K} - \omega^2\mathbf{M}$ is numerically calculated. For very small Δ, and in particular at low frequencies, some effective digits of the inertia terms will be rounded-off since K_{ij} might be much greater than $\omega^2 M_{ij}$. The criterion for the smallest permissible value of Δ could be therefore determined to satisfy

$$\log_{10}\left(\left|K_{jj}\right| / \omega^2 \left|M_{jj}\right|\right) < \alpha_{jj}, \qquad (5.20)$$

and $\alpha_{ij} < 16$ at the minimum frequency of interest using the double precision calculations for accurate results.

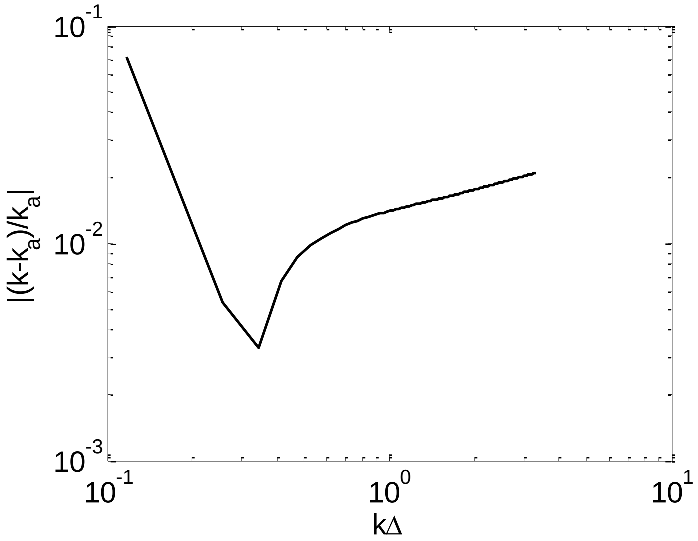

Figure 5.3 Relative errors of bending wavenumber from a thin plate strip model.

The relative errors of the wavenumber of a thin plate strip calculated using the WFE method are shown in Figure 5.3, in which the minimum error is around $k\Delta$=0.345. Above this point, the relative error increases due to the FE discretisation error and below this point, the relative error decreases due to the round-off of the inertia terms.

5.2 Waves in Thin Plate Strips

In this section the use of the WFE is illustrated in the calculation of the wavenumber distribution along non-uniform stripes of plate. We begin, by way of a review, with the analysis of uniform plate structures.

5.2.1 Uniform Plate Strips

The plate is assumed to be thin and isotropic with simply supported boundary conditions at the edges, as shown in Figure 5.4. For such a plate strip, the analytic wavenumber is given by (Graff, 1991)

$$k^2 = k_x^2 + k_y^2 = \pm\sqrt{\frac{\rho h}{D}}\omega, \tag{5.21}$$

where D is the bending rigidity, $D = Eh^3/12(1-\upsilon^2)$, υ is Poisson's ratio, ρ is material density, h is plate thickness. For the assumed simply supported boundary conditions, the displacement in the y direction can be assumed as (Leissa, 1969)

$$w(y) = A\sin\left(\frac{n\pi y}{L_y}\right), \tag{5.22}$$

where *n* is the order of the mode and *A* is the displacement magnitude, so that

$$k_y = \frac{n\pi}{L_y}. \tag{5.23}$$

Thus, the wavenumbers in the *x* direction are given by

$$k_{xn}^2 = \pm\sqrt{\frac{\rho h}{D}}\omega - \left(\frac{n\pi}{L_y}\right)^2 \quad (n = 1, 2, 3\cdots). \tag{5.24}$$

Substituting $k_{xn} = 0$ gives the cut-off frequency for the *n*-th wave mode as

$$\omega_{cn} = \sqrt{\frac{D}{\rho h}}\left(\frac{n\pi}{L_y}\right)^2. \tag{5.25}$$

In the case considered here, it is assumed that, L_y = 0.16 m, $E = 2.1\times10^{11}$ Pa, ρ = 7,800 kg/m^3, h = 0.002 m and υ = 0.30. Consider a plate strip model consisting of four elements in the radial direction, as shown in Figure 5.4 (b) with Δ_x = 0.02 m, Δ_y = 0.04 m. A four nodes plate element is chosen and there are 3 DOFs, transfer displacement *w*, rotation θ_x and θ_y, at each node. There are then 22 DOFs for each slice in this model, due to the defined boundary conditions. Since the *y* direction wavenumber is $k_y = n\pi / L_y$ for the *n*-th wave mode, only the wavenumber for the *n* = 1 wave mode could be expected to be accurately evaluated since $k_y \Delta_y = \pi/4 < 1$.

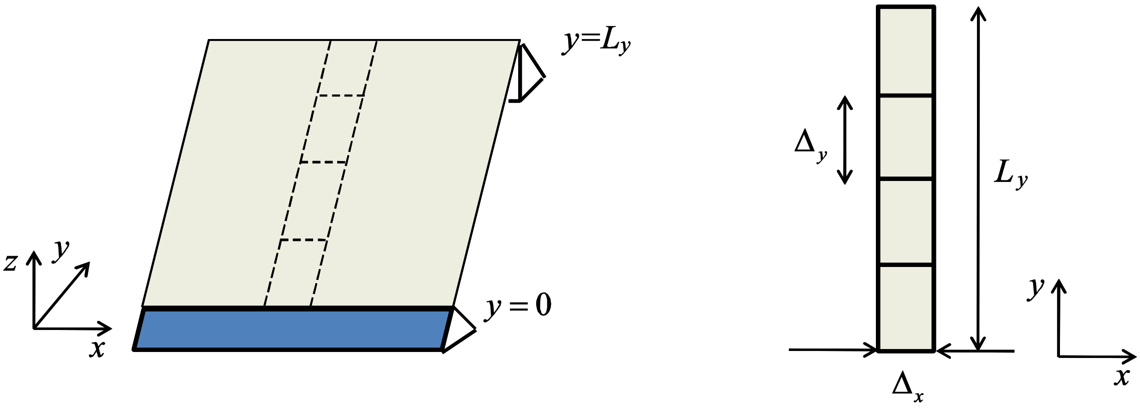

(a) (b)

Figure 5.4 (a) Plate strips with simply-supported boundary conditions at edges and (b) 4-element model.

The dispersion curves for the *n* = 1 mode are shown in Figure 5.5. There are two waves associated with the *n* = 1 mode; one is for a wave which propagates above its cut-off frequency and another is for a near-field wave. The cut-off frequency for this mode occurs at about 200 Hz in this case. The ordinate shows the non-dimensional wavenumber, $k_x L_y / \pi$, becomes –*i* for this wave mode at 0 Hz.

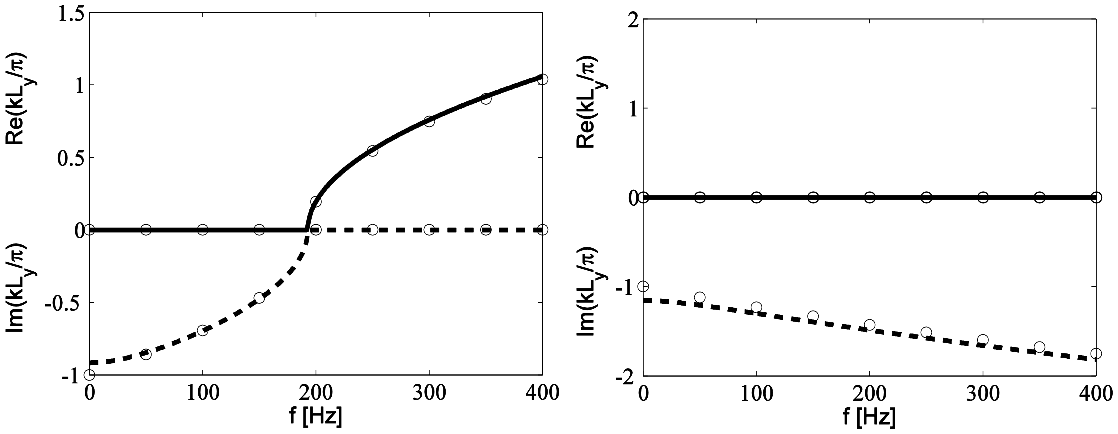

(a) (b)

Figure 5.5 (a) Flexural wave and (b) near-field wave in an isotropic plate strip with simply-supported edges for *n*=1 forward-going. Analytic solution is represented by lines (solid lines for the real part of the wavenumber and dashed lines for the imaginary part of the wavenumber) and numerical solution is indicated by “o”.

5.2.2 Non-uniform Plate Strips

If the material properties of the plate vary along its longitudinal direction, *x*, we can modify the analytic expression of the wavenumber of the isotropic plate, which is simply supported at y=0 and $y=L_y$, to vary against position as

$$k^2(x) = \pm\sqrt{\frac{\rho h}{D(x)}}\omega - (\frac{\pi}{L_y})^2, \tag{5.26}$$

where only the first mode is considered. In this example, $D(x)$ has a value of 4.5 × 10^{-9} N·m at x=0 and a value of 2.1 × 10^{-13} N·m at 35 mm away from the base, L_y is assumed to be 0.3 mm, the plate thickness h is 50 μm and the density of the plate is 1000 kg/m^3, which is assumed here to be as same as the BM in the cochlea. The values of $D(x)$ along the plate are thus assumed to be exponentially decaying, with a characteristic decay length l of 7 mm, i.e. $D(x) = D_0 e^{-2x/l}$, where D_0 is the value at x=0 which is 4.5 × 10^{-9} N·m in this case.

Figure 5.6 shows the distribution of wavenumber along the plate with varying stiffness at different positions. The dispersion curves for the n = 1 mode are similar to those obtained in Figure 5.5. For the assumed variation of $D(x)$, the term $(\pi/L_y)^2$ is much larger than $\sqrt{\rho h / D(x)}\omega$ at x=0, thus kL_y/π equal to $-i$ at x=0.

Similar to the uniform case, the cut-off frequency for the first flexural wave mode can be given by

$$\omega_c = \sqrt{\frac{D(x)}{\rho h}}\left(\frac{\pi}{L_y}\right)^2. \tag{5.27}$$

When for a given frequency, f, the cut-off position can be expressed as

$$x_c = -\frac{l}{2}\ln\left(\frac{4\rho h L_y^4 f^2}{\pi^2 D_0}\right). \tag{5.28}$$

It can be seen that the cut-off position moves towards x=0 if the driving frequency increases, since the term $D(x)$ is assumed to decay exponentially along x-axis.

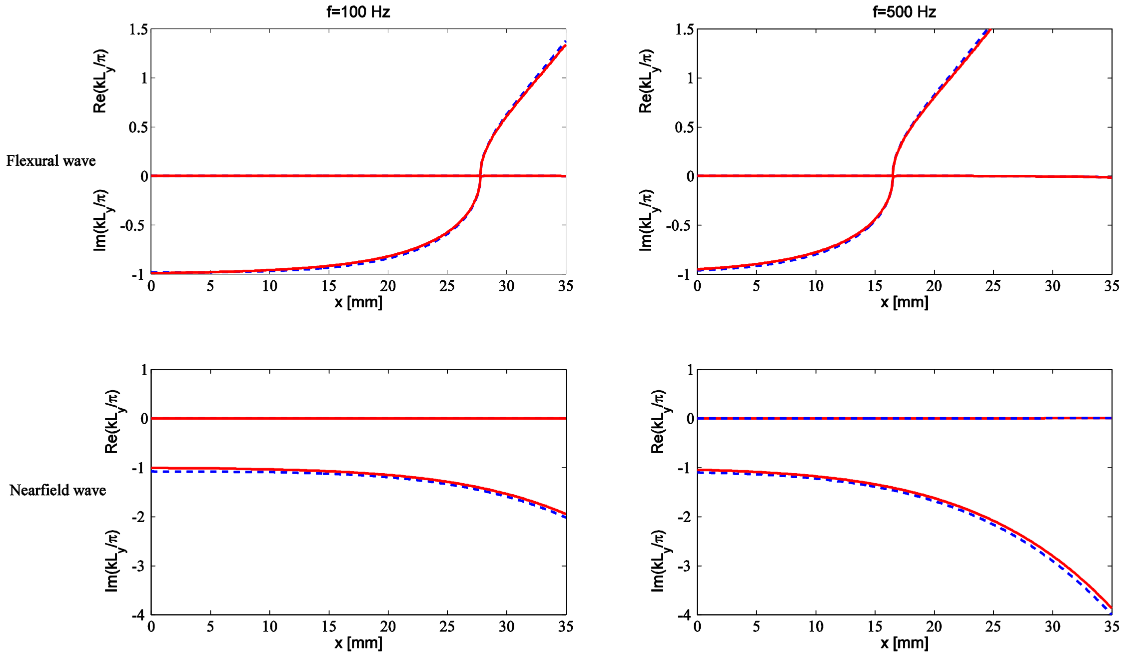

Figure 5.6 Flexural waves in a non-uniform isotropic plate strip with simply-supported edges when the flexural rigidity varies exponentially along the *x* direction calculated at 100 Hz (left column) and 500 Hz (right column). Analytic solution of the isotropic plate is represented by red solid lines and numerical solution using the WFE is represented by blue dashed lines.

5.3 Waves in Fluid Filled Ducts

5.3.1 Waves in Uniform Ducts

Acoustic wave propagation in a three-dimensional duct with rigid-walled boundary conditions filled with water is illustrated in this section using the WFE method. The dimensions of the three dimensional duct are $L_x \times L_y \times L_z$=68 μm ×1 mm ×1 mm, which are the same as the cochlear segment used in Chapter 6, and the sound speed in water is c=1,500 m/s. The relation between angular frequency ω and dimensions L_x, L_y and L_z is given by (Pain, 2006)

$$\omega(m,n) = c\sqrt{\left(\frac{l\pi}{L_x}\right)^2 + \left(\frac{m\pi}{L_y}\right)^2 + \left(\frac{n\pi}{L_z}\right)^2}, \tag{5.29}$$

where l, m and n are order of mode in the x, y and z directions respectively, so that the wavenumber can be expressed as

$$k\left(m,n\right)=\frac{\omega\left(m,n\right)}{c}=\sqrt{\left(\frac{l\pi}{L_x}\right)^2+\left(\frac{m\pi}{L_y}\right)^2+\left(\frac{n\pi}{L_z}\right)^2}\,. \tag{5.30}$$

The wavenumber can be rewritten as

$$k^2\left(m,n\right)=k_x^2+k_y^2+k_z^2=\left(\frac{l\pi}{L_x}\right)^2+\left(\frac{m\pi}{L_y}\right)^2+\left(\frac{n\pi}{L_z}\right)^2. \tag{5.31}$$

The $\left(m,n\right)$ mode wavenumber in the *x* direction $k_{mn,x}$ is derived from equations (5.30) and (5.31) as

$$k_{mn,x}^2=k^2\left(m,n\right)-k_y^2-k_z^2=\left(\frac{\omega}{c}\right)^2-\left(\frac{m\pi}{L_y}\right)^2-\left(\frac{n\pi}{L_z}\right)^2. \tag{5.32}$$

Substituting $k_{mn,x}=0$ into equation (5.32) gives the cut-off frequency for the (*m*, *n*)-th wave mode as

$$\omega_c\left(m,n\right)=c\sqrt{\left(\frac{m\pi}{L_y}\right)^2+\left(\frac{n\pi}{L_z}\right)^2}\,. \tag{5.33}$$

For numerical simulation, the duct is modelled by a mesh of 1×4×4 8-node hexahedral acoustic elements as shown in Figure 5.7.

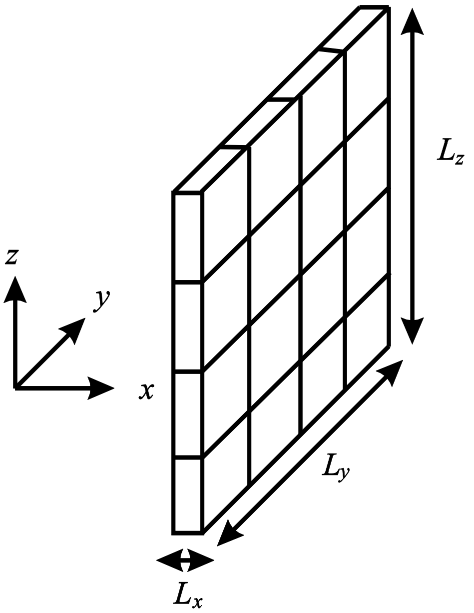

Figure 5.7 A three-dimensional acoustic duct filled with water and modelled using 1×4×4 8-node hexahedral acoustic elements.

The 8-node hexahedral acoustic element consists of eight nodes as shown in Figure 5.8. The details of deriving the stiffness and inertial matrices are given by Fahy and Gardonio (Fahy and Gardonio, 2007).

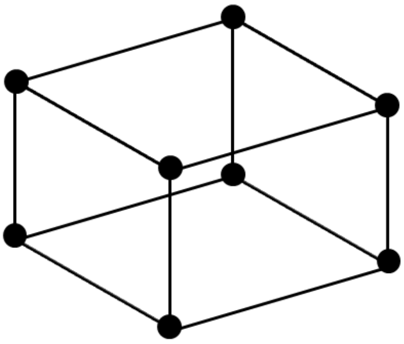

Figure 5.8 A sketch of an 8-node quadratic hexahedron fluid element.

The dispersion curves for mode (0, 0) and (0, 1) are shown in Figure 5.9. The abscissa represents frequency and the ordinate shows the non-dimensional wavenumber $k_x L_x$. Dispersion curves represent waves associated with mode (0, 0) which represents a fast wave propagating at 1,500 m/s, and (0, 1) which is a near-field wave below the cut-off frequency, which is 750 kHz for this case, and starts to propagate above the cut-off frequency. It can be seen that the numerical results have a good agreement with the analytic results.

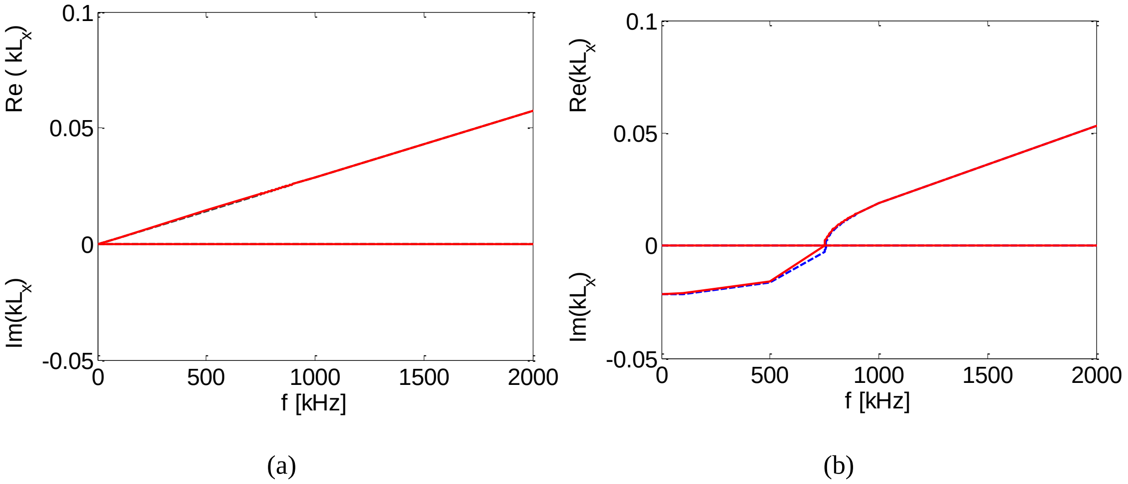

(a) (b)

Figure 5.9 Dispersion curves for wave mode (a) (0, 0) and (b) (0, 1). Analytic solution is indicated by red solid lines and the WFE solution is represented by blue dashed lines.

5.3.2 Waves in Non-uniform Ducts

If the acoustic duct used above is not uniform but has a varying cross-sectional area along its length, the WFE method can also be used to predict the wavenumber distribution at a given frequency. The variation of dimensions L_y and L_z of the duct are shown in Figure 5.10. The duct is assumed to be 35 mm long with rigid-walled boundary condition and filled with water.

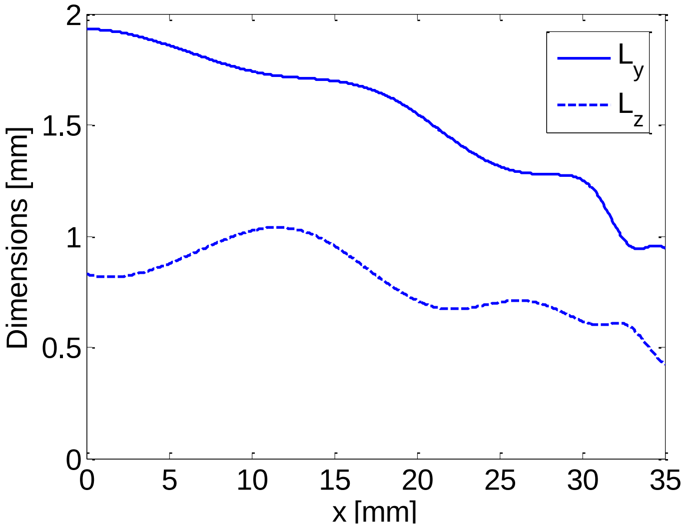

Figure 5.10 Assumed variation of the width of the duct (solid line), L_y, and the height (dashed line), L_z. The variation of the duct cross-sectional area is identical to that assumed for the non-uniform cochlear fluid chamber in Section 2.

Figure 5.11 shows the wavenumber distribution of wave mode (0, 1) along the length of the duct. The wave is evanescent and decays away along the duct due to the non-uniformity. The agreement between the numerical method and the analytic method is good which indicates that the WFE method can be applied to predict the wavenumber distribution in a non-uniform structure with slowly varying properties.

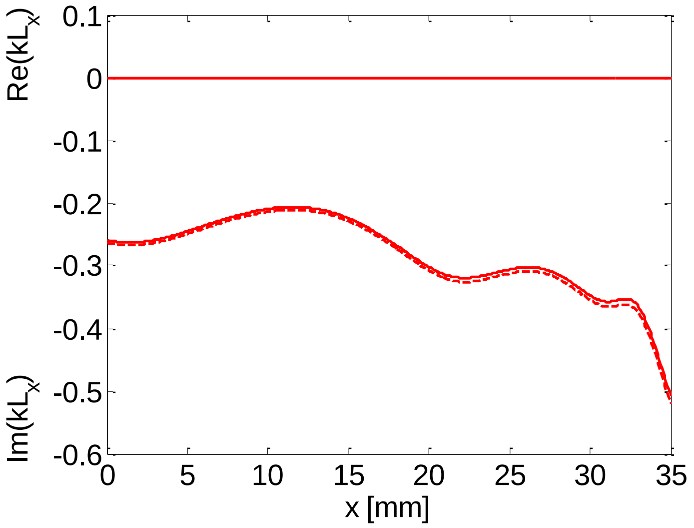

Figure 5.11 Dispersion curves for wave mode (0, 1) along the length of the duct at 20 kHz. Analytic solution is indicated by solid line and the WFE solution is represented by dashed line.

5.4 Waves in Loudspeaker Cones

The dynamics of an idealised loudspeaker cone provides a particularly interesting example of a non-uniform system. A loudspeaker typically consists of four primary components: the voice coil, the cone, the suspension and the enclosure, as shown in Figure 5.12. The loudspeaker cone is one of the core components of the loudspeaker and it can be manufactured from various materials, depending on driver implementation, desired frequency response for each driver, and cost. The loudspeaker cone is assumed here to be exactly conical.

At low frequency, below 500 Hz for an 8 inches woofer for example, the loudspeaker cone usually moves rigidly, with its shape almost unchanged during vibration (Petyt and Gélat, 1998). As the frequency is increased, the transverse velocity of the cone surface becomes non-uniform with the amplitude of the vibration increasing towards the outer edge. At still higher frequencies the outer edge starts to move in anti-phase, which is called cone break-up. If the transverse displacement of the cone surface is plotted against the axial position, as shown in Figure 5.13, the response has surprising similarities with that of the cochlea. They both increase gradually to a peak, which is dependent on driving frequency and then decrease sharply, although in the loudspeaker cone the response does not fall uniformly beyond the peak but appears to oscillate in amplitude. Thus, it is of interest to study the dynamics of the loudspeaker cone in order to help understanding of the cochlear functions, or, to help improving loudspeaker design from the cochlear modelling.

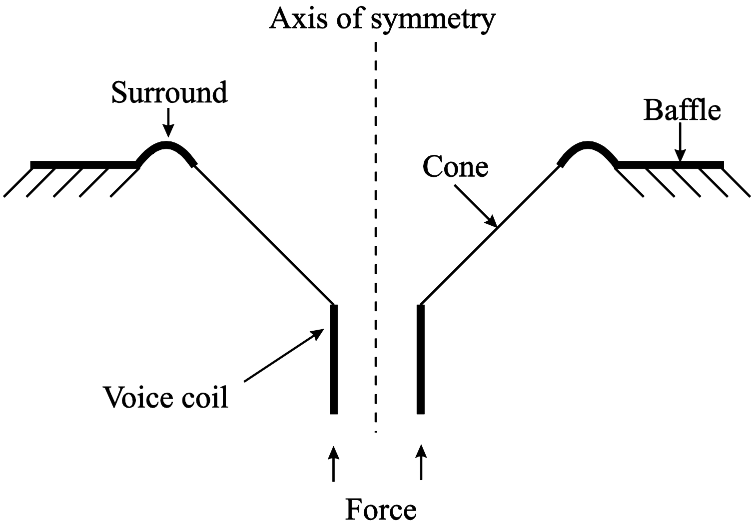

Figure 5.12 The primary components of a loudspeaker drive unit.

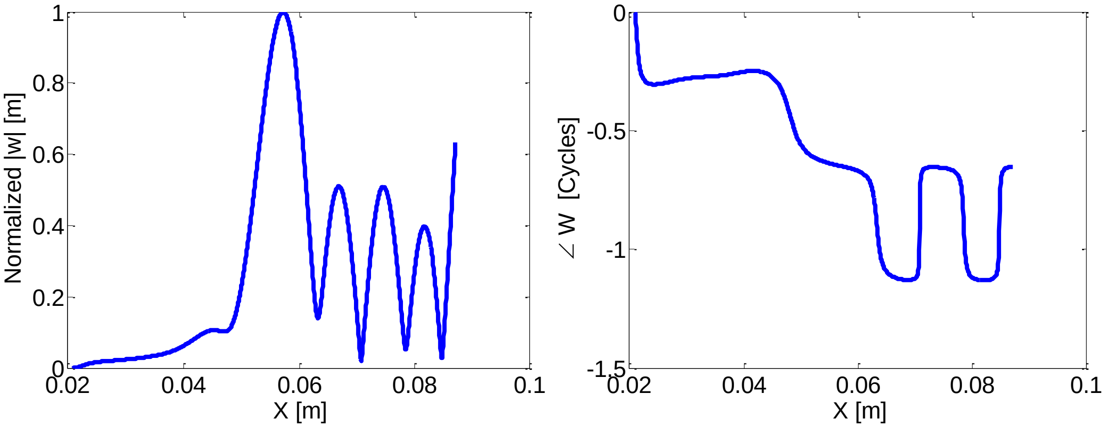

(a) (b)

Figure 5.13 The distribution of (a) normalized transverse displacement and (b) phase of the cone surface, calculated at a frequency of 3 kHz for the cone described by Table 5.1.

5.4.1 Forced Response Using the Dynamic Stiffness Matrix Method

To study the dynamic response of the loudspeaker cone, here we assume that the loudspeaker is represented by an axisymmetric conical cone, as shown in Figure 5.14, based on thin shell theory (Leissa, 1993) and the dynamic stiffness matrix, DSM, method is used here to calculate the response of the cone under an axial sinusoidal force at different frequencies

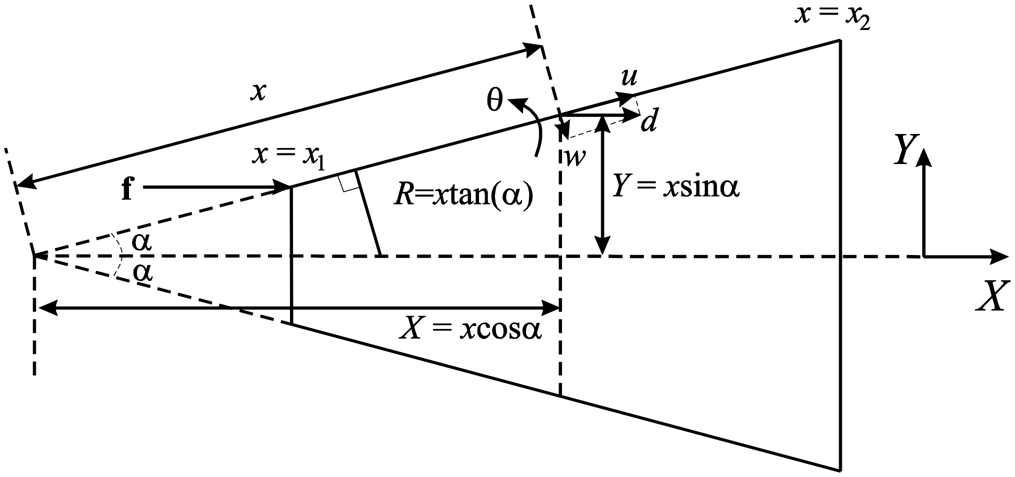

Figure 5.14 Side view of the conical cone in local coordinates, x denotes position along the cone meridian, X and Y are the axial and radial positions in the global coordinates, α is the angle between the axis and meridian.

In Figure 5.14, x denotes position along the cone surface, X denotes horizontal position in the global coordinate, u is displacement along the cone surface, w is transverse displacement, θ is rotation and d is displacement in the X direction where $d = u\cos\alpha + w\sin\alpha$.

5.4.1.1 Equation of Motion

The displacements and forces of the cone, which are shown in Figure 5.14, can be expressed by six first-order differential equations as (Goldberg, *et al.*, 1960)

$$\begin{cases} u' = -\upsilon \dfrac{u}{x} + \upsilon \dfrac{w}{x}\cot\alpha + \dfrac{\left(1-\upsilon^2\right)}{Eh} N_x \\ w' = \theta \\ \theta' = -\upsilon \dfrac{\theta}{x} + \dfrac{12\left(1-\upsilon^2\right)}{Eh^3} M_x \\ N_x' = Eh\left(\dfrac{1}{x^2} - \dfrac{\rho\omega^2}{E}\right)u - Eh\dfrac{w}{x^2}\cot\alpha + \left(\dfrac{\upsilon-1}{x}\right)N_x \\ Q_x' = -Eh\dfrac{\cot\alpha}{x^2}u - h\left(\dfrac{\cot^2\alpha}{x^2}E - \rho\omega^2\right)w - \upsilon\dfrac{\cot\alpha}{x}N_x - \dfrac{1}{x}Q_x \\ M_x' = -\dfrac{Eh^3}{12x^2}\theta - Q_x + \dfrac{\left(\upsilon-1\right)}{x}M_x \end{cases}, \tag{5.34}$$

where x is the position along the cone meridian, α is the half angle of the cone, u is the displacement along the meridian (positive in the direction of positive x), w is the displacement normal to the meridian (positive inward), θ is the rotation of the cone's normal in the direction shown in Figure 5.14, N_x is the membrane force in the direction of the meridian, Q_x is the normal shearing force, M_x is the bending moment in the direction of meridian, E is the Young's modulus of the cone material, h is the cone thickness, υ is Poisson's ratio, ρ is the density of cone material and ω is angular frequency. Equation (5.34) can be written in "state space" form as (Petyt and Gélat, 1998)

$$\frac{\partial \mathbf{y}(x)}{\partial x} = \mathbf{A}(x)\mathbf{y}(x), \tag{5.35}$$

where

$$\mathbf{y}(x) = \begin{bmatrix} u \\ w \\ \theta \\ N_x \\ Q_x \\ M_x \end{bmatrix}, \tag{5.36}$$

and

$$\mathbf{A}(x)=\begin{bmatrix} -\dfrac{\upsilon}{x} & \dfrac{\upsilon\cot\alpha}{x} & 0 & \dfrac{\left(1-\upsilon^2\right)}{Eh} & 0 & 0 \\ 0 & 0 & 1 & 0 & 0 & 0 \\ 0 & 0 & -\dfrac{\upsilon}{x} & 0 & 0 & \dfrac{12\left(1-\upsilon^2\right)}{Eh^3} \\ Eh\left(\dfrac{1}{x^2}-\dfrac{\rho\omega^2}{E}\right) & -\dfrac{Eh\cot\alpha}{x^2} & 0 & \left(\dfrac{\upsilon-1}{x}\right) & 0 & 0 \\ -\dfrac{Eh\cot\alpha}{x^2} & -h\left(\dfrac{\cot^2\alpha}{x^2}E-\rho\omega^2\right) & 0 & -\dfrac{\upsilon\cot\alpha}{x} & -\dfrac{1}{x} & 0 \\ 0 & 0 & -\dfrac{Eh^3}{12x^2} & 0 & -1 & \dfrac{(\upsilon-1)}{x} \end{bmatrix}. \tag{5.37}$$

The dynamic behaviour of a conical cone, whose geometry and material are listed in Table 5.1, is calculated using the dynamic stiffness matrix method (Petyt and Gélat, 1998).

Table 5.1 Assumed properties of the cone.

α [rad]	Cone length [m]	Initial value on the X axis [m]	E [Pa]	ρ [kg/m^3]	Loss factor η	Poisson's ratio v	Thickness h [m]
$2\pi/9$	0.108	0.0209	1.5×10^9	900	0.02	0.33	0.5×10^{-3}

The dynamic behaviour at a given position along the cone depends on whether the excitation is above or below the ring frequency at this location (Kaizer, 1979). Assuming the cone acts as a cylinder at a given location, the ring frequency is given by

$$f_R=\frac{c}{2\pi R}, \tag{5.38}$$

where c is the speed of longitudinal waves given by $\sqrt{E/\rho}$, R is the distance between the cone and cone axis measured perpendicular to the cone meridian, as shown in Figure 5.14, and this is plotted for the cone used below in Figure 5.15. Below the ring frequency the dynamics are dominated by the membrane stiffness, resulting in mostly in-plane motion. Above the ring frequency the dynamics are dominated by the bending stiffness, resulting in flexural motion. Since the ring frequency varies along the length of the cone, however, the dynamic behaviour of the cone depends on whether the frequency is in one of three regions, as shown in Figure 5.15. In region I, the excitation frequency is below the ring frequency at every position along the cone, so the cone moves entirely in phase as a quasi-rigid body. In region II, the excitation frequency is below the ring frequency at the apex of the cone but above it at the base of the cone, so that part of the cone is still moving as a quasi-rigid body and part of the cone has "broken up" into flexural motion. In region III, the excitation frequency is above the ring frequency all along the cone, so the dynamics are dominated by bending waves at all positions.

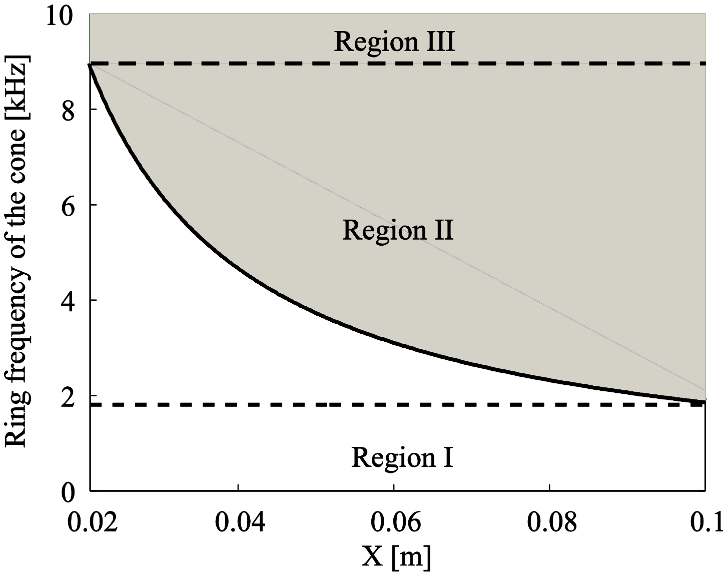

Figure 5.15 The ring frequency as a function of position along the cone axis indicating the transition between mostly in-plane (unshaded) and mostly bending (shaded) behaviour.

5.4.1.2 Forced Response

To calculate the forced response of the cone, the boundary condition at the inner edge, small end, is that the cone can only move along its meridian and at its outer edge, big end, is assumed to be free. The cone is driven by a sinusoidal force at the inner edge in the x direction. The dynamic stiffness matrix, **D**, of the cone is calculated by the Runge-Kutta approximation (Petyt and Gélat, 1998). The accuracy of the response depends mainly upon the step size, which is 0.1 mm in this case, used in the Runge-Kutta analysis rather than the number of segments of the cone. The cone thus can be expressed as

$$\mathbf{Dq} = \mathbf{f}, \tag{5.39}$$

where **q** is the vector of displacement, u, w, and θ at each segment along the cone and **f** is the corresponding vector of forces N_x, M_x and Q_x at each element, which in this case is applied on the cone at the apex.

The forced response of the cone due to a harmonic force **f,** which is applied uniformly over the circumference of the narrow apex of the cone in the axial direction, is calculated at different frequencies and harmonic forces and an instantaneous snap shot of the resulting vibration patterns are shown in Figure 5.16. The dashed lines in each subfigure are the undeformed middle surfaces and the solid lines denote the deformed middle surfaces. The forces have been increased beyond those encountered in a typical loudspeaker to emphasise the amplitude of the motion.

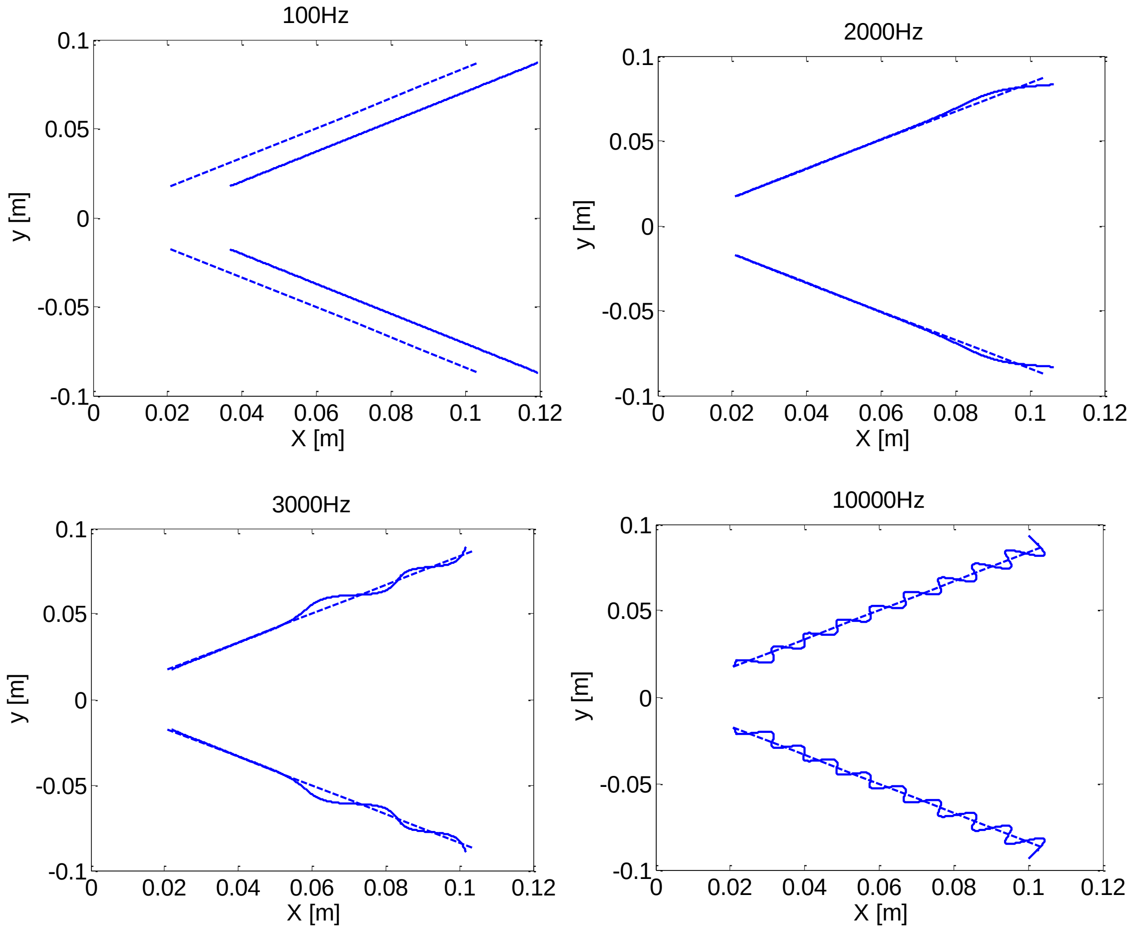

Figure 5.16 Cone vibration at different frequencies.

It can be seen that at low frequencies in region I, 100 Hz for example, the cone moves as a rigid body and the amplitude of motion in the axial direction, x, is much greater than that in the vertical direction, y. Also, the real part of the displacement in the axial direction is much greater than its imaginary part and is constant along the cone. The amplitude of this displacement is about 15.8 mm, for a driving force of 100 N, which is close to theoretical result calculated using Newton’s Second Law of Motion assuming the cone acts as a mass.

At higher frequencies, 2 kHz and 3 kHz when the excitation frequency is in region II, cone “break-up” occurs, in which the cone no longer vibrates as a rigid body, but some sections of the cone still move in phase. In this frequency range, the bending wave cannot propagate in the region close to the apical edge of the cone, due to the high stiffness, but can propagate on the outer part of the cone and then build up into a standing wave. The “transition point”, where bending wave starts to cut-on, moves towards the apical edge as the driving frequency increases. At 10 kHz the excitation frequency is in region III and the whole cone moves with a bending motion. The more detailed behaviours of bending and longitudinal motions are studied and discussed below using the WFE method.

5.4.2 Numerical Dispersion Curve Using the WFE Method

By using the dynamic stiffness matrix, **D**, in equation (5.39), the transfer matrix of each of the 512 segments of the cone model can be formed. After solving the eigenvalue problem of the transfer matrix, the eigenvalue and eigenvector of each slice of the cone can be obtained. Figure 5.17 shows the distribution of the real and imaginary parts of the wavenumber along the cone meridian at 3000 Hz, calculated using the WFE method at each slice. Since the DSM cone model for each of the 512 segments of the cone has 3 degrees of freedom on each face of the cone section, there are thus 3 pairs of eigenvalues for the transfer matrix $\mathbf{T}(n)$. Half of these, whose imaginary part is negative, are forward-going waves. For an excitation frequency of 3 kHz, we can divide the cone into 2 regions along the cone axis, region A includes apex to about 0.06 m corresponding to the transition point at 3 kHz shown in Figure 5.17 and region B corresponds to from 0.06 m to the base of the cone. It can be seen that not all waves can propagate along the cone in region A, since they have non-zero imaginary wavenumber indicating they are oscillating and decaying. Specifically, wave 1 propagates with a gradually decreasing speed and decays less than the other two waves, since wave 1 has a small non-zero imaginary part of wavenumber. This shows that in region A, the longitudinal motion dominates the vibration pattern of the cone. Beyond the position 0.06 m, wave 2 starts to propagate towards the base. Wave 1 becomes an evanescent wave beyond this position. Wave 3 has a large non-zero imaginary part of wavenumber along the whole range of the cone, which indicates that this wave does not play a significant role in cone vibration and can be identified as an evanescent near-field wave.

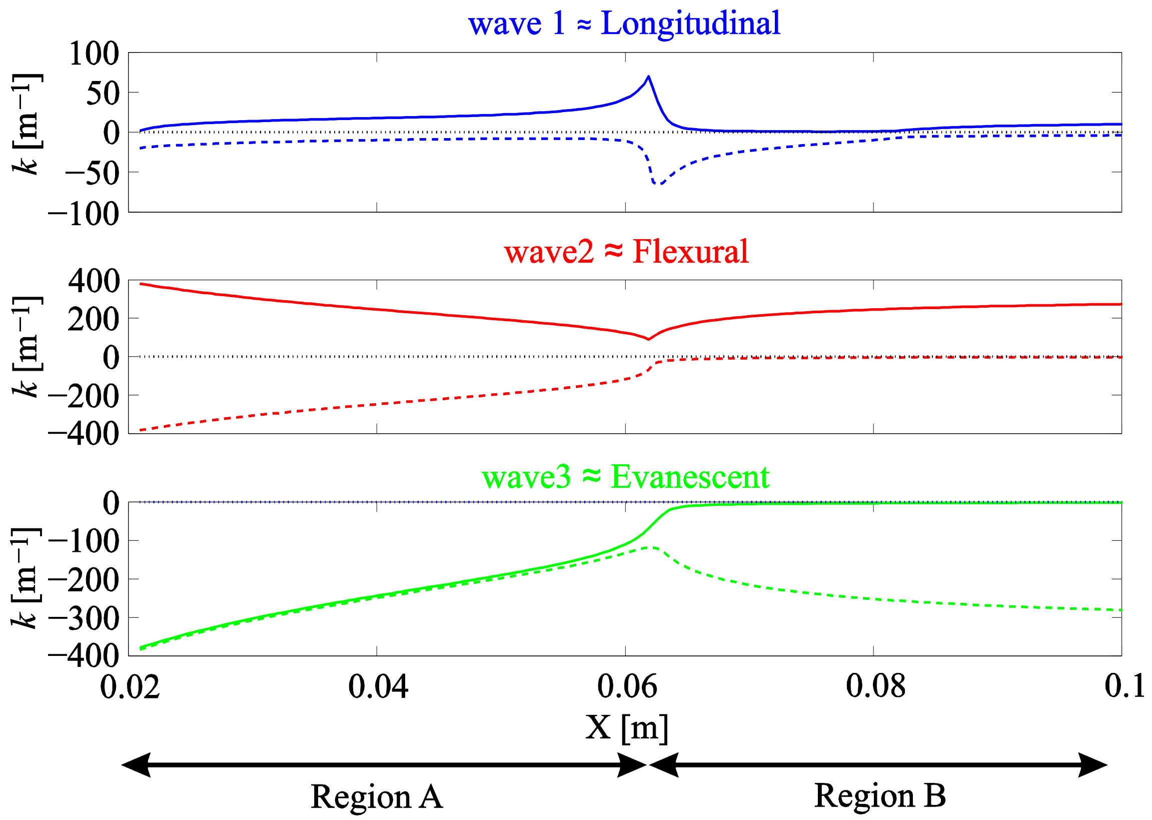

Figure 5.17 Wavenumber distribution along the cone axis at 3000 Hz using the WFE method, with only wavenumbers, solid lines for the real part and dashed lines for the imaginary part, corresponding to forward-going waves plotted.

Figure 5.18 shows the distribution of the real and imaginary parts of the wavenumber associated with backward-going waves, whose imaginary part is positive, along the cone axis at 3 kHz. These backward-going waves, due to the reflection from the free basal end of the cone, have the same wavenumber distribution but with opposite sign from those of the forward-going waves. The interactions between the backward-going component and the forward-going component of wave 2 give rise to the standing wave seen in the DSM results, as shown in Figure 5.16 at 3 kHz.

Although we can find the properties of each wave from the wavenumber variations, the transition in the vibration pattern and the contribution of each wave to the cone vibration cannot be directly seen from this analysis. The forced response from the DSM analysis can be decomposed into the wave components calculated using the WFE method, however, as described in the next section, which can show the contribution of each wave to the cone vibration.

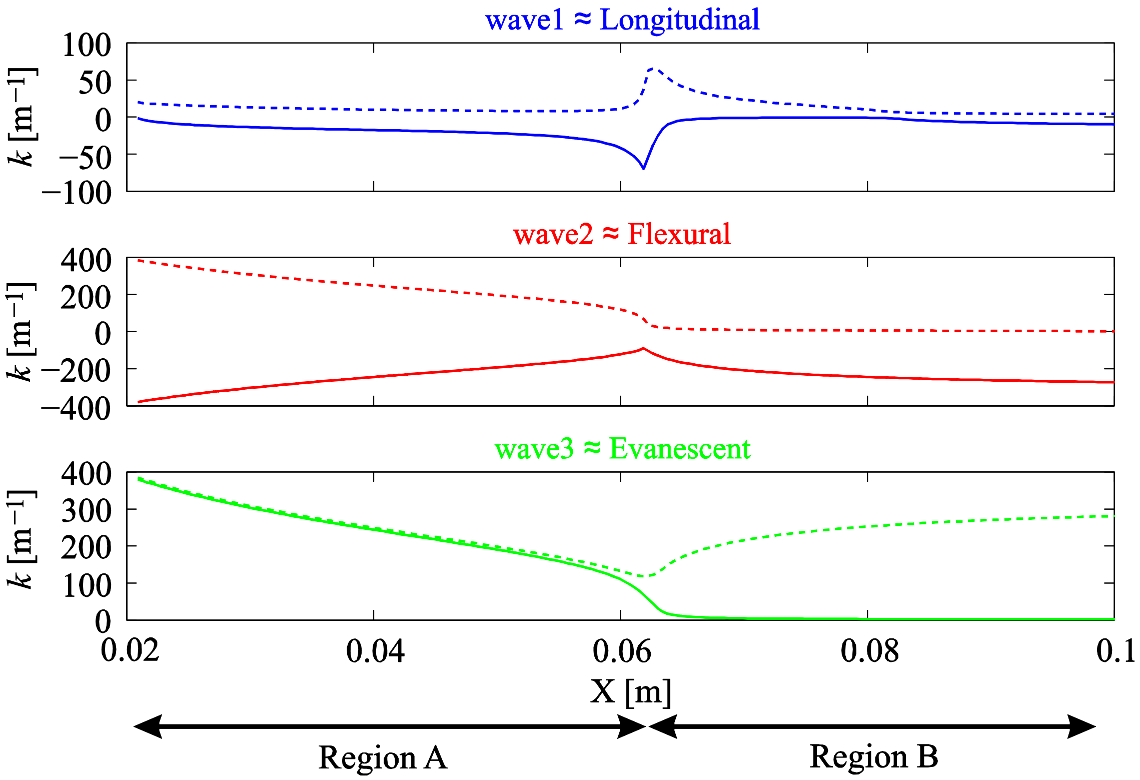

Figure 5.18 Wavenumber distribution along the cone axis at 3000 Hz using the WFE, with only wavenumbers corresponding to backward-going waves plotted, and solid lines being the real component of the wavenumber *k*, and dashed lines being the imaginary component.

5.4.3 Decomposition into Wave Components

In general, the $N \times N$ transfer matrix $\mathbf{T}$ for each slice of the cone has a linearly independent set of N eigenvectors and we can express the eigenvalue, eigenvector decomposition of the transfer matrix for the n-th section in the form

$$\mathbf{T}(n) = \boldsymbol{\varphi}(n)\boldsymbol{\Lambda}(n)\boldsymbol{\psi}(n), \tag{5.40}$$

so that

$$\mathbf{T}(n)\boldsymbol{\varphi}(n)=\boldsymbol{\varphi}(n)\boldsymbol{\Lambda}(n), \tag{5.41}$$

and

$$\boldsymbol{\psi}(n)\mathbf{T}(n)=\boldsymbol{\Lambda}(n)\boldsymbol{\psi}(n). \tag{5.42}$$

The right eigenvectors of **T**(n) thus correspond to the columns of $\boldsymbol{\varphi}(n)$ and the left eigenvectors of **T**(n) correspond to the rows of $\boldsymbol{\psi}(n)$. The wavenumbers are given by the elements of the diagonal eigenvalue matrix $\boldsymbol{\Lambda}(n)$.

Using equation (5.41) and (5.42), equation (5.5) can also be written as

$$\boldsymbol{\psi}(n)\begin{bmatrix}\mathbf{q}_{\mathrm{R}}(n)\\ -\mathbf{f}_{\mathrm{R}}(n)\end{bmatrix}=\boldsymbol{\Lambda}(n)\boldsymbol{\psi}(n)\begin{bmatrix}\mathbf{q}_{\mathrm{L}}(n)\\ \mathbf{f}_{\mathrm{L}}(n)\end{bmatrix}. \tag{5.43}$$

Since $\boldsymbol{\Lambda}(n)$ is diagonal, the inner product of each row of $\boldsymbol{\psi}(n)$, which is a left eigenvector of **T**(n), with the “state vectors” on the right and left hand side gives an equation of the form

$$a_{\mathrm{R}m}(n)=\lambda_m(n)a_{\mathrm{L}m}(n), \tag{5.44}$$

where $a_{\mathrm{R}m}(n)$ and $a_{\mathrm{L}m}(n)$ can be interpreted as the complex amplitudes of the m-th wave on the right and left hand side of the n-th section (Duhamel, *et al.*, 2006). The vector of all such wave amplitudes, on the right hand side of this segment, for example, can be written as

$$\mathbf{a}_{\mathrm{R}}(n)=\boldsymbol{\psi}(n)\begin{bmatrix}\mathbf{q}_{\mathrm{R}}(n)\\ -\mathbf{f}_{\mathrm{R}}(n)\end{bmatrix}, \tag{5.45}$$

which are shown for forward-going waves in Figure 5.19.

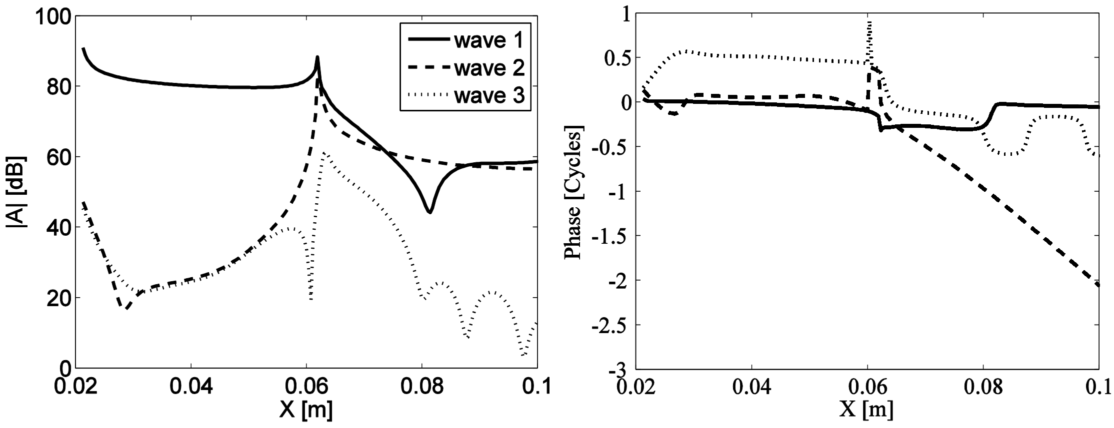

(a) (b)

Figure 5.19 The (a) amplitude and (b) phase of each forward-going wave at 3000 Hz.

The horizontal displacement, $d(n,m)$, due to *m*-th wave at *n*-th position is given by

$$d(n,m)=\mathbf{s}\mathbf{q}(n,m)a(n,m), \tag{5.46}$$

where $\mathbf{s}$ is a weighting vector, $\mathbf{s}=[\cos\alpha \;\; \sin\alpha]$, $\mathbf{q}(n,m)$ is the displacement vector for the *m*-th wave at *n*-th position, $\mathbf{q}(n,m)=\left[\mathbf{u}(n,m),\ \mathbf{w}(n,m)\right]^{\mathrm{T}}$, and $a(n,m)$ is the wave amplitude for the *m*-th wave at *n*-th position. The contributions to the displacement $d(n,m)$, from the full finite element model are shown for forward-going waves in Figure 5.20.

The contribution of the forward going component of wave 1 is seen to be in reasonable agreement with the overall result from the DSM method for positions apical to the peak response at this frequency, at about 0.06 m along the cone axis. The contribution of wave 1 is significantly less than the overall result of the DSM for positions beyond the peak response, region B, however, where the contribution of wave 2 dominates the overall response. There is also a negative-going component of wave 2 in this region, due to the reflection from the free basal end of the cone and the interaction between this and the positive-going wave 2 gives rise to the interaction pattern seen in the DSM results. The contribution of wave 3 decays away on either side of this peak, and the amplitude is too small to significantly affect the overall response. Inside region A the wavelength of wave 1 is about 0.31 m due to the predominance of longitudinal motion, with *k* being about 20 m^{-1} in Figure 5.17, and inside region B the wavelength of wave 2 is about 0.023 m due to the predominance of bending motion, with k being about 270 m^{-1} in Figure 5.17. The energy is converted from longitudinal motion to bending motion at the transition point.

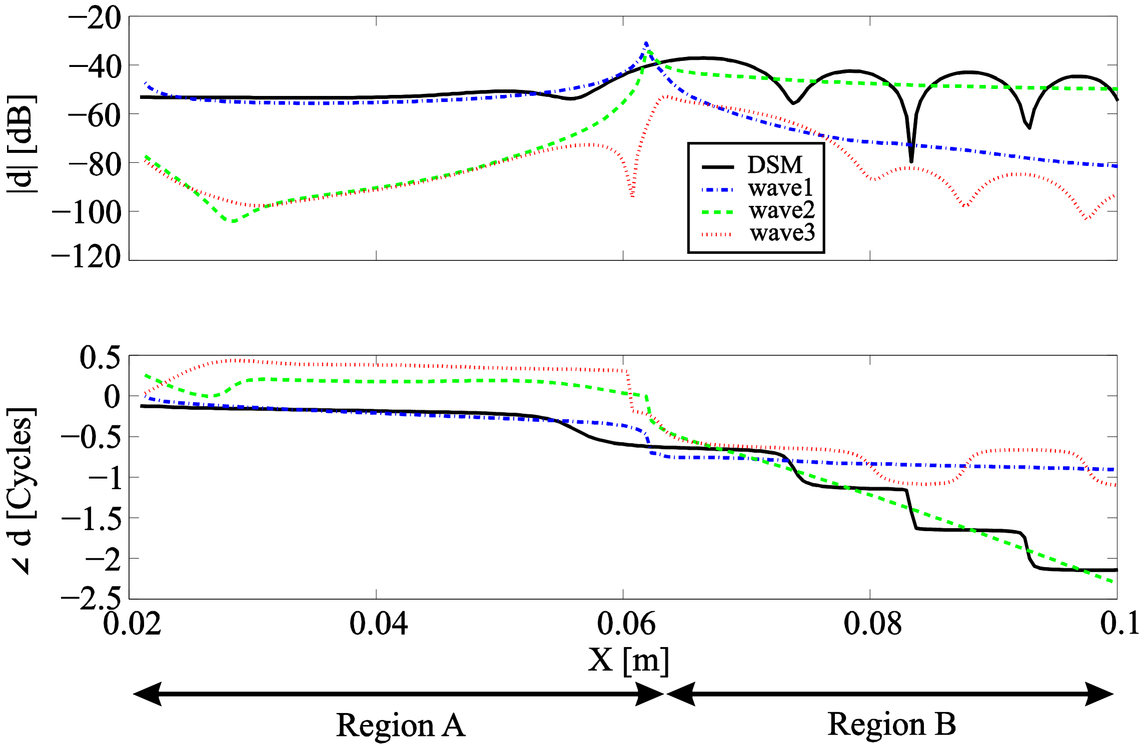

Figure 5.20 Decomposition of the overall horizontal displacement calculated from the DSM model into components due to forward-going waves in Figure 5.17, calculated from the wave finite element model at 3 kHz.

5.5 Conclusions

The theory of the wave finite element method has been reviewed and several applications of the method have been considered, which extend the method to structures having varying properties or geometry. The dispersion curves for the complex wavenumbers have been calculated and compared with analytic solutions.

Freely propagating in-plane waves were analysed for plate strips with simply supported boundary conditions. When the characteristics of the plate strips vary with position, the wavenumber distribution with position has a similar behaviour to the variation with frequency for the uniform cases. The cut-off position is frequency dependent, and moves towards the base when the driving frequency increases due to the assumed variation of the bending rigidity $D(x)$.

There are two main waves in a duct filled with water, one wave corresponding to the mode (0, 0) is a purely propagating plane wave, with speed of 1,500 m/s and the other one corresponding to the mode (0, 1) has a similar behaviour to the plate strips. This indicates that similar waves would occur in the cochlea structure since the cochlea is assumed to be a fluid-structural coupled system. Besides the well-known “slow wave”, there is also a fast wave travel at about 1,500 m/s which is the wave speed in the cochlear fluid. But this fast wave does not interact with the BM so would not be considered later in the cochlear model.

Another interesting application of the WFE method to a non-uniform geometry is to study the dynamics of the loudspeaker cone, in order to explain the vibration patterns of the cone in terms of waves. Although the vibration patterns of the cone have been widely studied numerically, using the dynamic stiffness matrix method for example (Petyt and Gélat, 1998), or theoretically (Kaizer, 1979, Zhang and Cheng, 2007), physical insight into the dynamic behaviour may be lost. In this chapter, the loudspeaker cone has been analysed using the DSM method and the WFE and the results from the DSM model was decomposed into wave components for illustrating the contribution of each wave to the overall response. The WFE method provides a way to study waves that travel in the loudspeaker cone and, more importantly, decompose the response of the DSM model into the components due to each of these waves, in order to explore how they interact. In this way the insight provided by the wave approach allows us to analyse the significance of different waves in the overall response.

Chapter 6. Wave Propagation and Decomposition in the Cochlea

6.1 Introduction

In this chapter wavenumber distributions along the cochlea for various types of waves are calculated first analytically and then numerically, using the WFE method. The cochlea is a complicated organ with considerable geometric and structural complexity. One of its most important functions is the mapping of different frequencies to a peak response at different longitudinal positions along its length. This process is commonly described in terms of the propagation of a single wave along the cochlea, generated by the interaction between the inertia of the fluid in the chambers and the local basilar membrane dynamics, as outlined in Chapter 1. The speed of this wave is relatively high at the base of the cochlea, where it is excited by the middle ear, but slows down as it propagates towards the apex and stalls when its velocity drops significantly at a frequency-dependent position determined by the distribution of BM mass and stiffness along the cochlea. The conventional theory of wave propagation along the cochlea with 1D fluid coupling is covered in more detail in Section 6.2. It is shown in this chapter how additional mechanisms of longitudinal couplings give rise to additional wave types. Specific examples will be described in Sections 6.3 and 6.4 of additional waves due to, (1) either an approximation to 3D fluid coupling that includes near-field components, or (2) due to longitudinal BM coupling. This study uses relatively simple analytic models to derive dispersion equations that can be solved to give the distribution of wavenumbers for the different waves along the cochlea. Sections 6.5 shows comparisons between the BM velocities from WKB reconstruction using wavenumbers calculated analytically and from discrete models.

Previous WKB solutions for the 2D and 3D cochlear model (de Boer and Viergever, 1982, Steele and Taber, 1979, Steele and Taber, 1979, Watts, 2000), showed good agreement with exact solutions except regions beyond the peak. The reason for these differences was attributed to the non-uniqueness of the complex WKB wavenumber in 2D and 3D models. The WFE method provides a practical way, as shown in Sections 6.6 and 6.7, to analyse all the waves in the cochlea, and can thus give further understanding of the WKB approximation and the cochlear mechanics in terms of waves.

In order to illustrate the results, a simple box model of the fluid coupling is assumed, as shown in Figure 6.1 together with a passive, single degree of freedom, model for the BM.

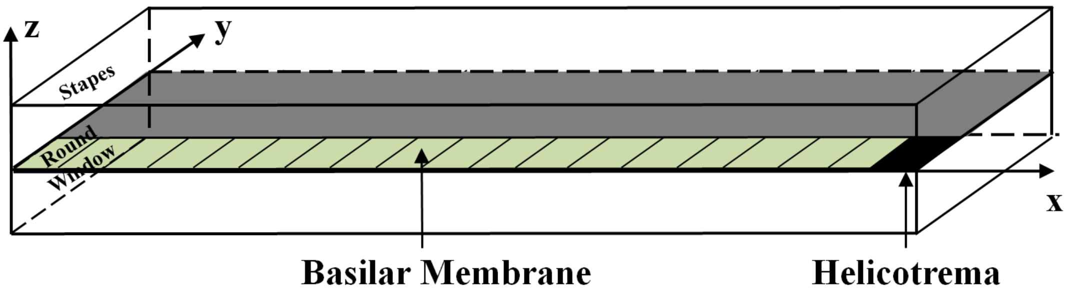

Figure 6.1 Box model of the cochlea.

The extra waves due to the additional forms of longitudinal BM coupling are generally heavily attenuated as they propagate along the cochlea. In general the wavenumbers are complex and so the disturbances they describe will have longitudinal changes in both phase and magnitude. It is thus difficult to distinguish between “waves” that predominantly propagate and near-fields that predominantly decay and so all such disturbances will be referred to as waves here. It is not, however, clear from this dispersion analysis the extent to which these additional waves are excited when the cochlea is driven at its base by the middle ear. Then a simpler discrete model of the cochlea is used to calculate the modal BM velocity along the cochlea. These velocity distributions are then compared with those calculated using the WKB methods, with the wavenumbers that are obtained analytically.

Finally the WFE method is used to calculate the characteristics of all the wave components that are obtained by a finite element model of the cochlea. This is used to decompose the response of the full finite element model into wave components, which includes 3D fluid coupling.

6.2 Local BM Dynamics and 1D Fluid Coupling

The simplest and most important type of wave propagation in the cochlea involves the interaction between the 1D component of the fluid coupling and the local BM dynamics, and is generally called the “slow wave”. Fluid coupling in the two chambers of the cochlea gives rise to a distribution of pressure difference due to BM motion (de Boer and Viergever, 1984). The fluid coupling can conveniently be split into two components

(Elliott, *et al.*, 2011). The first involves the spatially-averaged pressure in each cross-section of the chambers, so that the pressure distribution is one dimensional, 1D, and corresponds to a far-field or plane wave or to the far-field component of a wavenumber analysis. The second component involves the near-field part of the three dimensional flow of fluid round the BM and corresponds to the higher order modes, or the near-field components of a wavenumber analysis. The effect of both components together will be considered in the 3D fluid coupling case in Section 6.3, but the 1D component has the most significant effect and initially only this will be considered.

An equation for the far-field fluid coupling can be derived by combining those for the conservation of mass and of momentum in the fluid (Elliott, *et al.*, 2011). That for the conservation of mass is

$$\frac{\partial u(x)}{\partial x} = \frac{v(x)}{h}, \tag{6.1}$$

where $u(x)$ is the distribution of longitudinal velocity of the fluid along the cochlea, which is assumed uniform over each cross-section and $v(x)$ is the distribution of the transverse BM velocity, both being complex quantities at a single driving frequency, ω. The parameter h corresponds to the physical height of the two fluid chambers if the BM velocity is assumed to be uniform across its width. In a more complete analysis, in which the BM has some prescribed distribution of velocity across its width, an equation identical to equation (6.1) can be derived if h is interpreted as the effective height of the fluid chamber, as $\pi^2 WH/8B$ (Elliott, *et al.*, 2011), where W is the width of the cochlear partition, H is the physical height of the fluid chamber and B is the width of the BM. If W and H are both about 1 mm and B is about 0.3 mm, in the middle of the human cochlea, then h is about 4.1 mm.

Conservation of momentum is described by the equation

$$\frac{\partial p(x)}{\partial x} = -2i\omega\rho\, u(x), \tag{6.2}$$

where ρ is the fluid density and $p(x)$ is the distribution of the pressure difference along the cochlea, which is also assumed to be uniform across each cross-section of the chambers.

By differentiating equation (6.2) with respect to x and substituting equation (6.1), the one-dimensional fluid coupling equation is derived as

$$\frac{\partial^2 p(x)}{\partial x^2} = -\frac{2i\omega\rho}{h}\, v(x). \tag{6.3}$$

If the BM is assumed to respond only locally, then its complex velocity at position x, $v(x)$ is only determined by the complex pressure difference at the same position, $p(x)$. Assuming that the response is linear, it can be characterised by the local BM impedance, $Z_{\mathrm{BM}}(x)$ at the driving frequency, so that

$$v(x) = -\frac{p(x)}{Z_{\mathrm{BM}}(x)}, \tag{6.4}$$

where the minus sign indicates that a positive pressure difference generates a negative BM velocity in the sign convention adopted here.

By substituting equation (6.4) into (6.3), the wave equation for the interaction between the one dimensional fluid coupling and local BM dynamics is obtained as

$$\frac{\partial^2 p(x)}{\partial x^2} - \frac{2i\omega\rho}{h\, Z_{\mathrm{BM}}(x)}\, p(x) = 0. \tag{6.5}$$

This second order wave equation has a local solution of the form

$$p(x) = p_0 e^{-ik(x)x}, \tag{6.6}$$

where $k(x)$ is the wavenumber associated with the solution at position x. Differentiating this twice with respect to x, and substituting into equation (6.5), yields the dispersion equation for this type of wave as

$$k(x) = \pm\sqrt{\frac{-2i\omega\rho}{h\, Z_{\mathrm{BM}}(x)}}, \tag{6.7}$$

where the two solutions for k correspond to a forward and backward travelling wave. In principle the effective height, h, may also be a function of position, but this dependence can be incorporated into a slightly modified form of $Z_{\mathrm{BM}}(x)$ to retain the simple form of equation (6.7).

For high levels of excitation, the BM behaves almost passively and its impedance may be approximated by that of a single degree of freedom system having local mass, stiffness and damping, per unit area, equal to $m(x)$, $s(x)$ and $r(x)$, so that

$$Z_{\mathrm{BM}}\left(x\right)=i\omega m\left(x\right)+\frac{s\left(x\right)}{i\omega}+r\left(x\right). \tag{6.8}$$

The distribution of the wavenumber in equation (6.7), which in general is complex, will thus depend on the distribution of BM mass, stiffness and damping along the cochlea. In the example below it is assumed that the BM mass is uniform along the length of the cochlea, and equal to m_0, but that the stiffness varies such that the local natural frequency of the BM in isolation is given by

$$\omega_n\left(x\right)=\omega_{\mathrm{B}}e^{-x/l}, \tag{6.9}$$

where ω_{B} is the natural frequency at the base of the cochlea, assumed here to be $2\pi \times$ 20 kHz, and l is the natural frequency length scale, assumed here to be 7 mm. The assumed parameters of the cochlea are also listed in Table 2.1. The stiffness is assumed to vary exponentially, to give the distribution of natural frequencies in equation (6.9), so that

$$s\left(x\right)=\omega_n^2\left(x\right)m_0=\omega_{\mathrm{B}}^2m_0e^{-2x/l}. \tag{6.10}$$

Also, by assuming a constant damping ratio for the BM, ζ_0, the damping per unit area must be equal to

$$r\left(x\right)=2\zeta_0m_0\omega_n\left(x\right)=2\zeta_0m_0\omega_{\mathrm{B}}e^{-x/l}. \tag{6.11}$$

The range of natural frequencies thus extends from 20 kHz at the base to about 150 Hz at the apex of the cochlea, which is assumed to have a length of 35 mm, so that the model approximates the parameters of the human cochlea.

To provide some insight into the form of the wave it is helpful to consider the limiting case in which the damping term in the impedance is negligible compared with the mass and stiffness terms. We first assume that the BM is driven below its natural frequency, as it is at positions basal to the characteristic place, x_0, where the natural frequency is equal to the driving frequency, so that the BM is stiffness controlled. The wavenumber in this region is given by

$$k\left(x < x_0\right) \approx \pm\omega\sqrt{\frac{2\rho}{h\,s\left(x\right)}}, \tag{6.12}$$

which is entirely real, indicating a propagating wave, with phase speed given by

$$c\left(x\right) = \sqrt{\frac{h\,s\left(x\right)}{2\rho}}, \tag{6.13}$$

which is about 70 ms^{-1} at the base of the cochlea for the parameters assumed here, with h equal to 4 mm, ρ being 10^3 kg m^{-3} and the stiffness given by $\omega_n^2\left(x\right)m_0$ with m_0 equal to 0.3 kg m^{-2}. The wave then slows down as it propagates along the cochlea, since the stiffness decreases with position.

At the characteristic place, $Z_{\mathrm{BM}}(x)$ becomes zero if the BM is completely undamped and so the wavenumber tends to infinity and the velocity falls to zero. A small amount of damping is thus always included in the simulations below so that the wavenumber always remains finite, then

$$k\left(x = x_0\right) = \pm\sqrt{\frac{-i\rho}{h\zeta_0 m_0}}. \tag{6.14}$$

If we now assume that the BM is driven above its natural frequency, as it is at positions apical to x_0, so that it is mass controlled, then the wavenumber is

$$k\left(x < x_0\right) = \pm i\sqrt{\frac{2\rho}{h\,m_0}}, \tag{6.15}$$

where the BM mass, m_0, is assumed to be independent of x, as noted above. The wavenumber is now purely imaginary indicating an evanescent wave, having an exponential decay length, d, equal to

$$d = \sqrt{\frac{h\, m_0}{2\rho}}, \tag{6.16}$$

which is about 0.8 mm for the parameters assumed here.

Figure 6.2 shows the distribution of the real and imaginary parts of the wavenumber along the cochlea for a passive BM and 1D fluid coupling, at an excitation frequency of 1 kHz. The wavenumber for only the forward travelling wave, with a negative imaginary part, has been shown, since the backwards travelling wave must just have real and imaginary parts with the opposite sign to these, as indicated in equation (6.7).

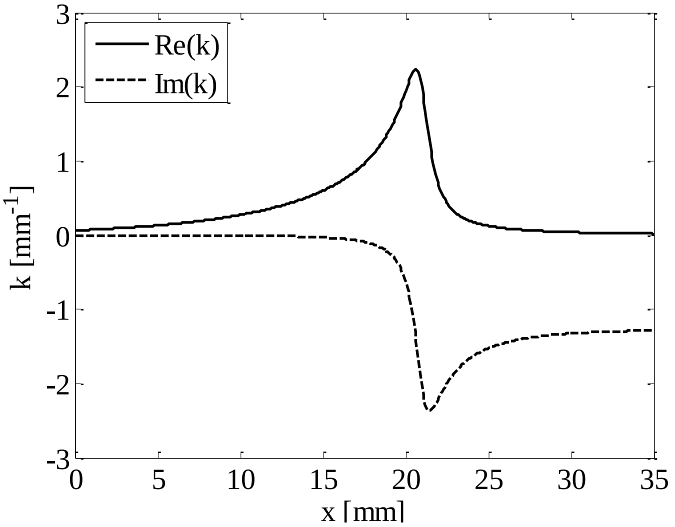

Figure 6.2 The distribution along the cochlea of the real and imaginary parts of the wavenumber, at an excitation frequency of 1 kHz, for the wave due to the interaction between the local passive BM dynamics and 1D fluid coupling.

For the assumed parameters, the result has a realistic value of the damping ratio for the passive cochlea, and shows a gradual transition from a mostly propagating to a mostly evanescent behaviour.

The WKB method provides a way of reconstructing the distributions of complex pressure and BM velocity along the cochlea from the knowledge of the wavenumber distribution. Using the WKB method (de Boer and Viergever, 1982), the pressure distribution can be written as

$$p(x) = \frac{A}{\sqrt{k(x)}} e^{-i\phi(x)}, \tag{6.17}$$

where A is the wave amplitude and

$$\phi(x) = \int_0^x k(x')dx', \tag{6.18}$$

is the cumulative phase.

Using the one-dimensional fluid coupling equation (6.3), we see that the local BM velocity is related to the pressure by

$$v(x) = \frac{h\,k^2(x)}{2i\omega\rho} p(x). \tag{6.19}$$

The velocity distribution can thus be calculated from the pressure distribution as

$$v(x) = \frac{Ah}{2i\omega\rho} k(x)^{3/2} e^{-i\phi(x)}. \tag{6.20}$$

The transverse BM velocity, which locally must also be proportional to $e^{-ik(x)x}$, is related to the longitudinal fluid velocity by equation (6.1) so that

$$v(x) = -ik(x)hu(x). \tag{6.21}$$

At the base of the cochlea the longitudinal fluid velocity must be equal to that of the stapes, u_S, where the difference in area between the stapes and fluid chamber is accounted for in the definition of u_S, so that

$$v(0) = -ik(0)hu_\mathrm{s}. \tag{6.22}$$

By setting equation (6.22) equal to equation (6.20) in the case where x is equal to zero, the amplitude of the WKB solution to the pressure can be shown to be

$$A = \frac{2\omega\rho u_s}{\sqrt{k(0)}}. \tag{6.23}$$

Figure 6.3 shows the distribution of complex BM velocity calculated using the WKB method.

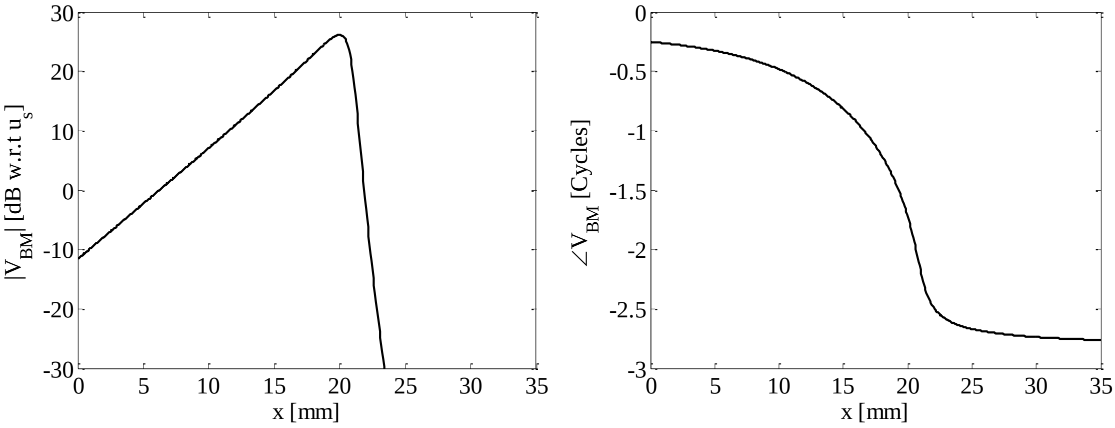

(a) (b)

Figure 6.3 The distribution of the (a) magnitude and (b) phase of the BM velocity along the cochlea, at an excitation frequency of 1 kHz, calculated using the WKB method for the wavenumber calculated analytically due to the interaction between the local, passive, BM dynamics and the 1D fluid coupling.

6.3 Local BM Dynamics and 3D Fluid Coupling

The fluid pressure due to the BM motion can be divided into two components: one due to the far-field of the source, involving 1D plane acoustic waves, and one due to the near-field, involving 3D evanescent higher order modes (Elliott, *et al.*, 2011). The 1D fluid coupling is described in the spatial domain by equation (6.3) but it is convenient to express the combined effect of the far and near-field using a wavenumber formulation (de Boer and Viergever, 1984, Elliott, *et al.*, 2011, Steele and Taber, 1979). The complex pressure difference in a uniform cochlea due to a velocity distribution that is spatially varying with a sinusoidal waveform having a wavenumber *k* can be expressed in terms of the fluid coupling impedance as equation (2.21).

The variation of Z_{FC} with *k* can be approximated with various polynomial functions of *k*. For example de Boer (de Boer, 1998) gave both fourth and sixth order polynomial approximations, and the former will be considered here. This can be written as

$$Z_{\mathrm{FC}}(k) = \frac{2i\omega\rho}{k^2 h}\left(\frac{1+ak^2}{1+bk^2}\right), \tag{6.24}$$

where h is again the effective height of the fluid chamber and a and b are fitted parameters, which in this case are a=5.5 ×10^{-7} m^2 and b=1×10^{-8} m^2. de Boer (de Boer, 1998) emphasised the need for $Z_{\mathrm{FC}}(k)$ to be an even function of k in order to obtain consistent solutions for forward and travelling waves. Figure 6.4 shows the exact and approximate values of $Z_{\mathrm{FC}}(k)$, together with the corresponding pressure distributions when excited at x = 10 mm, calculated as in Elliott *et al.* (Elliott, *et al.*, 2011). The approximation is seen to reproduce the main features of the exact formulation.

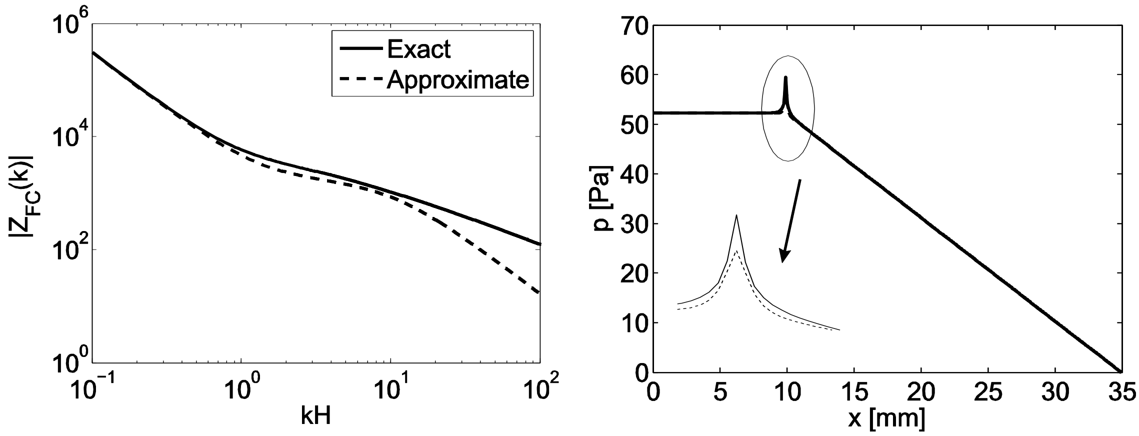

(a) (b)

Figure 6.4 The wavenumber distribution of (a) the fluid coupling for the exact expression, equation (2.22) and the approximation in equation (6.24), together with the resulting spatial distributions of (b) the pressure when the cochlea is excited at x=10 mm at 1 kHz.

If the BM again responds locally, so that its velocity only depends on the pressure difference at the same point, then in a wavenumber analysis its admittance does not depend on wavenumber, so we can write

$$V(k) = \frac{-P(k)}{Z_{\mathrm{BM}}}, \tag{6.25}$$

Substituting this and equation (6.24) for $Z_{\mathrm{FC}}(k)$ into equation (2.21) gives

$$k^2 h Z_{\mathrm{BM}} P(k) = -2i\omega\rho \left(\frac{1+ak^2}{1+bk^2} \right) P(k), \tag{6.26}$$

so that the dispersion equation can be written as

$$bhZ_{\mathrm{BM}} k^4 + \left(hZ_{\mathrm{BM}} + 2ai\omega\rho \right) k^2 + 2i\omega\rho = 0. \tag{6.27}$$

This is now a quadratic equation in k^2 and if we write $1/k^2$ as α it becomes

$$\frac{2i\omega\rho}{hZ_{\mathrm{BM}}} \alpha^2 + \left(1 + \frac{2ia\omega\rho}{hZ_{\mathrm{BM}}} \right) \alpha + b = 0, \tag{6.28}$$

so that

$$\alpha = \frac{-\left(1 + \dfrac{2ia\omega\rho}{hZ_{\mathrm{BM}}} \right) \pm \sqrt{\left(1 + \dfrac{2ia\omega\rho}{hZ_{\mathrm{BM}}} \right)^2 - \dfrac{8ib\omega\rho}{hZ_{\mathrm{BM}}}}}{\dfrac{4i\omega\rho}{hZ_{\mathrm{BM}}}}. \tag{6.29}$$

If a and b are small compared with $hZ_{\mathrm{BM}}/2i\omega\rho$, so that $2i\omega\rho/hZ_{\mathrm{BM}}$ is small compared with $1/a$ and $1/b$, then the two solutions for α correspond to the wavenumbers

$$k \approx \pm \sqrt{\frac{-2i\omega\rho}{hZ_{\mathrm{BM}}}} \quad \text{or} \quad \pm i\sqrt{\frac{1}{b}}. \qquad (6.30)(6.31)$$

The first pair of solutions for the wavenumber, in equation (6.30), corresponds to the slow wave in Section 6.2, generated by the interaction of the far-field fluid coupling and the local BM dynamics. The second pair, in equation (6.31), corresponds to an evanescent wave with length scale $\sqrt{b}$. The definition of $Z_{\mathrm{FC}}(k)$ and its approximation, in equations (2.21) and (6.24), can be used to derive the equation below relating $P(k)$ and $V(k)$

$$P(k) k^2 h \left(1 + bk^2 \right) = 2i\omega\rho \left(1 + ak^2 \right) V(k). \tag{6.32}$$

If the BM were rigid, so that $V(k)$ is equal to zero, then either $P(k)$ is also zero, or k is zero, corresponding to a fast wave of infinite speed in the incompressible fluid, or k is equal to $\pm i\sqrt{1/b}$, as above. This evanescent wave can thus exist in the fluid alone, in the absence of any flexibility of the BM, and can be interpreted as the evanescent higher order acoustic mode with a length scale of $\sqrt{b}$.

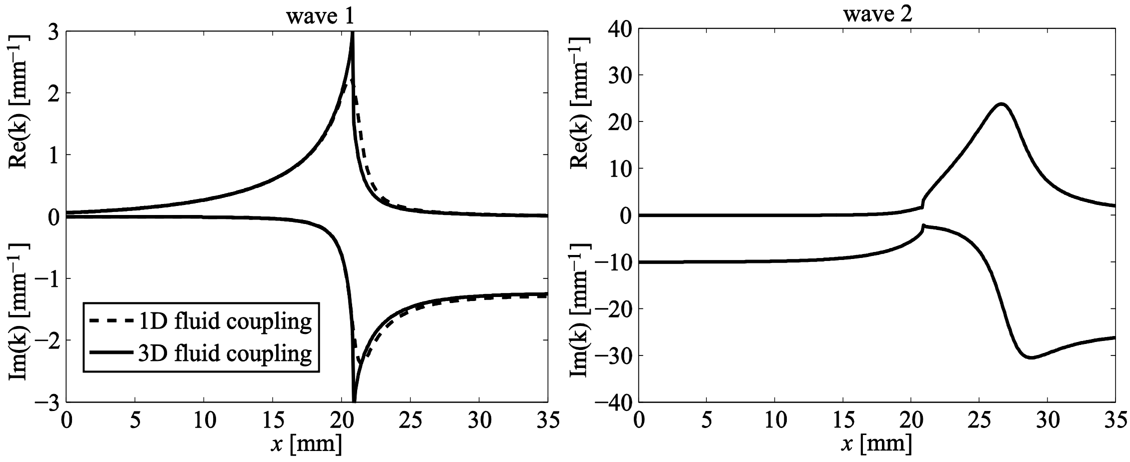

(a) (b)

Figure 6.5 The distribution along the cochlea of the wavenumber of (a) wave 1 and (b) wave 2, at an excitation frequency of 1 kHz, for the forward-going waves due to the interaction between the local passive BM dynamics and an approximation to 3D fluid coupling with a constant damping ratio, ζ_0=0.1. Also shown, dashed line, is the distribution of wave 1 from the analysis of 1D fluid coupling.

The wavenumber distributions of the forward travelling waves, calculated by solving equation (6.27), are shown in Figure 6.5. A similar approach to that used above was used by de La Rouchefoucauld and Olson (de La Rochefoucauld and Olson, 2007) to obtain the wavenumber distribution that they used to estimate BM mass and stiffness distributions from measured BM velocity frequency responses. Those authors, however, used an earlier approximation for $Z_{FC}(k)$ given by de Boer and Viergever (de Boer and Viergever, 1982), which involved odd powers of k and hence was not symmetrical for positive and negative values of k. The wavenumber distributions for the first wave are very similar to those for the 1D fluid coupling, also shown in Figure 6.5. The magnitude of this wavenumber is generally much smaller than the imaginary part of the second wave shown in Figure 6.5, indicating that the approximation leading to equations (6.30) and (6.31) is a reasonable one. This is confirmed when the magnitude of the imaginary part of the second wave, -10 mm^{-1} near the base, is compared with the predicted value from equation (6.31) with b equal to 10^{-8} m^2,which is also -10 mm^{-1}.

The BM velocity distributions corresponding to these wavenumber distributions, calculated using the WKB method, are shown in Figure 6.6. The WKB solution for the BM velocity is slightly modified in this case, since $v(x)$ and $p(x)$ are no longer related by equation (6.19) as they were in Section 6.2. In this case equation (6.24) governs the ratio of $p(x)$ to $v(x)$, for a given wavenumber, and so again assuming a solution of the form of equation (6.17) for $p(x)$, the BM velocity distribution is given by

$$v(x) = \frac{Ah}{2i\omega\rho} k^{3/2}(x) \left(\frac{1 + bk^2(x)}{1 + ak^2(x)} \right) e^{-i\phi(x)}. \tag{6.33}$$

The calculation of the wave amplitude, A, as a function of the stapes velocity also has to be slightly modified in this case, i.e.

$$A = \frac{2\omega\rho u_s \left[1 + ak^2(0) \right]}{\sqrt{k(0)} \left[1 + bk^2(0) \right]}. \tag{6.34}$$

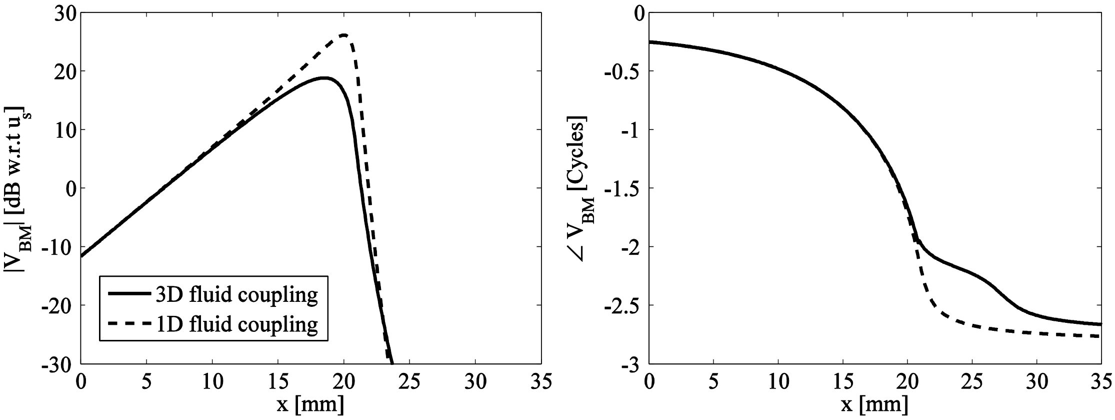

(a) (b)

Figure 6.6 The distribution of the (a) magnitude and (b) phase of the BM velocity along the cochlea, at an excitation frequency of 1 kHz, for the wave due to the interaction between the local, passive, BM dynamics and the 3D fluid coupling (solid lines) and 1D fluid coupling (dashed lines).

The BM velocity distributions for the slow wave are similar to those in Figure 6.3, from the 1D analysis, as is expected since their wavenumber distributions are also similar. It is interesting to note, however, that there is a difference of perhaps 8 dB in the peak value of the BM velocity between the 1D and 3D predictions when using the approximation to $Z_{FC}(k)$ given by equation (6.24), whereas when these distributions are calculated using the full fluid coupling equation (2.19), the 1D and 3D cases are more similar, as shown in Figure 2.7. The BM velocities for the second wave fall off very rapidly, due to the large negative value of the imaginary part of its wavenumber, indicating an exponential decay length scale of about 0.1 mm.

6.4 Longitudinal BM Dynamics and 1D Fluid Coupling

Longitudinal coupling in the BM is modelled here using an orthotropic plate model (Allen and Sondhi, 1979, Liu and White, 2008, Meaud and Grosh, 2010, Steele and Taber, 1979). The governing equation for the BM can then be written (Meaud and Grosh, 2010) as

$$\begin{aligned} p(x,y) = -\left[-\omega^2 m(x) + i\omega r(x)\right] w(x,y) - \Bigg[\frac{\partial^2}{\partial x^2}\left(D_x \frac{\partial^2 w(x,y)}{\partial x^2} + D_{xy} \frac{\partial^2 w(x,y)}{\partial y^2} \right) \\ + 4\frac{\partial^2}{\partial x \partial y}\left(D_s \frac{\partial^2 w(x,y)}{\partial x \partial y} \right) + \frac{\partial^2}{\partial y^2}\left(D_y \frac{\partial^2 w(x,y)}{\partial y^2} + D_{xy} \frac{\partial^2 w(x,y)}{\partial x^2} \right) \Bigg], \end{aligned} \tag{6.35}$$

where $p(x,y)$ is the complex pressure distribution acting on the BM, $w(x,y)$ is its complex displacement upwards, hence the negative sign as in equation (6.4), which each depend on both *x* and *y*. The parameters $m(x)$ and $r(x)$ are the mass per unit area and damping per unit area, as in Section 6.2, D_x, D_{xy} and D_y are the orthotropic bending stiffness in the *x*, *xy* and *y* directions, respectively, and D_s is torsional rigidity.

Defining the origin of the *y* axis along the centre of the BM, we now assume, again following Meaud and Grosh (Meaud and Grosh, 2010), that the BM vibrates as a single mode, such that its displacement is equal to

$$w(x,y) = \frac{v(x)}{i\omega} \sin\left(\frac{\pi y}{B}\right) \text{ for } 0 \le y \le B, \tag{6.36}$$

where *B* is the BM width, taken here as 0.3 mm, and $v(x)$ is the complex modal velocity (Elliott, *et al.*, 2011).

We also define the modal pressure difference as

$$p(x)=\frac{2}{B}\int_0^B p(x,y)\sin\left(\frac{\pi y}{B}\right)dy. \tag{6.37}$$

These assumptions, together with the assumption that the longitudinal variation of *B* and those of the orthotropic stiffness properties, apart from D_y, can be neglected, then simplifies the governing equation for the BM to

$$\begin{aligned}p(x)&=-\left[i\omega m(x)+r(x)\right]v(x)\\&-\frac{1}{i\omega}\left[D_x\frac{\partial^4 v(x)}{\partial x^4}-2\left(D_{xy}+2D_s\right)\left(\frac{\pi}{B}\right)^2\frac{\partial^2 v(x)}{\partial x^2}+D_y\left(\frac{\pi}{B}\right)^4 v(x)\right].\end{aligned} \tag{6.38}$$

If the longitudinal coupling in the plate is ignored, by setting D_x, D_{xy} and D_s to zero, equation (6.38) reduces to that for the locally acting BM dynamics in equation (6.8), with a local stiffness, $s(x)$, of $D_y(\pi/B)^4$. The variation of $s(x)$ with *x* in equation (6.10) is then used to define the longitudinal variation of D_y. So that, assuming *B* is equal to 0.3 mm, D_y has a value of 3.9×10^{-7} N m at the base and 20 mm along the cochlea has a value of 1.3×10^{-9} N m. The values of D_x, D_{xy} and D_s all along the cochlea are initially assumed to be the same all along the cochlea and equal to (Meaud and Grosh, 2010) 6.5×10^{-11} N m, 3.1×10^{-11} N m, and 4.3×10^{-11} N m. The ratio of longitudinal to radial stiffness, D_x/D_y, at the base is thus about 1.7×10^{-4} and it is about 0.05 when 20 mm along the cochlea, so the longitudinal coupling is weak.

If the local variation of $v(x)$ is proportional to e^{-ikx}, then we can write equation (6.38) as

$$P(k)=-\left\{\left(i\omega m_0+\frac{s(x)}{i\omega}+r(x)\right)+\frac{1}{i\omega}\left[D_x k^4+2\left(D_{xy}+2D_s\right)\left(\frac{\pi}{B}\right)^2 k^2\right]\right\}V(k), \tag{6.39}$$

where the term in the outer brackets can be defined to be $Z_{\mathrm{BM}}(k)$, by analogy with equation (6.4). The fluid coupling can also be quantified in general by writing

$$P(k)=Z_{\mathrm{FC}}(k)V(k), \tag{6.40}$$

where for 1D fluid coupling, equation (6.3) can be used to show that

$$Z_{\mathrm{FC}}^{1D}\left(k\right)=\frac{2i\omega\rho}{k^{2}h}. \tag{6.41}$$

In general the dispersion equation can thus be written as

$$Z_{\mathrm{BM}}\left(x\right)+Z_{\mathrm{FC}}\left(k\right)=0. \tag{6.42}$$

For the passive BM, modelled as an orthotropic plate, and 1D fluid coupling, the dispersion equation is thus

$$\frac{D_x}{i\omega}k^6+\frac{2\left(D_{xy}+2D_s\right)}{i\omega}\left(\frac{\pi}{B}\right)^2 k^4+Z_{\mathrm{BM}}k^2+\frac{2i\omega\rho}{h}=0, \tag{6.43}$$

where Z_{BM} is the locally reacting BM impedance given by equation (6.8) with $s(x)$ equal to $D_y(\pi/B)^4$, and the mass and damping as in Table 2.1.

There are thus 6 solutions for the wavenumber, corresponding to 3 waves propagating in each direction, whose wavenumbers are shown in Figure 6.7 for the passive BM, modelled as an orthotropic plate with the constants above and the other parameters taken from Section 6.2. It can be seen that the difference between the orthotropic model (longitudinal BM dynamics) and the isotropic model (local BM dynamics) can hardly be distinguished in this scale.

If k is assumed to be small, so that the first two terms in equation (6.43) are small compared with the second two terms, then the solution to this dispersion equation is almost the same as equation (6.7), for the conventional slow wave. The two additional waves in Figure 6.7 are presumably due to the interaction between the local BM dynamics and the orthotropic bending stiffness. In fact if we assume that k is large, so that fluid coupling is not important, and additionally assume that the torsional stiffness does not play an important role but that Z_{BM} is dominated by its stiffness, then we obtain

$$k^4=-\frac{s\left(x\right)}{D_x}, \tag{6.44}$$

so that

$$k = \left(\pm 1 \pm i\right)\sqrt[4]{\frac{s(x)}{D_x}}. \tag{6.45}$$

The forward-going waves are assumed to be the ones for which the wavenumber has negative imaginary components, and so the real part could either be positive, as in the second wave, or negative, as in the third wave.

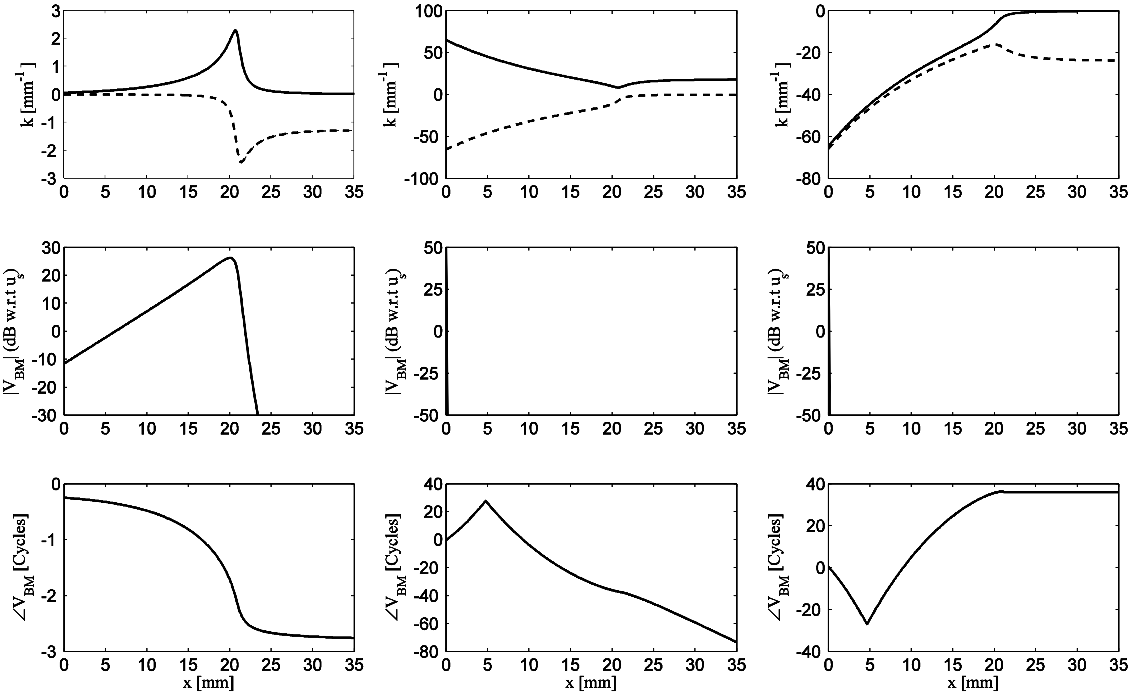

Figure 6.7 The distributions of the real and imaginary parts of the wavenumbers, the BM velocity and the BM phase along the cochlea, calculated using the WKB method, at an excitation frequency of 1 kHz, for the passive cochlear model using an orthotropic plate model for forward-going waves with the BM having constant orthotropic components and damping ratio, ζ_0=0.1. Also shown, dashed lines, is the wavenumber distribution for the first wave obtained from the locally reacting BM with 1D fluid coupling shown in Figure 6.2.

Near the base, the second and third waves correspond thus closely to solutions of this equation for large k, with real and imaginary parts that are either equal or of opposite sign and decrease with x, since D_x is constant and $s(x)$ is decreasing exponentially. The cut-off effect that occurs at about 20 mm for the second wave is reminiscent of that of a thin plate when simply supported at the edges. It is interesting to note that beyond this point the second wave is predicted to propagate with little attenuation.

Figure 6.7 also shows the WKB reconstruction of the BM velocity distribution assuming that each of these waves exists in isolation. The reconstruction of the first wave is similar to that in Section 6.2, as expected. The velocity distributions for the other two waves fall off very rapidly with position, because of the large negative imaginary component of the wavenumber at the base, although it is not clear why the phase apparently peaks about 5 mm along the cochlea. It is interesting to note that the imaginary part of the wavenumber for the second wave is only of the order of -0.8 mm^{-1} near the apex. If this wave was excited at this position, by bone conduction for example, it would decay significantly less slowly than for the case where the excitation is at the base, as shown in Figure 6.7.

In order to account for the longitudinal variations of those orthotropic stiffness properties, we assume that the values of D_x, D_{xy} and D_s are, like D_y, proportional to $e^{-2x/l}$, where l is the natural frequency length scale, 7 mm, and x is the position in the cochlear longitudinal direction. By defining $D_x = D_{x0}e^{-2x/l}$, $D_{xy} = D_{xy0}e^{-2x/l}$, $D_y = D_{y0}e^{-2x/l}$ and $D_s = D_{s0}e^{-2x/l}$, equation (6.35) can be written, in this case, as

$$p(x,y) = -\left[-\omega^2 m(x) + i\omega r(x)\right] w(x,y) - \left[\frac{\partial^2}{\partial x^2}\left(D_{x0}e^{-2x/l}\frac{\partial^2 w(x,y)}{\partial x^2} + D_{xy0}e^{-2x/l}\frac{\partial^2 w(x,y)}{\partial y^2}\right)\right.$$
$$\left. + 4\frac{\partial^2}{\partial x \partial y}\left(D_{s0}e^{-2x/l}\frac{\partial^2 w(x,y)}{\partial x \partial y}\right) + \frac{\partial^2}{\partial y^2}\left(D_{y0}e^{-2x/l}\frac{\partial^2 w(x,y)}{\partial y^2} + D_{xy0}e^{-2x/l}\frac{\partial^2 w(x,y)}{\partial x^2}\right)\right]. \tag{6.46}$$

Again, by defining a modal velocity, equation (6.36), and a modal pressure difference, equation (6.37), equation (6.46) can be reduced assuming a longitudinal variation proportional to e^{-ikx},

$$P(k) = -\left\{\left(i\omega m_0 + \frac{s(x)}{i\omega} + r(x)\right) + \frac{e^{-2x/l}}{i\omega}\left[D_{x0}k^4 - \frac{4i}{l}D_{x0}k^3 + 2\left(\frac{2}{l^2}D_{x0} + \left(\frac{\pi}{B}\right)^2\left(D_{xy0} + 2D_{s0}\right)\right)k^2\right.\right.$$
$$\left.\left. - \frac{4i}{l}\left(D_{xy0} + 2D_{s0}\right)\left(\frac{\pi}{B}\right)^2 k\right]\right\}V(k). \tag{6.47}$$

Recalling equation (6.42), dispersion equation can be given by

$$\begin{aligned} & k^6 - \frac{4i}{l}k^5 + 2\left(\frac{2}{l^2} + \left(\frac{\pi}{B}\right)^2\left(\frac{D_{xy0}}{D_{x0}} + \frac{2D_{s0}}{D_{x0}}\right)\right)k^4 \\ & -\frac{4i}{lD_{x0}}\left(D_{xy0} + 2D_{s0}\right)\left(\frac{\pi}{B}\right)^2 k^3 + \frac{i\omega Z_{BM}}{D_{x0}e^{-2x/l}}k^2 - \frac{2\rho\omega^2}{hD_{x0}e^{-2x/l}} = 0, \end{aligned} \tag{6.48}$$

where D_{y0} and D_{x0}, denote values at the base, taken here as 3.9×10^{-7} N m and 1.9×10^{-8} N m, so that D_x/D_y is equal to 5 × 10^{-2} all along the cochlea. The parameters D_{xy} and D_s are now defined as a function of D_y and are taken here as 5.9×10^{-9} N m, and 5.8 × 10^{-9} N m at the base.

The ratio of longitudinal to radial stiffness, D_x/D_y, determines the extent of the longitudinal static deflection on the BM compared with its radial deflection (Liu and White, 2008). Although these deflections were measured in cadaverous human BM by von Békésy (von Békésy, 1960), Voldřich (Voldřich, 1978) pointed out that the extent of the longitudinal is significantly smaller in fresh preparations. Liu and White (Liu and White, 2008) define an orthotropy ratio as E_y/E_x and show that in the gerbil this varies from about 60 at the base to about 10 towards the apex, suggesting that a reasonable value for D_x/D_y is perhaps 2% at the base and 10% at the apex. This range of values is very much less than the range of D_y along the cochlea, which here is about 2×10^4, to account for the range of natural frequencies. A constant ratio of D_x/D_y thus appears to be a reasonable model, and a numerical value of 5% has been chosen for the calculations here.

Figure 6.8 shows the wavenumber distributions calculated by solving this dispersion equation and the corresponding WKB reconstructions of the BM velocity distribution for the lightly damped and normally damped cases. The first wave again corresponds to the slow wave and has characteristics that are similar to those if the BM is only locally reacting. The two other waves again have large negative imaginary wavenumbers near the base, although these are now constant with position, implying that they are again dependent on an interaction between the different components of the bending stiffness, as in equation (6.44), but now these two components vary in proportion to each other so that their ratio is constant.

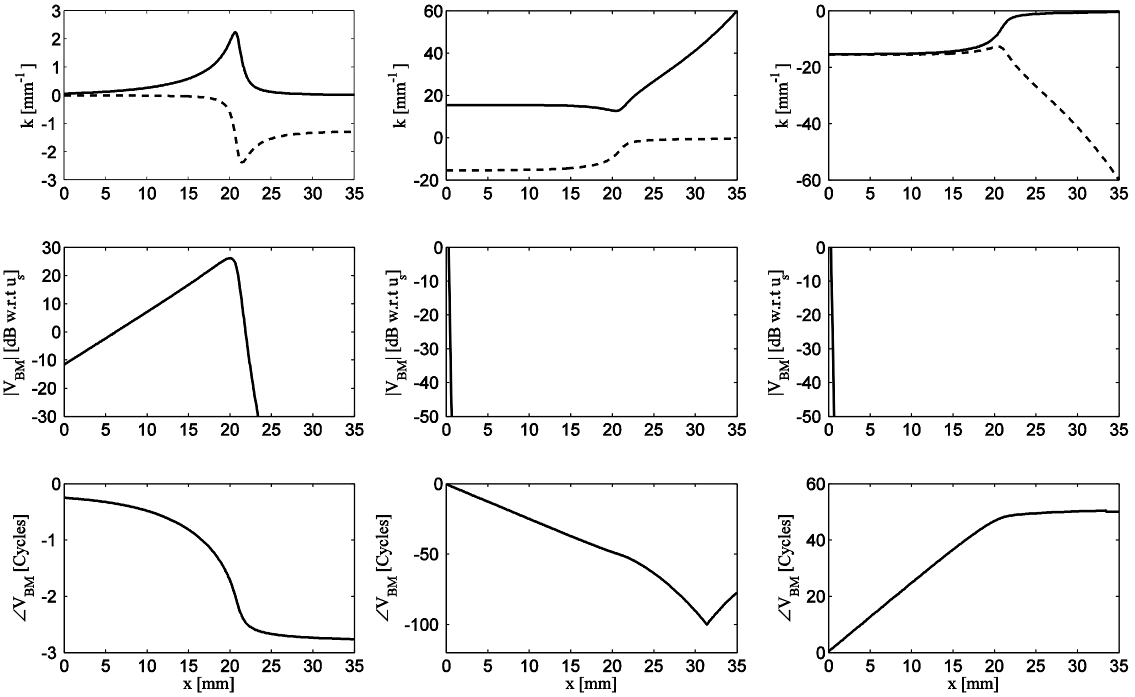

Figure 6.8 The distributions of the real and imaginary parts of the wavenumbers, the BM velocity and the BM phase along the cochlea, calculated using the WKB method, at an excitation frequency of 1 kHz, for the passive cochlear model using an orthotropic plate model (bold lines) and an isotropic plate model (faint lines) for forward-going waves with BM having longitudinally varying orthotropic components, such that D_x/D_y=0.05, and damping, ζ_0=0.1.

6.5 Discrete Model of the Cochlea

A discrete model of the cochlea is briefly described in this section, which can also be used to numerically compute its coupled response. The discrete model is simpler than the full FE model, since the fluid coupling and BM dynamics are analysed separately before being combined in a coupled matrix solution (Elliott, *et al.*, 2011). It is therefore interesting to investigate the extent to which this model could be used to test the assumption that only a single wave propagates in the cochlea. The BM velocity distribution that is predicted from this coupled analysis is compared with the WKB solution for the main forward travelling wave using the analytic wavenumbers discussed in Sections 6.2, 6.3 and 6.4.

There are approximations involved in both the WKB approximation and in the discrete model. If, however, these two methods produce similar results, taking only the dominant wave into account in the WKB solution, this would suggest that the extra wave types due to additional longitudinal BM coupling do not play a significant role in normal passive cochlear function.

The near-field component of the fluid coupling for the discrete model is calculated, as described by Elliott *et al.* (Elliott, *et al.*, 2011), by taking the inverse Fourier transform of the wavenumber transfer for the velocity of a single BM element, multiplied by the near-field component of the fluid coupling impedance in the wavenumber domain. This near-field component is defined to be the total fluid coupling impedance, $Z_{\mathrm{FC}}(k)$, minus that due to far-field coupling, $Z_{\mathrm{F}}(k)$, so that

$$Z_{\mathrm{N}}(k) = Z_{\mathrm{FC}}(k) - Z_{\mathrm{F}}(k), \tag{6.49}$$

where

$$Z_{\mathrm{F}}(k) = \frac{2i\omega\rho}{k^2 h}. \tag{6.50}$$

In the present case, where $Z_{\mathrm{FC}}(k)$ is assumed to be given by equation (6.24), $Z_{\mathrm{N}}(k)$ is given by

$$Z_{\mathrm{N}}(k) = \frac{2i\omega\rho(a-b)}{(1+bk^2)h}. \tag{6.51}$$

Figure 6.9 shows a comparison of the results from the 1D discrete model and the WKB reconstruction of the 1D model, in Figure 6.3, calculated at 1 kHz with a damping ratio of 0.1. Figure 6.10 shows a comparison of the results from the 3D discrete model and the WKB reconstruction of the 3D model, shown in Figure 6.6, at 1 kHz with a damping ratio of 0.1. Figure 6.11 shows a comparison of the results from the 1D discrete model and the WKB reconstruction of the longitudinal BM coupling model, shown in Figure 6.8, at 1 kHz with a damping ratio of 0.1.

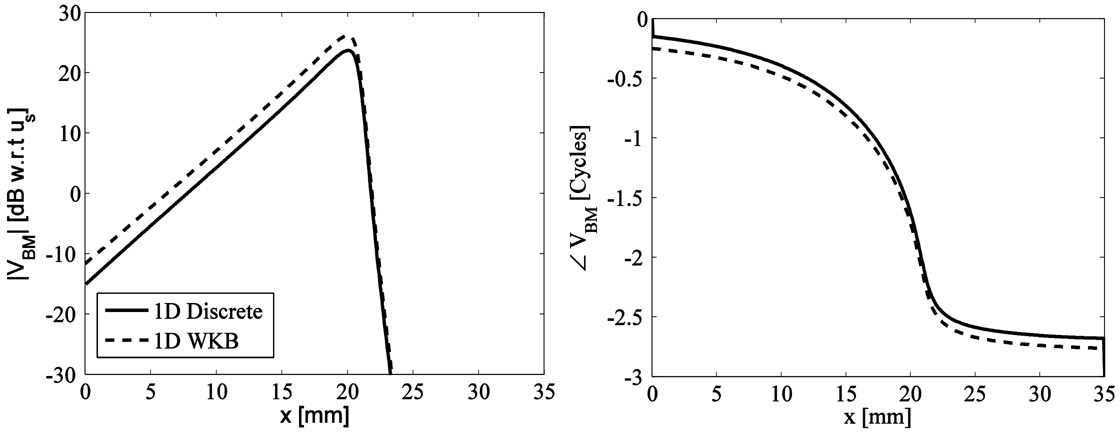

Figure 6.9 Comparison of the results from the discrete model (solid lines) and the WKB reconstruction of the 1D model (dashed lines) shown in Figure 6.3 at 1 kHz with a damping ratio of 0.1.

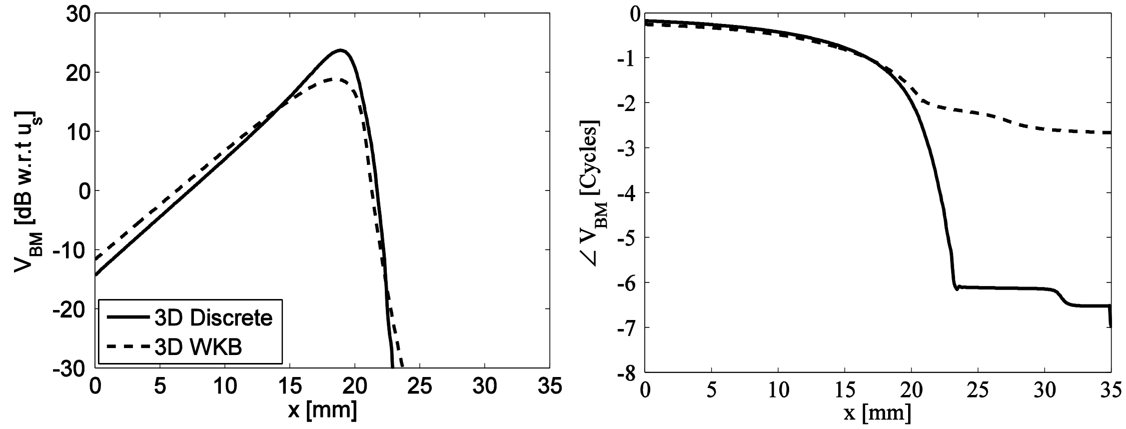

Figure 6.10 Comparison of the results from the discrete model (solid lines) and the WKB reconstruction of the 3D model (dashed lines) shown in Figure 6.6 at 1 kHz with a damping ratio of 0.1.

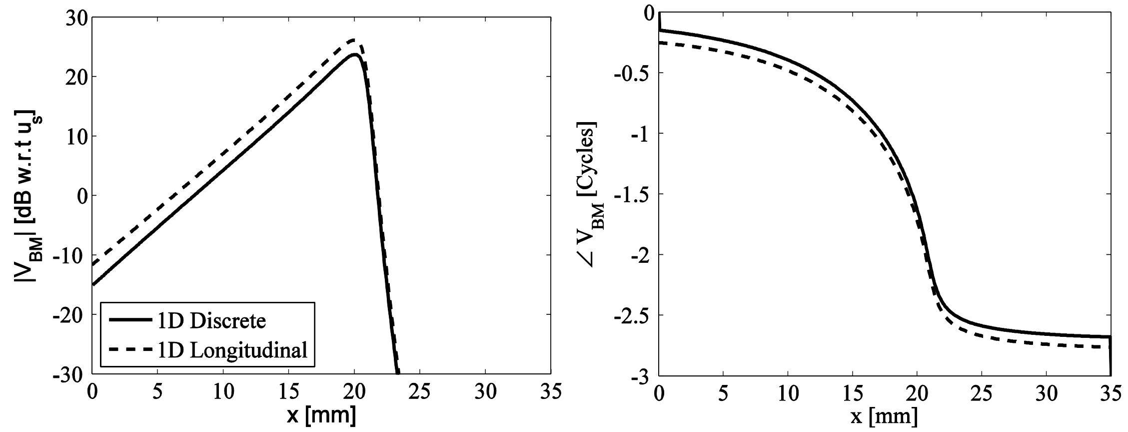

Figure 6.11 Comparison of the results from the discrete model (solid lines) and the WKB reconstruction of the longitudinal BM coupling model (dashed lines) shown in Figure 6.8 at 1 kHz with a damping ratio of 0.1.

6.6 Wave Decomposition with Local BM Dynamics

6.6.1 Wave Finite Element Model

A method of identifying the various waves that can propagate in the cochlea is to use wave finite elements (Duhamel, *et al.*, 2006, Mace, *et al.*, 2005). In this approach a finite element model is constructed of the structural and fluid components of an elemental segment of a discrete model of the cochlea, as shown in Figure 6.12. This is first used to describe all the complex forces, at a given excitation frequency, as a function of all the complex displacements multiplied by the corresponding dynamic stiffness. The vector of these forces and displacements is then partitioned into those on the left and right hand side of the *n*-th segment in the discrete model, so that

$$\begin{bmatrix} \mathbf{f}_{\mathrm{L}}(n) \\ \mathbf{f}_{\mathrm{R}}(n) \end{bmatrix} = \begin{bmatrix} \mathbf{D}_{\mathrm{LL}}(n) & \mathbf{D}_{\mathrm{LR}}(n) \\ \mathbf{D}_{\mathrm{RL}}(n) & \mathbf{D}_{\mathrm{RR}}(n) \end{bmatrix} \begin{bmatrix} \mathbf{q}_{\mathrm{L}}(n) \\ \mathbf{q}_{\mathrm{R}}(n) \end{bmatrix}, \tag{6.52}$$

where the square matrix is the dynamic stiffness matrix. Any forces and displacements due to internal degrees of freedom in the finite element model of the elemental segment can be incorporated into this a generalised definition of the elements $\mathbf{D}_{\mathrm{LL}}$, $\mathbf{D}_{\mathrm{LR}}$, $\mathbf{D}_{\mathrm{RL}}$ and $\mathbf{D}_{\mathrm{RR}}$, as described by Mace *et al*. (Mace, *et al.*, 2005).

In particular for the WFE model of the cochlea with local BM dynamics, the DOFs associated with the BM are condensed (Mace, *et al.*, 2005) since they are only vibrating locally and there is no longitudinal coupling, so there is no force between two adjacent segments. When decomposing the BM velocity into wave components, the DOFs associated with the BM need to be recovered from the condensed ones. The equation of motion of the cochlear system can be written as

$$\begin{bmatrix} \mathbf{M} & \mathbf{0} \\ \rho_f \mathbf{R} & \mathbf{Q} \end{bmatrix} \begin{Bmatrix} \ddot{\mathbf{w}} \\ \ddot{\mathbf{p}} \end{Bmatrix} + \begin{bmatrix} \mathbf{K} & -\mathbf{S} \\ \mathbf{0} & \mathbf{H} \end{bmatrix} \begin{Bmatrix} \mathbf{w} \\ \mathbf{p} \end{Bmatrix} = \begin{bmatrix} \mathbf{0} \\ \mathbf{q} \end{bmatrix}, \tag{6.53}$$

where **w** represents the DOFs associated with the BM, **p** represents the pressure vector of the fluid and **q** is the vector of external volume velocities acting on this segment of the FE model.

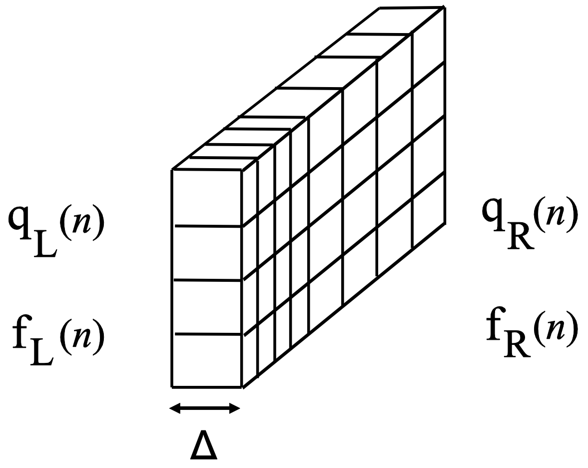

Figure 6.12 An elemental segment of the cochlea used in the wave finite element method showing the forces and displacement on the left hand and right hand side of this element. The internal structure of the cochlea is not shown.

For time harmonic vibration, partitioning matrices into the left and right hand sides gives

$$\left(\begin{bmatrix} \mathbf{K}_{\mathrm{LL}} & -\mathbf{S}_{\mathrm{LL}} & \mathbf{K}_{\mathrm{LR}} & -\mathbf{S}_{\mathrm{LR}} \\ \mathbf{0} & \mathbf{H}_{\mathrm{LL}} & \mathbf{0} & \mathbf{H}_{\mathrm{LR}} \\ \mathbf{K}_{\mathrm{RL}} & -\mathbf{S}_{\mathrm{RL}} & \mathbf{K}_{\mathrm{RR}} & -\mathbf{S}_{\mathrm{RR}} \\ \mathbf{0} & \mathbf{H}_{\mathrm{RL}} & \mathbf{0} & \mathbf{H}_{\mathrm{RR}} \end{bmatrix} - \omega^2 \begin{bmatrix} \mathbf{M}_{\mathrm{LL}} & \mathbf{0} & \mathbf{M}_{\mathrm{LR}} & \mathbf{0} \\ \rho_f \mathbf{R}_{\mathrm{LL}} & \mathbf{Q}_{\mathrm{LL}} & \rho_f \mathbf{R}_{\mathrm{LR}} & \mathbf{Q}_{\mathrm{LR}} \\ \mathbf{M}_{\mathrm{RL}} & \mathbf{0} & \mathbf{M}_{\mathrm{RR}} & \mathbf{0} \\ \rho_f \mathbf{R}_{\mathrm{RL}} & \mathbf{Q}_{\mathrm{RL}} & \rho_f \mathbf{R}_{\mathrm{RR}} & \mathbf{Q}_{\mathrm{RR}} \end{bmatrix}\right) \begin{bmatrix} \mathbf{w}_{\mathrm{L}} \\ \mathbf{p}_{\mathrm{L}} \\ \mathbf{w}_{\mathrm{R}} \\ \mathbf{p}_{\mathrm{R}} \end{bmatrix} = \begin{bmatrix} \mathbf{0} \\ \mathbf{q}_{\mathrm{L}} \\ \mathbf{0} \\ \mathbf{q}_{\mathrm{R}} \end{bmatrix}. \tag{6.54}$$

Since the DOFs associated with the BM, $\mathbf{w}_{\mathrm{L}}$ and $\mathbf{w}_{\mathrm{R}}$, are taken as internal DOFs, equation (6.54) can be rearranged into the form below

$$\left(\begin{bmatrix} \mathbf{H}_{\mathrm{LL}} & \mathbf{H}_{\mathrm{LR}} & \mathbf{0} & \mathbf{0} \\ \mathbf{H}_{\mathrm{RL}} & \mathbf{H}_{\mathrm{RR}} & \mathbf{0} & \mathbf{0} \\ -\mathbf{S}_{\mathrm{LL}} & -\mathbf{S}_{\mathrm{LR}} & \mathbf{K}_{\mathrm{LL}} & \mathbf{K}_{\mathrm{LR}} \\ -\mathbf{S}_{\mathrm{RL}} & -\mathbf{S}_{\mathrm{RR}} & \mathbf{K}_{\mathrm{RL}} & \mathbf{K}_{\mathrm{RR}} \end{bmatrix} - \omega^2 \begin{bmatrix} \mathbf{Q}_{\mathrm{LL}} & \mathbf{Q}_{\mathrm{LR}} & \rho_f \mathbf{R}_{\mathrm{LL}} & \rho_f \mathbf{R}_{\mathrm{LR}} \\ \mathbf{Q}_{\mathrm{RL}} & \mathbf{Q}_{\mathrm{RR}} & \rho_f \mathbf{R}_{\mathrm{RL}} & \rho_f \mathbf{R}_{\mathrm{RR}} \\ \mathbf{0} & \mathbf{0} & \mathbf{M}_{\mathrm{LL}} & \mathbf{M}_{\mathrm{LR}} \\ \mathbf{0} & \mathbf{0} & \mathbf{M}_{\mathrm{RL}} & \mathbf{M}_{\mathrm{RR}} \end{bmatrix}\right) \begin{bmatrix} \mathbf{p}_{\mathrm{L}} \\ \mathbf{p}_{\mathrm{R}} \\ \mathbf{w}_{\mathrm{L}} \\ \mathbf{w}_{\mathrm{R}} \end{bmatrix} = \begin{bmatrix} \mathbf{q}_{\mathrm{L}} \\ \mathbf{q}_{\mathrm{R}} \\ \mathbf{0} \\ \mathbf{0} \end{bmatrix}. \tag{6.55}$$

Equation (6.55) can also be written in terms of an uncondensed dynamic stiffness matrix, with $\mathbf{w}_{\mathrm{L}}$ and $\mathbf{w}_{\mathrm{R}}$ included as a single vector $\mathbf{w}$, as

$$\begin{bmatrix} \tilde{\mathbf{D}}_{\mathrm{LL}} & \tilde{\mathbf{D}}_{\mathrm{LR}} & \tilde{\mathbf{D}}_{\mathrm{LI}} \\ \tilde{\mathbf{D}}_{\mathrm{RL}} & \tilde{\mathbf{D}}_{\mathrm{RR}} & \tilde{\mathbf{D}}_{\mathrm{RI}} \\ \tilde{\mathbf{D}}_{\mathrm{IL}} & \tilde{\mathbf{D}}_{\mathrm{IR}} & \tilde{\mathbf{D}}_{\mathrm{II}} \end{bmatrix} \begin{bmatrix} \mathbf{p}_{\mathrm{L}} \\ \mathbf{p}_{\mathrm{R}} \\ \mathbf{w} \end{bmatrix} = \begin{bmatrix} \mathbf{q}_{\mathrm{L}} \\ \mathbf{q}_{\mathrm{R}} \\ \mathbf{0} \end{bmatrix}, \tag{6.56}$$

where the superscript ‘ ~ ’ denotes this dynamic stiffness matrix contains internal DOFs without condensation and

$$\begin{aligned}
&\tilde{\mathbf{D}}_{\mathrm{LL}} = \mathbf{H}_{\mathrm{LL}} - \omega^2\mathbf{Q}_{\mathrm{LL}}, \quad \tilde{\mathbf{D}}_{\mathrm{LR}} = \mathbf{H}_{\mathrm{LR}} - \omega^2\mathbf{Q}_{\mathrm{LR}}, \\
&\tilde{\mathbf{D}}_{\mathrm{LI}} = -\omega^2\rho_f\left(\mathbf{R}_{\mathrm{LL}} + \mathbf{R}_{\mathrm{LR}}\right), \quad \tilde{\mathbf{D}}_{\mathrm{RL}} = \mathbf{H}_{\mathrm{RL}} - \omega^2\mathbf{Q}_{\mathrm{RL}}, \\
&\tilde{\mathbf{D}}_{\mathrm{RR}} = \mathbf{H}_{\mathrm{RR}} - \omega^2\mathbf{Q}_{\mathrm{RR}}, \quad \tilde{\mathbf{D}}_{\mathrm{RI}} = -\omega^2\rho_f\left(\mathbf{R}_{\mathrm{RL}} + \mathbf{R}_{\mathrm{RR}}\right), \\
&\tilde{\mathbf{D}}_{\mathrm{IL}} = \begin{bmatrix} -\mathbf{S}_{\mathrm{LL}} \\ -\mathbf{S}_{\mathrm{RL}} \end{bmatrix}, \quad \tilde{\mathbf{D}}_{\mathrm{IR}} = \begin{bmatrix} -\mathbf{S}_{\mathrm{LR}} \\ -\mathbf{S}_{\mathrm{RR}} \end{bmatrix}, \\
&\tilde{\mathbf{D}}_{\mathrm{II}} = \begin{bmatrix} \mathbf{K}_{\mathrm{LL}} & \mathbf{K}_{\mathrm{LR}} \\ \mathbf{K}_{\mathrm{RL}} & \mathbf{K}_{\mathrm{RR}} \end{bmatrix} - \omega^2 \begin{bmatrix} \mathbf{M}_{\mathrm{LL}} & \mathbf{M}_{\mathrm{LR}} \\ \mathbf{M}_{\mathrm{RL}} & \mathbf{M}_{\mathrm{RR}} \end{bmatrix}.
\end{aligned} \tag{6.57}$$

The third row of equation (6.56) gives

$$\mathbf{w} = -\tilde{\mathbf{D}}_{\mathrm{II}}^{-1}\left(\tilde{\mathbf{D}}_{\mathrm{IL}}\mathbf{p}_{\mathrm{L}} + \tilde{\mathbf{D}}_{\mathrm{IR}}\mathbf{p}_{\mathrm{R}}\right), \tag{6.58}$$

so that the condensed form is thus

$$\begin{bmatrix} \mathbf{D}_{\mathrm{LL}} & \mathbf{D}_{\mathrm{LR}} \\ \mathbf{D}_{\mathrm{RL}} & \mathbf{D}_{\mathrm{RR}} \end{bmatrix} \begin{bmatrix} \mathbf{p}_{\mathrm{L}} \\ \mathbf{p}_{\mathrm{R}} \end{bmatrix} = \begin{bmatrix} \mathbf{q}_{\mathrm{L}} \\ \mathbf{q}_{\mathrm{R}} \end{bmatrix}, \tag{6.59}$$

where

$$\begin{aligned}
&\mathbf{D}_{\mathrm{LL}} = \tilde{\mathbf{D}}_{\mathrm{LL}} - \tilde{\mathbf{D}}_{\mathrm{LI}}\tilde{\mathbf{D}}_{\mathrm{II}}^{-1}\tilde{\mathbf{D}}_{\mathrm{IL}}, \quad \mathbf{D}_{\mathrm{LR}} = \tilde{\mathbf{D}}_{\mathrm{LR}} - \tilde{\mathbf{D}}_{\mathrm{LI}}\tilde{\mathbf{D}}_{\mathrm{II}}^{-1}\tilde{\mathbf{D}}_{\mathrm{IR}}, \\
&\mathbf{D}_{\mathrm{RL}} = \tilde{\mathbf{D}}_{\mathrm{RL}} - \tilde{\mathbf{D}}_{\mathrm{RI}}\tilde{\mathbf{D}}_{\mathrm{II}}^{-1}\tilde{\mathbf{D}}_{\mathrm{IL}}, \quad \mathbf{D}_{\mathrm{RR}} = \tilde{\mathbf{D}}_{\mathrm{RR}} - \tilde{\mathbf{D}}_{\mathrm{RI}}\tilde{\mathbf{D}}_{\mathrm{II}}^{-1}\tilde{\mathbf{D}}_{\mathrm{IR}},
\end{aligned} \tag{6.60}$$

which is dynamic condensation, although other formulations are possible (Friswell and Mottershead, 1995).

The condition number of the condensed dynamic stiffness matrix, **D**, is very important for solving the eigenvalue problem efficiently and accurately. It is difficult to verify if **D** is symmetric analytically, but numerically if the differences between $\mathbf{D}_{\mathrm{LR}}^{\mathrm{T}}$ and $\mathbf{D}_{\mathrm{RL}}$, $\mathbf{D}_{\mathrm{LL}}^{\mathrm{T}}$ and $\mathbf{D}_{\mathrm{LL}}$, $\mathbf{D}_{\mathrm{RR}}^{\mathrm{T}}$ and $\mathbf{D}_{\mathrm{RR}}$ are small enough, as shown in Figure 6.13, the condensed matrix **D** can be taken as a symmetric matrix. The normalised difference is defined as

$$\delta_{i,j}=\begin{cases}\dfrac{\left|\mathbf{D}_{\mathrm{LR}}^{\mathrm{T}}-\mathbf{D}_{\mathrm{RL}}\right|_{i,j}}{\sqrt{\mathbf{D}_{\mathrm{LR}}^{\mathrm{T}}\left(i,i\right)\mathbf{D}_{\mathrm{RL}}\left(j,j\right)}}\\ \dfrac{\left|\mathbf{D}_{\mathrm{LL}}^{\mathrm{T}}-\mathbf{D}_{\mathrm{LL}}\right|_{i,j}}{\sqrt{\mathbf{D}_{\mathrm{LL}}^{\mathrm{T}}\left(i,i\right)\mathbf{D}_{\mathrm{LL}}\left(j,j\right)}}\\ \dfrac{\left|\mathbf{D}_{\mathrm{RR}}^{\mathrm{T}}-\mathbf{D}_{\mathrm{RR}}\right|_{i,j}}{\sqrt{\mathbf{D}_{\mathrm{RR}}^{\mathrm{T}}\left(i,i\right)\mathbf{D}_{\mathrm{RR}}\left(j,j\right)}}\end{cases}, \qquad (6.61)$$

where the numerator stands for the difference between estimated matrices and the denominator is used for normalization.

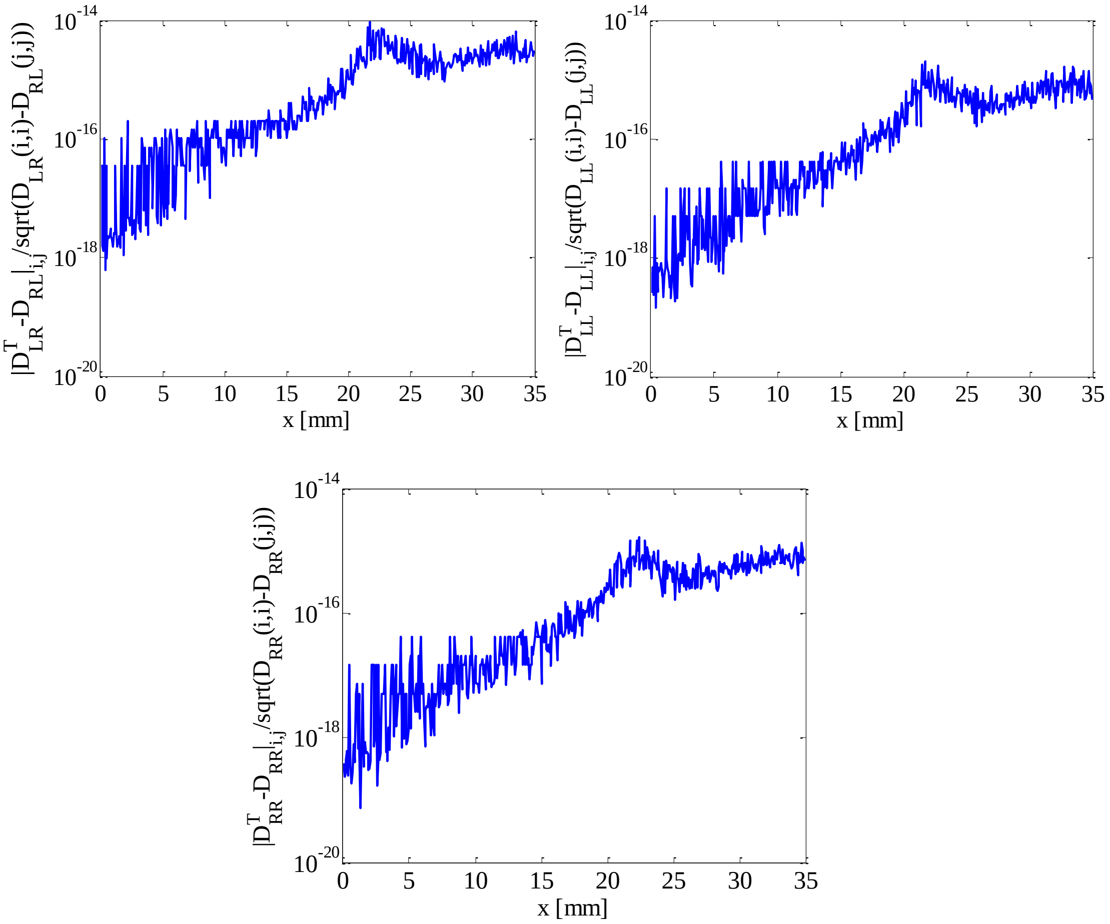

Figure 6.13 Distributions of normalized difference between estimated matrices at different position along the cochlear length. The very small difference numerically indicates the symmetry of the condensed matrix **D**.

Once $\mathbf{p}_{\mathrm{L}}$ and $\mathbf{p}_{\mathrm{R}}$ are calculated, the vectors $\mathbf{w}_{\mathrm{L}}$ and $\mathbf{w}_{\mathrm{R}}$ can then be calculated from $\mathbf{p}_{\mathrm{L}}$ and $\mathbf{p}_{\mathrm{R}}$ using equation (6.58). The terms in equation (6.52) can be re-arranged to express the forces and displacements on one side of the segment, at the *n*-th position in the discrete model, in terms of those on the other side, so that

$$\begin{bmatrix} \mathbf{q}_{\mathrm{R}}(n) \\ -\mathbf{f}_{\mathrm{R}}(n) \end{bmatrix} = \mathbf{T}(n) \begin{bmatrix} \mathbf{q}_{\mathrm{L}}(n) \\ \mathbf{f}_{\mathrm{L}}(n) \end{bmatrix}, \tag{6.62}$$

where $\mathbf{T}(n)$ is the transfer matrix, defined as

$$\mathbf{T}(n) = \begin{bmatrix} -\mathbf{D}_{\mathrm{LR}}^{-1}(n)\mathbf{D}_{\mathrm{LL}}(n) & \mathbf{D}_{\mathrm{LR}}^{-1}(n) \\ -\mathbf{D}_{\mathrm{RL}}(n) + \mathbf{D}_{\mathrm{RR}}(n)\mathbf{D}_{\mathrm{LR}}^{-1}(n)\mathbf{D}_{\mathrm{LL}}(n) & -\mathbf{D}_{\mathrm{RR}}(n)\mathbf{D}_{\mathrm{LR}}^{-1}(n) \end{bmatrix}. \tag{6.63}$$

The sign convention on the forces on the right hand side of this segment is reversed, so that it is in equilibrium with that defined on the left hand side of the adjacent, (*n*+1)-th, segment. We now assume that a particular distribution of displacements and forces, due to the *m*-th mode, on the right hand side of the element is equal to that on the left hand side of the element, apart from a complex constant of proportionality, so that

$$\begin{bmatrix} \mathbf{q}_{\mathrm{R}m}(n) \\ -\mathbf{f}_{\mathrm{R}m}(n) \end{bmatrix} = \lambda_m \begin{bmatrix} \mathbf{q}_{\mathrm{L}m}(n) \\ \mathbf{f}_{\mathrm{L}m}(n) \end{bmatrix}. \tag{6.64}$$

This distribution would thus propagate as a wave with an unaltered shape along a uniform cochlea with a wavenumber, k_m, determined by

$$\lambda_m = e^{-ik_m\Delta}, \tag{6.65}$$

where Δ is the length of the element. The right hand side of equation (6.64) must now be equal to the right hand side of equation (6.62), and so λ_m, and the corresponding distribution of displacements and forces, must be an eigenvalue, and the corresponding eigenvector, of the transfer matrix. Using the WFE method the wavenumbers are thus obtained directly from the eigenvalues of the transfer matrix, rather than the eigenvalue problem for the finite element model of a section being used to deduce a dispersion equation, which then has to be solved to give the wavenumber (Chadwick, *et al.*, 1996, Fuhrmann, *et al.*, 1987). Another advantage of the WFE method over that used in

Fuhrmann (Fuhrmann, *et al.*, 1987) and Chadwick (Chadwick, *et al.*, 1996), which is sometimes called the Spectral Finite Element method (Finnveden, 2004), is that elements of finite thickness can be analysed. In the context of cochlear mechanics, each segment could incorporate finite element models of several layers of hair cells, for example. It is also possible to incorporate asymmetries into the structure, by slanting the hair cells in the longitudinal direction, for example, in which case $\mathbf{T}(n)$ would not be equal to $\mathbf{T}^{-1}(n)$.

The analysis becomes a little more complicated when the structural parameters of the cochlea vary along its length, as considered by Ni *et al.* (Ni, *et al.*, 2010). In this case the eigenvector corresponding to a specific type of wave is not exactly the same when passing from one element to the next. If the longitudinal variation is gradual, however, the change in the mode shape corresponding to this eigenvector will not be very large from one element to the next. By calculating the inner products of the left eigenvectors for one element with the right eigenvector for the adjacent element (Houillon, *et al.*, 2005), it is then possible to track which eigenvalue, and hence which wavenumber, is associated with each mode travelling along the cochlea. Figure 6.14 (a), for example, shows the variation with longitudinal position of the real and imaginary parts of the wavenumber associated with different waves propagating along the cochlea at 1 kHz. The BM velocity distribution associated with each of these waves is plotted in Figure 6.14 (b).

Since the finite element model for each of the 512 segments of the cochlea has 8×4 hexahedral elements to describe the fluid motion in each chamber, and 4 quadrilateral elements along the BM to describe its radial structural response as a beam, there are thus 9×5 nodes on each face of the fluid chamber slice, each having 1 degree of freedom, and 5×1 nodes on each edge of the BM slice, each having 3 degrees of freedom. The BM elements are assumed to be separated from each other in the longitudinal direction, however, so that the degrees of freedom associated with the BM elements are all condensed, as described above, and the vectors in equation (6.62), for example, have 90 degrees of freedom. There are thus 90 eigenvalues of the transfer matrix $\mathbf{T}$ in equation (6.62) and hence the wavenumbers of 90 separate waves can be calculated. Only half of these will be forward-going waves, however, and most of these have wavenumbers with large imaginary components and thus are heavily attenuated even a short distance from the excitation position. Only the wave labelled 1 in Figure

6.14 (a) has a zero imaginary part to its wavenumber at the base and is thus able to propagate any significant distance along the cochlea. These wavenumber distributions, together with the results of the full finite element model do not change significantly if 256 or 1024 longitudinal elements are used instead of 512, as shown in Appendix D, indicating that the WFE assumption, that $k_m\Delta$ is small compared with unity, holds and that the system is reasonably well conditioned.

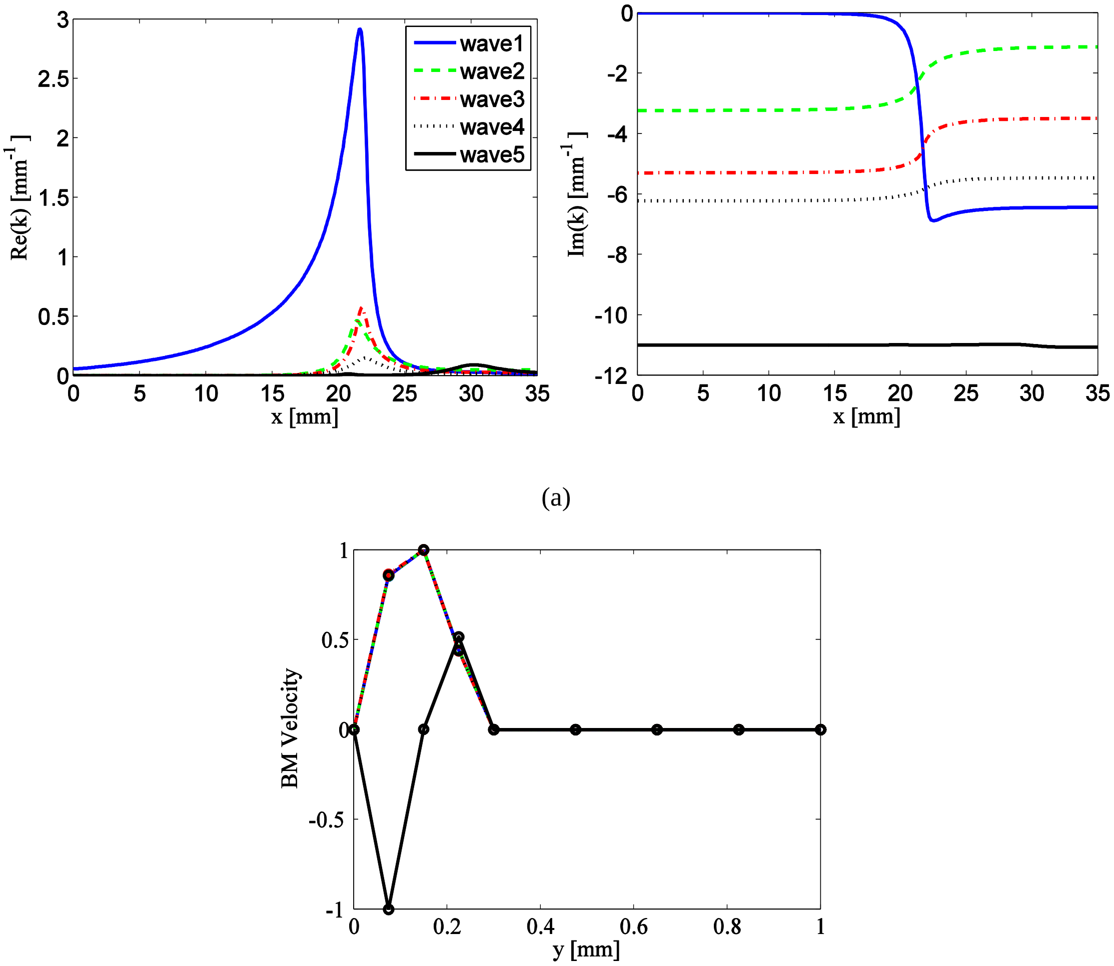

(a)

(b)

Figure 6.14 (a) The wavenumber distribution of 5 of the forward-going waves, calculated using the wave finite element model of the cochlea at 1 kHz. (b) The normalised BM velocity in the radial direction associated with the 5 selected waves, calculated at the place where the real part of their wavenumber is largest at 1 kHz. The normalized BM velocity of waves 1 to 5 lie on top of each other and that of wave 5 shows a second order bending shape.

The details of the wavenumber distributions in Figure 6.14 are, however, dependent on the number of fluid elements used in the cross section. In order to correctly reproduce the near-field fluid pressure very close to the BM a much denser grid of fluid elements would be required than has been used here. The only important property of this near-field pressure for wave 1, however, is the added mass of the fluid. This is somewhat smaller for the FE grid used here than it was for the analytic model, so that the BM mass needs to be increased to account for this effect. Waves 2 to 4 correspond to higher order fluid modes, which have relatively simple cross-sectional mode shapes that can be accurately reproduced with the current grid density in the FE model. The most important aspect of these waves is the value of the negative imaginary part of the wavenumber in the basal region, and this is not significantly affected if the number of fluid elements is increased. The relatively coarse grid of fluid elements used here thus correctly predicts the important features of the wavenumbers in the WFE analysis. The mode shapes of the BM velocity shown in Figure 6.14 (b), obtained by joining the nodal values, are not accurate representation of their true shapes due to the relatively coarse mesh in the radial, y, direction. The gradient at $y=B$ is in fact zero corresponding to the clamped boundary condition defined here.

Wave 1 involves the first radial mode of the BM and has a wavenumber distribution similar to that of the slow wave in Section 6.2. Waves 2, 3, and 4 also involve the first radial mode of the BM, but have wavenumber distributions that are similar to the higher order fluid mode in Section 6.3. Wave 5 has been included in Figure 6.14 since it is the first mode with a higher-order radial distribution of BM velocity, although it has a large negative imaginary component to its wavenumber and so is strongly evanescent.

The pressure distributions in the upper fluid chamber corresponding to the eigenvectors of waves 1, 2 and 3 at various positions along the cochlea are shown in Figure 6.15. The pressure distribution due to wave 1 is almost uniform before the characteristic place, which is about 22 mm here, but shows a complicated distribution beyond this position. Since the modal BM velocity decays very quickly beyond the characteristic place and the magnitude is also small, the pressure distributions are not as important as those before. The pressure distribution due to wave 2 is very similar to the (0, 1) acoustic mode close to the basal end, but again starts to become more complicated close to the characteristic place. It is interesting to see that the interaction between the BM and the fluid does not affect wave 2 very much until it reaches the characteristic place. The pressure distribution of wave 3 is similar to the (1, 0) acoustic mode close to the basal end although the interaction with the BM now moves the nodal line away from the centre.

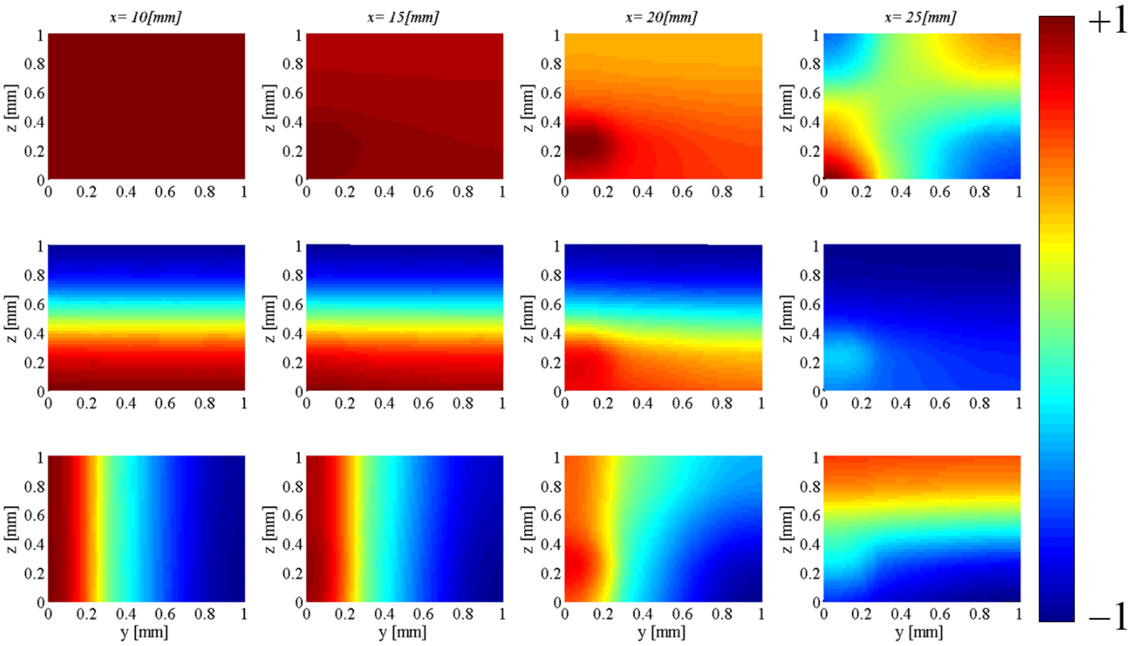

Figure 6.15 Pressure distribution in upper fluid chamber corresponding to waves 1, 2 and 3 in Figure 6.14 at different position along the cochlea.

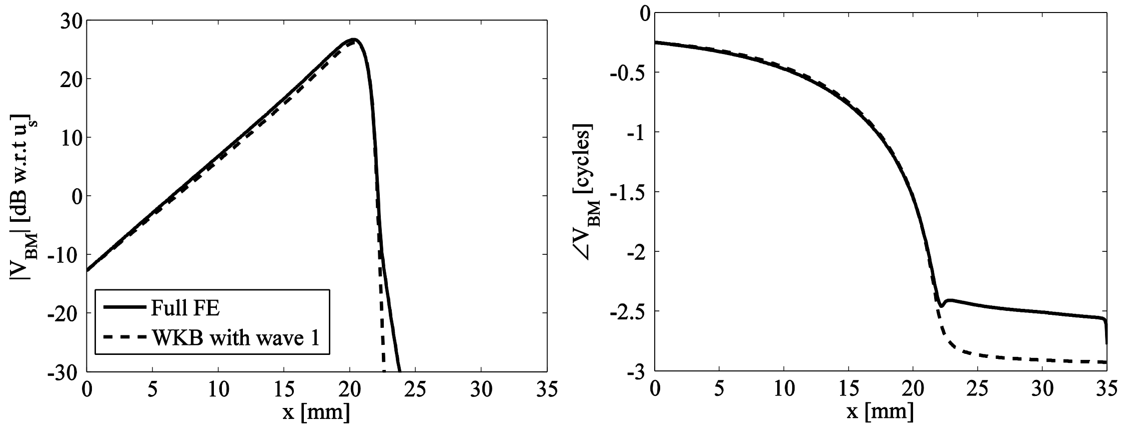

(a) (b)

Figure 6.16 The (a) magnitude and (b) phase of the modal BM velocity at 1 kHz, calculated from the full finite element model and the WKB method using the wavenumber distribution for the slow wave, wave 1, calculated using the WFE method.

Assuming that it propagates in isolation, the WKB method can be used with the wavenumber distribution of the slow wave, to calculate a longitudinal distribution of the

BM velocity, whose magnitude and phase is shown in Figure 6.16, together with the results of the full finite element method. The results of the full finite element model are thus in reasonable agreement with those predicted using only the slow wave labelled wave 1 in Figure 6.14 (a). The less rapid fall off in the results of the full finite element model just apical of the peak, compared those using the WKB method, has also been noted by Steele and Taber (Steele and Taber, 1979), de Boer and Viergever (de Boer and Viergever, 1982) and Watts (Watts, 2000).

6.6.2 Wave Decomposition

Using the approach shown in Section 5.4.3, we can consider a more detailed decomposition of the results of the full finite element analysis into wave components. The vector of all wave amplitudes, on the right hand side of this segment can be written as

$$\mathbf{a}_{\mathrm{R}}(n) = \boldsymbol{\psi}(n)\begin{bmatrix} \mathbf{p}_{\mathrm{R}}(n) \\ -\mathbf{q}_{\mathrm{R}}(n) \end{bmatrix}, \tag{6.66}$$

where the volume velocities, **q**, can be calculated from the pressures, **p**, using equation (6.59) and so the wave amplitudes in the *n*-th segment can be expressed entirely as a function of the vector of elemental pressures on the face of this segment, calculated from the full finite element model. Equation (6.66) has been used to decompose the state vectors at each longitudinal element derived from the full finite element model in Section 4.2 into amplitudes of the waves determined by the wave finite element method, with the results shown in Figure 6.17.

It is also possible to calculate the contributions to the modal BM velocity, calculated from the full finite element analysis, from each of these modes. The state vector at the *n*-th section due to all of the wave amplitudes can be written as

$$\begin{bmatrix} \mathbf{p}_{\mathrm{R}}(n) \\ -\mathbf{q}_{\mathrm{R}}(n) \end{bmatrix} = \boldsymbol{\varphi}(n)\mathbf{a}_{\mathrm{R}}(n), \tag{6.67}$$

so the contribution to the state vector due to the *m*-th wave on the right hand side of the *n*-th segment can be defined, using equation (6.67), as

$$\begin{bmatrix} \mathbf{p}_{\mathrm{R}}(n,m) \\ -\mathbf{q}_{\mathrm{R}}(n,m) \end{bmatrix} = \mathbf{r}(n,m)\, a_{\mathrm{R}}(n,m), \tag{6.68}$$

where $\mathbf{r}(n,m)$ is the *m*-th column vector of $\mathbf{Q}(n)$ and $a_{\mathrm{R}}(n,m)$ is an element of $\mathbf{a}_{\mathrm{R}}(n)$ in equation (6.67).

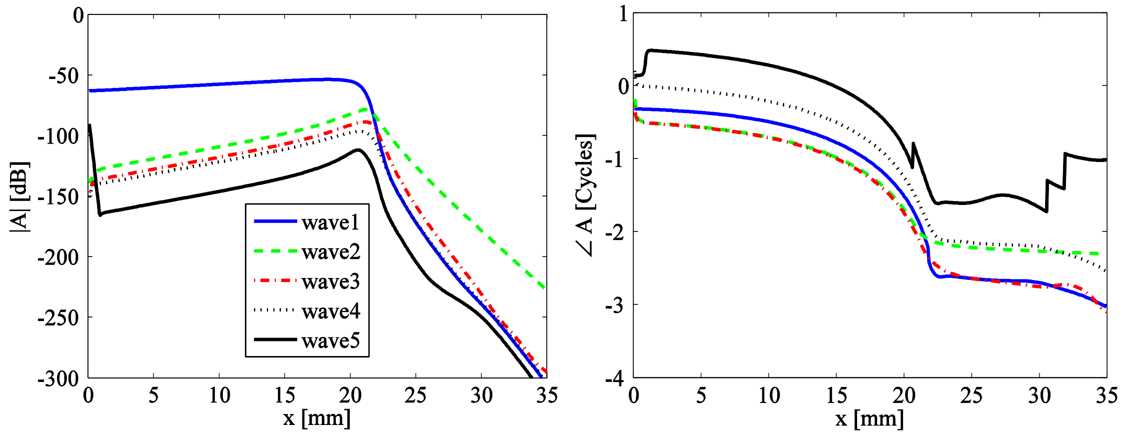

(a) (b)

Figure 6.17 The (a) amplitude and (b) phase of the forward-going waves in Figure 6.14 (a).

The vector of elemental BM displacements due to the *m*-th wave, $\mathbf{w}_{\mathrm{R}}(n,m)$, can then be calculated from the vector of elemental pressures using equation (6.58), from which the modal BM velocity due to the *m*-th wave on the right hand side of the *n*-th segment, $v_{\mathrm{BM}}(n,m)$, can be calculated using the form as

$$v_{\mathrm{BM}}(n,m) = 2i\omega\, \mathbf{s}_{\mathrm{BM}}^{\mathrm{T}} \mathbf{w}_{\mathrm{R}}(n,m), \tag{6.69}$$

where $\mathbf{w}_{\mathrm{R}}(n,m)$ is the elemental displacement vector associated with the *m*-th wave on the right hand side of the *n*-th segment and $\mathbf{s}_{\mathrm{BM}}^{\mathrm{T}}$ is the vector of normalised values of the BM mode shape.

The contributions to the modal BM velocity distributions, due to each of the forward-going waves selected in Figure 6.14, are plotted in Figure 6.18. The WKB result for wave 1 is seen to be in reasonable agreement with the calculated contribution of this wave to the full finite element results for positions basal to the peak response at this frequency, at about 20 mm along the cochlea in this case. The contribution of wave 1 is significantly less than the overall result of the full finite element, however, for positions beyond the peak response, where the contribution of wave 2 dominates the overall response. The contribution of wave 2, which is an evanescent higher-order fluid mode, decays away on either side of this peak, as do the contributions of waves 3, 4 and 5, although the amplitudes of these waves are too small to significantly affect the overall response.

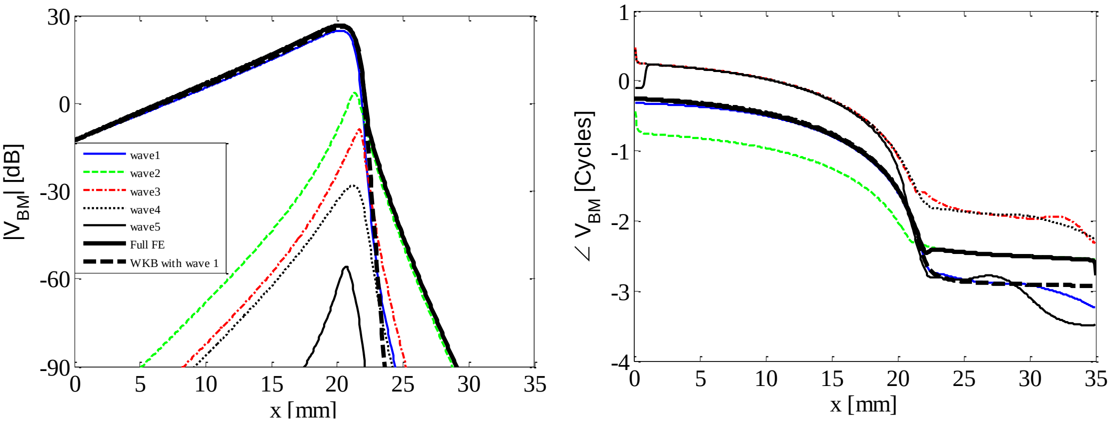

Figure 6.18 Decomposition of the modal BM velocity into components due to each of the forward-going waves in Figure 6.14 (a), the WKB reconstruction of the slow wave and the modal BM velocity from the full finite element model are also shown.

As well as being able to calculate the contributions of the forward-going waves to the overall finite element response, equation (6.68) can also be used to calculate the individual contributions of the backward-going waves, as shown in Figure 6.19, since their amplitudes are also calculated as elements of $\mathbf{a}_{\mathrm{R}}(n)$ in equation (6.67). It is interesting to see that there apparently is a backward-going component to wave 1, which is about 25 dB below the amplitude of the forward-going component at the peak, but only about 10 dB below the forward-going component at the base. The phase distribution of the contribution due to this negative going wave is almost the same as that of the positive-going component, however, which indicates that this does not represent a freely decaying wave, but is a component driven at each point along the cochlea by the positive-going wave, due to scattering as a result of the change in wavenumber with position. The contribution due to the backward-going component of wave 2 is far greater basal to the peak response than it is apical, and is larger there than the forward-going component, in Figure 6.18, although both of these components are so small compared to those from wave 1 in this region, that they are not expected to play a major role. Similarly the backward-going component of wave 5, involving the second mode of BM motion, is larger than the forward-going component, but is again very small compared with the contribution due to the slow mode.

It is clear that the amplitudes of waves 2, 3 are very much less than wave 1 except near the peak. The higher order fluid modes are excited close to the peak response, however, such that the contribution of wave 2 to the BM velocity dominates the overall response beyond this point. Beyond the peak position, the slow wave decays rapidly, so that the total response is somewhat larger than it would otherwise be, as noted by Watts (Watts, 2000). The decomposed BM velocity component due to the slow wave is almost the same as its amplitude calculated using the WKB approximation basal to the peak, as shown in Figure 6.16. This suggests that although there is some scattering of this wave into the higher order modes, this does not significantly affect the propagation of the slow wave. For a locally reacting passive BM, the overall behaviour of the cochlea to excitation of the stapes is thus approximated well by the propagation of a single, slow wave.

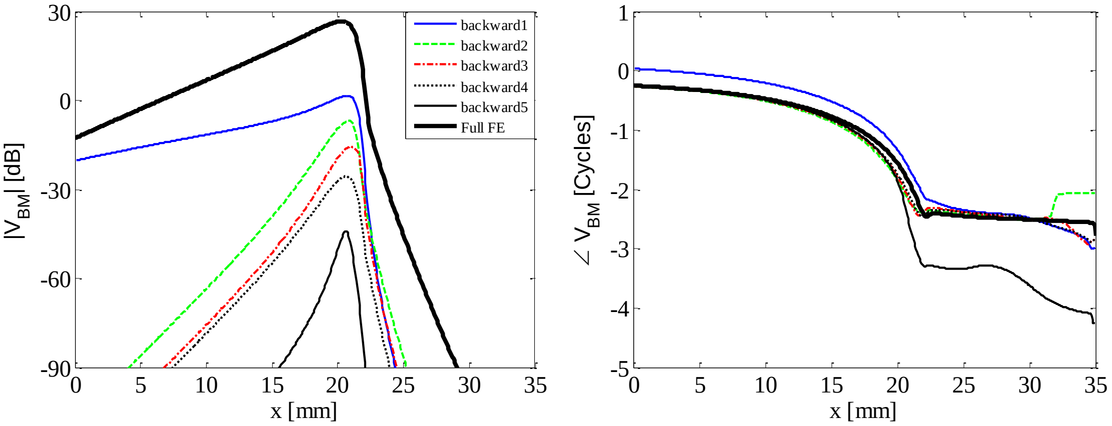

Figure 6.19 Decomposition of the modal BM velocity into components due to the backward-going version of the waves those in Figure 6.14 (a), and the modal BM velocity from the full finite element model.

6.6.3 Scattering

If the system under consideration was entirely uniform in the longitudinal direction, the set of eigenvalues and eigenvectors for the transfer matrices of each element would be exactly the same. In the cochlea, however, the properties are slowly changing, so that at a given frequency, there are gradual changes in the eigenvalues and eigenvectors with position, which give rise to the distribution of wavenumbers shown in Figure 6.14. Although in the uniform system each wave propagates completely independently, there is the possibility of interaction between these waves in the non-uniform system. This interaction can be quantified by defining a scattering matrix at the junctions between adjacent segments.

We first separate the wave amplitudes calculated from equation (6.66) into forward and backward travelling waves, according to whether $|\lambda_m| \le 1$, forward, or $|\lambda_m| > 1$, backward, as above, so that, referring to Figure 6.20 (a), the wave amplitudes on the right hand side of the *n*-th segment are

$$\begin{bmatrix} \mathbf{a}_{\mathrm{R}}^{+}(n) \\ \mathbf{a}_{\mathrm{R}}^{-}(n) \end{bmatrix} = \boldsymbol{\psi}(n) \begin{bmatrix} \mathbf{q}_{\mathrm{R}}(n) \\ -\mathbf{f}_{\mathrm{R}}(n) \end{bmatrix}. \tag{6.70}$$

The corresponding wave amplitudes on the left hand side of the (*n*+1)-th segment are

$$\begin{bmatrix} \mathbf{a}_{\mathrm{L}}^{+}(n+1) \\ \mathbf{a}_{\mathrm{L}}^{-}(n+1) \end{bmatrix} = \boldsymbol{\psi}(n+1) \begin{bmatrix} \mathbf{q}_{\mathrm{L}}(n+1) \\ \mathbf{f}_{\mathrm{L}}(n+1) \end{bmatrix}, \tag{6.71}$$

where $\boldsymbol{\psi}(n+1)$ is calculated from the eigen-decomposition of the transfer matrix for the (*n*+1)-th segment.

At the junction between these two adjacent segments, the nodal displacements and forces must be continuous or in equilibrium, so that

$$\boldsymbol{\varphi}(n) \begin{bmatrix} \mathbf{a}_{\mathrm{R}}^{+}(n) \\ \mathbf{a}_{\mathrm{R}}^{-}(n) \end{bmatrix} = \boldsymbol{\varphi}(n+1) \begin{bmatrix} \mathbf{a}_{\mathrm{L}}^{+}(n+1) \\ \mathbf{a}_{\mathrm{L}}^{-}(n+1) \end{bmatrix}, \tag{6.72}$$

and hence

$$\begin{bmatrix} \mathbf{a}_\mathrm{L}^+(n+1) \\ \mathbf{a}_\mathrm{L}^-(n+1) \end{bmatrix} = \boldsymbol{\psi}(n+1)\boldsymbol{\varphi}(n) \begin{bmatrix} \mathbf{a}_\mathrm{R}^+(n) \\ \mathbf{a}_\mathrm{R}^-(n) \end{bmatrix}. \tag{6.73}$$

The matrix of outgoing waves from the junction between the *n*-th and the (*n*+1)-th segments can now be represented as a scattering matrix, as in Figure 6.20 (b), so that

$$\begin{bmatrix} \mathbf{a}_\mathrm{L}^+(n+1) \\ \mathbf{a}_\mathrm{R}^-(n) \end{bmatrix} = \mathbf{S}(n) \begin{bmatrix} \mathbf{a}_\mathrm{R}^+(n) \\ \mathbf{a}_\mathrm{L}^-(n+1) \end{bmatrix}, \tag{6.74}$$

where

$$\mathbf{S}(n) = \begin{bmatrix} \mathbf{S}_{11}(n) & \mathbf{S}_{12}(n) \\ \mathbf{S}_{21}(n) & \mathbf{S}_{22}(n) \end{bmatrix} \tag{6.75}$$

and $\mathbf{S}_{11}(n)$ and $\mathbf{S}_{22}(n)$ are matrices of transmission coefficients of forward-going waves, from left to right, and backwards-going waves, from right to left, and $\mathbf{S}_{12}(n)$ and $\mathbf{S}_{21}(n)$ are matrices of refection coefficients from backwards-going waves on the right to forward-going waves on the right and forward going waves on the left to backwards-going waves on the left.

If we partition the matrix in equation (6.73) as

$$\boldsymbol{\psi}(n+1)\boldsymbol{\varphi}(n) = \begin{bmatrix} \mathbf{M}_{11} & \mathbf{M}_{12} \\ \mathbf{M}_{21} & \mathbf{M}_{22} \end{bmatrix}, \tag{6.76}$$

then the partitioned elements of equation (6.75) can be calculated to show that

$$\mathbf{S}(n) = \begin{bmatrix} \mathbf{S}_{11}(n) & \mathbf{S}_{12}(n) \\ \mathbf{S}_{21}(n) & \mathbf{S}_{22}(n) \end{bmatrix} = \begin{bmatrix} \mathbf{M}_{11} - \mathbf{M}_{12}\mathbf{M}_{22}^{-1}\mathbf{M}_{21} & \mathbf{M}_{12}\mathbf{M}_{22}^{-1} \\ -\mathbf{M}_{22}^{-1}\mathbf{M}_{21} & \mathbf{M}_{22}^{-1} \end{bmatrix}. \tag{6.77}$$

If the *n*-th and the (*n*+1)-th segments are identical then $\boldsymbol{\psi}(n+1)$ is equal to $\boldsymbol{\psi}(n)$, so that equation (6.76) is equal to the $N \times N$ identity matrix. Hence $\mathbf{M}_{11}$ and $\mathbf{M}_{22}$ are equal to the $N/2 \times N/2$ identity matrix and $\mathbf{M}_{12}$ and $\mathbf{M}_{21}$ have zero elements. In this case,

$\mathbf{S}_{11}(n)$ and $\mathbf{S}_{22}(n)$ in equation (6.77) are also $N/2 \times N/2$ identity matrix and $\mathbf{S}_{12}(n)$ and $\mathbf{S}_{21}(n)$ are zero, as expected.

Figure 6.21 shows the magnitude of the elements of one column of the scattering matrix in equation (6.74) corresponding to the scattering from wave 1 in Figure 6.14 into other forward-going waves, above, and the reflection of wave 1 into backwards travelling waves, below.

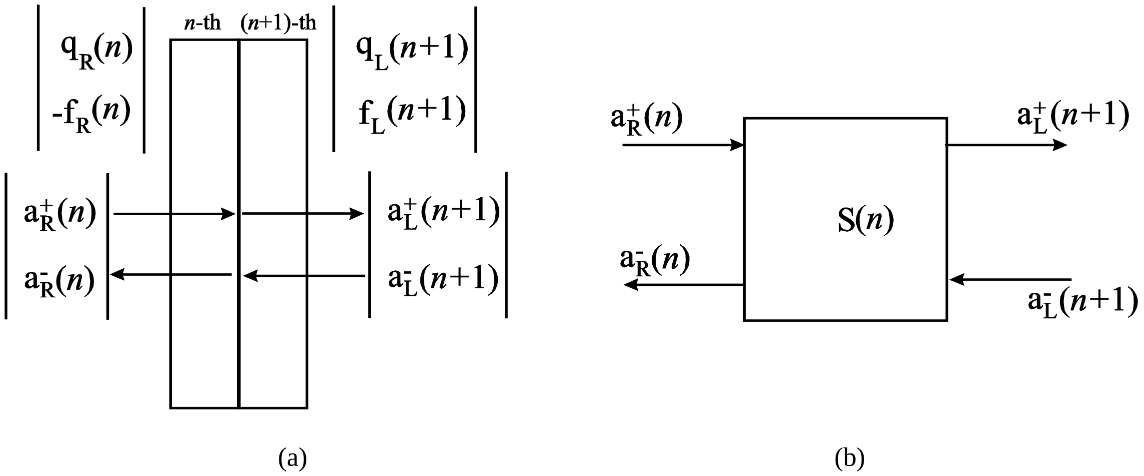

Figure 6.20 (a) The junction between the n-th and (n+1)-th segment with the corresponding states and wave amplitudes, and (b) the definition of the scattering matrix.

Near the base of the cochlea almost all the elements of $\mathbf{S}_{11}$ and $\mathbf{S}_{22}$ are close to zero except for those corresponding to the transmission coefficient of wave 1, which is about unity, and most the elements of $\mathbf{S}_{12}$ and $\mathbf{S}_{21}$ are close to zero, as expected in a uniform system. There is only significant scattering of wave 1 into the higher order modes at about $x \approx 20$ mm, which is the origin of the additional wave components in Figure 6.14. Close to the base, however, it is predicted that at each junction about 0.5% of the forward-going slow wave, wave 1, will be scattered into the backward-going slow wave. This helps explain the spurious backwards-going wave seen in Figure 6.19.

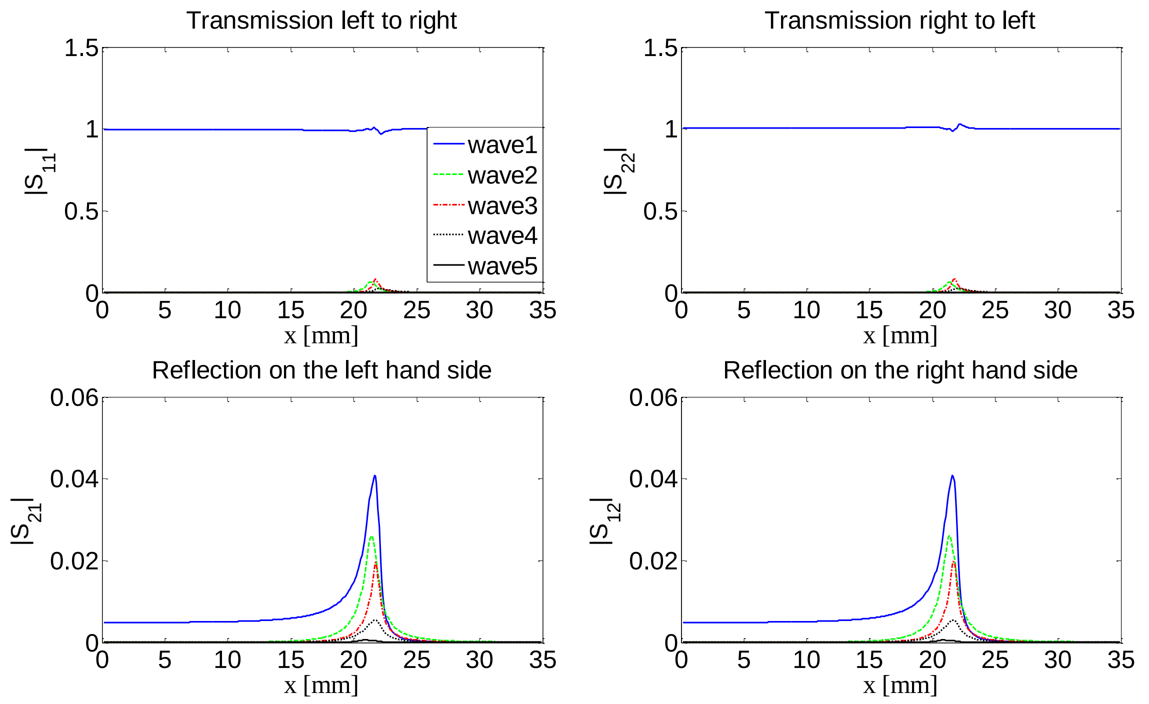

Figure 6.21 The magnitude of the scattering elements at each junction along the cochlea model from mode 1 into other forward-going waves at 1 kHz.

6.7 Wave Decomposition with Longitudinal BM Dynamics

In a similar way to the FE analysis described in Section 5.3, the finite element model for each of the 512 slices of the cochlea had 8 × 4 hexahedral elements to describe the fluid motion in each chamber and 4 plate elements along the BM to describe its radial structural response as a beam, but now with weak mechanical coupling due to orthotropy in the longitudinal direction. The cochlea was still assumed to be symmetric so that only one fluid chamber needed to be modelled. There are thus 9 × 5 nodes on each face of the fluid chamber slice, each having 1 degree of freedom, and 5 × 1 nodes on each edge of the BM slice, each having 3 degree of freedom which are transverse displacement w, rotations θ_x and θ_y. So that the vectors in equation (6.62), for example, have 112 degrees of freedom under the assumed boundary condition for the BM slice, which is simply supported at both y=0 and y=B, i.e. w=0 and θy=0.

Figure 6.22 (a) shows the distribution of the real and imaginary parts of the wavenumbers associated with some of the different waves propagating along the cochlea, modelled with the BM as an orthotropic plate, at 1 kHz. All of the components of stiffness vary with position as in equation (6.46), but with parameters $D_{x0} = 1.9 \times 10^{-8}$ N m, $D_{y0}= 3.9 \times 10^{-7}$ N m and $D_{t0} = 5.8 \times 10^{-9}$ N m at the base, so that $D_x/D_y=5 \times 10^{-2}$.

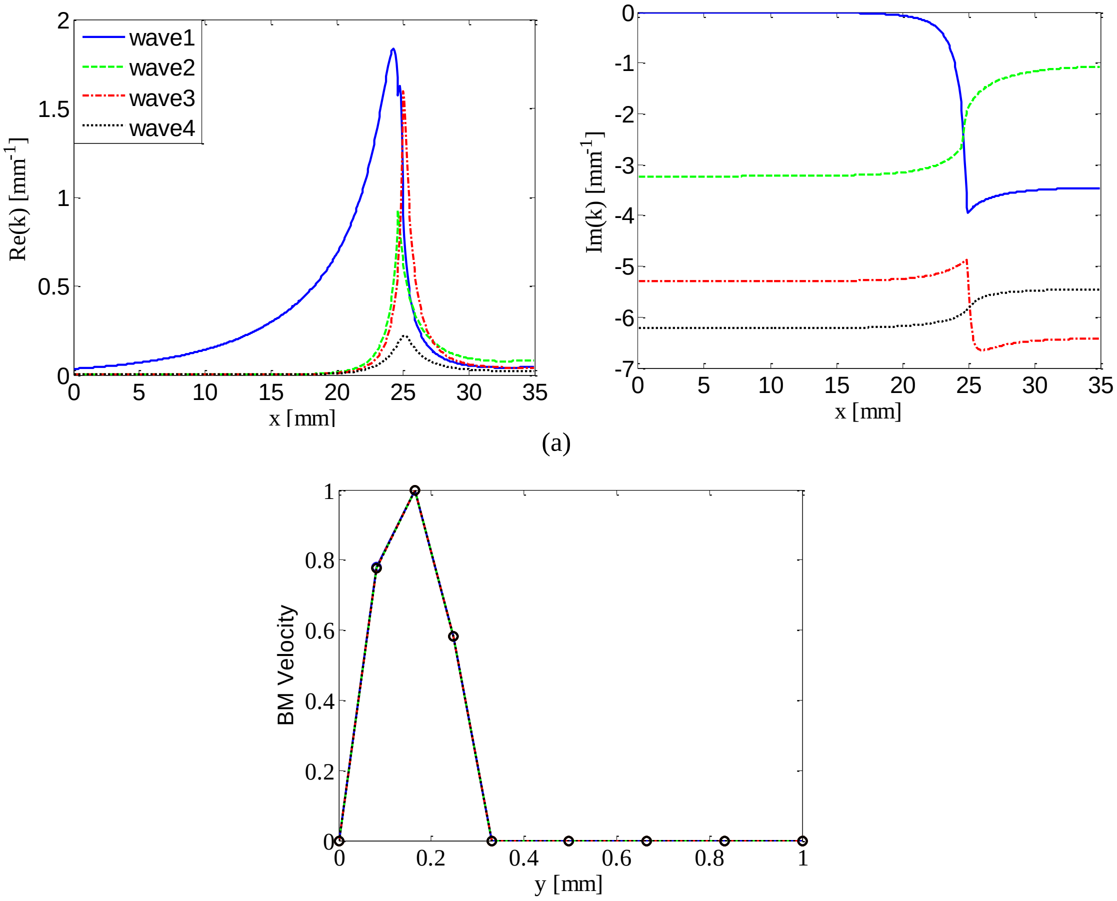

(a)

(b)

Figure 6.22 (a) Wave number distribution of the forward-going waves calculated using the orthotropic WFE model of the cochlea at 1 kHz and a damping ratio of 0.1; (b) The normalised BM velocity in the radial direction associated with the first 4 of these waves calculated at the place where the real part of their wavenumber is largest at 1 kHz. The normalized BM velocity of waves 1 to 4 lie on top of each other.

The imaginary part of the radial BM velocity distribution associated with each of these waves is plotted in Figure 6.22 (b). Forward-going waves have again been selected with the smallest magnitude of the imaginary part of the wavenumber. There are 112 eigenvalues, for the matrix **T** in equation (6.62) and hence the wavenumbers of 112 separate waves can be calculated. Only half of these will be propagating in the forward direction, however, and most of these have wavenumbers with large imaginary components at the base and thus are heavily attenuated, even a short distance from the excitation position at the stapes. In fact only the wave 1 in Figure 6.22 (a) has a zero imaginary part to its wavenumber at the base and can thus propagate along the cochlea when excited by the stapes.

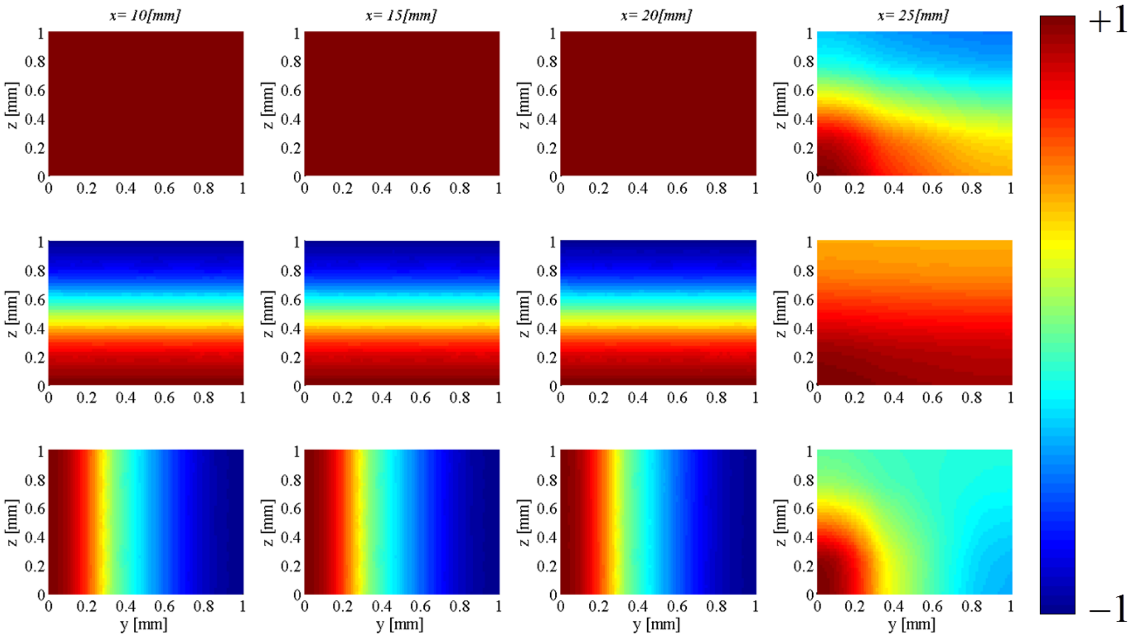

Figure 6.23 Each row of pressure distribution in upper fluid chamber corresponding to waves 1, 2 and 3 in Figure 6.22 at different position along the cochlea.

The pressure distributions in the upper fluid chamber using the model with the longitudinal BM dynamics are seen to be similar to those predicted from the model with the locally-reacting BM dynamics shown in Figure 6.15. Each row in Figure 6.23 corresponds to the eigenvectors of waves 1, 2 and 3 at various positions along the cochlea are shown in Figure 6.22 respectively. Wave 1 shows an almost uniform pressure distribution before the characteristic place, and then becomes complicated beyond this position. Wave 2 shows a (0, 1) and wave 3 shows a (1, 0) acoustic mode at the basal end, and the pressure distributions of wave 2 and wave 3 become more complicated when they are close to the characteristic place. The mode shapes of the BM velocity shown in Figure 6.22 (b) are not the same as their true shapes due to the relatively coarse mesh in the radial, y, direction. The gradient at $y=B$ is in fact zero corresponding to the clamped boundary condition defined here.

Figure 6.24 (a) and (b) show comparisons between magnitude and phase distributions along the cochlea calculated from the full FE orthotropic model and WKB method, when using the wavenumber for wave 1 predicted by the WFE method with the orthotropic plate. The difference between these graphs is rather larger than it was in the case of the locally-reacting BM, in Figure 6.16, and will be discussed below.

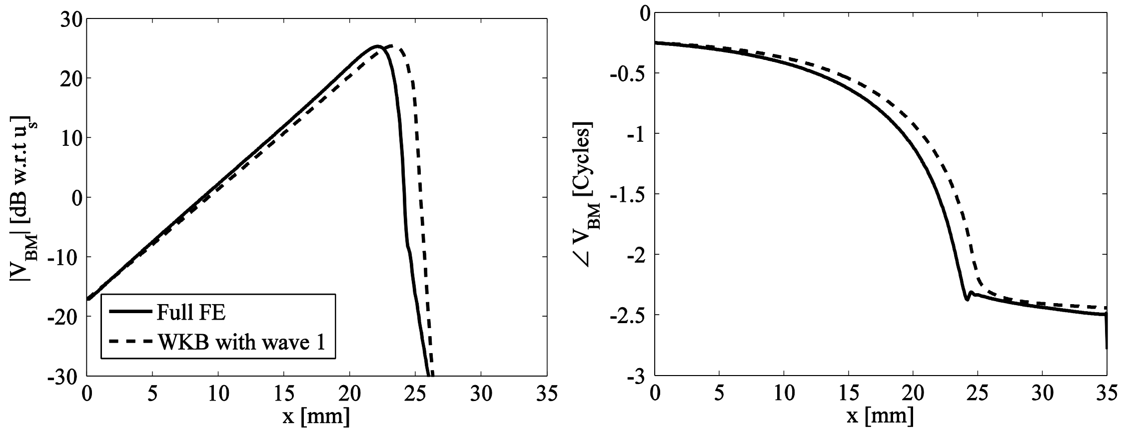

(a) (b)

Figure 6.24 The (a) amplitude and (b) phase of the modal BM velocity at 1 kHz.

The state vectors at each longitudinal element have again been used to decompose the full finite element orthotropic model into amplitudes of the waves determined by the wave finite element method, with the results shown in Figure 6.25. A modified version of equation (6.66) was used for this, in which the plate velocity as well as the fluid velocity was included. The decomposition of the modal BM velocity into forward-going and backward-going components is shown in Figure 6.26.

All of the results for the orthotropic plate model of the BM are similar to those in Section 6.6, for the locally-reacting BM model. This suggests that longitudinal coupling along the BM does not play a dominant role in determining the coupled dynamics of the cochlea, at least for the orthotropic parameters assumed here. The real part of the wavenumber for wave 1 in Figure 6.22 peaks at a position slightly further along the cochlea than in Figure 6.22, for the locally-reacting BM, perhaps reflecting the increased stiffness of the BM. A similar effect is seen in the peak of the calculated BM velocity, which was also observed by (Meaud and Grosh, 2010) and Grosh (2010) in their Fig 2. Also, the imaginary part of the wavenumber for wave 1 in Figure 6.22 does not fall to quite such a low value beyond the position of the peak response as for the locally-reacting BM in Figure 6.14. The WKB solution using this wavenumber distribution, now peaks just beyond the peak response predicted from the full FE model. Although the peak levels of the higher-order fluid modes are somewhat less than for the locally-reacting BM, the overall response is still dominated by wave 2 for positions beyond the peak response.

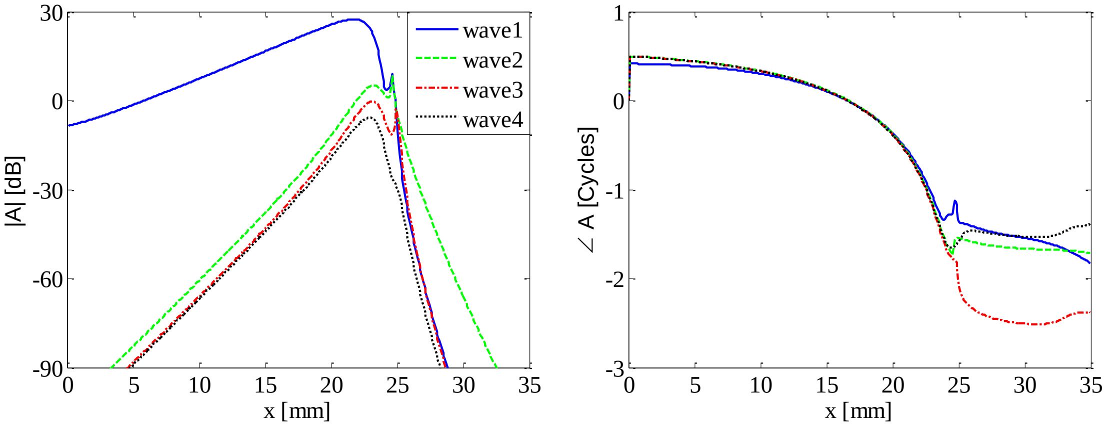

Figure 6.25 The (a) amplitude and (b) phase of the forward-going waves in Figure 6.22 (a).

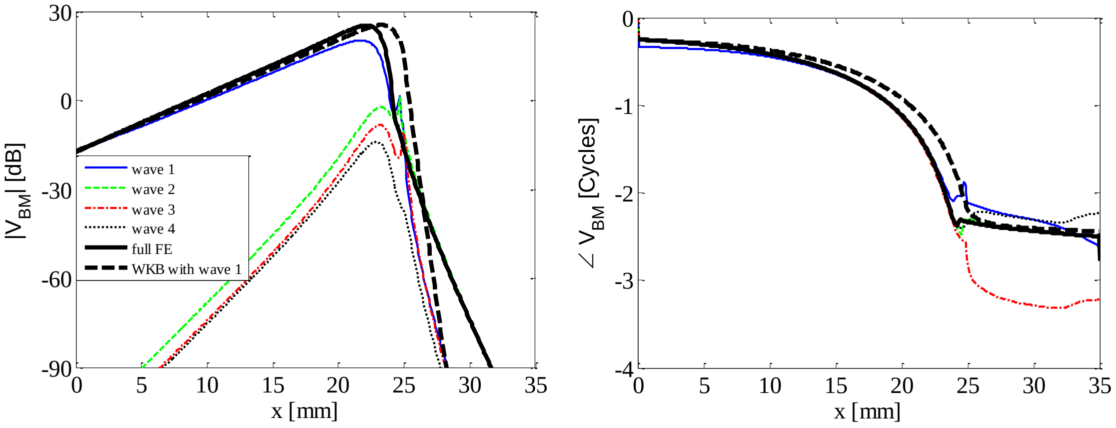

Figure 6.26 Decomposition of the modal BM velocity into components due to each of the forward-going waves in Figure 6.22 (a), the WKB reconstruction of the slow wave and the modal BM velocity from the full finite element model are also shown.

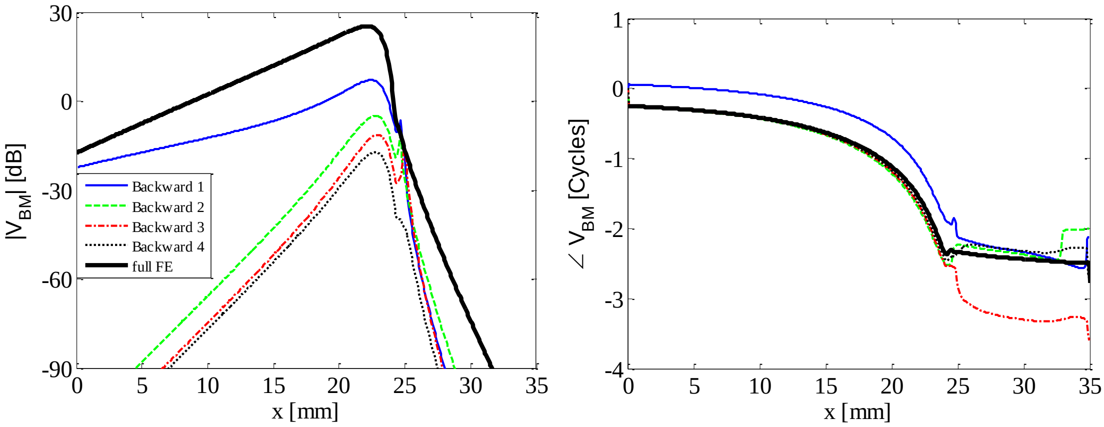

Figure 6.27 Decomposition of the modal BM velocity into components due to the backward-going version of the waves those in Figure 6.22 (a), and the modal BM velocity from the full finite element model.

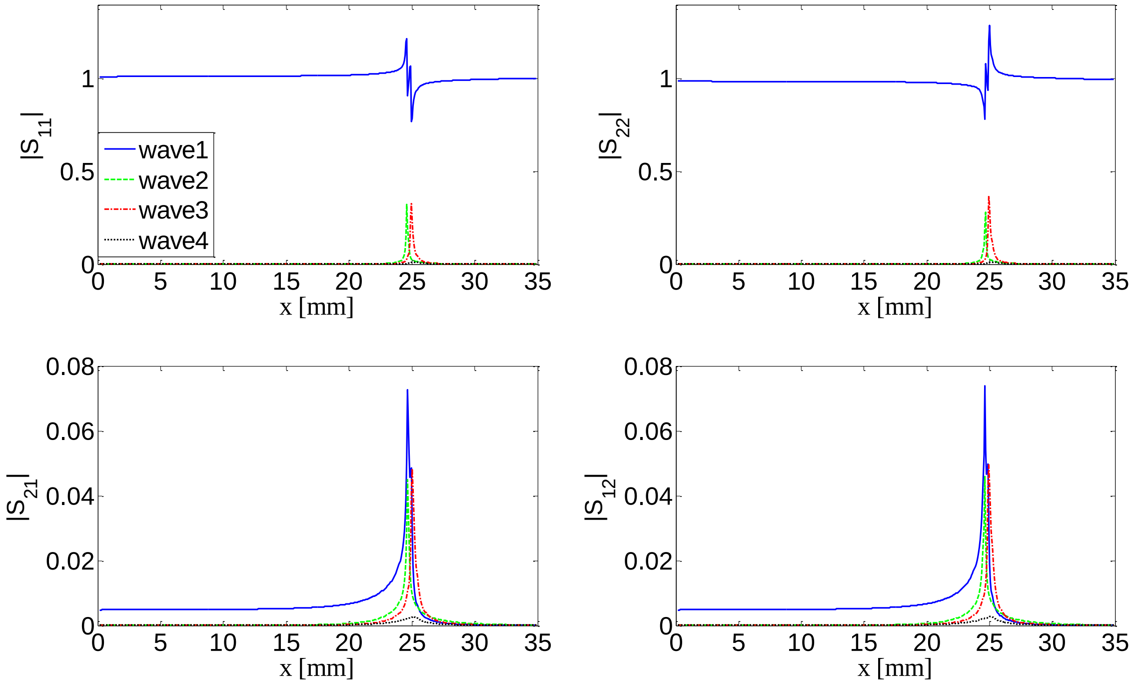

Figure 6.28 The magnitude of the scattering elements at each junction along the cochlea model from mode 1 into other forward-going waves above, and backwards-going waves, below.

Figure 6.28 shows the magnitude of the elements of one column of the scattering matrix in equation (6.74) corresponding the scattering from wave 1 in Figure 6.22 (a) into other forward-going waves, and the reflection of wave 1 into backwards-going waves, below. In Figure 6.28, $\mathbf{S}_{11}$ represents the transmission coefficient from left to right, $\mathbf{S}_{22}$ represents the transmission coefficient from right to left, $\mathbf{S}_{21}$ represents the reflection coefficient on left hand side, $\mathbf{S}_{12}$ represents the reflection coefficient on right hand side.

6.8 Conclusions

Our understanding of the cochlea is largely based, either explicitly or implicitly, on the assumption that only a single type of wave propagates along its length. The properties of this “slow wave” can be calculated from a simple model of the passive cochlea that includes a locally-reacting BM and 1D fluid coupling. The most useful description of such a wave, at a given frequency, is the distribution of the complex wavenumber along the length of the cochlea. The real part of this wavenumber describes the change of phase with distance and determines the wave speed. The imaginary part of the wavenumber describes the change of amplitude with distance and must be negative for a forward-going wave in the passive cochlea, since energy can only be dissipated. Assuming that the wavenumber does not change too rapidly with position, and that the wave travels without interaction from other waves, the coupled response of the cochlea can be deduced from the wavenumber distribution using the WKB method.

In general, however, there are many other mechanisms, apart from 1D fluid coupling, that give rise to longitudinal coupling in the cochlea, even if this is passive. These include the higher order modes associated with 3D fluid coupling and mechanical coupling along the BM. Simple models for both of these effects are considered in order to calculate the wavenumber distributions of the additional waves that they generate. The wavenumber spectrum derived from an approximation to 3D fluid coupling shows that the additional wave in the coupled system has similar characteristics to a cut off acoustic mode in a rigid duct, since the wavenumber is largely imaginary. Mechanical coupling along the BM is modelled by assuming that it behaves as an orthotropic plate, in which case two additional waves are predicted, both of which decay rapidly close to the base, as did the higher order fluid wave. Even though these additional waves may exist, it is not clear what role they play in normal cochlear function. Of particular interest is the extent to which they are excited when the cochlea is driven normally, at the stapes, from the middle ear.

In general the fully coupled response of the cochlea to middle ear excitation can be calculated using a numerical model, such as obtained with the finite element method, although in the insight gained from the wave approach is then lost. The wave finite element, WFE, method is used here to decompose the results of a full finite element model of the coupled cochlea into wave components. The WFE method predicts the properties of as many types of waves as there are degrees of freedom across each cross section of the finite element model. Almost all of the forward-going components of these waves have large negative imaginary components, indicating that they decay away very quickly. Examples of such evanescent waves include the higher order fluid modes and also modes associated with more complicated radial distributions of BM motion than is associated with the slow wave.

The mode shapes associated with the waves predicted from the WFE analysis can then be used to decompose the results of the full finite element model into wave components. In a uniform system there would be no coupling between the modes, but due to the distribution of parameters along the cochlea, the wavenumbers are functions of longitudinal position and one wave is able to excite other types of waves. This is only seen to occur, in the passive cochlea model with the locally reacting BM, in the region where the slow wave is rapidly decaying. It is believed to be associated with the fact that the rapidly decaying slow wave cannot match the boundary conditions. The initial predictions are more complicated if the behaviour when the BM is modelled as an orthotropic plate. The dominant contribution of the slow wave is still observed on the basal side of the peak response, however.

Although additional types of wave are thus predicted to exist, in addition to the conventional slow wave, in the passive cochlea, they do not appear to play a dominant role in normal cochlear function. The framework produced by the WFE method can also be used with more detailed models, of the active cochlea for example, where there are far greater opportunities for additional forms of longitudinal coupling to significantly affect the cochlear response.

Chapter 7. Conclusion and Future Work

This chapter summarises the work has been done in this thesis and the conclusions from the modelling and simulations. Based on this experience some other potential research areas have also been pointed out for the further interest.

7.1 Summary of Present Work

This work consists of two main parts, fluid coupling in the cochlea and the propagation of waves in the cochlea. The work was carried out using both analytic and numerical approaches. The analytic results have been used to validate those from numerical simulation, and the numerical methods provide the possibility of considering more complicated models.

7.1.1 Fluid Coupling in the Cochlea

The coupled behaviour of the linear cochlear dynamics can be expressed using matrix representations of two separate phenomena, assuming only a single radial mode shape for the BM vibration. The first phenomenon is the way that the pressure distribution is determined by the fluid coupling within the cochlear chambers when driven by the BM and stapes velocities, and the second phenomenon is the way in which the BM dynamics respond to the imposed pressure distribution.

In this work the coupled response is studied using a "uniaxial" discrete model that allows the three-dimensional fluid coupling to be described as a function of a single longitudinal variable, assuming a given radial distribution for the BM velocity. This reduces the three-dimensional fluid coupling problem which can be described in terms of far and near-field components down to one with a single dimension. By dividing up the uniaxial formulation into a discrete number of longitudinal sections, the problem becomes tractable numerically, since it can be described using linear algebra. This elemental approach avoids the singularity in the fluid coupling with a continuous spatial domain, by using the Green's function approach, due to the implicit assumption of a spatial delta function for the driving velocity. The near-field component of the fluid coupling was initially obtained from a conventional wavenumber analysis. An approximation based on the theory of acoustic modes in a duct was then derived which was shown to be in a good agreement with the conventional wavenumber analysis. In this way, the near-field component of the fluid coupling can be associated with the evanescent, higher order, modes in the fluid chambers, while the far-field pressure component can be associated with the plane wave, which provides an insight for physical interpretation of the two components.

Realistic longitudinal variations in the geometry, including asymmetric fluid chambers, have also been incorporated into the elemental model of fluid coupling. This includes a new analytic formulation for the far-field component. The coupled responses of the passive cochlea with non-uniform fluid chambers do not, however, look very different from those calculated assuming a uniform cochlea, except for a difference of the accumulation of phase lag.

A finite element model of fluid coupling was also used to provide an independent check of the results of the analytic model. The agreement between the analytic model and the finite element model is reasonably good. An advantage of using a finite element model of the fluid coupling is that various geometric complexities, which are difficult to account for analytically, can be readily incorporated. In this work the flexibility of the finite element method was used to investigate the effect of fluid compressibility and the effects of the coiling on the fluid coupling. Results for the parameters used here show that the coiling does reduce the modal pressure distribution and the coupled BM velocity, especially close to the apex indicating that the coiling decreases the fluid impedance in the apical region. The compressibility is seen to have a huge effect on fluid coupling near a duct resonance, but a far smaller effect on the coupled cochlear response.

7.1.2 Waves in the Cochlea

The wave finite element, WFE, method was introduced and its use extended from previous applications in uniform structures, to also consider structures with slowly changing parameters. Examples were considered of plates whose stiffness varied with position, and also conically shaped shells. The latter are particularly interesting partly because they are relevant to the analysis of loudspeaker cones, and partly because they show a transition from one kind of wave propagation to another, that occurs at a frequency-dependent position along the cone.

The WFE method has the advantage of studying all waves, whose number depends on the number of DOFs in the segment. By combining results of the WFE analysis with the full FE solution, the overall responses have been decomposed into wave component and physical insight can be given in terms of waves.

Using the conventional FE method, the uncoiled cochlea was modelled as a fluid-structural coupled system with three-dimensional fluid and two dimensional BM elements. By driving the stapes at given frequency, a numerical predication of the BM response can be obtained. Two cochlear models, which include the local BM dynamics or longitudinal BM dynamics, are constructed and studied. Generally for both cases, the BM velocity increases gradually to a peak, whose location depends on driving frequency and starts to decrease quickly after the peak which is similar to that predicted using matrix presentations for the discrete cochlear model.

The classic travelling wave theory of the cochlear mechanics is based on the hypothesis that only a single type of wave propagates along cochlear length. In this work, the properties of this “slow wave” were first calculated from an analytic model of the passive cochlea that includes locally-reacting BM and 1D fluid coupling, locally-reacting BM and 3D fluid coupling, longitudinal BM coupling and 1D fluid coupling. For models with 3D fluid coupling or longitudinal BM coupling, the higher order modes associated with 3D fluid coupling or mechanical coupling along the BM give raise to the additional evanescent waves as well as the expected “slow wave”. Assuming that the wavenumber does not change too rapidly with position, and that the wave travels without interaction from other waves, the coupled response of the cochlea can be deduced from the wavenumber distribution using the WKB method.

The WFE method was used to decompose the results of a full finite element model of the coupled cochlea into wave components. The WFE method predicts the properties of as many types of waves as there are degrees of freedom across each cross section of the finite element model. Almost all of the forward-going components of these waves have large negative imaginary components, indicating that they decay away very quickly. The mode shapes associated with the waves predicted from the WFE analysis were used to decompose the results of the full finite element model into wave components. Although many additional types of wave are predicted to exist apart from the “slow wave” in the passive cochlea, they do not appear to play a dominant role in normal passive cochlear function. For a locally reacting passive BM, the overall behaviour of the cochlea to excitation of the stapes can be approximated well by the propagation of a single, slow wave. For a passive BM with longitudinal coupling modelled using the orthotropic plate, the results are similar to those for the locally-reacting BM model, which suggests that longitudinal BM coupling does not play a dominant role in determining the coupled dynamics of the cochlea, at least for the orthotropic parameters assumed in this work.

7.2 Suggestions for Future Research

7.2.1 Refining the Cochlear Model

The fluid coupling in the cochlea has been discussed in detail with 1D and 3D cochlear geometries, but the BM dynamics are assumed to be passive. In the living cochlea at low levels, the amplitude of the "slow wave" will be increased by an active cochlear amplification mechanism, involving the inner and outer hair cells. Henaff *et al*. (Henaff, *et al.*, 2003) developed a cochlear model with 1D fluid coupling and locally-active BM, but did not consider the effect of 3D fluid coupling. An interesting direction is thus to take both the 3D fluid coupling and the active BM into account to predict the coupled response of the cochlea. The non-uniformity, asymmetry and non-linear component could also be included to give a more realistic model of the cochlea.

The flexibility of the meshing allowed in the finite element model gives the possibility of building a more detailed cochlear model with sub-structures, such as the tectorial membrane (TM) and the organ of Corti, to study the interaction between the TM and its local surroundings on the OC (Ghaffari, *et al.*, 2007, Jones, *et al.*, 2011), or active BM to study the active amplification process in the cochlea.

7.2.2 Developing the WFE Method

The problem with the spurious negative-going wave found in the current cochlear model appears to be due to the fact that the eigenvectors of the transfer matrix do not take the spatial variation of the wavenumbers into account, even though this variation changes slowly. One way in which this variation could be accounted for is by assuming a WKB solution to the propagating wave in the definition of the transfer matrix, instead of just a uniformly propagating solution. Some preliminary work has been done (Elliott, *et al.*,

2012) to take the variation into account using a modified transfer matrix and the effect of the spurious negative-going wave then becomes negligible, at about 120 dB below the corresponding positive-going wave at the position of the characteristic place. This suggests that the modified WFE method could be applied to study non-uniform structures by linking the non-uniformity more accurately into account.

7.2.3 Testing the Single Wave Hypothesis

The detailed numerical models of the cochlea used by both Steele *et al*. (Lim and Steele, 2002, Tuck-Lee, *et al.*, 2008, Yoon, *et al.*, 2007) and Chadwick *et al*. (Cai and Chadwick, 2003, Cai, *et al.*, 2004) are only even analysed one cross-section at a time. This analysis is used to identify the wavenumber of a single “slow wave”, which is then assumed to be the only wave of importance so that this overall response can be computed using the WKB approximation. The WFE method developed here provides a way of testing this hypothesis on a more complicated cochlear geometry that only a single wave is of importance by decomposing the overall coupled behaviour into individual wave components.

Appendix A: WKB Approximation to Long Wavelength Component

For a 1D, long wave, model of the cochlea, the 1D Helmholtz equation can be expressed as

$$\frac{\partial^2 p(x,t)}{\partial x^2} = \frac{1}{c(x)^2} \frac{\partial^2 p(x,t)}{\partial t^2}, \tag{A.1}$$

where $c(x)$ is a function with respect to *x*.

Assuming time harmonic vibration, the pressure can be expressed as $p(x,t) = P(x)e^{i\omega t}$, so equation (A.1) can be rewritten as

$$\frac{d^2P(x)}{dx^2} + \frac{\omega^2}{c^2(x)} P = 0. \tag{A.2}$$

We can rewrite equation (A.2) as

$$\varepsilon^2 \frac{d^2P(x)}{dx^2} - Q^2 P(x) = 0, \tag{A.3}$$

where

$$\varepsilon = \omega^{-1}, \tag{A.4}$$

and

$$Q = \frac{i}{c(x)}. \tag{A.5}$$

The approximate solution of equation (A.3) based on the WKB theory can be expressed by a single exponential power series of the form (Bender, 1999)

$$P(x) \approx e^{\frac{1}{\delta}\sum_{j=0}^{n} Z_j \delta^j}, \quad \delta \to 0. \tag{A.6}$$

Differentiating equation (A.6) twice gives

$$\frac{dP(x)}{dx} \approx \left(\frac{1}{\delta} \sum_{j=0}^{n} \frac{dZ_j}{dx} \delta^j \right) e^{\frac{1}{\delta}\sum_{j=0}^{n} Z_j \delta^j}, \quad \delta \to 0, \tag{A.7}$$

and

$$\frac{d^2P(x)}{dx^2} \approx \left[\frac{1}{\delta^2} \left(\sum_{j=0}^{n} \frac{dZ_j}{dx} \delta^j \right)^2 + \frac{1}{\delta} \sum_{j=0}^{n} \frac{d^2Z_j}{dx^2} \delta^j \right] e^{\frac{1}{\delta}\sum_{j=0}^{n} Z_j \delta^j}, \quad \delta \to 0. \tag{A.8}$$

Substituting equations (A.7) and (A.8) into equation (A.3) and dividing off the exponential factors $e^{\frac{1}{\delta}\sum_{j=0}^{n} Z_j \delta^j}$ yields:

$$\frac{\varepsilon^2}{\delta^2} \left(\frac{dZ_0}{dx} \right)^2 + \frac{2\varepsilon^2}{\delta} \left(\frac{dZ_0}{dx} \right) \left(\frac{dZ_1}{dx} \right) + \frac{\varepsilon^2}{\delta} \left(\frac{d^2Z_0}{dx^2} \right) + \cdots = Q^2. \tag{A.9}$$

The largest term on the left side of equation (A.9) is $\frac{\varepsilon^2}{\delta^2} \left(\frac{dZ_0}{dx} \right)^2$. By dominant balance this term must have the same order of magnitude as Q^2 on the right side. Assuming δ is proportional to ε and for simplicity set $\delta = \varepsilon$. After comparing powers of ε gives a sequence of equations which determine Z_0, Z_1, Z_2…

$$\left(\frac{dZ_0}{dx} \right)^2 = Q^2, \quad n = 0, \tag{A.10}$$

$$2 \left(\frac{dZ_0}{dx} \right) \left(\frac{dZ_1}{dx} \right) + \frac{d^2Z_0}{dx^2} = 0, \quad n = 1, \tag{A.11}$$

and

$$2 \frac{dZ_0}{dx} \frac{dZ_n}{dx} + \frac{dZ_{n-1}^2}{dx^2} + \sum_{j=1}^{n-1} \frac{dZ_j}{dx} \frac{dZ_{n-j}}{dx} = 0, \quad n \geq 2. \tag{A.12}$$

The equation (A.10) is called the *eikonal* equation and its solution is

$$Z_0 = \pm \int_0^x Q dx'. \tag{A.13}$$

Substituting equation (A.13) into equation (A.11) and after integration

$$Z_1 = -\frac{1}{2}\ln Q. \tag{A.14}$$

Substituting equations (A.13) and (A.14) into equation (A.6) gives the **first order** approximation to the equation (A.3) as

$$P(x) \approx \frac{C_1}{\sqrt{Q}}\exp\left(-\frac{1}{\varepsilon}Z_0\right) + \frac{C_2}{\sqrt{Q}}\exp\left(\frac{1}{\varepsilon}Z_0\right), \tag{A.15}$$

where C_1 and C_2 are constants to be determined from initial conditions.

The first order WKB approximations to pressure are given by

$$P^{(1)}(x) = \frac{C_1}{\sqrt{Q}}\exp\left(\omega\int_0^x Q dx'\right) + \frac{C_2}{\sqrt{Q}}\exp\left(-\omega\int_0^x Q dx'\right). \tag{A.16}$$

Substituting $Q = i/c(x)$ into equation (A.16) gives

$$P^{(1)}(x) = \frac{A_1}{\sqrt{k(x)}}\exp\left(i\int_0^x k(x) dx'\right) + \frac{A_2}{\sqrt{k(x)}}\exp\left(-i\int_0^x k(x) dx'\right). \tag{A.17}$$

If only forward travelling wave is concerned, the pressure due to far-field component in the cochlea can be expressed as

$$P(x) = \frac{A}{\sqrt{k(x)}}\exp\left(-i\int_0^x k(x) dx'\right). \tag{A.18}$$

where *A* is a coefficient needs to be determined.

For the cochlear model, the 1D fluid coupling equation is given by

$$\frac{\partial^2 P(x)}{\partial x^2} = -\frac{2i\omega\rho}{h}\ V(x), \tag{A.19}$$

so the local BM velocity, *V*(x), is related to the pressure by

$$V(x)=\frac{h\,k^2(x)}{2i\omega\rho}P(x). \tag{A.20}$$

The BM velocity distribution can thus be calculated from the pressure distribution as

$$V(x)=\frac{Ah}{2i\omega\rho}k(x)^{3/2}e^{-i\int_0^x k(x)dx'}. \tag{A.21}$$

Since $v(x)=-Y_{\mathrm{BM}}(x)\,p(x)$, that if $p(x)$ is given by equation (6.17), the general WKB approximation for $v(x)$ should be

$$v(x)=-Y_{\mathrm{BM}}(x)\frac{A}{\sqrt{k(x)}}e^{-i\phi(x)}, \tag{A.22}$$

where $Y_{\mathrm{BM}}(x)$ is the mobility of the BM. In this 1D fluid coupling case, then from equation (6.7) we can obtain

$$Y_{\mathrm{BM}}(x)=\frac{ik^2(x)h}{2\omega\rho}, \tag{A.23}$$

so that

$$v(x)=\frac{Ak^{3/2}(x)h}{2i\omega\rho}e^{-i\phi(x)}. \tag{A.24}$$

Figure A. 1 shows a comparison of the modal BM velocity calculated using equation (6.33)and (A.22). Although there is no visual difference can be found, equation (A.22) provides a more general form of the WKB approximation for the modal BM velocity.

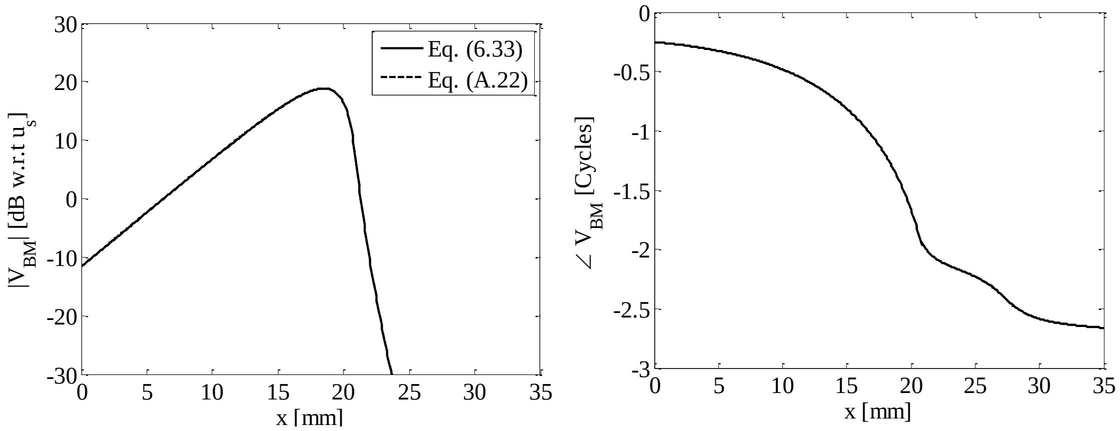

Figure A. 1 A comparison between the BM velocities using equation (6.33), solid lines, and equation (A.22), dashed lines, calculated at an excitation frequency of 1 kHz, for the wave due to the interaction between the local, passive, BM dynamics and the 3D fluid coupling with a constant damping ratio, ζ_0=0.1.

Appendix B: Condensation of Internal Nodes

In this appendix, several methods are described for condensing the internal DOFs of a section. The condensations can be used to reduce the round-off errors of inertia terms and also eliminate longitudinal coupling in the locally-reacting cochlear model used in this thesis for example. The methods do not need to remodel the section since the global stiffness and mass matrices can be formed from those of the original section (Petyt, 1990). If the section has internal nodes which are not condensed, equation (5.4) can be expressed as

$$\begin{bmatrix} \tilde{\mathbf{D}}_{\mathrm{EE}} & \tilde{\mathbf{D}}_{\mathrm{EI}} \\ \tilde{\mathbf{D}}_{\mathrm{IE}} & \tilde{\mathbf{D}}_{\mathrm{II}} \end{bmatrix} \begin{bmatrix} \mathbf{q}_{\mathrm{E}} \\ \mathbf{q}_{\mathrm{I}} \end{bmatrix} = \begin{bmatrix} \mathbf{f}_{\mathrm{E}} \\ 0 \end{bmatrix}, \tag{B.1}$$

where

$$\begin{cases} \tilde{\mathbf{D}}_{\mathrm{EE}} = \begin{bmatrix} \tilde{\mathbf{D}}_{\mathrm{LL}} & \tilde{\mathbf{D}}_{\mathrm{LR}} \\ \tilde{\mathbf{D}}_{\mathrm{RL}} & \tilde{\mathbf{D}}_{\mathrm{RR}} \end{bmatrix} \\ \tilde{\mathbf{D}}_{\mathrm{EI}} = \begin{bmatrix} \tilde{\mathbf{D}}_{\mathrm{LI}} \\ \tilde{\mathbf{D}}_{\mathrm{RI}} \end{bmatrix} \\ \tilde{\mathbf{D}}_{\mathrm{IE}} = \begin{bmatrix} \tilde{\mathbf{D}}_{\mathrm{IL}} & \tilde{\mathbf{D}}_{\mathrm{IR}} \end{bmatrix} \\ \mathbf{q}_{\mathrm{E}} = \begin{bmatrix} \mathbf{q}_{\mathrm{L}} \\ \mathbf{q}_{\mathrm{R}} \end{bmatrix} \\ \mathbf{f}_{\mathrm{E}} = \begin{bmatrix} \mathbf{f}_{\mathrm{L}} \\ \mathbf{f}_{\mathrm{R}} \end{bmatrix} \end{cases}, \tag{B.2}$$

and the superscript ~ denotes that the section has internal nodes and have not been condensed. The subscript E and I represent that DOFs are associated with edge nodes or internal nodes of the section respectively. When the section has internal nodes, the DOFs associated with the internal nodes always need to be condensed. Three ways to condense the DOFs associated with the internal nodes are described here.

(1) ***Dynamic Condensation*** (Friswell and Mottershead, 1995)

The internal DOFs can be dynamically condensed by rewriting equation (B.1) as

$$\tilde{\mathbf{J}}^{\mathrm{T}}\tilde{\mathbf{D}}\tilde{\mathbf{J}}\mathbf{q}_{\mathrm{E}} = \mathbf{f}_{\mathrm{E}}, \tag{B.3}$$

where

$$\tilde{\mathbf{J}} = \begin{bmatrix} \mathbf{I} \\ -\tilde{\mathbf{D}}_{\mathrm{II}}^{-1}\tilde{\mathbf{D}}_{\mathrm{IE}} \end{bmatrix}, \tag{B.4}$$

and the superscript T denotes the transpose, $\mathbf{I}$ indicates the identity matrix. The matrix $\tilde{\mathbf{J}}$ transforms the original basis into the condensed basis. Substituting relation (B.4) into equation (B.3) and expanding gives

$$\mathbf{D}\mathbf{q}_{\mathrm{E}} = \mathbf{f}_{\mathrm{E}}, \tag{B.5}$$

where

$$\mathbf{D} = \tilde{\mathbf{D}}_{\mathrm{EE}} - \tilde{\mathbf{D}}_{\mathrm{EI}}\tilde{\mathbf{D}}_{\mathrm{II}}^{-1}\tilde{\mathbf{D}}_{\mathrm{IE}}, \tag{B.6}$$

is the condensed dynamic stiffness matrix. These dynamically condensed element matrices become frequency dependent and the dynamic condensation method is used throughout this thesis.

(2) ***Static Condensation*** (Friswell and Mottershead, 1995)

The inverse of the dynamic stiffness matrix associated with internal DOFs can be expressed as

$$\tilde{\mathbf{D}}_{\mathrm{II}}^{-1} = \left(\tilde{\mathbf{K}}_{\mathrm{II}} - \omega^2\tilde{\mathbf{M}}_{\mathrm{II}}\right)^{-1} = \left(\mathbf{I} - \omega^2\tilde{\mathbf{K}}_{\mathrm{II}}^{-1}\tilde{\mathbf{M}}_{\mathrm{II}}\right)^{-1}\tilde{\mathbf{K}}_{\mathrm{II}}^{-1}. \tag{B.7}$$

For small $\tilde{\mathbf{K}}_{\mathrm{II}}^{-1}\tilde{\mathbf{M}}_{\mathrm{II}}$, equation (B.7) can be approximated as

$$\tilde{\mathbf{D}}_{\mathrm{II}}^{-1} = \tilde{\mathbf{K}}_{\mathrm{II}}^{-1} + O\left(\omega^2\tilde{\mathbf{K}}_{\mathrm{II}}^{-1}\tilde{\mathbf{M}}_{\mathrm{II}}\tilde{\mathbf{K}}_{\mathrm{II}}^{-1}\right). \tag{B.8}$$

According to equation (B.5), the condensed dynamic matrix is expanded as

$$\begin{aligned} \mathbf{D} &= \tilde{\mathbf{D}}_{\mathrm{EE}} - \tilde{\mathbf{D}}_{\mathrm{EI}}\tilde{\mathbf{D}}_{\mathrm{II}}^{-1}\tilde{\mathbf{D}}_{\mathrm{IE}} \\ &\approx \tilde{\mathbf{K}}_{\mathrm{EE}} - \tilde{\mathbf{K}}_{\mathrm{EI}}\tilde{\mathbf{K}}_{\mathrm{II}}^{-1}\tilde{\mathbf{K}}_{\mathrm{IE}} - \omega^2\left(\tilde{\mathbf{M}}_{\mathrm{EE}} - \tilde{\mathbf{K}}_{\mathrm{EI}}\tilde{\mathbf{K}}_{\mathrm{II}}^{-1}\tilde{\mathbf{M}}_{\mathrm{IE}} - \tilde{\mathbf{M}}_{\mathrm{EI}}\tilde{\mathbf{K}}_{\mathrm{II}}^{-1}\tilde{\mathbf{K}}_{\mathrm{IE}}\right). \end{aligned} \tag{B.9}$$

For small ω, the condensed stiffness and mass matrices can be approximated by

$$\begin{aligned}\mathbf{K} &\approx \tilde{\mathbf{K}}_{\mathrm{EE}} - \tilde{\mathbf{K}}_{\mathrm{EI}}\tilde{\mathbf{K}}_{\mathrm{II}}^{-1}\tilde{\mathbf{K}}_{\mathrm{IE}},\\ \mathbf{M} &\approx \tilde{\mathbf{M}}_{\mathrm{EE}} - \tilde{\mathbf{K}}_{\mathrm{EI}}\tilde{\mathbf{K}}_{\mathrm{II}}^{-1}\tilde{\mathbf{M}}_{\mathrm{IE}} - \tilde{\mathbf{M}}_{\mathrm{EI}}\tilde{\mathbf{K}}_{\mathrm{II}}^{-1}\tilde{\mathbf{K}}_{\mathrm{IE}}.\end{aligned} \tag{B.10}$$

It should be noted that this static condensation is only accurate at very low frequencies (Waki, *et al.*, 2006) since the inertia associated with $\tilde{\mathbf{D}}_{\mathrm{II}}$ is removed.

(3) ***The Second Order Approximation*** (Waki, 2007)

Equation (B.7) can be expanded to the second order as

$$\begin{aligned}\tilde{\mathbf{D}}_{\mathrm{II}}^{-1} = &\left(\mathbf{I} + \omega^2\tilde{\mathbf{K}}_{\mathrm{II}}^{-1}\tilde{\mathbf{M}}_{\mathrm{II}}\right)^{-1}\tilde{\mathbf{K}}_{\mathrm{II}}^{-1}\\ &+ O\left(\omega^4\tilde{\mathbf{K}}_{\mathrm{II}}^{-1}\tilde{\mathbf{M}}_{\mathrm{II}}\tilde{\mathbf{K}}_{\mathrm{II}}^{-1}\tilde{\mathbf{M}}_{\mathrm{II}}\tilde{\mathbf{K}}_{\mathrm{II}}^{-1}\right).\end{aligned} \tag{B.11}$$

Then condensed dynamic matrix $\mathbf{D}$ can be given by

$$\begin{aligned}\mathbf{D} \approx\ & \tilde{\mathbf{K}}_{\mathrm{EE}} - \tilde{\mathbf{K}}_{\mathrm{EI}}\tilde{\mathbf{K}}_{\mathrm{II}}^{-1}\tilde{\mathbf{K}}_{\mathrm{IE}}\\ & -\omega^2\left(\tilde{\mathbf{M}}_{\mathrm{EE}} - \tilde{\mathbf{K}}_{\mathrm{EI}}\tilde{\mathbf{K}}_{\mathrm{II}}^{-1}\tilde{\mathbf{M}}_{\mathrm{IE}} - \tilde{\mathbf{M}}_{\mathrm{EI}}\tilde{\mathbf{K}}_{\mathrm{II}}^{-1}\tilde{\mathbf{K}}_{\mathrm{IE}} + \tilde{\mathbf{K}}_{\mathrm{EI}}\tilde{\mathbf{K}}_{\mathrm{II}}^{-1}\tilde{\mathbf{M}}_{\mathrm{II}}\tilde{\mathbf{K}}_{\mathrm{II}}^{-1}\tilde{\mathbf{K}}_{\mathrm{IE}}\right)\\ & -\omega^4\left(\tilde{\mathbf{M}}_{\mathrm{EI}}\tilde{\mathbf{K}}_{\mathrm{II}}^{-1}\tilde{\mathbf{M}}_{\mathrm{IE}} - \tilde{\mathbf{K}}_{\mathrm{EI}}\tilde{\mathbf{K}}_{\mathrm{II}}^{-1}\tilde{\mathbf{M}}_{\mathrm{II}}\tilde{\mathbf{K}}_{\mathrm{II}}^{-1}\tilde{\mathbf{M}}_{\mathrm{IE}} - \tilde{\mathbf{M}}_{\mathrm{EI}}\tilde{\mathbf{K}}_{\mathrm{II}}^{-1}\tilde{\mathbf{M}}_{\mathrm{II}}\tilde{\mathbf{K}}_{\mathrm{II}}^{-1}\tilde{\mathbf{K}}_{\mathrm{IE}}\right).\end{aligned} \tag{B.12}$$

Similarly, the condensed stiffness and mass matrices can be expressed as

$$\begin{aligned}\mathbf{K} =\ & \tilde{\mathbf{K}}_{\mathrm{EE}} - \tilde{\mathbf{K}}_{\mathrm{EI}}\tilde{\mathbf{K}}_{\mathrm{II}}^{-1}\tilde{\mathbf{K}}_{\mathrm{IE}}\\ & + \omega^4\left(\tilde{\mathbf{M}}_{\mathrm{EI}}\tilde{\mathbf{K}}_{\mathrm{II}}^{-1}\tilde{\mathbf{M}}_{\mathrm{IE}} - \tilde{\mathbf{K}}_{\mathrm{EI}}\tilde{\mathbf{K}}_{\mathrm{II}}^{-1}\tilde{\mathbf{M}}_{\mathrm{II}}\tilde{\mathbf{K}}_{\mathrm{II}}^{-1}\tilde{\mathbf{M}}_{\mathrm{IE}} - \tilde{\mathbf{M}}_{\mathrm{EI}}\tilde{\mathbf{K}}_{\mathrm{II}}^{-1}\tilde{\mathbf{M}}_{\mathrm{II}}\tilde{\mathbf{K}}_{\mathrm{II}}^{-1}\tilde{\mathbf{K}}_{\mathrm{IE}}\right),\\ \mathbf{M} =\ & \tilde{\mathbf{M}}_{\mathrm{EE}} - \tilde{\mathbf{K}}_{\mathrm{EI}}\tilde{\mathbf{K}}_{\mathrm{II}}^{-1}\tilde{\mathbf{M}}_{\mathrm{IE}} - \tilde{\mathbf{M}}_{\mathrm{EI}}\tilde{\mathbf{K}}_{\mathrm{II}}^{-1}\tilde{\mathbf{K}}_{\mathrm{IE}} + \tilde{\mathbf{K}}_{\mathrm{EI}}\tilde{\mathbf{K}}_{\mathrm{II}}^{-1}\tilde{\mathbf{M}}_{\mathrm{II}}\tilde{\mathbf{K}}_{\mathrm{II}}^{-1}\tilde{\mathbf{K}}_{\mathrm{IE}}\\ & + 2\omega^2\left(\tilde{\mathbf{M}}_{\mathrm{EI}}\tilde{\mathbf{K}}_{\mathrm{II}}^{-1}\tilde{\mathbf{M}}_{\mathrm{IE}} - \tilde{\mathbf{K}}_{\mathrm{EI}}\tilde{\mathbf{K}}_{\mathrm{II}}^{-1}\tilde{\mathbf{M}}_{\mathrm{II}}\tilde{\mathbf{K}}_{\mathrm{II}}^{-1}\tilde{\mathbf{M}}_{\mathrm{IE}} - \tilde{\mathbf{M}}_{\mathrm{EI}}\tilde{\mathbf{K}}_{\mathrm{II}}^{-1}\tilde{\mathbf{M}}_{\mathrm{II}}\tilde{\mathbf{K}}_{\mathrm{II}}^{-1}\tilde{\mathbf{K}}_{\mathrm{IE}}\right).\end{aligned} \tag{B.13}$$

The numerical results obtained by applying the second order approximation are much more accurate than the static condensation for wide range of frequency (Waki, *et al.*, 2006).

Appendix C: Wavenumber of an Orthotropic Plate Strip

C.1 Uniform Orthotropic Plate Strip

The governing equation of a bending orthotropic plate can be expressed as (Leissa, 1969)

$$\begin{aligned}\frac{\partial^2}{\partial x^2}\left(D_x\frac{\partial^2 w(x,y)}{\partial x^2}+D_{xy}\frac{\partial^2 w(x,y)}{\partial y^2}\right)+4\frac{\partial^2}{\partial x\partial y}\left(D_s\frac{\partial^2 w(x,y)}{\partial x\partial y}\right)\\+\frac{\partial^2}{\partial y^2}\left(D_y\frac{\partial^2 w(x,y)}{\partial y^2}+D_{xy}\frac{\partial^2 w(x,y)}{\partial x^2}\right)+\rho\frac{\partial^2 w}{\partial t^2}=0,\end{aligned}\tag{C.1}$$

where $w(x,y)$ is transfer displacement, ρ is the density of the plate material, D_x, D_{xy} and D_y are the orthotropic bending stiffness in the *x* and *y* directions, respectively, and D_s is torsional rigidity.

The assumption of simple harmonic motion and constant material properties gives

$$\begin{aligned}D_x\frac{\partial^4 w(x,y)}{\partial x^4}+2D_{xy}\frac{\partial^4 w(x,y)}{\partial x^2\partial y^2}+4D_s\frac{\partial^4 w(x,y)}{\partial x^2\partial y^2}\\+D_y\frac{\partial^4 w(x,y)}{\partial y^4}=\rho\omega^2 w(x,y).\end{aligned}\tag{C.2}$$

It is difficult to find an analytic wavenumber of such a complicated structure, however, the advantage of numerical method, such as the WFE method, allows solving the wavenumber distribution of this bending orthotropic plate numerically.

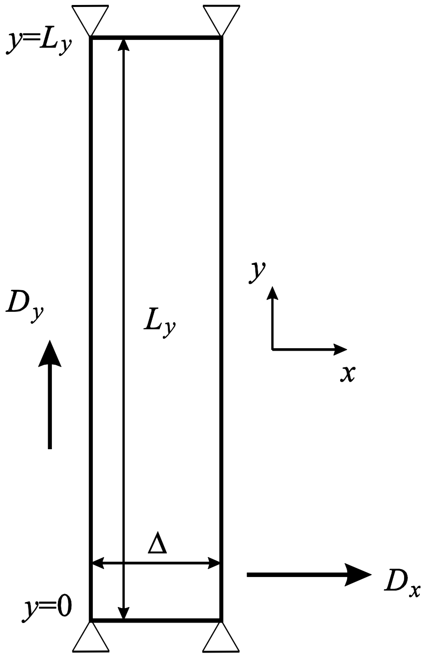

Figure C.1 Diagram of an orthotropic plate with edges y = 0 and y = L_y simply supported.

In this case it is assumed that L_y = 0.16 m, E_y = 2.1×10^{11} Pa, ρ = 7,800 kg/m^3, h = 0.002 m and υ = 0.30. Results were calculated at different ratio of D_x/D_y to illustrate effects of the orthotropy. When D_x/D_y =1, which means the plate is actually isotropic, predicted dispersion curves are identical to Figure 5.5.

To explore the effect of the orthotropy, several values for the ratio of D_x/D_y were used to calculate the corresponding dispersion curves of the orthotropic plate and shown in Figure C. 1. It can be found even when the orthotropy has been introduced the cut-off frequency does not change with the ratio D_x/D_y, since the value of D_y which determines ω_n in equation (5.25) is assumed to be the same as that in the isotropic case. However, the ratio D_x/D_y does have an influence on wave speed above the cut-off frequency and the decay length below the cut-off frequency. The wave speed is determined by the real part of the wavenumber and can be given by

$$c = \frac{\omega}{\Re(k)}, \tag{C.3}$$

and the decaying length is determined by the imaginary part of the wavenumber and can be given by

$$l = \frac{1}{\Im(k)}. \tag{C.4}$$

The variation of wave speed at 400 Hz and decaying length at 0 Hz against can be seen in Figure C. 2. It can be found that as the plate becomes more orthotropic, so that D_x/D_y becomes smaller, the wave speed decreases, since the plate tends towards being locally reacting and the wave cannot propagate in the limit of $D_x/D_y=0$. The decaying length also decreases as the ratio of D_x/D_y decreases, indicating the wave decreases much faster if the plate is more isolated. The other issue raised by the orthotropy is that at very low frequencies, the real part of the wavenumber is not zero as it is for the isotropic case, but the value is much smaller than the corresponding imaginary part and thus will not play a significant part in wave propagation.

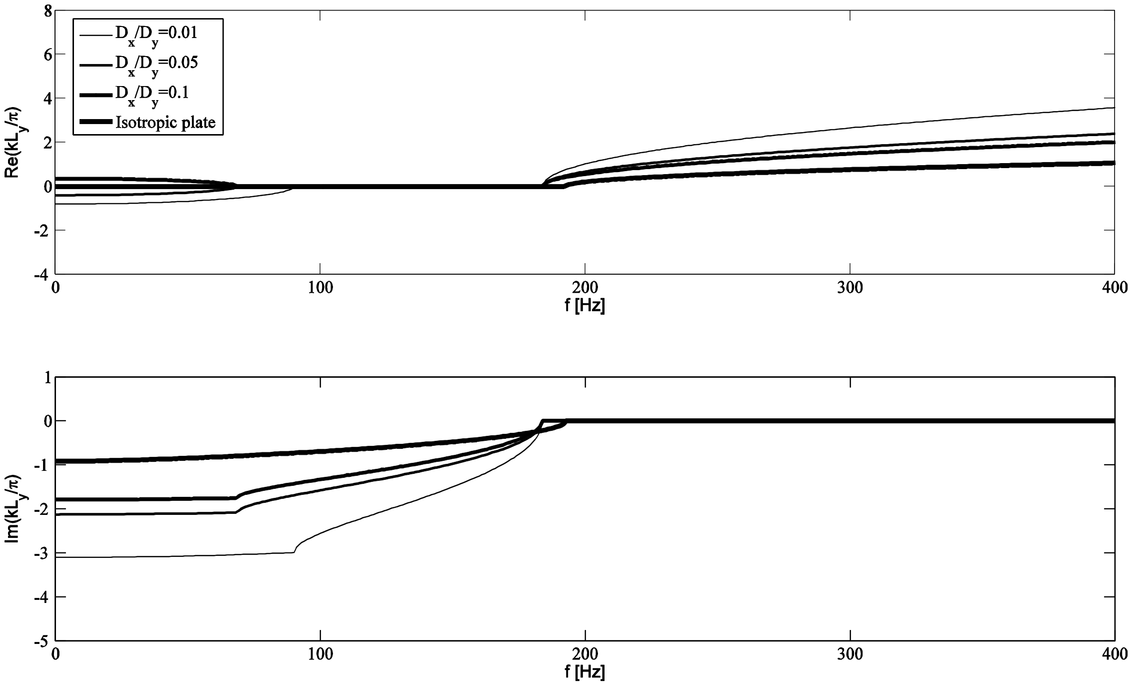

Figure C. 1 Dispersion curves for flexural waves in an orthotropic plate strip with simply-supported edges for different D_x/D_y values. The solid lines are for the real part of the wavenumber (above) and the dashed lines are for the imaginary part of the wavenumber (bottom).

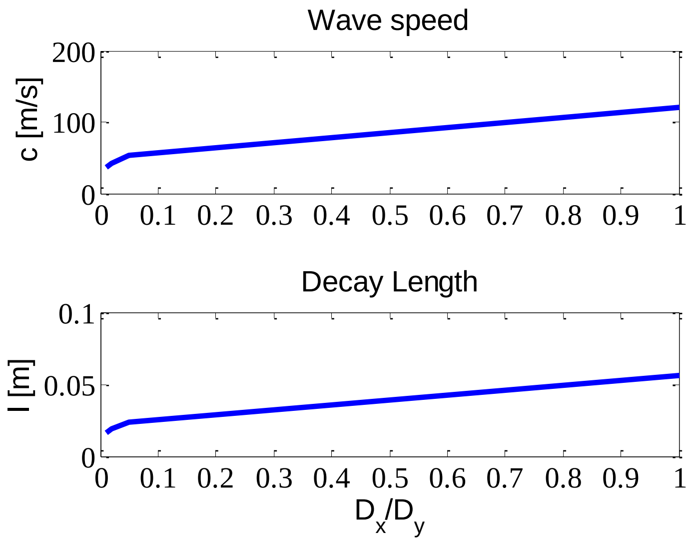

Figure C. 2 Variation of wave speed at 400 Hz and decay length at 0 Hz again the ratio of D_x/D_y for the orthotropic plate example.

As long as the property D_y is constant, the cut-off frequency remains the same, even for different ratios of D_x/D_y. When the orthotropy is increased, namely D_x/D_y decreasing, the wave speed decreases and also the wave decays slower below the cut-off frequency, as the plate tends towards being locally reacting.

C.2 Non-uniform Orthotropic Plate Strip

For the orthotropic plate case, whose D_y is identical to E of the isotropic plate and D_x/D_y =0.05, the dispersion curves can be seen in Figure C. 3. The dispersion curves are similar to those observed in non-uniform isotropic plate beyond the cut-off position, but waves are more complicated and decay much faster before the cut-off position than those in the isotropic plate.

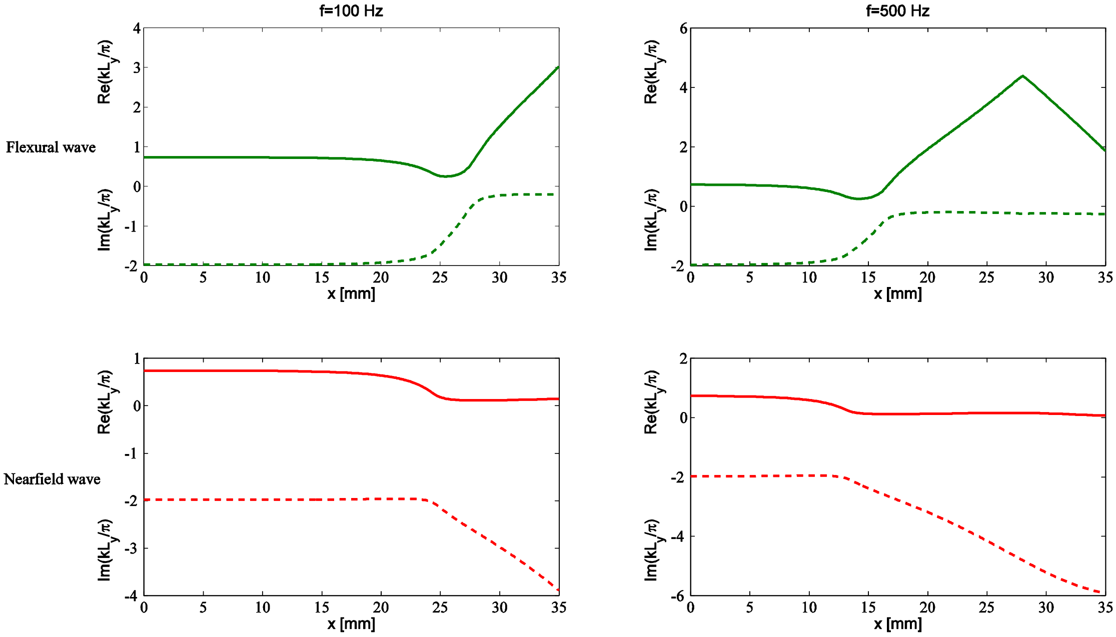

Figure C. 3 Flexural waves in an orthotropic plate strip at 100 Hz (left column) and 500 Hz (right column) with simply-supported boundary edges when the flexural rigidity D_y varies exponentially along the x direction and D_x/D_y is taken as 0.05 all along the plate. Solid lines for the real part of the wavenumber and dashed lines for the imaginary part of the wavenumber.

The non-uniform orthotropic plate strips also give a similar wavenumber distribution to the non-uniform isotropic case, apart from the real part of the wavenumber no longer being zero before the cut-off position, which is due to the effect of the orthotropy.

Appendix D: Factors Influencing the Dynamics and Waves in the Cochlea

D.1 Effect of BM Boundary Conditions

The basilar membrane, BM, is a stiff structural element which separates two fluid chambers that run along the cochlea, the scala media and the scala tympani. The BM converts sound-evoked pressure differences between the two chambers into transverse structural motion. This transverse motion then is converted into shearing motion between the tectorial membrane and reticular lamina, which excites the inner and outer hair cells and gives rise to the perception of hearing (Dallos, *et al.*, 1996). The distribution of the transverse motion across the width of the BM is complicated and level-dependant in the real cochlea (Cooper, 1999). Homer and Champneys (Homer, *et al.*, 2004) developed a mathematical beam model of the BM to study the effect of boundary conditions at the two ends and by comparing their predictions with experimental data (Cooper, 1999), they found that the best fit is obtained by assuming the BM is simply supported at the arcuate end and clamped at the other end.

The purpose of this section is to investigate the effect of different radial BM velocity distributions on the fluid coupling and the coupled response in the cochlea. Various BM radial profiles are defined analytically using an Euler-Bernoulli beam model for the BM, with different boundary conditions. A discrete model of the cochlea (Elliott, *et al.*, 2011), which assumes a single mode across the width of the BM, is used to study the fluid coupling, although it is noted that other, finite element, models make the same assumption (Ramamoorthy, *et al.*, 2007, Steele, 1974, Steele and Taber, 1979). Although the shape of the BM radial velocity distribution is seen to depend on the boundary conditions at the two ends of the BM, the fluid coupling is seen to be relatively insensitive to these variations.

The BM mode shape is assumed to be that of an Euler-Bernoulli beam with various boundary conditions (Homer, *et al.*, 2004). The beam is assumed to have a constant bending stiffness *EI* in the BM radial direction, where *E* is the elastic modulus and *I* is the area moment of inertia. Then the equation governing the transverse displacement *w*, as a function of position along the beam, is given by

$$EI\frac{\partial^4 w(y,t)}{\partial y^4}+\rho_{\mathrm{b}} A\frac{\partial^2 w(y,t)}{\partial t^2}=0, \tag{D.1}$$

where ρ_{b} is the beam density and A is the cross-sectional area. For time harmonic vibration, the transverse displacement and the natural frequency of the beam are given by (Rao, 2004)

$$W(y)=C_1\cos(\beta y)+C_2\sin(\beta y)+C_3\cosh(\beta y)+C_4\sinh(\beta y), \tag{D.2}$$

and

$$\omega_n=\alpha\sqrt{\frac{EI}{\rho AB^4}}, \tag{D.3}$$

where B is the width of the BM, C_1, C_2, C_3, C_4 and α are coefficients depend on boundary conditions. The values of the non-dimensional constant, $\alpha=(\beta B)^2$, which determines beam natural frequency, for the four combinations of boundary conditions are reported in Table D. 1.

Table D. 1 Effective thickness and equivalent height at different BM boundary conditions.

Boundary conditions		Normalized equivalent height *h*/*H*	Normalized effective thickness *T*/*H*	Coefficient *α*
y=0	y=*B*			
Simply supported (S)	Simply supported (S)	4.11	0.177	π^2
Simply supported (S)	Clamped (C)	4.51	0.173	15.4
Clamped (C)	Simply supported (S)	4.51	0.160	15.4
Clamped (C)	Clamped (C)	4.80	0.158	22.1

In this study, we consider four possible combinations of clamped ($W=0$, $dW/dy=0$) and simply supported ($W=0$, $d^2W/dy^2=0$) boundary conditions at the two ends of the BM. Throughout this paper we use *C* to represent clamped boundary condition and *S* to represent simply supported boundary condition. The modal shape of the BM with different boundary condition can be seen in Figure D. 1 (a). In the cases of S-C and C-S the BM motion is asymmetric about the BM's mid-point, whereas the cases of S-S and

C-C the BM motion is symmetric. The experimentally measured shape of the transverse BM velocity is, in fact, most closely modelled as having a simply supported boundary condition at one end and a clamped boundary condition at the other (Homer, *et al.*, 2004). Whereas the exact expressions for the BM modal shapes, except for the simply supported boundary conditions at both ends, have no explicit form, so the results for the fluid coupling and later the coupled response are calculated numerically approximating the integrals in equations (2.14) and (2.15) by the sum of 200 terms.

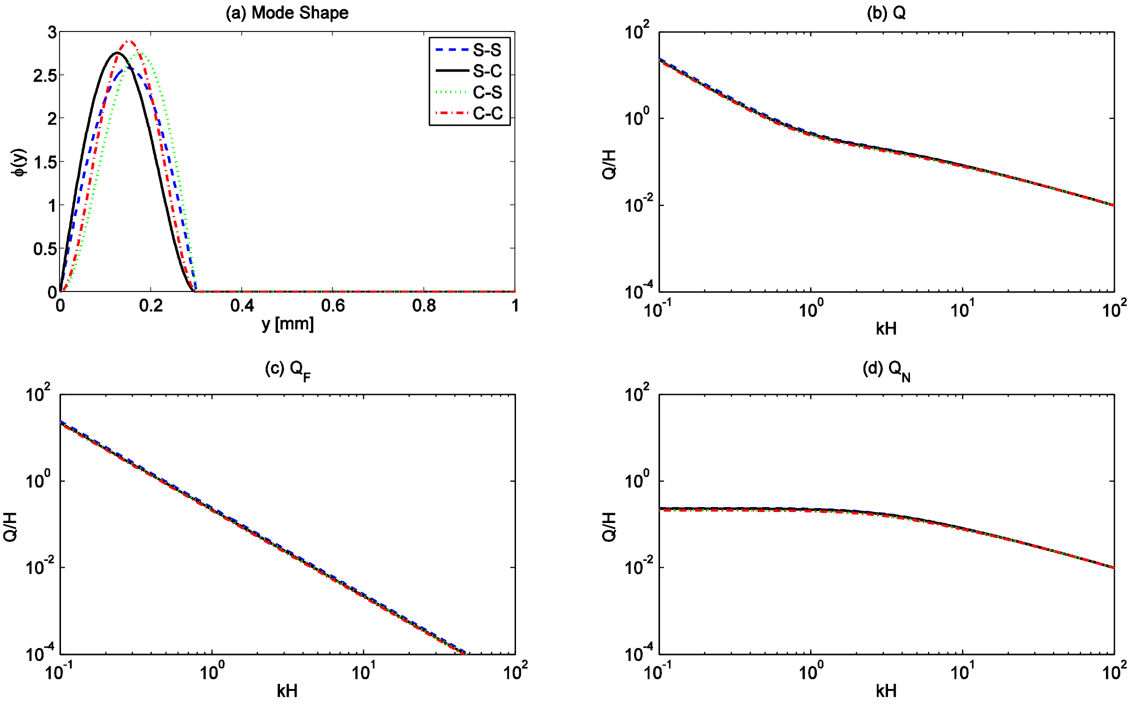

Figure D. 1 The (a) normalized mode shape, (b) total equivalent height due to fluid coupling as a function of wavenumber, (c) equivalent height due to far-field component and (d) equivalent height due to near-field component, calculated from the discrete model with different boundary conditions.

Figure D. 1 shows the variations of $Q(k)/H$ with kH, where H is the physical height of one fluid chamber, for the parameters listed in Table 2.1 with different BM boundary conditions. The BM is assumed to be located on one side of the cochlear partition, as shown in Figure D. 1 (a) and to have a width, B, where is assumed to be $0.3W$ here. Figure D. 1 (c) and (d), show the two components of $Q(k)$, corresponding to the far-field and near-field components for the various boundary conditions. For small values of k the near-field term becomes a constant which can be interpreted as an effective fluid thickness, T, due to the fluid coupling, which adds to the physical mass of the BM (Neely, 1985). The values of T, calculated from Figure D. 1 (d) as k tends to zero, are listed in Table D. 1, and change slightly with different BM boundary conditions, indicating that the effect of BM radial motion distribution is small on the near-field component of the fluid coupling.

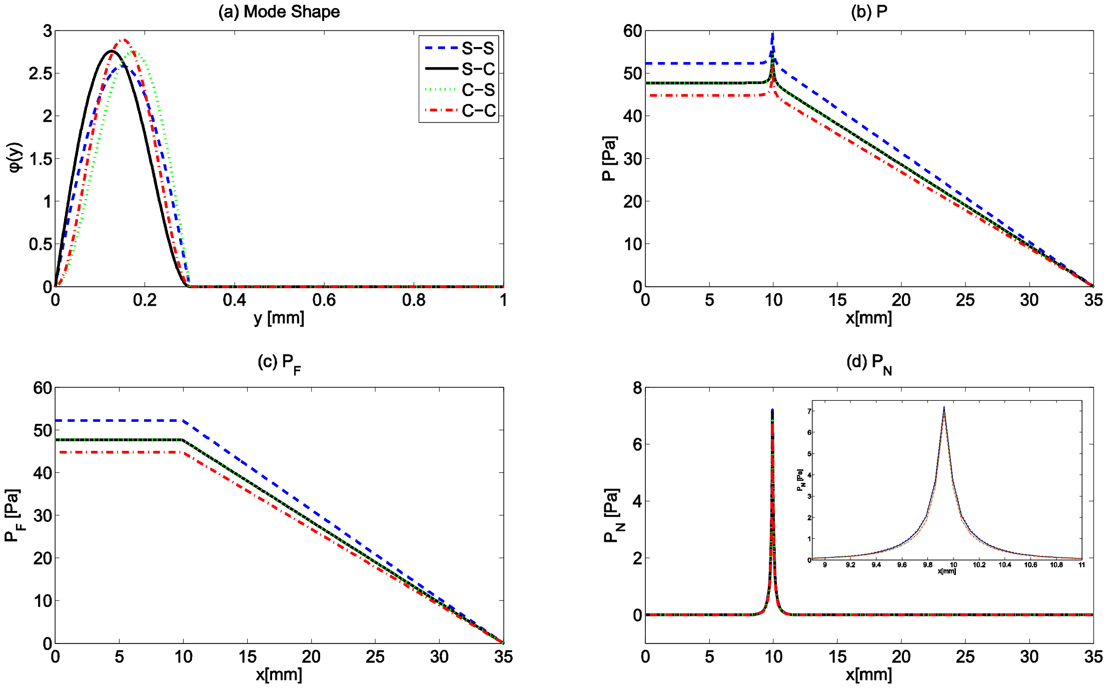

Figure D. 2 Spatial distribution of the pressure difference along the cochlea due to the far field component of the fluid coupling when only a single element of the 512 elements in the discrete BM at x=10 mm is driven sinusoidally with a velocity of 10 mm s^{-1} at a frequency of 1 kHz. The (a) normalized mode shapes are again shown together with the distribution of (b) overall fluid pressure difference which is the divided into (c) far-field and (d) near-field components.

Figure D. 2 shows spatial distribution of the pressure difference, also split into far and near field components, along the cochlea when only a single element of the 512 elements in the discrete BM at x=10 mm is driven sinusoidally with a velocity of 10 mm s^{-1} at a frequency of 1 kHz. These are calculated by numerically taking the Inverse Fourier Transform of the wavenumber results (Elliott, *et al.*, 2011) and show the differences between the assumed boundary conditions more clearly since they are plotted on a linear scale. It can be seen that the boundary conditions do not affect the pressure difference due to the near-field component very much, since the equivalent thickness, T, which determines the near-field fluid coupling, is relatively insensitive to the assumed boundary conditions. The magnitude of the far-field fluid coupling does vary somewhat with different assumed boundary conditions, however, since the far-field fluid coupling is inversely proportional to the equivalent height, *h*, which does change with the assumed boundary condition according to equation (2.26). Given the fluid coupling impedances and assuming a single degree of freedom model for a passive BM, the coupled response of the cochlea can now be calculated using equation (1.19).

Figure D. 3 shows a comparison of the predicted BM velocity distribution, calculated using the discrete model of the passive cochlea, with different assumed BM boundary conditions. The BM dynamics are modelled by locally-reacting single degree of freedom models with the parameters shown in Table 2.1. The magnitudes are similar for all conditions, although the final phase lag is somewhat larger for the S-S boundary conditions.

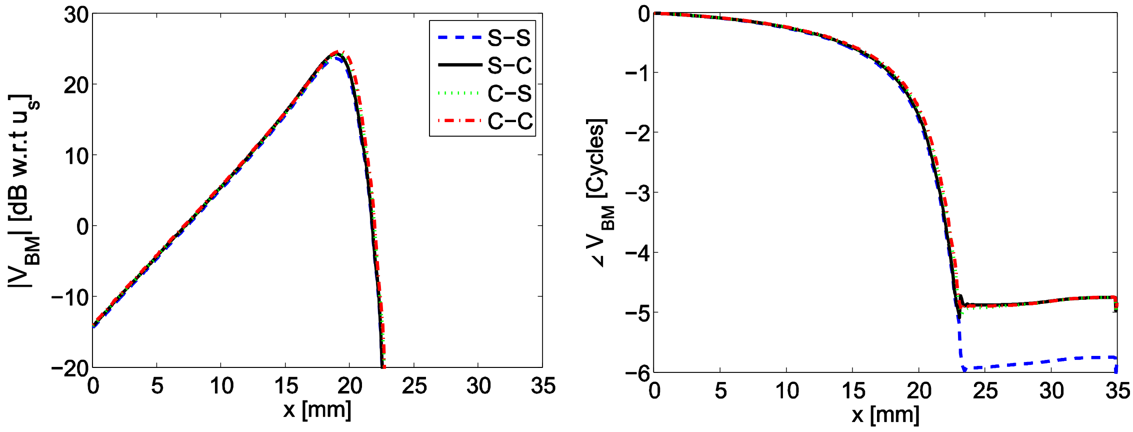

(a) (b)

Figure D. 3 The (a) magnitude and (b) phase of the modal BM velocity calculated at 1 kHz from the analytic model with locally reacting passive BM, with a damping ratio of 0.1, at different BM boundary conditions.

Although experimental observations (Cooper, 1999) and modelling studies (Homer, *et al.*, 2004) suggest that the best fit to experimental data is obtained for a beam which is simply supported at the arcuate end and clamped at the other end. The results presented here show that the fluid coupling and its effect on the coupled response are not critically dependent on this assumption. More generally it supports the assumption that the fluid coupling in cochlear models can be reasonably well estimated by assuming a single, fixed, radial profile for the BM velocity, even though in practice it may change slightly with frequency or excitation level. These results show that it is reasonable to use other combinations of the boundary conditions to calculate the fluid coupling and the coupled response.

D.2 Effect of BM Damping

It is interesting to investigate how these wavenumber distributions change with the BM damping, and Figure D. 4 shows the distributions of the real and imaginary parts of the wavenumbers for a damping ratio of 0.2, 0.14 and 0.1 respectively. What is striking about these results is the way that the imaginary part of wave 1 does not have the very significant dip after the characteristic place that it did when the damping ratio was 0.1, as shown in Figure 6.14, but now remains less negative than the imaginary parts of waves 2, 3 and 4, as seen in the analytic model in Section 6.2. This difference in the behaviour of the wavenumbers is important, since without it the difference between the numerical results and the WKB method remarked on above does not occur. In fact Watts (2000) shows a similar transition in the structure of the wavenumber distributions in his Figure 4. In his model example the damping factor of the BM, β, is assumed to be independent of frequency and position, so that the damping ratio decreases as either the excitation frequency or the natural frequency get larger. Thus Watts' results at an excitation frequency of 400 Hz correspond to a damping ratio of about 1.32 at the characteristic place for this frequency and his results at an excitation frequency of 800 Hz correspond to a damping ratio of about 0.66 at the characteristic place for that frequency.

Figure D. 4 shows the polar plot for the wavenumbers of the first four waves, calculated using the WFE method for different BM damping ratios. It can be seen that a similar transition of the behaviour of wave 1, which Watts calls the travelling wave mode, is seen to that seen in his Figure 4, with the loop corresponding to wave 2, which Watts calls the cut-off mode occurring at more negative imaginary wavenumbers for a damping ratio of greater than about 0.14 in the WFE model, and less negative imaginary wavenumbers for damping ratios of less than this value.

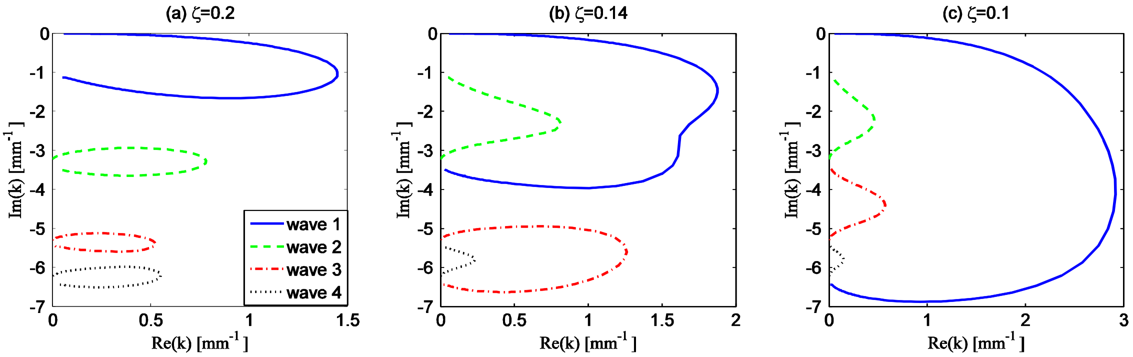

Figure D. 4 Polar plots of the locus of the real and imaginary parts of the wavenumber for wave 1 to wave 4 as the position along the cochlea increases, as shown by the arrows, calculated using the WFE model for damping ratios of (a) 0.2, (b) 0.14, (c) 0.1.

D.3 Effect of Mesh Density

The details of the wavenumber distributions in the model of the cochlea are, however, dependent on the number of fluid elements used in the cross section. In order to correctly reproduce the near-field fluid pressure very close to the BM, a fine mesh of fluid would be required. The only important property of this near-field pressure for the “slow wave”, however, is the added mass of the fluid. This is somewhat smaller for the FE grid used for the FE models than it was for the analytic models, so that the effective BM mass was increased to account for this effect, as mentioned above. It can be seen from Figure D. 5 that although the effective thickness increases with the number of element in the vertical direction, *z*, its value is less than half of the analytic value. The computation cost becomes extremely large when the number of fluid elements in the *z* direction exceeds 32.

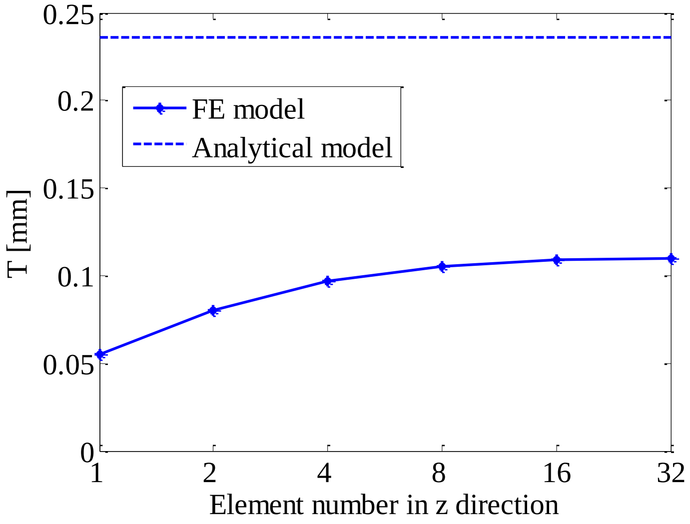

Figure D. 5 Variation of the effective thickness due to the mesh size of the FE model (solid line) and the analytic value using equation (2.25).

Although the mesh has a large effect on the fluid coupling, it is shown in Figure D. 6 that the overall responses calculated using different mesh sizes are similar on magnitude and phase basal to the characteristic place. Differences beyond this point are small in magnitude, thereby indicating that they are not very important.

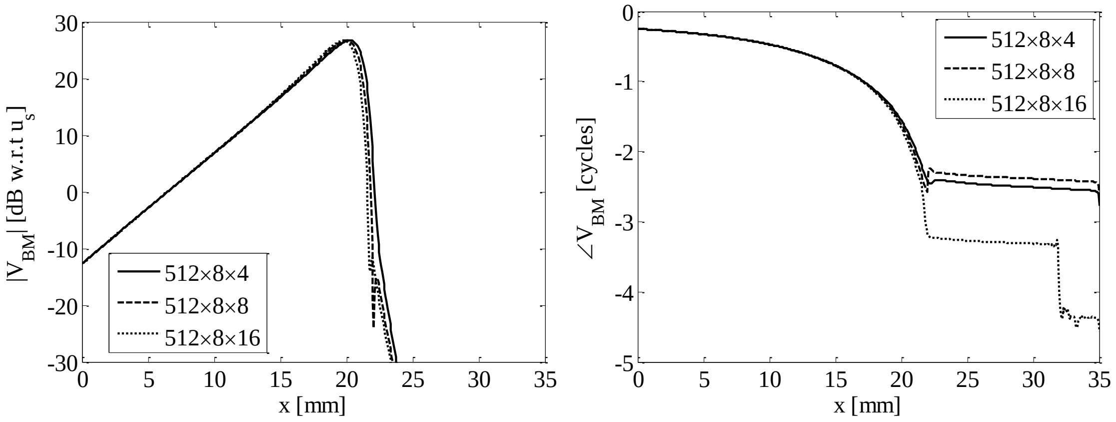

(a)

(b)

Figure D. 6 The (a) magnitude and (b) phase of the modal BM velocity calculated at 1 kHz with a damping ratio of 0.1, using the full finite element model with a mesh density of 512×8×4 (solid lines), 512×8×8 (dashed lines) and 512×8×16 (dotted lines).

The finite element model of the cochlea is also a discrete description to the real structure thus the number of elements along the cochlear model will affect the accuracy of the result. Although it is shown in literatures that the cochlea is by nature longitudinally discrete, owing to the individual rows of OHCs, the rows are typically about 5 μm apart (Pickles, 2003), which would require dividing the human cochlea up into approximately 7000 segments to create an 'accurate' model by this reasoning, this will make the computation cost extremely large and also increase the round-off error. Based on the wavenumber distribution calculated from the 1D model, as shown in Figure 6.2, the shortest wavelength is about 2.6 mm at the characteristic place, so as long as the element size meets the criterion that there are at least six elements within the shortest wavelength present, the model can be taken as an accurate representation of the continuous system (Fahy and Gardonio, 2007). The element number along the cochlear length used in this thesis is 512 which corresponds to an element size of 68 μm is sufficient enough to make the model accurate. Figure D. 7 shows variation of the BM velocity calculated using the model with 256 and 512 elements along its length. It can be seen that results calculated using 256 and 512 elements have a good agreement.

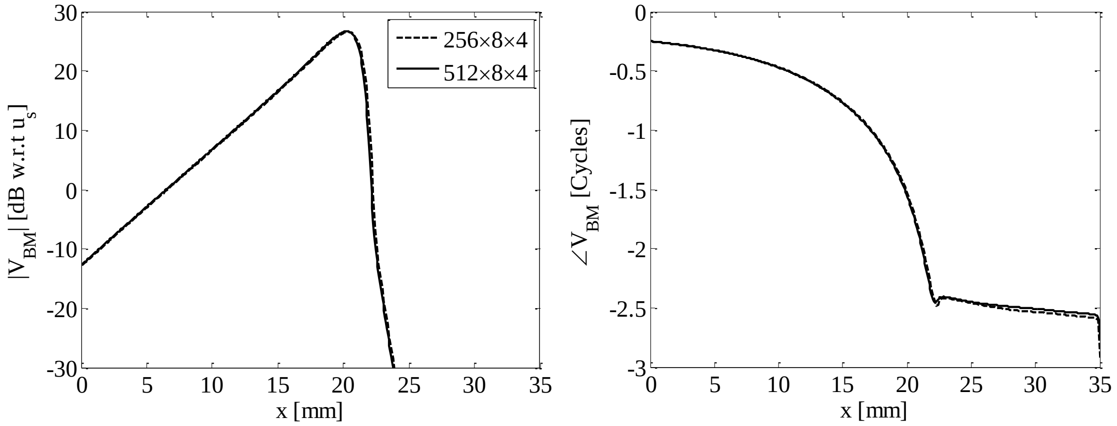

(a) (b)

Figure D. 7 Comparison of the BM velocity (a) magnitude and (b) phase calculated using different values of spatial discretisation size at 1 kHz.

Figure D. 8 shows the effects of mesh density on wavenumber distribution. Roughly speaking, increasing the number of elements in the *z* direction does not change the shape of wave 1 very much, although the magnitude of both the real and imaginary parts becomes greater. From Figure D. 5 we can see that the effective thickness will increase with the element number in the *z* direction, in other words, the added mass on the BM due to fluid loading will increase with element number in the *z* direction. For the 1D case, the wavenumber magnitude is predicted to decrease when the effective mass of the BM increases, based on equation (6.7), which is not seen in these simulations, since the wave in this 3D cochlear model is more complicated than that of the 1D model. It is not currently clear why the magnitude of the wavenumber increased with the number of elements in the FE model, as seen in Figure D. 8. This does not appear to have very much effect on the distribution of BM velocity, as seen in Figure D. 6, or on the decomposition of this into wave components, as seen below.

Figure D. 9 shows the contribution of each wave to the overall finite element response, calculated using different mesh sizes. It can be seen that a finer mesh does not change the contributions of each wave very much.

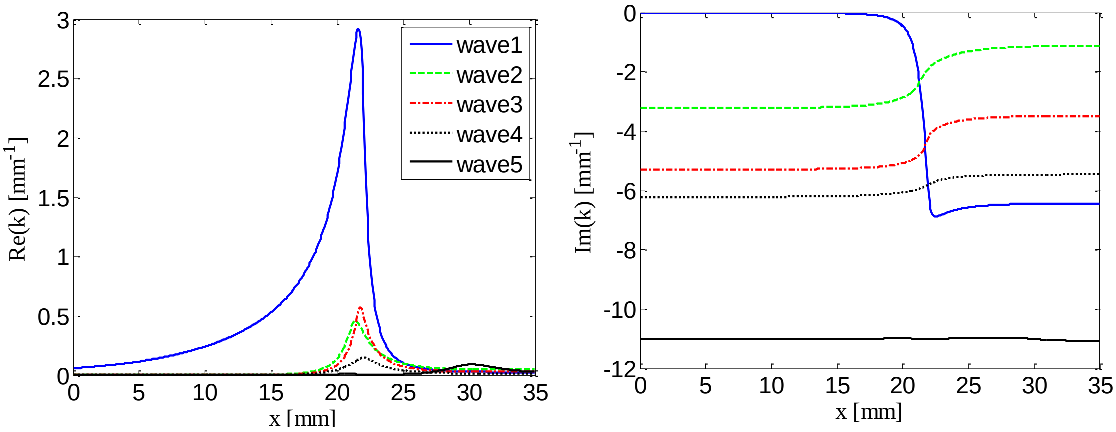

(a) Wavenumber distribution with a mesh of 512×8×4.

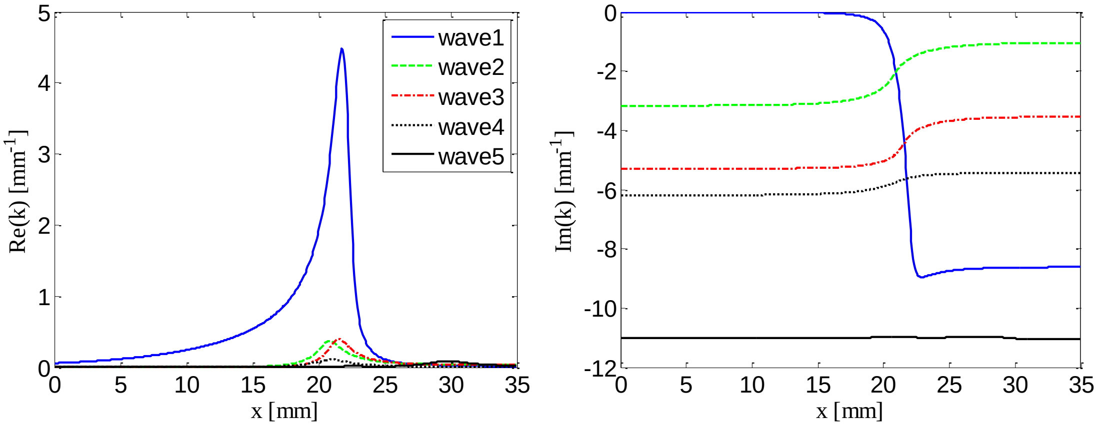

(b) Wavenumber distribution with a mesh of 512×8×8.

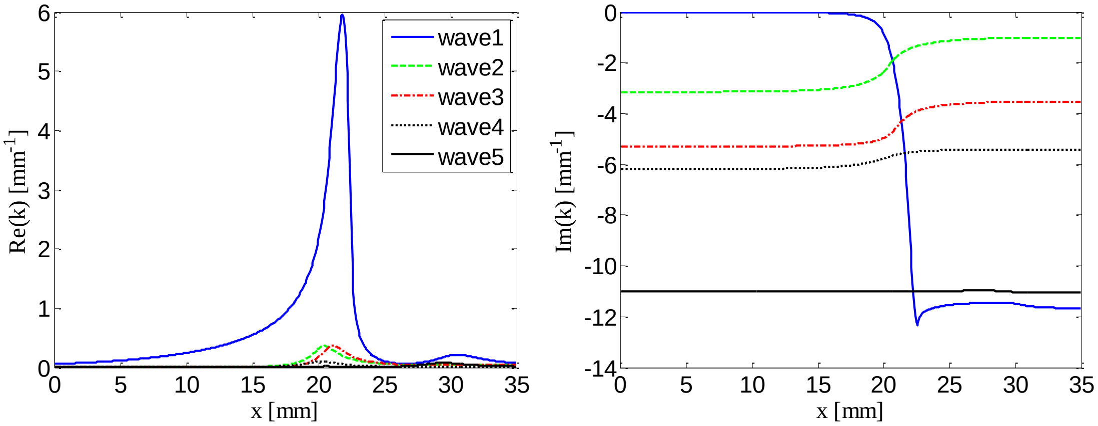

(c) Wavenumber distribution with a mesh of 512×8×16.

Figure D. 8 Wavenumber distribution of 5 of the forward-going waves, calculated using the wave finite element model of the cochlea at 1 kHz with a BM damping ratio of 0.1 with different mesh density of (a) 512×8×4, (b) 512×8×8 and (c) 512×8×16.

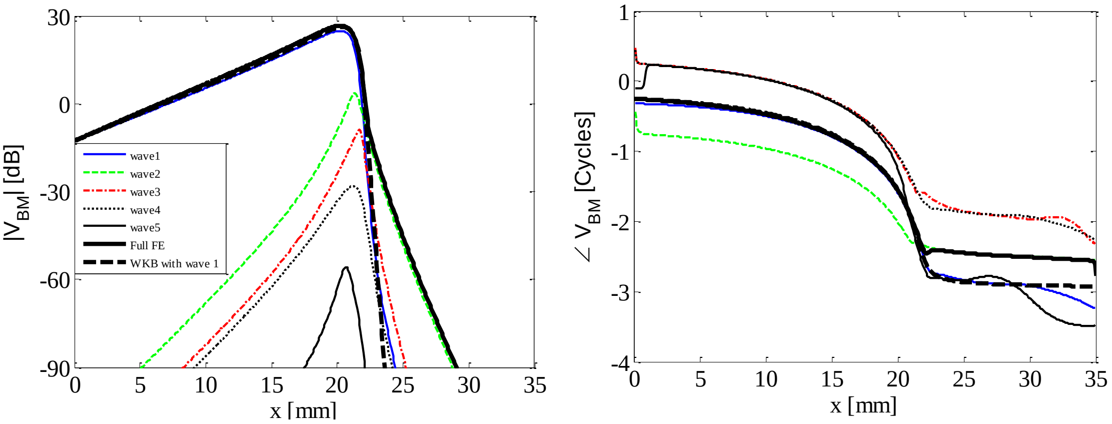

(a) Wavenumber distribution with a mesh of 512×8×4.

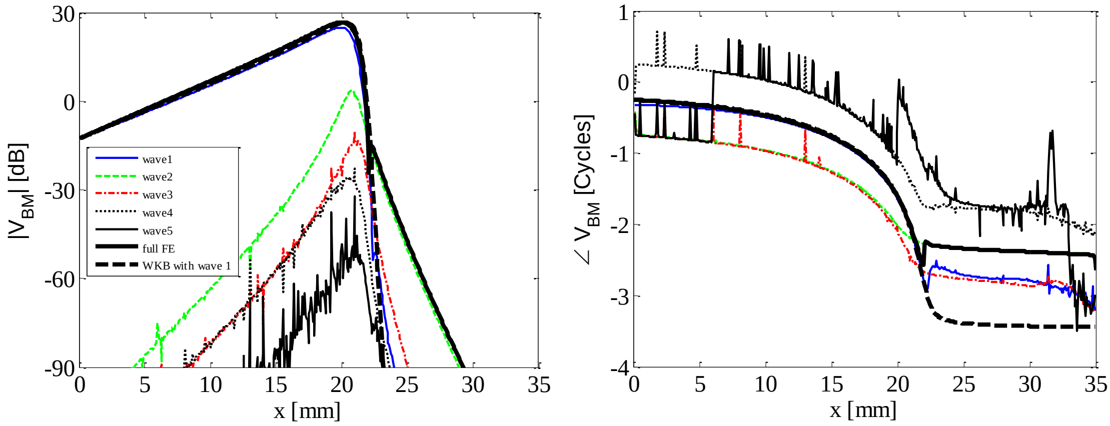

(b) Wavenumber distribution with a mesh of 512×8×8.

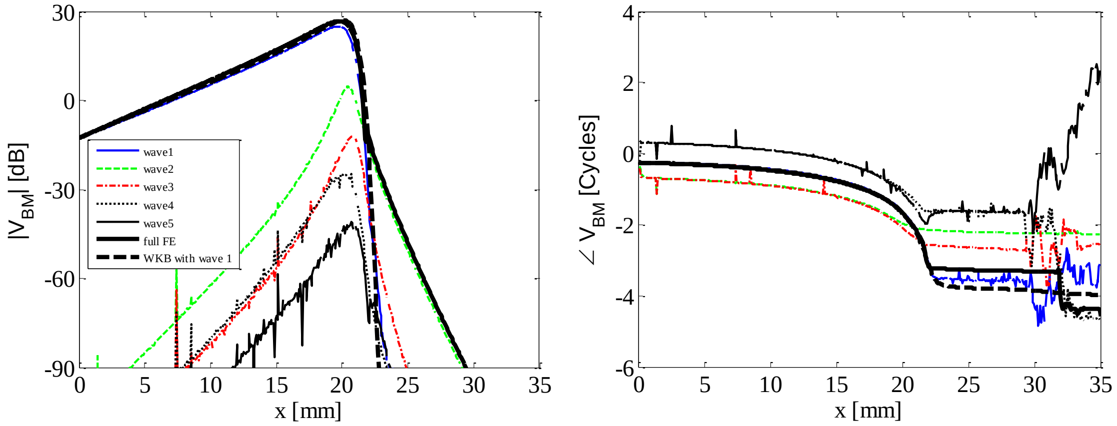

(c) Wavenumber distribution with a mesh of 512×8×16.

Figure D. 9 Decomposition of the modal BM velocity into components due to each of the forward-going waves in Figure D. 8 at 1 kHz with a BM damping ratio of 0.1 with different mesh density of (a) 512×8×4, (b) 512×8×8 and (c) 512×8×16.

References

Abdel-Rahmen, A. Y. A. (**1980**). *Matrix analysis of wave propagation in periodic systems*, PhD, University of Southampton, Southampton.

Allaire, P., Raynor, S. and Billone, M. (**1974**). Cochlear partition stiffness-a composite beam model, *The Journal of the Acoustical Society of America*, 55(6), 1252-1258.

Allemang, R. J. (**2003**). The modal assurance criterion - Twenty years of use and abuse, *Sound and Vibration*, 37(8), 14-23.

Allen, J. B. and Sondhi, M. M. (**1979**). Cochlear macromechanics: Time domain solutions, *The Journal of the Acoustical Society of America*, 66(1), 123-132.

Cai, H. and Chadwick, R. (**2003**). Radial structure of traveling waves in the inner ear, *SIAM Journal on Applied Mathematics*, 63(4), 1105-1120.

Cai, H., Manoussaki, D. and Chadwick, R. S. (**2005**). Effects of coiling on the micromechanics of the mammalian cochlea, *Journal of the Royal Society Interface*, 2(4), 341-348.

Cai, H., Shoelson, B. and Chadwick, R. S. (**2004**). Evidence of tectorial membrane radial motion in a propagating mode of a complex cochlear model, *Proceedings of the National Academy of Sciences of the United States of America*, 101(16), 6243-6248.

Carterette, E. C. (**1978**). Historical notes on research in hearing, in *Handbook of Perception*, edited by Carterette, E. C. and Friedman, M. P., Academic Press, New York,

Chadwick, R. S., Dimitriadis, E. K. and Iwasa, K. H. (**1996**). Active control of waves in a cochlear model with subpartitions, *Proceedings of the National Academy of Sciences*, 93(6), 2564-2569.

Cooper, N. P. (**1999**). Radial variation in the vibrations of the cochlear partition, 109-115.

Craggs, A. (**1971**). The transient response of a coupled plate-acoustic system using plate and acoustic finite elements, *Journal of Sound and Vibration*, 15(4), 509-528.

Crawford, A. C. and Fettiplace, R. (**1981**). An electrical tuning mechanism in turtle cochlear hair cells, *Journal of Physiology*, 312, 377-412.

Dallos, P. (**1992**). The active cochlea, *The Journal of Neuroscience*, 12(12), 4575-4585.

Dallos, P., Popper, A. N. and Fay, R. R., eds (**1996**). *The Cochlea*, Springer, New York.

de Boer, E. (**1981**). Short waves in three-dimensional cochlea models: Solution for a ‘block’ model, *Hearing Research*, 4(1), 53-77.

de Boer, E. (**1984**). Auditory physics. Physical principles in hearing theory. II, *Physics Reports*, 105(3), 141-226.

de Boer, E. (**1991**). Auditory physics. Physical principles in hearing theory. III., *Physics Reports*, 203(3), 125-231.

de Boer, E. (**1996**). Mechanics of the cochlea: Modelling efforts, in *The cochlea*, edited by Dallos, P., *et al.*, Springer, New York, 258-317.

de Boer, E. (**1998**). A method for forward and inverse solutions of a three-dimensional model of the cochlea, *The Journal of the Acoustical Society of America*, 103(6), 3725-3728.

de Boer, E. and Viergever, M. A. (**1982**). Validity of the Liouville-Green (or WKB) method for cochlear mechanics, *Hearing Research*, 8(2), 131-155.

de Boer, E. and Viergever, M. A. (**1984**). Wave propagation and dispersion in the cochlea, *Hearing Research*, 13(2), 101-112.

de La Rochefoucauld, O. and Olson, E. S. (**2007**). The role of organ of corti mass in passive cochlear tuning, *Biophysical Journal*, 93(10), 3434-3450.

Doak, P. E. (**1973**). Excitation, transmission and radiation of sound from source distributions in hard-walled ducts of finite length (I): The effects of duct cross-section geometry and source distribution space-time pattern, *Journal of Sound and Vibration*, 31(1), 1-72.

Duhamel, D., Mace, B. R. and Brennan, M. J. (**2006**). Finite element analysis of the vibrations of waveguides and periodic structures, *Journal of Sound and Vibration*, 294(1-2), 205-220.

Elliott, S. J., Lineton, B. and Ni, G. (**2011**). *Fluid coupling between the elements in a discrete model of cochlear mechanics*, ISVR Technical Memorandum 990, ISVR, University of Southampton, Southampton, 1-97.

Elliott, S. J., Lineton, B. and Ni, G. (**2011**). Fluid coupling in a discrete model of cochlear mechanics, *The Journal of the Acoustical Society of America*, 130(3), 1441-1451.

Elliott, S. J., Ni, G., Mace, B. R., *et al.* (**2012**). *Wave propagation in the cochlea*, ISVR Technical Memorandum 996, ISVR, University of Southampton, 1-95.

Everstine, G. C. (**1981**). A Symmetric Potential Formulation for Fluid-Structure interaction *Journal of Sound and Vibration*, 79(1), 157-160.

Fahy, F. and Gardonio, P. (**2007**). *Sound and structural vibration: Radiation, transmission and response*, Elsevier Academic Press, Oxford, UK.

Finnveden, S. (**2004**). Evaluation of modal density and group velocity by a finite element method, *Journal of Sound and Vibration*, 273(1-2), 51-75.

Fleischer, M., Schmidt, R. and Gummer, A. W. (**2010**). Compliance profiles derived from a three-dimensional finite-element model of the basilar membrane, *The Journal of the Acoustical Society of America*, 127(5), 2973-2991.

Fletcher, H. (**1958**). *Speech and hearing in communication*, Van Nostrand, Michigan.

Fletcher, N. H. and Rossing, T. D. (**1998**). *The physics of musical instruments*, Springer, New York.

Friswell, M. I. and Mottershead, J. E. (**1995**). *Finite element model updating in structural dynamics*, Springer, Boston.

Fuchs, P. A., Nagai, T. and Evans, M. G. (**1988**). Electrical tuning in hair cells isolated from the chick cochlea, *Journal of Neuroscience*, 8(2460-2467),

Fuhrmann, E., Schneider, W. and Schultz, M. (**1987**). Wave propagation in the cochlea (inner ear): Effects of Reissner's membrane and non-rectangular cross-section, *Acta Mechanica*, 70(1), 15-30.

Ghaffari, R., Aranyosi, A. J. and Freeman, D. M. (**2007**). Longitudinally propagating traveling waves of the mammalian tectorial membrane, *Proceedings of the National Academy of Sciences*, 104(42), 16510-16515.

Givelberg, E. and Bunn, J. (**2003**). A comprehensive three-dimensional model of the cochlea, *Journal of Computational Physics*, 191(2), 377-391.

Gold, T. (**1948**). Hearing. II. The physical basis of the action of the cochlea, *Proceedings of the Royal Society of London. Series B: Biological Sciences*, 135(881), 492-498.

Goldberg, J. E., Bogdanoff, J. L. and Marcus, L. (**1960**). On the calculation of the axisymmetric modes and frequencies of conical shells, *The Journal of the Acoustical Society of America*, 32(6), 738-742.

Graff, K. G. (**1991**). *Wave motion in elastic solids*, Oxford University Press, London.

Gry, L. (**1996**). Dynamic modelling of railway track based on wave propagation, *Journal of Sound and Vibration*, 195(3), 477-505.

Gry, L. and Gontier, C. (**1997**). Dynamic modelling of railway track: A periodic model based on a generalized beam formulation, *Journal of Sound and Vibration*, 199(4), 531-558.

Gummer, A. W., Smolders, J. W. T. and Klinke, R. (**1987**). Basilar membrane motion in the pigeon measured with the Mössbauer technique, *Hearing Research*, 26, 63-92.

Henaff, B. L., Elliott, S. J. and Maury, C. (**2003**). *Modelling wave propagation in the cochlea*, ISVR Technical Memorandum 925, ISVR, University of Southampton, 1-72.

Homer, M., Champneys, A., Hunt, G., *et al.* (**2004**). Mathematical modeling of the radial profile of basilar membrane vibrations in the inner ear, *The Journal of the Acoustical Society of America*, 116(2), 1025-1034.

Houillon, L., Ichchou, M. N. and Jezequel, L. (**2005**). Wave motion in thin-walled structures, *Journal of Sound and Vibration*, 281(3-5), 483-507.

Huxley, A. F. (**1969**). Is resonance possible in the cochlea after all?, *Nature*, 221(5184), 935-940.

Johnstone, B. M., Patuzzi, R. and Yates, G. (**1986**). Basilar membrane measurements and the travelling wave, *Hearing Research*, 22, 147-154.

Jones, G., Russell, I. and Lukashkin, A. (**2011**). Laser interferometer measurements of the visco-elastic properties of the tectorial membrane mutants, in *What Fire is in Mine Ears: Progress in Auditory Biomechanics*, edited by Shera, C. A. and Olson, E. S., Williamstown, Massachusetts, US, 419-422.

Kaizer, A. J. M. (**1979**). Theory and numerical calculation of the vibration and sound radiation of non-rigid loudspeaker cones,*62nd Convention of the Audio Engineering Society* Brussels,.

Kaizer, A. J. M. (**1979**). *Theory and numerical calculation of the vibration and sound radiation of non-rigid loudspeaker cones*, Philips Internal Report, Phiplips Research Laboratoies, Eindhoven,

Kemp, D. T. (**1978**). Stimulated acoustic emissions from within the human auditory system, *The Journal of the Acoustical Society of America*, 64(5), 1386-1391.

Kiang, N. Y. S. and Moxon, E. C. (**1974**). Tails of tuning curves of auditory-nerve fibers, *The Journal of the Acoustical Society of America*, 55(3), 620-630.

Kohllöffel, L. U. E. (**1990**). Cochlear mechanics: Coiling effects (I, II) and the absorption equation (III), *Hearing Research*, 49(1-3), 19-27.

Kolston, P. J. (**2000**). The importance of phase data and model dimensionality to cochlear mechanics, *Hearing Research*, 145, 25-36.

Kolston, P. J. and Ashmore, J. F. (**1996**). Finite element micromechanical modeling of the cochlea in three dimensions, *The Journal of the Acoustical Society of America*, 99(1), 455-467.

Kros, C. J., Rusch, A. and Richardson, G. P. (**1992**). Mechano-electrical transducer currents in hair cells of the cultured neonatal mouse cochlea, *Proceedings of the Royal Society B: Biological Sciences*, 249, 185-193.

Leissa, A. W. (**1969**). *Vibration of plates*, Scientific and Technical Information Division, National Aeronautics and Space Administration, USA.

Leissa, A. W. (**1993**). *Vibration of shells*, American Institute of Physics for the Acoustical Society of America, New York.

Liberman, M. C. (**1978**). Auditory-nerve response from cats raised in a low-noise chamber, *The Journal of the Acoustical Society of America*, 63(2), 442-455.

Lieberstein, H. M. (**1972**). The basilar membrane as a uniformly loaded plate clambed on two spiral boundaries in a plane or on two helical-spiral boundaries: relevance of the species record, *Mathematical Biosciences*, 13(1-2), 139-148.

Lighthill, M. J. (**1981**). Energy flow in the cochlea, *Journal of Fluid Mechanics*, 106, 149-213.

Lim, K.-M. and Steele, C. R. (**2002**). A three-dimensional nonlinear active cochlear model analyzed by the WKB-numeric method, *Hearing Research*, 170(1-2), 190-205.

Liu, S. and White, R. D. (**2008**). Orthotropic material properties of the gerbil basilar membrane, *The Journal of the Acoustical Society of America*, 123(4), 2160-2171.

Luo, Z., Ruf, I., Schultz, J. A., *et al.* (**2011**). Fossil evidence on evolution of inner ear cochlea in Jurassic mammals, *Proceedings of the Royal Society B: Biological Sciences*, 278, 28-34.

Lyon, R. F. (**1990**). Automatic Gain Control in Cochlear Mechanics, in *The Mechanics and Biophysics of Hearing*, edited by al., P. D. e., Springer-Verlag, Berlin,

Lyon, R. F. and Mead, C. A. (**1988**). *Cochlear hydrodynamics demystied*, Caltech Computer Science Technical Report, California Institute of Technology, Pasadena, California,

Mace, B. R., Duhamel, D., Brennan, M. J., *et al.* (**2005**). Finite element prediction of wave motion in structural waveguides, *The Journal of the Acoustical Society of America*, 117(5), 2835-2843.

Maess, M. and Gaul, L. (**2006**). Substructuring and model reduction of pipe components interacting with acoustic fluids, *Mechanical Systems and Signal Processing*, 20(1), 45-64.

Mammano, F. and Nobili, R. (**1993**). Biophysics of the cochlea: Linear approximation, *The Journal of the Acoustical Society of America*, 93(6), 3320-3332.

Manoussaki, D. and Chadwick, R. S. (**2000**). Effects of geometry on fluid loading in a coiled cochlea, *SIAM Journal on Applied Mathematics,* 61(2), 369-386.

Manoussaki, D., Dimitriadis, E. K. and Chadwick, R. S. (**2006**). Cochlea's graded curvature Effect on low frequency waves, *Physical Review Letters,* 96(8), 088701.

Manoussaki, D., Dimitriadis, E. K. and Chadwick, R. S. (**2006**). Radial profile of the basilar membrane in a coiled cochlea: Results and biological implications, *Journal of Biomechanics*, 39, Supplement 1(0), S433.

Meaud, J. and Grosh, K. (**2010**). The effect of tectorial membrane and basilar membrane longitudinal coupling in cochlear mechanics, *Journal of the Acoustical Society of America*, 127(3), 1411-1421.

Mencik, J. M. and Ichchou, M. N. (**2007**). Wave finite elements in guided elastodynamics with internal fluid, *International Journal of Solids and Structures,* 44(7-8), 2148-2167.

Morand, H. J. P. and Ohayon, R. (**1995**). *Fluid structure interaction: Applied Numerical Methods,* Wiley, New York.

Neely, S. T. (**1981**). Finite difference solution of a two-dimensional mathematical model of the cochlea, *The Journal of the Acoustical Society of America*, 69(5), 1386-1393.

Neely, S. T. (**1985**). Mathematical modelling of cochlear mechanics, *The Journal of the Acoustical Society of America*, 78(1), 345-352.

Neely, S. T. and Kim, D. O. (**1986**). A model for active elements in cochlear biomechanics, *The Journal of the Acoustical Society of America*, 79(5), 1472-1480.

Ni, G., Elliott, S. J. and Mace, B. R. (**2010**). A fluid-structural model of the cochlea using wave finite element method, 12 pp.

Nilsson, C. M. (**2004**). *Waveguide finite elements applied on a car tyre*, PhD, Royal Institute of Technology, Stockholm, Sweden.

Orris, R. M. and Petyt, M. (**1974**). A finite element study of harmonic wave propagation in periodic structures, *Journal of Sound and Vibration*, 33(2), 223-236.

Orris, R. M. and Petyt, M. (**1975**). Random response of periodic structures by a finite element technique, *Journal of Sound and Vibration*, 43(1), 1-8.

Pain, H. J. (**2006**). *The physics of vibrations and waves*, John Wiley and Sons, Chichester.

Parthasarathi, A. A., Grosh, K. and Nuttall, A. L. (**2000**). Three-dimensional numerical modeling for global cochlear dynamics, *The Journal of the Acoustical Society of America*, 107(1), 474-485.

Peterson, L. C. and Bogert, B. P. (**1950**). A dynamical theory of the cochlea, *The Journal of the Acoustical Society of America*, 22(3), 369-381.

Petyt, M. (**1990**). *Introduction to finite element vibration analysis*, Cambridge University Press, Cambridge.

Petyt, M. and Gélat, P. N. (**1998**). Vibration of loudspeaker cones using the dynamic stiffness method, *Applied Acoustics*, 53(4), 313-332.

Pickles, J. O. (**2003**). *An introduction to the physiology of hearing*, Academic Press, London.

Ramamoorthy, S., Deo, N. V. and Grosh, K. (**2007**). A mechano-electro-acoustical model for the cochlea: Response to acoustic stimuli, *The Journal of the Acoustical Society of America*, 121(5), 2758-2773.

Rao, S. S. (**2004**). *Mechanical Vibrations*, Pearson Education, Inc, New Jersey.

Rhode, W. S. (**1971**). Observations of the vibration of the basilar membrane in squirrel monkeys using the Mossbauer technique, *Journal of the Acoustical Society of America*, 49(4B), 1218-1231.

Ruggero, M. A. and Rich, N. C. (**1991**). Furosemide alters organ of Corti mechanics: evidence for feedback of outer hair cells upon the basilar membrane, *Journal of Neuroscience*, 11, 1057-1067.

Shera, C. A. (**2007**). Laser amplification with a twist: Traveling-wave propagation and gain functions from throughout the cochlea, *The Journal of the Acoustical Society of America*, 122(5), 2738-2758.

Shera, C. A., Tubis, A. and Talmadge, C. L. (**2004**). Do forward- and backward-traveling waves occur within the cochlea? Countering the critique of Nobili et al., *Journal of the Association for Research in Otolaryngology*, 5, 349-359.

Shera, C. A., Tubis, A. and Talmadge, C. L. (**2005**). Coherent reflection in a two-dimensional cochlea: Short-wave versus long-wave scattering in the generation of reflection-source otoacoustic emissions, *Journal of the Acoustical Society of America*, 118(1), 287-313.

Shorter, P. J. (**2004**). Wave propagation and damping in linear viscoelastic laminates, *The Journal of the Acoustical Society of America*, 115(5), 1917-1925.

Steele, C. R. (**1974**). Behavior of the basilar membrane with pure-tone excitation, *The Journal of the Acoustical Society of America*, 55(1), 148-162.

Steele, C. R. and Miller, C. E. (**1980**). An improved WKB calculation for a two-dimensional cochlear model, *The Journal of the Acoustical Society of America*, 68(1), 147-148.

Steele, C. R. and Taber, L. A. (**1979**). Comparison of WKB and finite difference calculations for a two-dimensional cochlear model, *The Journal of the Acoustical Society of America*, 65(4), 1001-1006.

Steele, C. R. and Taber, L. A. (**1979**). Comparison of WKB calculations and experimental results for three-dimensional cochlear models, *The Journal of the Acoustical Society of America*, 65(4), 1007-1018.

Steele, C. R. and Zais, J. G. (**1985**). Effect of coiling in a cochlear model, *The Journal of the Acoustical Society of America*, 77(5), 1849-1852.

Szilard, R. (**2004**). *Theories and applications of plate analysis: classical, numerical and engineering methods*, John Wiley and sons, Hoboken.

Taber, L. A. and Steele, C. R. (**1981**). Cochlear model including three-dimensional fluid and four modes of partition flexibility, *The Journal of the Acoustical Society of America*, 70(2), 426-436.

Thorne, M., Salt, A., Mott, J. E. d., *et al.* (**1999**). Cochlear fluid spaces for six species derived from reconstructions of three-dimensional magnetic resonant images., *Journ. American Laryngological, Rhinological and Otological Soc*, 109(10), 161-168.

Tuck-Lee, J. P., Pinsky, P. M., Steele, C. R., *et al.* (**2008**). Finite element modeling of acousto-mechanical coupling in the cat middle ear, *The Journal of the Acoustical Society of America*, 124(1), 348-362.

Viergever, M. A. (**1978**). Basilar membrane motion in a spiral-shaped cochlea, *The Journal of the Acoustical Society of America*, 64(4), 1048-1053.

Voldřich, L. (**1978**). Mechanical properties of basilar membrane, *Acta Otolaryngol*, 86(5-6), 331-335.

von Békésy, G. (**1960**). *Experiments in hearing*, McGraw-Hill, New York.

von Békésy, G. (**1970**). Travelling waves as frequency analysers in the cochlea, *Nature*, 225(5239), 1207-1209.

Waki, Y. (**2007**). *On the application of finite element analysis to wave motion in one-dimensional waveguides*, PhD, University of Southampton, Southampton.

Waki, Y., Mace, B. R. and Brennan, M. J. (**2006**). *On numerical issues for the wave/finite element method*, ISVR Technical Memorandum 964, University of Southampton, 1-55.

Waki, Y., Mace, B. R. and Brennan, M. J. (**2009**). Numerical issues concerning the wave and finite element method for free and forced vibrations of waveguides, *Journal of Sound and Vibration*, 327(1-2), 92-108.

Watts, L. (**2000**). The mode-coupling Liouville-Green approximation for a two-dimensional cochlear model, *The Journal of the Acoustical Society of America*, 108(5), 2266-2271.

Werner, S. (**2004**). *Vibrations of Shells and Plates*, Marcel Dekker, Inc., New York.

Wilson, J. P. (**1980**). Evidence for a cochlear origin for acoustic re-emissions, threshold fine-structure and tonal tinnitus, *Hearing Research*, 2(3-4), 233-252.

Wittbrodt, M. J., Steele, C. R. and Puria, S. (**2004**). Fluid-structure interaction in a physical model of the human cochlea, *The Journal of the Acoustical Society of America*, 116(4), 2542-2543.

Yoon, Y., Puria, S. and Steele, C. R. (**2007**). Intracochlear pressure and derived quantities from a three-dimensional model, *The Journal of the Acoustical Society of America*, 122(2), 952-966.

Zakis, J. and Witte, M. (**2001**). Modelling of the cochlea using Java 3D,

Zhang, Z. and Cheng, C. (**2007**). Analytical solutions for axisymmetric vibration of loudspeaker cones in transitional range, *Applied Acoustics*, 68(10), 1135-1155.

Zhong, W., Lin, J. and Qiu, C. (**1991**). Eigenproblem of substructure chain and the expansion solution, *Acta Mechanica Sinica*, 7(2), 169-177.

Zhong, W. X. and Williams, F. W. (**1995**). On the direct solution of wave propagation for repetitive structures, *Journal of Sound and Vibration*, 181(3), 485-501.

Zweig, G., Lipes, R. and Pierce, J. R. (**1976**). The cochlear compromise, *The Journal of the Acoustical Society of America*, 59(4), 975-982.

Zwislocki, J. J. (**1948**). Theorie der Schneckenmechanik: Qualitative und quantitative Analyse (Theory of the mechanics of the cochlea), *Acta Oto-Laryngologica*, 72 (Suppl.), 1-76.

Zwislocki, J. J. (**1953**). Review of recent mathematical theories of cochlear dynamics, *Journal of the Acoustical Society of America*, 25(4), 743-751.

Zwislocki, J. J. (**1974**). Cochlear waves: interaction between theory and experiments, *The Journal of the Acoustical Society of America*, 55(3), 578-583.

Zwislocki, J. J., Rosowski, A. J. J. and Reviewer (**2003**). Auditory sound transmission: An autobiographical perspective, *The Journal of the Acoustical Society of America*, 113(3), 1191.